HADAMARD-BABICH ANSATZ AND FAST HUYGENS SWEEPING METHOD FOR POINT-SOURCE ELASTIC WAVE EQUATIONS IN AN INHOMOGENEOUS MEDIUM AT HIGH FREQUENCIES

By

Jian Song

A DISSERTATION

Submitted to
Michigan State University
in partial fulfillment of the requirements
for the degree of

Applied Mathematics — Doctor of Philosophy
Computational Mathematics, Science and Engineering — Dual Major

2022

ABSTRACT

HADAMARD-BABICH ANSATZ AND FAST HUYGENS SWEEPING METHOD FOR POINT-SOURCE ELASTIC WAVE EQUATIONS IN AN INHOMOGENEOUS MEDIUM AT HIGH FREQUENCIES

By

Jian Song

Asymtotic methods are efficient for solving wave equations in the high frequency regime. In the thesis, we first develop a new asymptotic ansatz for point source elastic wave equations in an inhomogeneous medium. Then, we propose a fast Huygens sweeping method to construct a globally valid Green's functions in the presence of caustics. Finally, an Eulerian partial-differential-equation method is proposed to compute complex-valued eikonals in attenuating media.

In Chapter 3, we develop the Hadamard-Babich (H-B) ansatz for frequency-domain point source elastic wave equations in an inhomogeneous medium in the high-frequency regime. First, we develop a novel asymptotic series, dubbed Hadamard's ansatz, to form the fundamental solution of the Cauchy problem for the time-domain point-source (TDPS) elastic wave equations in the region close to the source. Then, the governing equations for the unknown asymptotics of the ansatz are derived including the traveltime functions and dyadic coefficients. A matching condition is proposed to initialize the data of unknowns at the source. To treat singularity of dyadic coefficients at the source, smoother dyadic coefficients are then introduced. Finally, we obtain the H-B ansatz for the frequency-domain point-source (FDPS) elastic wave equations by directly taking the Fourier transform of Hadamard's ansatz in time. Numerical examples demonstrate the accuracy of our method.

In Chapter 4, we propose a new truncated Hadamard-Babich ansatz based globally valid asymptotic method, dubbed the fast Huygens sweeping method, for computing Green's

functions of FDPS elastic wave equations in inhomogeneous media in the high-frequency regime and in the presence of caustics. The first novelty of the fast Huygens sweeping method is that the Huygens-Kirchhoff secondary-source principle is used to construct a globally valid asymptotic solution by integrating many locally valid asymptotic solutions so that caustics can be treated automatically and implicitly. The precomputed asymptotic ingredients can be used to construct Green's functions of elastic wave equations for many different point sources and for arbitrary frequencies. The second novelty is that a butterfly algorithm is adapted to accelerate matrix-vector products induced by the discretization of the Huygens-Kirchhoff integral. The computational cost of the butterfly algorithm is $O(N \log N)$ which is in nearly optimal complexity in terms of the total number of mesh points N. Numerical examples are presented to demonstrate the performance and accuracy of the new method.

In Chapter 5, we propose a Eulerian partial-differential-equation method to solve complex-valued eikonals in attenuating media. In the regime of high-frequency asymptotics, a complex-valued eikonal is an essential ingredient for describing wave propagation in attenuating media, where the real and imaginary parts of the eikonal function capture dispersion effects and amplitude attenuation of seismic waves, respectively. Therefore, a unified framework to eulerianize several popular approximate real-space ray-tracing methods for complex-valued eikonals is proposed so that the real and imaginary parts of the eikonal function satisfy the classical real-space eikonal equation and a novel real-space advection equation, respectively, and we dub the resulting method the Eulerian partial-differential-equation method. We further develop highly efficient high-order methods to solve these two equations by using the factorization idea and the Lax-Friedrichs weighted essentially non-oscillatory (WENO) schemes. Numerical examples demonstrate that the proposed method yields highly accurate complex-valued eikonals, analogous to those from ray-tracing methods.

ACKNOWLEDGMENTS

Firstly, I would like to express my deepest gratitude to my advisor Prof. Qian, Jianliang, for his sincere support and useful advise during my research. His invaluable patience and feedback helped me in all the time of my research. I am extremely grateful for his assistance and suggestions throughout my study at MSU.

I am also grateful to Prof. Zhou, Zhengfang, Prof. Christlieb, Andrew, and Prof. Yang, Yang for serving on my thesis committee and insightful comments and suggestions. I would like to extend my sincere thanks to all the professors who I took the classes from and the support staff of Department of Mathematics.

I would like to thank Dr. Lu, Wangtao, Dr. Hu, Jiangtao, and Dr. Liu, Yang for their helpful advise and suggestions in my research. I would also like to thank all my friends for moral support and encouragement in my life.

Lastly, I would like to offer my special thanks to my family, especially my parents. Their belief in me has kept my spirits and motivation high throughout writing the thesis.

TABLE OF CONTENTS

LIST OF TABLES . . . viii

LIST OF FIGURES . . . ix

Chapter 1 Introduction . . . 1
1.1 Hadamard-Babich ansatz for the Helmholtz equation and Maxwell's equations 1
1.2 Hadamard-Babich ansatz for frequency-domain point-source elastic wave equations . . . 4
1.3 Fast Huygens sweeping method for time-harmonic elastic wave equations in inhomogeneous media . . . 6
1.4 Eulerian partial-differential-equation methods for complex-valued eikonals in attenuating media . . . 9
1.5 Contents . . . 13

Chapter 2 Hardmard-Babich ansatz for the Helmholtz equation and Maxwell's equations . . . 15
2.1 Babich ansatz for the Helmholtz equation . . . 15
2.2 Babich-like ansatz for Maxwell's equations . . . 17
2.3 High order Eulerian asymptotics . . . 19
2.3.1 High order factorization of eikonal . . . 19
2.3.2 High-order factorization of amplitudes v_s for the Helmholtz equation 20
2.3.3 High-order factorization of amplitudes $\tilde{\boldsymbol{A}}_s$ for Maxwell's equations . . 22
2.4 High-order schemes for computing the eikonal and transport equations . . . 23
2.5 High-order Lax-Friedrichs WENO schemes . . . 24
2.5.1 Lax-Friedrichs Hamiltonian . . . 25
2.5.2 High order Lax-Friedrichs WENO schemes . . . 27
2.6 Numerical example of high-order Lax-Friedrichs WENO-based schemes for computing traveltime τ . . . 28
2.7 Expected convergence behavior . . . 29

Chapter 3 Hadamard-Babich ansatz for point-source Elastic wave equations . . . 32
3.1 Cauchy problem of point-source elastic wave equations . . . 33
3.1.1 Solution of Cauchy problem in a homogeneous medium . . . 34
3.2 Hadamard's method for deriving asymptotic series for the case of an inhomogeneous medium . . . 37
3.3 Case I, the S wave: $\nabla\mathcal{T}\cdot\boldsymbol{A}_j^0=0$ and $4\rho\mathcal{T}-\mu|\nabla\mathcal{T}|^2=0$ . . . 41
3.3.1 S-wave transport equations for $\boldsymbol{A}^0$ and $\boldsymbol{A}^1$ . . . 42
3.3.2 S-wave transport equations for general $\boldsymbol{A}^l$ . . . 46
3.3.3 S wave: verification in a homogeneous medium . . . 47

3.3.4 S wave: governing equations for desingularizing $\boldsymbol{A}^l$ . . . 50
3.4 Case II, P wave: $\boldsymbol{A}_j^0 \parallel \nabla\mathcal{T}$ and $4\rho\mathcal{T} - (\lambda+2\mu)|\nabla\mathcal{T}|^2 = 0$ . . . 52
3.4.1 P-wave transport equations for $\boldsymbol{A}^0$ and $\boldsymbol{A}^1$ . . . 53
3.4.2 P-wave transport equations for general $\boldsymbol{A}^l$ . . . 57
3.4.3 P wave: verification in a homogeneous medium . . . 58
3.4.4 P wave: governing equations for desingularized $\boldsymbol{A}^l$ . . . 60
3.5 Initial conditions for the traveltime and amplitudes . . . 61
3.5.1 Initial conditions for S-wave . . . 61
3.5.2 Initial conditions for P-wave . . . 70
3.6 Hadamard-Babich ansatz in the frequency domain . . . 78
3.7 Numerical implementation . . . 79
3.7.1 Numerical computation for S waves . . . 79
3.7.2 Numerical computation for P waves . . . 81
3.8 Numerical examples . . . 82
3.8.1 Example 1: Constant model . . . 83
3.8.2 Example 2: A variable density model . . . 85
3.8.3 Example 3: A Gaussian model . . . 87

Chapter 4 Fast Huygens' sweeping method for time-harmonic high-frequecy elastic wave equations in inhomogeneous media . . . 90
4.1 Numerics for the truncated H-B ansatz . . . 92
4.1.1 Truncating the ansatz for the S-wave . . . 92
4.1.1.1 Computing take-off directions . . . 95
4.1.1.2 Computing $\tilde{\boldsymbol{A}}^{S0}$ . . . 96
4.1.1.3 Computing $\tilde{\boldsymbol{A}}^{S1}$ . . . 98
4.1.2 Truncating the ansatz for the P-wave . . . 100
4.2 Huygens' principle based globally valid Green's functions . . . 102
4.2.1 Huygens-Kirchhoff formula for elastic wave fields . . . 102
4.2.2 Huygens principle based sweeping method . . . 109
4.2.3 Planer-layer based Huygens sweeping . . . 110
4.2.4 Data tables and compression . . . 112
4.2.5 Discretization of Huygens-Kirchhoff integral . . . 113
4.2.6 A butterfly algorithm . . . 117
4.2.7 Complexity analysis of the overall algorithm . . . 124
4.2.7.1 Preprocessing: computing asymptotic ingredients . . . 125
4.2.7.2 Postprocessing: constructing global Green's functions . . . 126
4.3 Numerical examples . . . 127
4.3.1 Example 1: Constant model . . . 128
4.3.2 Example 2: A Gaussian model . . . 130
4.3.3 Example 3: A Gaussian model . . . 134
4.3.4 Example 4: A waveguide model . . . 136

Chapter 5 Eulerian partial-differential-equation methods for complex-valued eikonals in attenuating media . . . 145

5.1 High-order numerical methods for computing complex-valued traveltimes . . 146
5.1.1 Eulerian PDE framework for complex-valued traveltimes 146
5.1.2 Case (1): Viscoacoustic ray tracing and Eulerian equations 147
5.1.3 Case (2): Real viscoelastic ray tracing and Eulerian equations 149
5.1.4 Case (3): Real elastic ray tracing and Eulerian equations 150
5.1.5 Factorized Eulerian PDEs 151
5.1.6 Third-order LxF-WENO sweeping method 153
5.2 Numerical examples 157
5.2.1 Eulerian examples for viscoacoustic ray tracing 157
5.2.2 Eulerian examples for real-elastic and real-viscoelastic ray tracing . . 162

Chapter 6 Conclusion 171

APPENDICES 173
Appendix A Derivation of some ingredients for governing equations of S and P waves174
Appendix B Hadamard ansatz for anisotropic wave equations 178
Appendix C High-order factorization for computing T^* 182

BIBLIOGRAPHY 185

LIST OF TABLES

Table 2.1: L^2-norm error of traveltime τ computed by first-, third-, fifth-order Lax-Friedrichs WENO schemes with varying h. 29

Table 3.1: Example 1: L^2-norm errors between the new ansatz based solutions and the FDTD solution in a region excluding a neighborhood of the source. . . 85

Table 3.2: Example 3: L^2-norm errors between the two-term ansatz solution and the FDTD solution in a region excluding a neighborhood of the source. 89

Table 4.1: Example 1 for the constant parameters. L_∞-norm errors between the numerical solutions of fast Huygens sweeping method and exact solutions. ω: the frequency parameter; NPW: the number of points per wavelength; p: the Chebyshev nodes used in each dimension; E_∞: the L_∞-norm errors between solutions by two different approaches. 130

Table 4.2: Example 1 for the constant parameters. Computational time using the butterfly algorithm. ω: the frequency parameter; NPW: the number of points per wavelength; T_M (unit: s): CPU time for the construction of total nine elements of the Green's function for the S-wave in the receiver domain Ω_2 by the butterfly algorithm; p: the Chebyshev nodes used in each dimension; E_∞: the L_∞-norm errors between solutions by two different approaches. 130

Table 4.3: Example 2 for the Gaussian model. Computational time using the butterfly algorithm. ω: the frequency parameter; NPW: the number of points per wavelength; T_M (unit: s): CPU time for the construction of total nine elements of the Green's function for the S-wave in the receiver domain Ω_2 by the butterfly algorithm; p: the Chebyshev nodes used in each dimension; E_∞: the L_∞-norm errors between solutions by two different approaches. 134

LIST OF FIGURES

Figure 3.1: Example 1 with $\boldsymbol{r}_0 = (0.25, 0.25, 0.25)^T$ and $\omega = 16\pi$. The real part of the yy-component of $\boldsymbol{G}(\boldsymbol{r}; \boldsymbol{r}_0)$ at $x = 0.25$ computed via (a) one-term ansatz $\boldsymbol{G}_1$; (b) two-term ansatz $\boldsymbol{G}_2$; (c) exact solution $\boldsymbol{G}_{hom}$. 84

Figure 3.2: Example 1 with $\boldsymbol{r}_0 = (0.25, 0.25, 0.25)^T$ and $\omega = 16\pi$. The real part of the yy-component of $\boldsymbol{G}(\boldsymbol{r}; \boldsymbol{r}_0)$ at $x = 0.25$ and at (a) $y = 0.25$; (b) $y = 0.23$; (c) $y = 0.15$. Green dash line: $\boldsymbol{G}_1$; black circle line: $\boldsymbol{G}_2$; red solid line: exact solution $\boldsymbol{G}_{hom}$. 84

Figure 3.3: Example 1 with $\boldsymbol{r}_0 = (0.25, 0.25, 0.25)^T$ and $\omega = 32\pi$. The real part of the zz-component of $\boldsymbol{G}(\boldsymbol{r}; \boldsymbol{r}_0)$ at $y = 0.25$ computed via (a) one-term ansatz $\boldsymbol{G}_1$; (b) two-term ansatz $\boldsymbol{G}_2$; (c) exact solution $\boldsymbol{G}_{hom}$. 84

Figure 3.4: Example 1 with $\boldsymbol{r}_0 = (0.25, 0.25, 0.25)^T$ and $\omega = 32\pi$. The real part of the zz-component of $\boldsymbol{G}(\boldsymbol{r}; \boldsymbol{r}_0)$ at $y = 0.25$ and at (a) $x = 0.25$; (b) $x = 0.23$; (c) $x = 0.15$. Green dash line: $\boldsymbol{G}_1$; black circle line: $\boldsymbol{G}_2$; red solid line: exact solution $\boldsymbol{G}_{hom}$. 85

Figure 3.5: Example 2 with $\boldsymbol{r}_0 = (0.25, 0.25, 0.25)^T$ and $\omega = 8\pi$. The real part of the yy-component of $\boldsymbol{G}(\boldsymbol{r}; \boldsymbol{r}_0)$ at $x = 0.25$ computed via (a) one-term ansatz $\boldsymbol{G}_1$; (b) two-term ansatz $\boldsymbol{G}_2$; (c) FDTD method. 86

Figure 3.6: Example 2 with $\boldsymbol{r}_0 = (0.25, 0.25, 0.25)^T$ and $\omega = 8\pi$. The real part of the yy-component of $\boldsymbol{G}(\boldsymbol{r}; \boldsymbol{r}_0)$ at $x = 0.25$ and at (a) $y = 0.25$; (b) $y = 0.23$; (c) $y = 0.15$. Green dash line: $\boldsymbol{G}_1$; black circle line: $\boldsymbol{G}_2$; red solid line: FDTD-based solution. 86

Figure 3.7: Example 2 with $\boldsymbol{r}_0 = (0.25, 0.25, 0.25)^T$ and $\omega = 16\pi$. The real part of the yy-component of $\boldsymbol{G}(\boldsymbol{r}; \boldsymbol{r}_0)$ at $x = 0.25$ computed via (a) one-term ansatz $\boldsymbol{G}_1$; (b) two-term ansatz $\boldsymbol{G}_2$; (c) FDTD method. 87

Figure 3.8: Example 2 with $\boldsymbol{r}_0 = (0.25, 0.25, 0.25)^T$ and $\omega = 16\pi$. The real part of the yy-component of $\boldsymbol{G}(\boldsymbol{r}; \boldsymbol{r}_0)$ at $x = 0.25$ and at (a) $y = 0.25$; (b) $y = 0.23$; (c) $y = 0.15$. Green dash line: $\boldsymbol{G}_1$; black circle line: $\boldsymbol{G}_2$; red solid line: FDTD-based solution. 87

Figure 3.9: Example 3 with $\boldsymbol{r}_0 = (0.25, 0.25, 0.25)^T$ and $\omega = 16\pi$. The real part of the zz-component of $\boldsymbol{G}(\boldsymbol{r}; \boldsymbol{r}_0)$ at $y = 0.25$ computed via (a) one-term ansatz $\boldsymbol{G}_1$; (b) two-term ansatz $\boldsymbol{G}_2$; (c) FDTD method. Mesh in (a) and (b): $51 \times 51 \times 51$; mesh in (c): $101 \times 101 \times 101$. 88

Figure 3.10: Example 3 with $\boldsymbol{r}_0 = (0.25, 0.25, 0.25)^T$ and $\omega = 16\pi$. The real part of the zz-component of $\boldsymbol{G}(\boldsymbol{r}; \boldsymbol{r}_0)$ at $y = 0.25$ and at (a) $x = 0.25$; (b) $x = 0.23$; (c) $x = 0.15$. Green dash line: $\boldsymbol{G}_1$; black circle line: $\boldsymbol{G}_2$; red solid line: FDTD-based solution. 88

Figure 3.11: Example 3 with $\boldsymbol{r}_0 = (0.25, 0.25, 0.25)^T$ and $\omega = 16\pi$. The real part of the yy-component of $\boldsymbol{G}(\boldsymbol{r}; \boldsymbol{r}_0)$ at $x = 0.25$ computed via (a) one-term ansatz $\boldsymbol{G}_1$; (b) two-term ansatz $\boldsymbol{G}_2$; (c) FDTD method. Mesh in (a) and (b): $51 \times 51 \times 51$; mesh in (c): $101 \times 101 \times 101$. 89

Figure 3.12: Example 3 with $\boldsymbol{r}_0 = (0.25, 0.25, 0.25)^T$ and $\omega = 16\pi$. The real part of the yy-component of $\boldsymbol{G}(\boldsymbol{r}; \boldsymbol{r}_0)$ at $x = 0.25$ and at (a) $y = 0.25$; (b) $y = 0.23$; (c) $y = 0.15$. Green dash line: $\boldsymbol{G}_1$; black circle line: $\boldsymbol{G}_2$; red solid line: FDTD-based solution. 89

Figure 4.1: Huygens-Kirchhoff formula for wave field extrapolation. (a) Spherical domains. (b) Planar domains. 103

Figure 4.2: The computational domain is partitioned into three layers: Ω_1, Ω_2, and Ω_3. The first layer Ω_1 contains the primary source $\boldsymbol{r}_0$; the source plane S_1 is placed in Ω_1 and is d_f wide away from Ω_2; the source plane S_2 is d_f wide away from Ω_3 and locates in Ω_2. 111

Figure 4.3: Example 1 with $\boldsymbol{r}_0 = (1.0, 1.0, 0.2)^T$ and $\omega = 24\pi$. The real part of xx-component of $\boldsymbol{G}(\boldsymbol{r}; \boldsymbol{r}_0)$ at $y = 1.0$ computed via (a) butterfly-algorithm−based Huygens sweeping method with $p = 13$; (b) exact solution. The detailed comparison of the real part of xx-component of $\boldsymbol{G}(\boldsymbol{r}; \boldsymbol{r}_0)$ at (c): line x=1.0, y=1.0 and (d): line x =0.8, y=1.0. Red solid line: exact solution; Black circle: Huygens sweeping solution. Mesh $121 \times 121 \times 121$. 131

Figure 4.4: Example 1 with $\boldsymbol{r}_0 = (1.0, 1.0, 0.2)^T$ and $\omega = 24\pi$. The real part of zz-component of $\boldsymbol{G}(\boldsymbol{r}; \boldsymbol{r}_0)$ at $y = 1.0$ computed via (a) butterfly-algorithm−based Huygens sweeping method with $p = 13$; (b) exact solution. The detailed comparison of the real part of zz-component of $\boldsymbol{G}(\boldsymbol{r}; \boldsymbol{r}_0)$ at (c): line x=1.0, y=1.0 and (d): line x =0.8, y=1.0. Red solid line: exact solution; Black circle: Huygens sweeping solution. Mesh $121 \times 121 \times 121$. 132

Figure 4.5: Example 1 with $\boldsymbol{r}_0 = (1.0, 1.0, 0.2)^T$ and $\omega = 24\pi$. The real part of xz-component of $\boldsymbol{G}(\boldsymbol{r}; \boldsymbol{r}_0)$ at $y = 1.0$ computed via (a) butterfly-algorithm−based Huygens sweeping method with $p = 13$; (b) exact solution. The detailed comparison of the real part of xz-component of $\boldsymbol{G}(\boldsymbol{r}; \boldsymbol{r}_0)$ at (c): line x=1.0, y=1.0 and (d): line x =0.8, y=1.0. Red solid line: exact solution; Black circle: Huygens sweeping solution. Mesh $121 \times 121 \times 121$. 133

Figure 4.6: Example 2 with $\boldsymbol{r}_0 = (1.0, 1.0, 0.2)^T$ and $\omega = 10\pi$. The real part of xx-component of $\boldsymbol{G}(\boldsymbol{r}; \boldsymbol{r}_0)$ at $y = 1.0$ computed via (a) the Huygens sweeping method with $p = 13$; (b) FDTD method. The detailed comparison of the real part of xx-component of $\boldsymbol{G}(\boldsymbol{r}; \boldsymbol{r}_0)$ at (c): line x=1.0, y=1.0 and (d): line x =0.8, y=1.0. Red solid line: FDTD solution; Black circled line: solution of the Huygens sweeping method. Mesh in (a): $121 \times 121 \times 121$; mesh in (b): $401 \times 401 \times 401$. 135

Figure 4.7: Example 2 with $\boldsymbol{r}_0 = (1.0, 1.0, 0.2)^T$ and $\omega = 10\pi$. The real part of zz-component of $\boldsymbol{G}(\boldsymbol{r}; \boldsymbol{r}_0)$ at $y = 1.0$ computed via (a) the Huygens sweeping method with $p = 13$; (b) FDTD solution. The detailed comparison of the real part of zz-component of $\boldsymbol{G}(\boldsymbol{r}; \boldsymbol{r}_0)$ at (c): line x=1.0, y=1.0 and (d): line x =0.8, y=1.0. Red solid line: FDTD solution; Black circled line: solution of the Huygens sweeping method. Mesh in (a): $121 \times 121 \times 121$; mesh in (b): $401 \times 401 \times 401$. 136

Figure 4.8: Example 2 with $\boldsymbol{r}_0 = (1.0, 1.0, 0.2)^T$ and $\omega = 20\pi$. The real part of (a): xx- and (b): zz- component of $\boldsymbol{G}(\boldsymbol{r}; \boldsymbol{r}_0)$ at $y = 1.0$ computed by the Huygens sweeping method with $p = 13$. Mesh $241 \times 241 \times 241$. 137

Figure 4.9: Example 3 with $\boldsymbol{r}_0 = (0.8, 1.0, 0.2)^T$ and $\omega = 12\pi$. The real part of xx-component of $\boldsymbol{G}(\boldsymbol{r}; \boldsymbol{r}_0)$ at $y = 1.0$ computed via (a) the Huygens sweeping method with $p = 13$; (b) FDTD method. The detailed comparison of the real part of xx-component of $\boldsymbol{G}(\boldsymbol{r}; \boldsymbol{r}_0)$ at (c): line x=1.0, y=1.0 and (d): line x =1.2, y=1.0. Red solid line: FDTD solution; Black circled line: solution of the Huygens sweeping method. Mesh in (a): $121 \times 121 \times 121$; mesh in (b): $401 \times 401 \times 401$. 138

Figure 4.10: Example 3 with $\boldsymbol{r}_0 = (0.8, 1.0, 0.2)^T$ and $\omega = 12\pi$. The real part of zz-component of $\boldsymbol{G}(\boldsymbol{r}; \boldsymbol{r}_0)$ at $y = 1.0$ computed via (a) the Huygens sweeping method with $p = 13$; (b) FDTD method. The detailed comparison of the real part of zz-component of $\boldsymbol{G}(\boldsymbol{r}; \boldsymbol{r}_0)$ at (c): line x=1.0, y=1.0 and (d): line x =1.2, y=1.0. Red solid line: FDTD solution; Black circled line: solution of the Huygens sweeping method. Mesh in (a): $121 \times 121 \times 121$; mesh in (b): $401 \times 401 \times 401$. 139

Figure 4.11: Example 3 with $\boldsymbol{r}_0 = (0.8, 1.0, 0.2)^T$ and $\omega = 12\pi$. The real part of xz-component of $\boldsymbol{G}(\boldsymbol{r}; \boldsymbol{r}_0)$ at $y = 1.0$ computed via (a) the Huygens sweeping method with $p = 13$; (b) FDTD method. The detailed comparison of the real part of xz-component of $\boldsymbol{G}(\boldsymbol{r}; \boldsymbol{r}_0)$ at (c): line x=1.0, y=1.0 and (d): line x =1.2, y=1.0. Red solid line: FDTD solution; Black circled line: solution of the Huygens sweeping method. Mesh in (a): $121 \times 121 \times 121$; mesh in (b):$401 \times 401 \times 401$. 140

Figure 4.12: Example 4 with $\boldsymbol{r}_0 = (1.0, 1.0, 0.2)^T$ and $\omega = 10\pi$. The real part of xx-component of $\boldsymbol{G}(\boldsymbol{r}; \boldsymbol{r}_0)$ at $y = 1.0$ computed via (a) the Huygens sweeping method with $p = 13$; (b) FDTD method. The detailed comparison of the real part of xx-component of $\boldsymbol{G}(\boldsymbol{r}; \boldsymbol{r}_0)$ at (c): line x=1.0, y=1.0 and (d): line x =0.8, y=1.0. Red solid line: FDTD solution; Black circled line: solution of the Huygens sweeping method. Mesh in (a): $101 \times 101 \times 81$; mesh in (b): $401 \times 401 \times 321$. 141

Figure 4.13: Example 4 with $\boldsymbol{r}_0 = (1.0, 1.0, 0.2)^T$ and $\omega = 10\pi$. The real part of zz-component of $\boldsymbol{G}(\boldsymbol{r}; \boldsymbol{r}_0)$ at $y = 1.0$ computed via (a) the Huygens sweeping method with $p = 13$; (b) FDTD method. The detailed comparison of the real part of zz-component of $\boldsymbol{G}(\boldsymbol{r}; \boldsymbol{r}_0)$ at (c): line x=1.0, y=1.0 an (d): line x =0.8, y=1.0. Red solid line: FDTD solution; Black circled line: solution of the Huygens sweeping method. Mesh in (a): $101 \times 101 \times 81$; mesh in (b): $401 \times 401 \times 321$. 142

Figure 4.14: Example 4 with $\boldsymbol{r}_0 = (0.8, 1.0, 0.12)^T$ and $\omega = 12\pi$. The real part of xx-component of $\boldsymbol{G}(\boldsymbol{r}; \boldsymbol{r}_0)$ at $y = 1.0$ computed via (a) the Huygens sweeping method with $p = 13$; (b) FDTD method. The detailed comparison of the real part of xx-component of $\boldsymbol{G}(\boldsymbol{r}; \boldsymbol{r}_0)$ at (c): line x=0.8, y=1.0 and (d): line x =1.2, y=1.0. Red solid line: FDTD solution; Black circled line: solution of the Huygens sweeping method. Mesh in (a): $121 \times 121 \times 97$; mesh in (b): $401 \times 401 \times 321$. 143

Figure 4.15: Example 4 with $\boldsymbol{r}_0 = (0.8, 1.0, 0.12)^T$ and $\omega = 12\pi$. The real part of zz-component of $\boldsymbol{G}(\boldsymbol{r}; \boldsymbol{r}_0)$ at $y = 1.0$ computed via (a) the Huygens sweeping method with $p = 13$; (b) FDTD method. The detailed comparison of the real part of zz-component of $\boldsymbol{G}(\boldsymbol{r}; \boldsymbol{r}_0)$ at (c): line x=0.8, y=1.0 an (d): line x =1.2, y=1.0. Red solid line: FDTD solution; Black circled line: solution of the Huygens sweeping method. Mesh in (a): $121 \times 121 \times 97$; mesh in (b): $401 \times 401 \times 321$. 144

Figure 4.16: Example 4 with $\boldsymbol{r}_0 = (1.0, 1.0, 0.2)^T$ and $\omega = 20\pi$. The real part of (a): xx- and (b): zz- component of $\boldsymbol{G}(\boldsymbol{r}; \boldsymbol{r}_0)$ at $y = 1.0$ computed by the Huygens sweeping method with $p = 13$. Mesh $201 \times 201 \times 161$. 144

Figure 5.1: The real and imaginary parts of the complex-valued eikonal for the constant gradient velocity model. (a) Real part and (c) its difference with the analytic solution; (b) imaginary part and (d) its difference with the analytic solution under the weakly attenuating approximation. 159

Figure 5.2: An attenuation model with gas cloud. (a) The acoustic velocity, (b) Q. Two black curves in (a) are two ray paths with takeoff angles being 0° and 20°. 160

Figure 5.3: The real and imaginary parts of the complex-valued eikonal for the gas clouded attenuating model. (a) Real part; (b) Imaginary part. 161

Figure 5.4: Wavefield snapshot overlaid by the contour of the real part at 3s. The red curve is the contour of the real part. 162

Figure 5.5: Comparison between the imaginary parts obtained by the Eulerian PDE method and the ray-tracing method for the gas clouded attenuating model. The imaginary part for rays with (a) 0° and (b) 20° takeoff angle. The red curve and blue dotted curve are the imaginary parts obtained by the ray tracing method and the Eulerian PDE method, respectively. 163

Figure 5.6: The attenuation model for a land scenario. (a) Acoustic velocity; (b) Q. Two black curves in (a) are two ray paths with takeoff angles being 0° and 20°. 164

Figure 5.7: The real and imaginary parts of the complex-valued eikonal for the land attenuating model. (a) Real part and (b) Imaginary part. 165

Figure 5.8: Wavefield snapshot overlaid by the contour of the real part at 2s. The red curve is the contour of the real part. 166

Figure 5.9: Comparison between the imaginary parts obtained by the Eulerian PDE method and the ray tracing method for the land attenuating model. The imaginary parts for rays with (a) 0° and (b) 20° takeoff angle. The red curve and blue dotted curve are the imaginary parts obtained by the ray tracing method and the Eulerian PDE method, respectively. 167

Figure 5.10: The real and imaginary parts of the complex-valued eikonal for the 3-D model. (a) Real part and (b) Imaginary part. 167

Figure 5.11: (a) Real and (b) Imaginary parts of the complex velocity in Case A. . . . 168

Figure 5.12: The complex-valued eikonal for the real-elastic Eulerian PDE method in Case A. (a) Real part and (c) its difference with the analytic solution; (b) imaginary part and (d) its difference with the analytic solution. 168

Figure 5.13: The complex-valued eikonal for the real-viscoelastic Eulerian PDE method in Case A. (a) Real part and (c) its difference with the analytic solution; (b) imaginary part and (d) its difference with the analytic solution. . . . 169

Figure 5.14: (a) Real and (b) imaginary parts of the complex velocity in Case B. . . . 169

Figure 5.15: The complex-valued eikonal for the real-elastic Eulerian PDE method in Case B. (a) Real part and (c) its difference with the analytic solution; (b) imaginary part and (d) its difference with the analytic solution. 170

Figure 5.16: The complex-valued eikonal for the real-viscoelastic Eulerian PDE method in Case B. (a) Real part and (c) its difference with the analytic solution; (b) imaginary part and (d) its difference with the analytic solution. . . . 170

Chapter 1

Introduction

Green's functions for hyperbolic equations are fundamental in many applications. Direct methods such as finite-difference or finite-element methods are usually employed to compute numerical solutions. However, at high frequencies, direct methods suffer from the so-called pollution errors [5, 4], and it is very costly to directly resolve these highly oscillatory waves. Therefore, alternative methods, such as asymptotic methods or methods of geometrical optics (GO), are necessary to carry out scale separation so that we can solve wave equations at large frequencies. We first discuss the limitations of the classical GO ansatz and then introduce the new asymptotic ansatz for both the Helmholtz equation and Maxwell's equations.

1.1 Hadamard-Babich ansatz for the Helmholtz equation and Maxwell's equations

The Helmholz equation with a point source condition is stated as

$$\Delta u + \omega^2 n^2(\boldsymbol{r}) u = -\delta(\boldsymbol{r} - \boldsymbol{r}_0), \tag{1.1}$$

where the Sommerfeld radiation condition is imposed at infinity, $\boldsymbol{r}_0$ is the source point, position $\boldsymbol{r} = [x_1, \cdots, x_m]^T$, u is the wavefield, ω is the angular frequency, and n is the

refractive index.

The usual GO ansatz [3] for the Helmholtz equation is given as

$$u = e^{i\omega\tau} \sum_{s=0}^{\infty} \frac{w_s}{(i\omega)^{s-\frac{1}{2}(m-1)}}, \tag{1.2}$$

where τ is the traveltime function, w_s are the amplitudes, and m is the dimension. But difficulties arise immediately. One difficulty is how to choose initial data for the asymptotic ingredients. The other difficulty is that the series does not give a uniform asymptotic form close to the source when m is even.

To resolve these issues for solving the scalar point-source Helmholtz equation, Babich proposed an asymptotic series based on Hankel functions, dubbed Babich's ansatz, to expand the highly oscillatory wavefield [3]. This ansatz yields a uniform asymptotic solution as $\omega \to \infty$ in the region of space containing the point source but no other caustics. The method of finding such an ansatz is closely bound up with Hadamard's method of forming the fundamental solution of the Cauchy problem for the time-domain point-source acoustic wave equation; details were given in [25] and then were outlined by Courant and Hilbert [17].

We consider the point source Maxwell's equations

$$\nabla \times \nabla \times \boldsymbol{G} - \omega^2 n^2(\boldsymbol{r})\boldsymbol{G} = -\boldsymbol{I}\delta(\boldsymbol{r} - \boldsymbol{r}_0), \tag{1.3}$$

where $\boldsymbol{G}$ is the so-called dyadic Green's functions the source $\boldsymbol{r}_0$, $\boldsymbol{I}$ is the identity dyad, ω is the frequency, and n is the refractive index of the medium.

The GO ansatz for Green's functions [9, 37, 56] is given as

$$\boldsymbol{G}(\boldsymbol{r};\boldsymbol{r}_0) = \sum_{s=0}^{\infty} \frac{\tilde{\boldsymbol{A}}_s(\boldsymbol{r};\boldsymbol{r}_0)}{\omega^s} e^{i\omega\tau(\boldsymbol{r};\boldsymbol{r}_0)}, \tag{1.4}$$

where τ is the traveltime function and $\tilde{\boldsymbol{A}}_s$ are the dyadic amplitudes.

Usually, the first term is used to approximate the Green's functions. However, there are shortcomings. First, the first term exhibits singularities which are different from the true singularities [45]. Second, components of $\tilde{\boldsymbol{A}}_0$ may vanish along certain directions. Keeping more terms may fix this. However, a difficulty arises immediately: how to initialize those amplitudes $\tilde{\boldsymbol{A}}_s$ since they are singular at the source.

To address these initialization issues for point source Maxwell's equations, Lu, Qian, and Burridge proposed a novel ansatz in [44], dubbed the Babich-like ansatz, based on the spherical Hankel functions, and they have demonstrated that the Babich-like ansatz gives a uniform asymptotic expansion of the underlying solution in the region of space containing a point source but no other caustics. Later on, by using Hadamard's method, it is further showed in [46] that Babich-like ansatz in fact is Babich's ansatz for the point source Maxwell's equations, and it is called the Hadamard-Babich ansatz for the frequency-domain point-source Maxwell's equations.

With the above as the backdrop, we are motivated to develop the Hadamard-Babich ansatz for the frequency-domain point-source elastic wave equations .

1.2 Hadamard-Babich ansatz for frequency-domain point-source elastic wave equations

We consider the following frequency-domain point-source (FDPS) elastic wave equations in $\mathbb{R}^3$:

$$\rho\omega^2\boldsymbol{G}+(\lambda+\mu)\nabla(\nabla\cdot\boldsymbol{G})+\mu\nabla^2\boldsymbol{G}+\nabla\lambda(\nabla\cdot\boldsymbol{G})+\nabla\mu\times(\nabla\times\boldsymbol{G})+2(\nabla\mu\cdot\nabla)\boldsymbol{G}=-\boldsymbol{I}\delta(\boldsymbol{r}-\boldsymbol{r}_0), \tag{1.5}$$

where $\boldsymbol{G}=\boldsymbol{G}(\boldsymbol{r};\boldsymbol{r}_0)$ is the so-called Green's tensor at the source $\boldsymbol{r}_0$, $\boldsymbol{I}$ is the 3×3 identity dyad, ω is the frequency, $\rho(\boldsymbol{r})$ is the mass density, $\lambda(\boldsymbol{r})$ and $\mu(\boldsymbol{r})$ are so-called Lamé's stiffness parameters, and $\boldsymbol{r}=(x_1,x_2,x_3)^T$. Tacitly, the Sommerfeld radiation condition is assumed at infinity.

Why we develop new asymptotic ansatz. An intuitive approach is to use the following Wentzel-Kramers-Brillouin(WKB) GO ansatz

$$\mathbf{G}(\boldsymbol{r};\boldsymbol{r}_0)=\sum_{l=0}^{\infty}\frac{\bar{\boldsymbol{A}}^l}{\omega^l}(\boldsymbol{r};\boldsymbol{r}_0)e^{i\omega\tau(\boldsymbol{r};\boldsymbol{r}_0)}, \tag{1.6}$$

where the unknowns $\bar{\boldsymbol{A}}^l$ and τ are independent of ω. Karal and Keller [35] derived the governing equations for $\bar{\boldsymbol{A}}^l$ and τ without specifying how to initialize these quantities in computation. However, since the overall isotropic elastic waves consist of superpositions of two waves, the compressional (P) wave and the shear (S) wave, the common GO wisdom of keeping only the leading order term does not suffice to capture correct singularities of the Green's tensor at the source which in turn will affect the overall accuracy of the asymptotic solution, as will be seen in our numerical examples. Moreover, such drawbacks cannot be

easily resolved by using two or more terms in (1.6), since a critical challenge is how to initialize $\bar{\mathbf{A}}_l$ at the source $\mathbf{r}_0$.

Motivated by the work in [3, 44, 46], a new ansatz based on generalized functions, dubbed Hadamard's ansatz, is developed for solving the time-domain point-source elastic wave equations using Hadamard's method in a region close to the source but no other caustics. This Hadamard's expansion consists of Gelfand-Shilov (G-S) functions [24]. Since the singularity induced by the point source is absorbed into the basis functions, this new ansatz enables us to develop systematic approaches to initialize the GO ingredients easily so that source singularities of Green's functions can be captured faithfully.

Based on the properties of generalized functions [44, 46], the eikonal equations for both S and P waves and recursive systems of advection equations for dyadic coefficients are derived [58]. Since the explicit form of the second time derivative of the Green's tensor in a homogeneous elastic medium in terms of the G-S function can be written out, hence, by comparing Hadamard's ansatz with the homogeneous-medium fundamental solution, a matching condition at the source can be proposed which in turn gives the initial data for the unknown asymptotic coefficients. Once the time-domain Hadamard's ansatz is available with appropriate initial conditions for asymptotic ingredients in place, the ansatz can be obtained in the frequency domain, dubbed the Hadamard-Babich ansatz, for the FDPS elastic wave equations (1.5) by taking the Fourier transform of Hadamard's ansatz in time. To verify the feasibility of the newly obtained ansatz, we truncate the ansatz to keep only first two terms so that we are able to compute the resulting asymptotic solutions.

The new method for constructing the wavefield of (1.5) enjoys the following unique features. First, the asymptotic ingredients such as traveltime and amplitudes can be precomputed on uniform discretized meshes, and the mesh size is independent of the angular

frequency ω since the ansatz enables scale separation in ω. Second, those computed asymptotic ingredients can be used to assemble Green's functions for arbitrary frequencies. Third, the truncated ansatz with keeping the first two terms of the asymptotic expansion can faithfully reproduce the source singularity.

1.3 Fast Huygens sweeping method for time-harmonic elastic wave equations in inhomogeneous media

Motivated by the work [58], we develop a new Hadamard-Babich (H-B) ansatz based globally valid asymptotic method, which we call the fast Huygens sweeping (FHS) method, for the time-harmonic elastic wave equation in an inhomogeneous medium in the high frequency regime and in the presence of caustics [59].

The new method consists of three critical components: a truncated H-B ansatz for computing locally valid asymptotic solutions, the Huygens-Kirchhoff (H-K) secondary-source principle for integrating many local solutions into a global solution, and a butterfly algorithm for accelerating matrix-vector multiplication. We now motivate these three crucial elements.

The advantages of using the H-B ansatz have been discussed above and also in [58]. We will focus on discussing the other two elements.

Why we use the Huygens principle. When applying the GO ansatz (1.6) or the H-B ansatz to solve the elastic wave equation (1.5), it is implicitly assumed that the phase τ is a single-valued, well-defined function in the sense that there is a unique ray connecting any observation point to the given source point. In fact, such an observation holds in general when applying the GO or H-B ansatz to solve other point-source wave equations.

However, for waves propagating in an isotropic, generic inhomogeneous medium, there is a high probability that caustics may occur [79] so that some observation points may be connected to the given source point via multiple rays, making τ multivalued! Moreover, since the wavefield in the GO or H-B ansatz depends nonlinearly upon the phase τ, we cannot simply add up multi-branched wavefields induced by the multivalued phase function. To tackle this challenge, we then apply the Huygens principle.

According to [2, 71], in an isotropic medium there always exists a small neighborhood of the source in which any observation point is connected to the source via a unique ray, so that the phase τ is single-valued in this neighborhood; therefore, the GO or H-B ansatz is valid in this local neighborhood to yield a locally valid asymptotic solution. To go beyond caustics so as to account for multivalued phases implicitly, we use the Huygens secondary-source principle. Mathematically, to construct globally valid asymptotic solutions, we use the H-K integral to integrate many locally valid asymptotic solutions in terms of waves rather than phases so that caustics are treated implicitly.

We sketch the methodology of using the Huygens secondary-source principle. We first choose as the first layer a neighborhood of the primary point source where the Green's function is locally valid. This can be achieved by locating a region where both the S- and P-wave phase functions are single-valued. Then we choose the boundary of this layer as the secondary-source surface and identify the second layer as the region where the asymptotic Green's functions excited by secondary sources are locally valid. Afterwards, the primary-source Green's function in the second layer can be computed by integrating those locally valid secondary-source Green's functions via the H-K integral on the secondary-source surface. By repeating this process, we can sweep through the entire domain to construct the globally valid primary-source Green's function so that caustics are treated automatically and implicitly.

The question now is how to implement this sweeping strategy efficiently. To tackle this challenge, there are two major obstacles. The first obstacle is how to construct many locally valid secondary-source Green's functions rapidly, which boils down to how to rapidly construct corresponding asymptotic ingredients, such as phases and H-B coefficients. To achieve this task, we propose to first compute phases and H-B coefficients at each secondary source to higher order accuracy and then compress these functions or their relatives into low-rank separated representations in terms of tensor-product multivariate Chebyshev polynomials. Computationally, since the information of each computed asymptotic ingredient is encoded into a small number of Chebyshev coefficients, such compression leads to significant storage reduction and efficient memory access.

Why we use the butterfly algorithm. The second obstacle is how to carry out efficiently dense matrix-vector multiplications induced by the discretized H-K integral. To illustrate the point, we use the 3-D scalar Helmholtz equation as an example [45]. Let n be the number of mesh points along each coordinate direction of the computational domain, so that the total number of mesh points is $N = n^3$ in the 3-D case. Because we are interested in the globally valid asymptotic solution everywhere in the entire computational domain, the solutions at observation points (receivers or nodes) correspond to the result of some matrix-vector products. In the 3-D case, straightforward implementation of the above matrix-vector products will lead to $O(N^{\frac{2}{3}})$ operations for each receiver point, and the total cost will be $O(N^{\frac{5}{3}})$ as we need to carry out such matrix-vector products for roughly N points of receivers. Such computational cost is far too high to make our strategy practical.

Therefore, to tackle this difficulty, we adapt to our problem the multilevel matrix decomposition based butterfly algorithm [11, 84, 49, 57, 45, 56]. The resulting algorithm allows us to carry out the required matrix-vector products with the total cost of $O(N \log N)$ complex-

ity, where the prefactor depends only on the specified accuracy and is independent of the frequency ω. Such low-rank rapid matrix-vector products are responsible for the adjective "fast" in our "fast Huygens sweeping method".

Our FHS method also has two unique merits which may be attributed to precomputed tables of asymptotic ingredients. The first merit is that because asymptotic ingredients such as phase and H-B coefficients are independent of ω, those tables can be used to construct asymptotic Green's functions at a given primary source for arbitrary frequencies. The second merit is that those tables can be used to construct asymptotic Green's functions at many other primary sources for arbitrary frequencies as well. These two merits are much desired in many applications, such as medical imaging and inverse problems.

1.4 Eulerian partial-differential-equation methods for complex-valued eikonals in attenuating media

Seismic wave propagation in earth media is intrinsically attenuating [1, 16, 14] due to the influence of material properties and fractures and due to porosity and granularity of subsurface rocks. Without properly taking attenuation effects into account, seismic data processing may produce unreliable delineation of geological structures. Therefore, it is crucial to develop efficient modeling methods for wave propagation in attenuating media. Direct modeling methods such as finite-difference and finite-element methods are sometimes inconvenient to use and suffer from dispersion errors [68, 7, 8, 12, 15, 13, 86, 80]. We seek alternative modeling methods such as high-frequency asymptotic methods or the methods of Geometric optics [23, 16, 74, 26, 29, 30]. Apply such an asymptotic method to viscoelastic isotropic wave equations with complex-valued frequency-dependent elastic parameters and then vanish the

leading-order singularity in terms of reciprocal of large frequency yielding the complex eikonal equations satisfied by the complex-valued eikonal functions for P- and S- waves, respectively. The question then boils down to: how to solve such a complex eikonal equation efficiently? We propose a unified framework to eulerianize several popular real-space Lagrangian ray-tracing methods so that we can develop efficient Eulerian partial-differential-equation (PDE) methods for computing complex-valued eikonals, where the real and imaginary parts of the eikonal function describe wave propagation and attenuation effects, respectively.

Why we develop real-space ray-tracing method. As a first-order nonlinear PDE, the complex eikonal equation can be solved by the method of characteristics to yield complex-valued eikonal functions, leading to the so-called complex-space ray-tracing method, which theoretically enables us to solve the complex eikonal equation without any approximation. However, since sources and receivers are usually located in real space in most applications, the complex-space ray-tracing method brings about unusual complications in that rays are now situated in complex space so that the dimension of the ambient space becomes doubled; consequently, the resulting ray tracing system is high dimensional and is costly to solve. Moreover, it is hard to build complex-valued elastic-parameter models from real-valued ones which are usually available from measurements in real space [74, 26]. Therefore, some further approximations were pursued to develop real-space ray-tracing methods for computing complex-valued eikonal functions.

Viscoacoustic ray tracing. In viscoacoustic media, the widely used weakly attenuating approximation (i.e., the inverse of quality factor $\ll 1$) [23, 16, 36, 81, 82, 28] can be used to reduce the complex-space ray-tracing system to a real-space ray-tracing system approximately in terms of quality factor. Numerical experiments in [23] demonstrated that the weakly attenuating assumption is applicable to a substantial range of quality factor encountered in

exploration geophysics. [36] showed that the ray path under weakly attenuating approximation is identical to that in the corresponding non-attenuating medium, so that the ray tracing method in a non-attenuating medium can be used to obtain the real and imaginary parts of the complex-valued eikonal, where the ray-tracing system is defined in real space since both the reference velocity and quality factor are real. In this approximate real-space ray-tracing model, both the real and imaginary parts of the complex-valued eikonal at each receiver have to be found indirectly via solving nonlinear systems or numerical quadratures.

Real elastic ray tracing. Viewing a viscoelastic medium as the perturbation of a perfectly elastic medium, one may account for attenuation effects by using first-order perturbations and tracing rays in the elastic reference medium which is specified in real space [75, 39, 26]. According to [76], we call this method the real-elastic ray-tracing method. Here again the real part of the complex-valued eikonal at each receiver has to be found indirectly, and, accordingly, the corresponding imaginary part has to be found from numerical quadratures.

Real viscoelastic ray tracing. Another real-space ray-tracing method for viscoelastic media, the real viscoelastic ray-tracing method, is proposed by [74]. This method modifies the Hamiltonian for viscoelastic media so that the rays are constrained as trajectories in real space [76]. The resulting ray-tracing system is based on a certain real-valued reference velocity calculated from the complex-valued phase velocity for the P- or S- wave, respectively. Although this approach is still approximate, this method is highly accurate and applicable to strongly attenuating media [76, 26], where the real and imaginary parts of the complex-valued eikonal are obtained in the same way as the real elastic ray-tracing method.

Why we develop efficient Eulerian methods. So far, since all the rays are traced from an arbitrary source point to receivers by solving an initial value problem for ordi-

nary differential equations (ODEs), all these real-space ray-tracing methods yield the real and imaginary parts of the complex-valued eikonal at irregularly distributed points, and such irregular distributions of complex-valued eikonals hinder their applications to seismic migration and tomography as these applications are usually posed on regular mesh points. Therefore, we are motivated to develop efficient methods to produce complex-valued eikonals on regular grids by formulating the above three real-space ray-tracing systems into partial differential equations.

Assuming that there is a unique ray connecting any source to any receiver, one possibility is to solve an eikonal equation with an appropriate reference velocity for the real part of the complex-valued eikonal and solve an advection equation with an appropriate quality-factor function for the imaginary part of the complex-valued eikonal, where the advection equation is weakly coupled to the eikonal equation in the sense that the advection coefficients are defined by the gradient of the real part of the complex-valued eikonal; the resulting Eulerian method yields a single-valued approximate solution for the complex eikonal equation. Because the unique-ray assumption is very restrictive, we in fact will solve the above-mentioned eikonal equation for the real part in the sense of viscosity solution [73, 40] so that we end up with computing the first-arrival based real part of the complex-valued eikonal.

Now the question is how to solve the weakly coupled eikonal and advection equations efficiently with high-order accuracy so as to obtain the real and imaginary parts of the complex-valued eikonal. Supposing that we wish to compute the imaginary part to first-order accuracy which is in fact a minimum requirement, we need to have at least first-order accurate gradient of the real part since the numerically differentiated gradient of the real part serves as coefficients for the advection equation satisfied by the imaginary part. This in turn implies that the computed real part be of at least second-order accuracy so that

its numerical gradient is of first-order accuracy, and the upshot is that we need high-order accurate eikonal solvers. Such an accuracy requirement has been first observed by [61] for solving transport equations of amplitudes. Although first-order accurate eikonal solvers are abundant [77, 73, 55, 67, 61, 70, 34, 88, 65, 66, 54, 85, 33, 20, 69, 48, 78], only a few high-order accurate point-source eikonal solvers are available [61, 38, 87, 69, 50, 45, 64]. Following the work in [64] in which the eikonal and transport equations are solved to high-order accuracy with proper initializations at the point source, we develop high-order Lax-Friedrichs weighted essentially non-oscillatory (LxF-WENO) schemes for the eikonal and advection equations under consideration. The WENO approximation of derivatives [31, 64] provides better numerical stability when complex wavefronts are encountered. Moreover, the point-source singularities of the eikonal and advection equations are treated by systematic factorizations [54, 85, 20, 50, 64, 45].

1.5 Contents

The rest of this thesis is organized as follows. In Chapter 2, we discuss the Hadamard-Babich ansatz for the Helmholtz equation and Maxwell's equations. The governing equations for traveltime and amplitudes are also given. Next, we introduce the factorization technique for initialization and numerical schemes for computing those asymptotic ingredients. The convergence behavior is also discussed.

In Chapter 3, we develop Hadamard's method for elastic wave equations. In this chapter, we first derive the fundamental solution for elastic wave equations in a homogeneous medium, and this fundamental solution motivates us to propose a novel generalized-function based Hadamard's ansatz for solving elastic wave equations. This new ansatz leads us to

solve governing equations for asymptotic ingredients of S and P waves. We further propose matching conditions to derive initial conditions so as to initialize those asymptotic ingredients. Numerical examples are performed to validate our methodology.

In Chapter 4, we first introduce the truncated H-B ansatz. Then, numerical methods to compute asymptotic ingredients are discussed. We further develop the fast Huygens sweeping method for constructing globally valid asymptotic Green's tensors. Last, numerical examples are given to illustrate the performance, effectiveness and accuracy of our method.

In Chapter 5, we first propose a unified framework to compute the real and imaginary parts of the complex-valued eikonal, and we put three popular real-space ray-tracing models for viscous wave motion into this framework; then, we develop factorized PDEs to solve the resulting eikonal and advection equations by using the high-order LxF-WENO schemes. Numerical experiments demonstrate the feasibility and accuracy of the proposed method.

Chapter 2

Hardmard-Babich ansatz for the Helmholtz equation and Maxwell's equations

2.1 Babich ansatz for the Helmholtz equation

Considering the Helmholtz equation

$$\Delta u + \omega^2 n^2(\boldsymbol{r}) u = -\delta(\boldsymbol{r} - \boldsymbol{r}_0), \tag{2.1}$$

a usual way to seek the asymptotic solution is as follows

$$u = e^{i\omega\tau} \sum_{s=0}^{\infty} \frac{w_s}{(i\omega)^{s-\frac{1}{2}(m-1)}}, \tag{2.2}$$

where n is the refractive index, τ is the traveltime, ω is the angular frequency, m is the dimension, $\boldsymbol{r}_0$ is the source location, and position $\boldsymbol{r} = [x_1, \cdots, x_m]^T$. The corresponding governing equations for τ and w_s can be derived by plugging (2.2) into (2.1). When computing the asymptotic ingredients, the difficulties arise immediately. One is how to choose initial data for the asymptotic ingredients. Second, the series does not give a uniform asymptotic

form close to the source when m is even since w_s is singular at the source.

Instead, Babich proposed a new asymptotic expansion using Hankel functions [3] as follows

$$u = \sum_{s=0}^{\infty} v_s f_{-\frac{m-2}{2}+s}(\omega, \tau), \tag{2.3}$$

where f_s is defined as

$$f_s(\omega, \tau) = i\frac{\pi}{2} e^{\pi i \omega} \left(\frac{2\tau}{\omega}\right)^s H_s^{(1)}(\omega\tau). \tag{2.4}$$

Here, $H_s^{(1)}$ is the s-th Hankel function of first kind.

Inserting (2.3) into (2.1), we obtain the eikonal equation for τ and transport equations for v_s as follows [3, 43]

$$|\nabla\tau| = n, \tag{2.5}$$

$$\nabla\tau^2 \cdot \nabla v_s + \left[\frac{\Delta\tau^2}{2} + (2s-m)n^2\right] v_s = \frac{\Delta v_{s-1}}{2}, \quad s = 0, 1, 2, \cdots. \tag{2.6}$$

This new asymptotic expansion ensures that if $n(\boldsymbol{r})$ is analytic, the v_s are analytic. Thus the uniform smallness of discrepancy as $\omega \to \infty$ in the neighborhood of the source can be guaranteed. Notice, that (2.3) can also be obtained by Hadamard's method [3].

2.2 Babich-like ansatz for Maxwell's equations

Considering the point source Maxwell's equations in $\mathbb{R}^3$:

$$\nabla \times \nabla \times \boldsymbol{G} - \omega^2 n^2(\boldsymbol{r})\boldsymbol{G} = -\boldsymbol{I}\delta(\boldsymbol{r} - \boldsymbol{r}_0), \tag{2.7}$$

the GO ansatz [9, 37, 56] approximating the Green's functions $\boldsymbol{G}$ is given as

$$\boldsymbol{G}(\boldsymbol{r}; \boldsymbol{r}_0) = \sum_{s=0}^{\infty} \frac{\tilde{\boldsymbol{A}}_s(\boldsymbol{r}; \boldsymbol{r}_0)}{\omega^s} e^{i\omega\tau(\boldsymbol{r};\boldsymbol{r}_0)}. \tag{2.8}$$

Usually, we keep the first term of (2.8) to approximate $\boldsymbol{G}$. But, the resulting approximation will exhibit the different field singularities comparing to the true solutions [44]. Moreover, components of $\tilde{\boldsymbol{A}}_0$ may vanish along certain directions. A way to fix this is to add more terms. However, a difficulty arises immediately: how to initialize those amplitudes $\tilde{\boldsymbol{A}}_s$ at the source.

To overcome the initialization difficulties and motivated by the Babich's expansion for the Helmholtz equation, an asymptotic solution of (2.7) using spherical Hankel functions [44] is proposed as follows:

$$\boldsymbol{G}(\boldsymbol{r}; \boldsymbol{r}_0) = \sum_{s=0}^{\infty} \frac{\tilde{\boldsymbol{A}}_s(\boldsymbol{r}; \boldsymbol{r}_0)}{\tau^{2s}(\boldsymbol{r}; \boldsymbol{r}_0)} f_s(\omega, \tau(\boldsymbol{r}; \boldsymbol{r}_0)), \tag{2.9}$$

where f_s is defined as

$$f_s(\omega, \tau) = -\frac{\tau^{s-2} h_{s-3}^{(1)}(\omega\tau)}{\omega^{s-1}}. \tag{2.10}$$

Here, $h_s^{(1)}$ denotes the first-kind spherical Hankel functions of order $s \in \mathbb{Z}$.

In order to obtain the governing equations for amplitudes $\tilde{\boldsymbol{A}}_s$, we need to use the following properties of f_s. For any $s \geq 0$ and when $\tau \neq 0$, we have

$$\frac{\partial}{\partial \tau} f_s(\omega, \tau) = \tau f_{s-1}(\omega, \tau); \tag{2.11}$$

$$\omega^2 f_s(\omega, \tau) = (2s-7) f_{s-1}(\omega, \tau) - \tau^2 f_{s-2}(\omega, \tau); \tag{2.12}$$

$$\Big| \frac{f_{s+1}(\omega, \tau)}{f_s(\omega, \tau)} \Big| = O(\omega^{-1}) \quad \text{and} \quad |f_s(\omega, \tau)| = O(\omega^{-s}) \quad \text{as} \quad \omega \to \infty. \tag{2.13}$$

The governing equations for τ and $\tilde{\boldsymbol{A}}_s$ can be obtained by inserting (2.9) into (2.7). Hence we get

$$|\nabla \tau| = n, \tag{2.14}$$

$$\nabla \tau^2 \cdot \nabla \tilde{\boldsymbol{A}}_s + \left[\frac{\Delta \tau^2}{2} - (2s+7) n^2 \right] \tilde{\boldsymbol{A}}_s = -\nabla \tau^2 \frac{\nabla n^2 \cdot \tilde{\boldsymbol{A}}_{s-1}}{n^2} + \boldsymbol{R}_{s-1}, \quad s = 0, 1, 2, \cdots, \tag{2.15}$$

where $\boldsymbol{R}_{s-1}$ is defined as

$$\begin{aligned} \boldsymbol{R}_{s-1} = & -\tau^2 \nabla \left(\frac{\nabla n^2 \cdot \tilde{\boldsymbol{A}}_{s-1}}{n^2} \right) + (s-1) \frac{\nabla n^2 \cdot \tilde{\boldsymbol{A}}_{s-1}}{n^2} \nabla \tau^2 \\ & - (s-1) s n^2 \tilde{A}_{s-1} - \tau^2 \Delta \tilde{\boldsymbol{A}}_{s-1} \\ & + (s-1)(2 \nabla \tilde{\boldsymbol{A}}_{s-1} \cdot \nabla \tau^2 + \tilde{\boldsymbol{A}}_{s-1} \Delta \tau^2). \end{aligned} \tag{2.16}$$

The new proposed ansatz has following properties. First, the resulting transport equations for amplitudes $\tilde{\boldsymbol{A}}_s$ can be easily initialized. Second, it yields a uniform asymptotic solution as $\omega \to \infty$ in a neighborhood of the point source.

In [46], Lu, Qian, and Burridge also showed that the proposed ansatz (2.9) is closely

bound up with Hadamard's method of forming the fundamental solution of the Cauchy problem of Maxwell's equations.

2.3 High order Eulerian asymptotics

The new asymptotic expansions resolve the issue of initialization since the amplitudes are no longer singular at source. Furthermore, they yields a uniform asymptotic expansion near the source. Notice that keeping first two terms of the asymptotic expansion for computation is enough. In [64, 45, 44], the numerical experiments are presented for performance and accuracy of the new asymptotic method. In order to obtain first-order accurate approximation of v_1 in (2.6) or $\tilde{\boldsymbol{A}}_1$ in (2.15), we need third-order accurate approximation of v_0 or $\tilde{\boldsymbol{A}}_0$, respectively. Since the right hand side of (2.6) or (2.15) involves second order derivative of v_1 or $\tilde{\boldsymbol{A}}_1$. Similarly, to obtain third-order accurate approximation of v_1 or $\tilde{\boldsymbol{A}}_1$, we need fifth-order accurate approximation of traveltime τ. Numerically, in order to obtain the asymptotic approximation with desired order of accuracy, high order numerical methods are needed for computing the traveltime and the amplitudes.

In order to have high order approximation, we first need to have high order initialization of those asymptotic ingredients near the source.

2.3.1 High order factorization of eikonal

Notice, that when the slowness n is analytic, then the square of traveltime $\mathcal{T} = \tau^2$ is also analytic [3, 64, 44]. Hence we have the following expansion near the source point:

$$\mathcal{T}(\boldsymbol{r}) = \sum_{k=0}^{\infty} T_k(\boldsymbol{r}), \quad S(\boldsymbol{r}) = \sum_{k=0}^{\infty} S_k(\boldsymbol{r}), \tag{2.17}$$

where $S = n^2$.

Inserting (2.17) into the equation

$$\nabla \mathcal{T} \cdot \nabla \mathcal{T} = 4\mathcal{T} S, \tag{2.18}$$

we can obtain

$$T_0 = 0, \quad T_1 = 0, \quad T_2 = S_0 \boldsymbol{r}^2, \tag{2.19}$$

and the recursive formula for computing T_p for $P \geq 3$

$$(P-1) S_0 T_p = \sum_{k=1}^{P-2} S_k T_{P-k} - \frac{1}{4} \nabla T_{k+1} \cdot \nabla T_{P-k+1}. \tag{2.20}$$

Depending on the desired order of accuracy, one can choose the truncated sum $\tilde{T}_p = \sum_{k=1}^{P} T_k$ to approximate T near the source. Then τ can be approximate by $\sqrt{\tilde{T}_p}$ with accuracy $O(|\boldsymbol{r}|^P)$ near the source.

2.3.2 High-order factorization of amplitudes v_s for the Helmholtz equation

Similarly, to obtain high order approximation to v_s, we need high order schemes to initialize v_s near the source. v_s are assumed to be analytic near the source.

First, we have the expansion for v_0

$$v_0 = \sum_{k=1}^{\infty} V_k(\boldsymbol{r}), \tag{2.21}$$

with

$$V_0 = \frac{n_0^{m-2}}{2\pi^{(m-1)/2}}. \tag{2.22}$$

Inserting (2.17) and (2.21) into (2.6), we can obtain the recursive formula for V_P for $P \geq 2$ as follows

$$2PS_0V_p = \sum_{k=1}^{P-1}\left[-\nabla V_k \cdot \nabla T_{P+2-k} - \frac{1}{2}V_k\Delta T_{P+2-k} + mV_kS_{P-k}\right]. \tag{2.23}$$

Then we can use the truncated sum $\tilde{V}_P = \sum_{k=1}^{P} V_k$ to approximate v_s near the source with the accuracy $O(|\boldsymbol{r}|^P)$.

Second, the expansion for v_1 is as follows

$$v_1 = \sum_{k=1}^{\infty} \bar{V}_k(\boldsymbol{r}). \tag{2.24}$$

Then, for $\bar{V}_0$ and $\bar{V}_1$, we have the following formulas

$$2S_0\bar{V}_0 = \frac{1}{2}\Delta V_2, \quad 4S_0\bar{V}_1 = \frac{1}{2}\Delta V_2 - \frac{1}{2}\Delta T_3\bar{V}_0 - (2-m)S_1\bar{V}_0. \tag{2.25}$$

The recursive formula for $\bar{V}_P$ with $P \geq 2$ is as follows

$$2(P+1)S_0\bar{V}_p = \frac{1}{2}\Delta V_{P+2} + \sum_{k=1}^{P-1}\left[-\nabla\bar{V}_k \cdot \nabla T_{P+2-k} - \frac{1}{2}\bar{V}_k\Delta T_{P+2-k} + (m+2)\bar{V}_kS_{P-k}\right]. \tag{2.26}$$

Analogously, the high-order approximation for v_s, $s \geq 3$, can be obtained by using the

same approach.

2.3.3 High-order factorization of amplitudes $\tilde{\boldsymbol{A}}_s$ for Maxwell's equations

In [46], a matching condition

$$G = G_{\text{hom}} + O(1), \quad \text{as } r \to 0, \tag{2.27}$$

is proposed and the asymptotic behaviors of $\tilde{\boldsymbol{A}}_0$, $\tilde{\boldsymbol{A}}_1$, and $\tilde{\boldsymbol{A}}_2$ is obtained as follows

$$\tilde{\boldsymbol{A}}_0 = \frac{(\boldsymbol{I} - 3\tilde{\boldsymbol{r}}\tilde{\boldsymbol{r}}^T)n_0\tau^2 + (\boldsymbol{I} + \tilde{\boldsymbol{r}}\tilde{\boldsymbol{r}}^T)n_0^3 r^2}{8\pi}\left(\frac{\tau}{n_0 r}\right)^3 + O(\tau^3), \quad \text{as } r \to 0, \tag{2.28}$$

$$\tilde{\boldsymbol{A}}_1 = 3\tilde{\boldsymbol{A}}_0 - \frac{1}{4\pi}(\boldsymbol{I} - 3\tilde{\boldsymbol{r}}\tilde{\boldsymbol{r}}^T)n_0\tau^2\left(\frac{\tau}{n_0 r}\right)^3 + O(\tau^4), \quad \text{as } r \to 0, \tag{2.29}$$

$$\tilde{\boldsymbol{A}}_2 = 3\tilde{\boldsymbol{A}}_0 - \tilde{\boldsymbol{A}}_1 - \frac{1}{4\pi}(\boldsymbol{I} - 3\tilde{\boldsymbol{r}}\tilde{\boldsymbol{r}}^T)n_0\tau^2\left(\frac{\tau}{n_0 r}\right)^3 + O(\tau^5), \quad \text{as } r \to 0. \tag{2.30}$$

Further, assume that $\tilde{\boldsymbol{A}}_s$ are analytic, then $\boldsymbol{R}_{s-1}$ is also analytic in (2.15). Then the expansions near source are

$$\tilde{\boldsymbol{A}}_s = \sum_{k=1}^{\infty} \tilde{\boldsymbol{A}}_{sk}, \quad \boldsymbol{R}_{s-1} = \sum_{k=1}^{\infty} R_{s-1,k}, \tag{2.31}$$

The recursive formula for A_{sP} can be obtained as follows

$$
\begin{aligned}
0 &= (2P-(2l+4))S_0\tilde{\boldsymbol{A}}_{sq} \\
&+ \frac{1}{2}\sum_{l=0}^{P-1}\sum_{j+k=q-l,j,k\geq 0}\nabla T_{2+k}(\nabla S_j\cdot\tilde{\boldsymbol{A}}_{sl}) + \sum_{l=0}^{P-1}\sum_{j+k=q-l,j,k\geq 0} S_j(\nabla T_{2+k}\cdot\nabla)\tilde{\boldsymbol{A}}_{sl} \\
&+ \sum_{l=0}^{P-1}\sum_{j+k=q-l,j,k\geq 0} S_j\left(\frac{\Delta T_{2+k}}{2}-(2s+7)S_k\right)\tilde{\boldsymbol{A}}_{sl} - \sum_{j+k=P,j,k\geq 0} S_j\tilde{R}_{s-1,k}. \qquad (2.32)
\end{aligned}
$$

2.4 High-order schemes for computing the eikonal and transport equations

In previous section, we discussed how to obtain high order initialization for asymptotic ingredients. To obtain high order approximation of those asymptotic ingredients, we need high order numerical schemes. Since τ is singular at point source, the schemes developed on the original eikonal equation (2.5) is at most first order accurate. To tackle this difficulty, a factorization approach is developed in [20, 47, 51, 50]. The idea is to introduce a predetermined term $\tilde{\tau}$ to capture the source singularity. For instance, $\tilde{\tau}$ can be chosen to be $n(\boldsymbol{r}_0)|\boldsymbol{r}-\boldsymbol{r}_0|$. Then τ is factored as

$$\tau = \tilde{\tau}\bar{\tau}, \qquad (2.33)$$

where $\bar{\tau}$ is the new unknown and is smooth at the source. The factored eikonal equation for $\bar{\tau}$ is as follows

$$|\tilde{\tau}\nabla\bar{\tau}+\bar{\tau}\nabla\tilde{\tau}| = n. \qquad (2.34)$$

This is a Hamilton-Jacobi equation and the high-order Lax-Friedrichs WENO-based schemes designed in [34, 47, 51, 50, 83, 87] can be applied to solve (2.34). Computationally, to obtain P-th order accurate approximation of τ, we need to initialize τ in a neighborhood of size $2(P-1)h$ centered at source. These initial values will be fixed during the iterations.

For computing the amplitudes in (2.6), the high-order Lax-Friedrichs WENO schemes can be applied with the initial data given in (2.26). Those initial data will be fixed in a neighborhood of the point source, and the size of this neighborhood is depending on the order of accuracy we need. Details of computing the amplitudes refer to [64].

To compute the amplitudes in (2.15), we first need to decouple the governing equations. This technique is discussed in [56, 44]. The high-order Lax-Friedrichs WENO schemes can then be applied to the decoupled equations.

2.5 High-order Lax-Friedrichs WENO schemes

We focus on static Hamilton-Jacobi equations of the following form

$$\begin{cases} H(\boldsymbol{x}, \nabla\varphi(\boldsymbol{x})) = R(\boldsymbol{x}), & \boldsymbol{x} \in \Omega, \\ \varphi(\boldsymbol{x}) = q(\boldsymbol{x}), & \boldsymbol{x} \in \Gamma, \end{cases} \tag{2.35}$$

Where H, q and $R \geq 0$ are lipschitz continuous, and Γ is a subset of $\Omega \subset \mathbb{R}^d$. Here d is the dimension.

The upwind scheme is commonly used when the Hamiltonian is convex. However, the upwind scheme would be hard to carry out when the Hamiltonian in (2.5) is nonconvex. Hence we use the Lax-Friedrichs Hamiltonian to avoid a complicated optimization process

which is always needed for the Godunov Hamiltonian.

2.5.1 Lax-Friedrichs Hamiltonian

For simplicity, we start from case with one dimension. When $d = 1$, the Lax-Friedrichs Hamiltonian is defined as

$$\tilde{H}^{LF}(p^-, p^+) = H(\frac{p^- + p^+}{2}) - \sigma_x \frac{p^+ - p^-}{2} \tag{2.36}$$

where $p = \partial\varphi/\partial x$, $p^\pm$ are corresponding forward and backward difference approximation of $\partial\varphi/\partial x$, and σ_x is the artificial viscosity satisfying

$$\sigma_x \geq \max_{p\in[A,B]} |\frac{\partial H}{\partial p}|, \tag{2.37}$$

where $[A, B]$ is the range of $p^\pm$.

Consider an uniform discretization $\{x_i,\ i = 1, 2, 3\cdots\}$ of Ω with grid size Δx. At the mesh point x_i, we have the following numerical approximation

$$\tilde{H}^{LF} = R, \tag{2.38}$$

which implies

$$H\left(x_i, \frac{\varphi_{i+1} - \varphi_{i-1}}{2\Delta x}\right) - \sigma_x \frac{\varphi_{i+1} - 2\varphi_i + \varphi_{i-1}}{2\Delta x} = R(x_i). \tag{2.39}$$

In order to have a simple update formula, we solve for φ_i in the above

$$\varphi_i^{n+1} = \frac{\Delta x}{\sigma_x}\left(R(x_i) - H\left(x_i, \frac{\varphi_{i+1} - \varphi_{i-1}}{2\Delta x}\right)\right) + \frac{\varphi_{i+1} + \varphi_{i-1}}{2}. \tag{2.40}$$

This gives the first-order Lax-friedrichs schemes [34].

The formula for two and three dimensions can be obtained by similar procedures:

$$\begin{aligned}\varphi_{i,j}^{n+1} =& \frac{1}{\frac{\sigma_x}{\Delta x} + \frac{\sigma_y}{\Delta y}}\left(R(\boldsymbol{x}_{i,j}) - H\left(\boldsymbol{x}_{i,j}, \frac{\varphi_{i+1,j} - \varphi_{i-1,j}}{2\Delta x}, \frac{\varphi_{i,j+1} - \varphi_{i,j-1}}{2\Delta y}\right)\right. \\ &\left. + \frac{\varphi_{i+1,j} + \varphi_{i-1,j}}{2\Delta x} + \frac{\varphi_{i,j+1} + \varphi_{i,j-1}}{2\Delta y}\right).\end{aligned} \tag{2.41}$$

$$\begin{aligned}\varphi_{i,j,k}^{n+1} =& c\left(R(\boldsymbol{x}_{i,j,k}) - H\left(\boldsymbol{x}_{i,j,k}, \frac{\varphi_{i+1,j,k} - \varphi_{i-1,j,k}}{2\Delta x}, \frac{\varphi_{i,j+1,k} - \varphi_{i,j-1,k}}{2\Delta y}, \frac{\varphi_{i,j,k+1} - \varphi_{i,j,k-1}}{2\Delta z}\right)\right. \\ &\left. + \frac{\varphi_{i+1,j,k} + \varphi_{i-1,j,k}}{2\Delta x} + \frac{\varphi_{i,j+1,k} + \varphi_{i,j-1,k}}{2\Delta y} + + \frac{\varphi_{i,j,k+1} + \varphi_{i,j,k-1}}{2\Delta z}\right).\end{aligned} \tag{2.42}$$

where $q = \partial\varphi/\partial y$ and where $r = \partial\varphi/\partial z$,

$$c = \frac{1}{\frac{\sigma_x}{\Delta x} + \frac{\sigma_y}{\Delta y} + \frac{\sigma_z}{\Delta z}}, \tag{2.43}$$

and σ_x, σ_y and σ_z are artificial viscosities satisfying

$$\sigma_x \geq \max\left|\frac{\partial H}{\partial p}\right|,\ \sigma_y \geq \max\left|\frac{\partial H}{\partial q}\right|,\ \sigma_z \geq \max\left|\frac{\partial H}{\partial r}\right|. \tag{2.44}$$

2.5.2 High order Lax-Friedrichs WENO schemes

We consider the case $d = 2$.The high order schemes for higher dimension can be derived similarly. From the first order Lax-Friedrichs scheme we construct above

$$\begin{aligned}\varphi_{i,j}^{n+1} =& \frac{1}{\frac{\sigma x}{\Delta x} + \frac{\sigma y}{\Delta y}} \left(R(\boldsymbol{x}_{i,j}) - H\left(\boldsymbol{x}_{i,j}, \frac{\varphi_{i+1,j} - \varphi_{i-1,j}}{2\Delta x}, \frac{\varphi_{i,j+1} - \varphi_{i,j-1}}{2\Delta y}\right)\right. \\ &\left. + \frac{\varphi_{i+1,j} + \varphi_{i-1,j}}{2\Delta x} + \frac{\varphi_{i,j+1} + \varphi_{i,j-1}}{2\Delta y}\right),\end{aligned} \tag{2.45}$$

we replace $\varphi_{i-1,j}$, $\varphi_{i+1,j}$, $\varphi_{i,j-1}$ and $\varphi_{i,j+1}$ with $\varphi_{i,j} - \Delta x \cdot (\varphi_x)_{i,j}^-$, $\varphi_{i,j} + \Delta x \cdot (\varphi_x)_{i,j}^+$, $\varphi_{i,j} - \Delta y \cdot (\varphi_y)_{i,j}^-$, and $\varphi_{i,j} + \Delta y \cdot (\varphi_y)_{i,j}^+$, respectively, where $(\varphi_x)_{i,j}^-$, $(\varphi_x)_{i,j}^+$, $(\varphi_y)_{i,j}^-$ and $(\varphi_y)_{i,j}^+$ are high order WENO approximations for partial derivatives of φ [87, 64].

Then the high order Lax-Friedrichs sweeping schemes for static H-J equations can be written as

$$\begin{aligned}\varphi_{i,j}^{n+1} =& \frac{1}{\frac{\sigma x}{\Delta x} + \frac{\sigma y}{\Delta y}} \left(R(x_{i,j}) - H\left(x_{i,j}, \frac{(\varphi_x)_{i,j}^+ + (\varphi_x)_{i,j}^-}{2\Delta x}, \frac{(\varphi_y)_{i,j}^+ + (\varphi_y)_{i,j}^-}{2\Delta y}\right)\right. \\ &\left. + \frac{(\varphi_x)_{i,j}^+ - (\varphi_x)_{i,j}^-}{2\Delta x} + \frac{(\varphi_y)_{i,j}^+ - (\varphi_y)_{i,j}^-}{2\Delta y}\right) + \varphi_{i,j}^n.\end{aligned} \tag{2.46}$$

The third-order WENO approximations for derivatives $(\varphi_x)_{i,j}^-$, $(\varphi_x)_{i,j}^+$, $(\varphi_y)_{i,j}^-$ and $(\varphi_y)_{i,j}^+$ are calculated from the following formula [31].

The approximation for φ_x at the grid point (i, j) when the wind "blows" form the left to right is

$$(\varphi_x)_{i,j}^- = (1 - \omega_-)\left(\frac{\varphi_{i+1,j} - \varphi_{i-1,j}}{2\Delta x}\right) + \omega_-\left(\frac{3\varphi_{i,j} - 4\varphi_{i-1,j} + \varphi_{i-2,j}}{2\Delta x}\right), \tag{2.47}$$

where

$$\omega_- = \frac{1}{1+2r_-^2}, \quad r_- = \frac{\epsilon + (\varphi_{i,j} - 2\varphi_{i-1,j} + \varphi_{i-2,j})^2}{\epsilon + (\varphi_{i+1,j} - 2\varphi_{i,j} + \varphi_{i-1,j})^2}. \tag{2.48}$$

ϵ is the small number to avoid division by zero.

The approximation for φ_x at the grid point (i, j) when the wind "blows" form the right to left is

$$(\varphi_x)_{i,j}^+ = (1-\omega_+)\left(\frac{\varphi_{i+1,j} - \varphi_{i-1,j}}{2\Delta x}\right) + \omega_+\left(\frac{-\varphi_{i+2,j} + 4\varphi_{i+1,j} - 3\varphi_{i,j}}{2\Delta y}\right), \tag{2.49}$$

where

$$\omega_- = \frac{1}{1+2r_+^2}, \quad r_+ = \frac{\epsilon + (\varphi_{i+2,j} - 2\varphi_{i+1,j} + \varphi_{i,j})^2}{\epsilon + (\varphi_{i+1,j} - 2\varphi_{i,j} + \varphi_{i-1,j})^2} \tag{2.50}$$

Similarly we can define $(\varphi_y)_{i,j}^-$ and $(\varphi_y)_{i,j}^+$.

The formula for fifth-order WENO approximation can also be found in [31], and is omitted here.

2.6 Numerical example of high-order Lax-Friedrichs WENO-based schemes for computing traveltime τ

Here, a numerical example is implemented to see the performance of high-order Lax-Friedrichs WENO-based schemes for computing traveltime τ. The slowness is $n(\boldsymbol{r}) = 1/(0.5 - 0.8(y -$

0.26)). In this case, we have exact solution for traveltime τ as

$$\tau(\boldsymbol{r}, \boldsymbol{r}_0) = \frac{1}{|\boldsymbol{g}_0|}\text{arccosh}\left(1 + \frac{n(\boldsymbol{r})n(\boldsymbol{r}_0)}{2}|\boldsymbol{g}_0|^2|\boldsymbol{r} - \boldsymbol{r}_0|^2\right), \tag{2.51}$$

where $\boldsymbol{g}_0 = [0, -0.8, 0]$. The computation is implemented in the domain $[0, 0.52]^3$.

We use the first-, third- and fifth-order Lax-Friedrichs WENO-based schemes to compute traveltime τ. The L^2-norm error is computed, and the results are as follows.

	1st order	3rd order	5th order
h = 0.02	4.1589e-04	2.8952e-06	1.2697e-07
h = 0.01	1.9166e-04	1.6556e-07	3.7309e-09
h = 0.005	9.1920e-05	2.8824e-08	1.1211e-10
h = 0.0025	4.5002e-05	3.5576e-09	3.4310e-12

Table 2.1: L^2-norm error of traveltime τ computed by first-, third-, fifth-order Lax-Friedrichs WENO schemes with varying h.

From the table, we can see that the approximation of traveltime τ with desired order of accuracy can be obtained by high-order schemes.

2.7 Expected convergence behavior

We focus on analyzing the convergence behavior of the H-B ansatz of the Helmholtz equation. The similar analysis can be naturally extended to Maxwell's equations. The new algorithm has two principle sources of numerical errors [19, 42]. One is due to the numerical computation for asymptotic ingredients, such as traveltime τ, amplitudes v_0 and v_1. As mentioned above, in order to have first-order accurate v_1, we need third-order accurate v_0 and fifth-order accurate τ. Hence, we apply the fifth-order Lax-Friedrichs WENO schemes to compute τ, v_0 and v_1 with fifth-, third-, fifth-order accuracy, respectively. The computational errors can be denoted as $O(h^\alpha)$, where h is the mesh size and α is the order of accuracy.

The other one is due to the truncation of H-B ansatz. When we keep the leading-order term of H-B ansatz of (2.3), we are expecting the first-order asymptotic convergence convergence in the form of $O((1/\omega)^{1-(m-3)/2})$; when we keep the first two terms of H-B ansatz of (2.3), we are expecting the second-order asymptotic convergence convergence in the form of $O((1/\omega)^{2-(m-3)/2})$. Similarly, if we truncate the ansatz to keep first (N+1) terms of H-B ansatz, we get

$$u_N = \sum_{s=0}^{N} v_s f_{-\frac{m-2}{2}+s}(\omega, \tau). \tag{2.52}$$

Then the truncation error can be estimated asymptotically in ω as follows

$$\|u_N - u\|_{L^\infty} \leq O\Big((1/\omega)^{N+1-(m-3)/2}\Big). \tag{2.53}$$

To compute the overall error of the numerical algorithm, we first introduce u_N^h which is denoted as the numerical solution of u_N with mesh size h. Then, for $N = 0$, the total error can be estimated as

$$\begin{aligned} E_{\text{total}} =& \|u_N^h - u\|_{L^\infty} \leq \|u_N^h - u_N\|_{L^\infty} + \|u_N - u\|_{L^\infty} \\ \leq& \|v_0^h f_0(\omega, \tau^h) - v_0 f_0(\omega, \tau)\|_{L^\infty} + O\Big((1/\omega)^{N+1-(m-3)/2}\Big) \\ \leq& O(h^3) + O(\omega h^5) + O\Big((1/\omega)^{N+1-(m-3)/2}\Big); \end{aligned} \tag{2.54}$$

and for $N = 1$, we have

$$
\begin{aligned}
E_{\text{total}} =& \|u_N^h - u\|_{L^\infty} \leq \|u_N^h - u_N\|_{L^\infty} + \|u_N - u\|_{L^\infty} \qquad (2.55)\\
\leq& \|v_0^h f_0(\omega, \tau^h) - v_0 f_0(\omega, \tau)\|_{L^\infty} + \|v_1^h f_1(\omega, \tau^h) - v_1 f_1(\omega, \tau)\|_{L^\infty} + O\Big((1/\omega)^{N+1-(m-3)/2}\Big)\\
\leq& O(h^3) + O(\omega h^5) + O(\frac{h}{\omega}) + O(h^5) + O\Big((1/\omega)^{N+1-(m-3)/2}\Big).
\end{aligned}
$$

Chapter 3

Hadamard-Babich ansatz for point-source Elastic wave equations

This chapter is based on a modified version of the published work in [58]. To motivate the method, let's restate the frequency-domain point-source (FDPS) elastic wave equations in $\mathbb{R}^3$:

$$\rho\omega^2\boldsymbol{G}+(\lambda+\mu)\nabla(\nabla\cdot\boldsymbol{G})+\mu\nabla^2\boldsymbol{G}+\nabla\lambda(\nabla\cdot\boldsymbol{G})+\nabla\mu\times(\nabla\times\boldsymbol{G}))+2(\nabla\mu\cdot\nabla)\boldsymbol{G}=-\boldsymbol{I}\delta(\boldsymbol{r}-\boldsymbol{r}_0), \tag{3.1}$$

where $\boldsymbol{G}=\boldsymbol{G}(\boldsymbol{r};\boldsymbol{r}_0)$ is the so-called Green's tensor at the source $\boldsymbol{r}_0$, $\boldsymbol{I}$ is the 3×3 identity dyad, ω is the frequency, $\rho(\boldsymbol{r})$ is the mass density, $\lambda(\boldsymbol{r})$ and $\mu(\boldsymbol{r})$ are so-called Lamé's stiffness parameters, and $\boldsymbol{r}=(x_1,x_2,x_3)^T$. Tacitly, the Sommerfeld radiation condition is assumed at infinity.

We have discussed the challenges that the usual GO ansatz has to obtain accurate approximation of Green's tensor. To tackle these challenges, in [58] we have developed a new asymptotic ansatz based on generalized functions for solving the time-domain point-source elastic wave equations using Hadamard's method in a region close to the source but no other caustics.

3.1 Cauchy problem of point-source elastic wave equations

To apply Hadamard's method, we consider the following Cauchy problem in time of the point-source elastic wave equations:

$$\rho\ddot{\boldsymbol{G}} - (\lambda+\mu)\nabla(\nabla\cdot\boldsymbol{G}) - \mu\nabla^2\boldsymbol{G} - \nabla\lambda(\nabla\cdot\boldsymbol{G}) \tag{3.2}$$

$$-\nabla\mu\times(\nabla\times\boldsymbol{G})) - 2(\nabla\mu\cdot\nabla)\boldsymbol{G} = \boldsymbol{I}\delta(\boldsymbol{r}-\boldsymbol{r}_0)\delta(t),$$

$$\boldsymbol{G}(\boldsymbol{r},t;\boldsymbol{r}_0)|_{t<0} = 0, \tag{3.3}$$

and we may write it in the form

$$\rho\ddot{G}_{ij} - (\lambda+\mu)G_{kj,ki} - \mu G_{ij,kk} - \lambda_{,i}G_{kj,k} - \mu_{,k}G_{ij,k} - \mu_{,k}G_{kj,i} = \delta_{ij}\delta(\boldsymbol{r}-\boldsymbol{r}_0)\delta(t), \tag{3.4}$$

$$G_{ij} = 0, \text{ for } t<0. \tag{3.5}$$

Here, the subscript and comma notation are employed, and $\boldsymbol{r}=\boldsymbol{x}=(x_1,x_2,x_3)^T$. Specifically, G_{ij} denotes the ij-th entry of $\boldsymbol{G}$, $G_{ij,k}$ denotes the x_k-derivative of G_{ij}, so $G_{ij,kl}$ denotes $\partial^2_{x_kx_l}G_{ij}$ for $1\le i,j,k,l\le 3$. Furthermore, the Einstein summation convention is assumed so that $G_{ij,kk}=\Delta G_{ij}$, and δ_{ij} is the Kronecker delta.

Using Duhamel's principle (P. 202 and pp. 729-730 in [17]), we may rewrite (3.4) and (3.5) for $t>0$ as

$$\rho\ddot{G}_{ij} - (\lambda+\mu)G_{kj,ki} - \mu G_{ij,kk} - \lambda_{,i}G_{kj,k} - \mu_{,k}G_{ij,k} - \mu_{,k}G_{kj,i} = 0, \tag{3.6}$$

with initial conditions

$$G_{ij}(\boldsymbol{r}, 0; \boldsymbol{r}_0) = 0, \tag{3.7}$$

$$\dot{G}_{ij}(\boldsymbol{r}, 0; \boldsymbol{r}_0) = \frac{1}{\rho_0}\delta_{ij}\delta(\boldsymbol{r} - \boldsymbol{r}_0), \tag{3.8}$$

where ρ_0 is the density at the source point $\boldsymbol{r}_0$.

3.1.1 Solution of Cauchy problem in a homogeneous medium

In the case when all elastic parameters are constants, we may write the isotropic elastic wave equations in a homogeneous medium in the form

$$\rho\ddot{G}_{ij} - (\lambda + \mu)G_{kj,ki} - \mu G_{ij,kk} = 0, \tag{3.9}$$

with initial conditions

$$G_{ij}(\boldsymbol{r}, 0; \boldsymbol{r}_0) = 0, \tag{3.10}$$

$$\dot{G}_{ij}(\boldsymbol{r}, 0; \boldsymbol{r}_0) = \frac{1}{\rho}\delta_{ij}\delta(\boldsymbol{r} - \boldsymbol{r}_0). \tag{3.11}$$

Following a suggestion of Friedlander [21] as we have done in [46], we will seek a solution

to (3.9)-(3.11) in the form

$$G_{ij} = \varphi_{,ij} + \delta_{ij}\psi_{,kk} - \psi_{,ij} = \delta_{ij}\psi_{,kk} + (\varphi_{,ij} - \psi_{,ij}), \tag{3.12}$$

where φ and ψ are to be determined. On substituting this into (3.9), we obtain

$$\partial_i\partial_j[\rho\ddot{\varphi} - (\lambda + 2\mu)\Delta\varphi] + [\delta_{ij}\Delta - \partial_i\partial_j][\rho\ddot{\psi} - \mu\Delta\psi] = 0. \tag{3.13}$$

Let us now decompose the initial condition (3.11) in a similar way using the fact

$$\delta(\boldsymbol{r} - \boldsymbol{r}_0) = \Delta\left(\frac{-1}{4\pi r}\right), \tag{3.14}$$

where $r = |\boldsymbol{r} - \boldsymbol{r}_0|$. Thus we may write

$$\delta_{ij}\delta(\boldsymbol{r} - \boldsymbol{r}_0) = \partial_i\partial_j\left(\frac{-1}{4\pi r}\right) + [\delta_{ij}\Delta - \partial_i\partial_j]\left(\frac{-1}{4\pi r}\right). \tag{3.15}$$

Consequently, we see that G_{ij} given by (3.13) will satisfy (3.9)-(3.11) if

$$\rho\ddot{\varphi} - (\lambda + 2\mu)\Delta\varphi = 0, \quad t > 0, \tag{3.16}$$

$$\varphi = 0,\ \dot{\varphi} = \frac{-1}{4\rho\pi r}, \quad t = 0, \tag{3.17}$$

and

$$\rho\ddot{\psi} - \mu\Delta\psi = 0, \quad t > 0, \tag{3.18}$$

$$\psi = 0,\ \dot{\psi} = \frac{-1}{4\rho\pi r}, \quad t = 0. \tag{3.19}$$

We easily verify that (3.16)-(3.19) are satisfied by

$$\varphi = \frac{R(t-\gamma^P r)}{4\pi\rho r} - \frac{t}{4\pi\rho r} = \begin{cases} \frac{-\gamma^P}{4\pi\rho}, \ \gamma^P r \le t, \\ \frac{-t}{4\pi\rho r}, \ \gamma^P r > t, \end{cases} \tag{3.20}$$

$$\psi = \frac{R(t-\gamma^S r)}{4\pi\rho r} - \frac{t}{4\pi\rho r} = \begin{cases} \frac{-\gamma^S}{4\pi\rho}, \ \gamma^S r \le t, \\ \frac{-t}{4\pi\rho r}, \ \gamma^S r > t, \end{cases} \tag{3.21}$$

where

$$R(\xi) = \begin{cases} \xi, \ \xi > 0, \\ 0, \ \xi \le 0, \end{cases} \tag{3.22}$$

and

$$\gamma^S = \sqrt{\frac{\rho}{\mu}} \quad \text{and} \quad \gamma^P = \sqrt{\frac{\rho}{\lambda+2\mu}}. \tag{3.23}$$

Carrying out the differentiations indicated in (3.13), we finally arrive at

$$\begin{aligned} G_{ij} =& \frac{{\gamma^S}^2(\delta_{ij}-t_i t_j)}{4\pi\rho r}\delta(t-\gamma^S r) + \frac{(\delta_{ij}-3t_i t_j)}{4\pi\rho}\left[\frac{\gamma^S}{r^2}H(t-\gamma^S r) + \frac{1}{r^3}R(t-\gamma^S r)\right] \\ &+ \frac{{\gamma^P}^2 t_i t_j}{4\pi\rho r}\delta(t-\gamma^P r) - \frac{(\delta_{ij}-3t_i t_j)}{4\pi\rho}\left[\frac{\gamma^P}{r^2}H(t-\gamma^P r) + \frac{1}{r^3}R(t-\gamma^P r)\right], \end{aligned} \tag{3.24}$$

where $r = |\boldsymbol{r} - \boldsymbol{r}_0|$, and $\boldsymbol{t} = (\boldsymbol{r} - \boldsymbol{r}_0)/r$.

Here the superscripts S and P refer to the S and P wave, respectively. γ^S and γ^P are the S and P wave slowness, respectively, as will become apparent later. The vector $\boldsymbol{t} = \{t_1, t_2, t_3\}$ is the unit tangent vector to the S or P ray as the case may be, and the S and P rays coincide

in this special case of a uniform medium.

3.2 Hadamard's method for deriving asymptotic series for the case of an inhomogeneous medium

Generally, the exact solutions may not exist for the point-source elastic wave equation in an inhomogeneous medium. And, we seek the solution to (3.4) and (3.5) in terms of the generalized functions $f_+^{(k)}$ defined to be

$$f_+^{(\lambda)}(x) = \frac{x_+^\lambda}{\lambda!} = \begin{cases} \frac{x_+^\lambda}{\lambda!} & \text{for } x \geq 0, \\ 0 & \text{otherwise,} \end{cases} \tag{3.25}$$

for $\lambda > -1$; for other values of λ, $f_+^{(\lambda)}$is defined by analytic continuation. Also, since

$$f_+^{(\lambda)\prime} = f_+^{(\lambda-1)}, \tag{3.26}$$

$f_+^{(\lambda)}$ can be defined for negative integer values of λ by successive differentiation in the sense of distribution. Since $f_+^{(0)}(x) = H(x)$, the Heaviside unit function, $f_+^{(-\lambda-1)}(x) = \delta^{(\lambda)}(x)$, the λ-th derivative of δ-function for $\lambda = 0, 1, 2, \cdots$. For further discussion of $f_+^{(\lambda)}$ and related functions, see Chapter I, Section 3.4 and 3.5 of [24].

Notice that we can figure out the relation between G_{ij} and the generalized functions f_+^λ for the homogeneous case. It turns out that the second-order time derivative of G_{ij} has a simple relation with $f_+^{(-3)}$ and $f_+^{(-2)}$. In fact, adopting similar techniques as used in proving

Proposition 2.1 in [46], we can obtain

$$\ddot{G}_{ij} = \ddot{G}^S_{ij} + \ddot{G}^P_{ij}, \tag{3.27}$$

$$\ddot{G}^S_{ij} = \frac{\gamma^{S^3}}{\rho\pi}\left[2\gamma^{S^2} r^2(\delta_{ij} - t_i t_j) f_+^{(-3)}(t^2 - \gamma^{S^2} r^2) - 2\delta_{ij} f_+^{(-2)}(t^2 - \gamma^{S^2} r^2)\right], \tag{3.28}$$

and

$$\ddot{G}^P_{ij} = \frac{\gamma^{P^3}}{\rho\pi}\left[2\gamma^{P^2} r^2 t_i t_j f_+^{(-3)}(t^2 - \gamma^{P^2} r^2) - \delta_{ij} f_+^{(-2)}(t^2 - \gamma^{P^2} r^2)\right]. \tag{3.29}$$

Motivated by the form of solution in homogeneous case, and when the elastic coefficients vary with $\boldsymbol{r}$, the formulas (3.28) and (3.29) for the constant case motivate us to seek the solution of (3.1) in the following form of asymptotic series

$$\ddot{\boldsymbol{G}}(\boldsymbol{r}, t; \boldsymbol{r}_0) = \sum_{l=0}^{\infty} \boldsymbol{A}^l(\boldsymbol{r}; \boldsymbol{r}_0) f_+^{(-3+l)}(t^2 - \mathcal{T}(\boldsymbol{r}; \boldsymbol{r}_0)), \tag{3.30}$$

or in subscript notation

$$\ddot{G}_{ij} = \sum_{l=0}^{\infty} A^l_{ij} f_+^{(-3+l)}(t^2 - \mathcal{T}), \tag{3.31}$$

where $\mathcal{T}(\boldsymbol{r}; \boldsymbol{r}_0) = \tau^2(\boldsymbol{r}; \boldsymbol{r}_0)$, and $\tau(\boldsymbol{r}; \boldsymbol{r}_0)$ is the traveltime from the source $\boldsymbol{r}_0$ to $\boldsymbol{r}$. We shall define $\boldsymbol{A}^l(\boldsymbol{r}; \boldsymbol{r}_0) \equiv 0$ for $l < 0$.

To derive the governing equations for $\boldsymbol{A}^l$ and $\mathcal{T}$, we need to use two simple properties of $f_+^{(k)}(x)$,

$$f_+^{(k)'}(x) = f_+^{(k-1)}(x), \tag{3.32}$$

$$x f_+^{(k)}(x) = (k+1) f_+^{(k+1)}(x). \tag{3.33}$$

Taking double time derivatives of (3.6) yields

$$\rho\partial_t^4 G_{ij} = (\lambda+\mu)\ddot{G}_{kj,ki} + \mu\ddot{G}_{ij,kk} + \lambda_{,i}\ddot{G}_{kj,k} + \mu_{,k}\ddot{G}_{ij,k} + \mu_{,k}\ddot{G}_{kj,i}. \tag{3.34}$$

To write (3.34) in terms of the generalized functions $f_+^{(k)}$, we compute the following double time derivative of $\ddot{\boldsymbol{G}}$,

$$\begin{aligned}
\partial_t^4 G_{ij} &= \sum_{l=0}^{\infty} A_{ij}^l \partial_t^2 f_+^{(-3+l)}(t^2-\mathcal{T}) \qquad (3.35)\\
&= \sum_{l=0}^{\infty} 4t^2 A_{ij}^l f_+^{(-5+l)}(t^2-\mathcal{T}) + 2A_{ij}^l f_+^{(-4+l)}(t^2-\mathcal{T})\\
&= \sum_{l=0}^{\infty} 4\mathcal{T} A_{ij}^l f_+^{(-5+l)}(t^2-\mathcal{T}) + 2(2l-7)A_{ij}^l f_+^{(-4+l)}(t^2-\mathcal{T})\\
&= \sum_{l=0}^{\infty} f_+^{(-5+l)}(t^2-\mathcal{T})[4\mathcal{T}A_{ij}^l + 2(2l-9)A_{ij}^{l-1}],
\end{aligned}$$

and the following spatial derivatives of $\ddot{\boldsymbol{G}}$,

$$\begin{aligned}
\ddot{G}_{ij,k} &= \sum_{l=0}^{\infty} -\mathcal{T}_{,k} A_{ij}^l f_+^{(-4+l)}(t^2-\mathcal{T}) + A_{ij,k}^l f_+^{(-3+l)}(t^2-\mathcal{T}) \qquad (3.36)\\
&= \sum_{l=0}^{\infty} f_+^{(-5+l)}(t^2-\mathcal{T})[-\mathcal{T}_{,k}A_{ij}^{l-1} + A_{ij,k}^{l-2}],
\end{aligned}$$

$$\ddot{G}_{kj,i} = \sum_{l=0}^{\infty} f_+^{(-5+l)}(t^2-\mathcal{T})[-\mathcal{T}_{,i}A_{kj}^{l-1} + A_{kj,i}^{l-2}], \tag{3.37}$$

$$\ddot{G}_{kj,k} = \sum_{l=0}^{\infty} f_+^{(-5+l)}(t^2-\mathcal{T})[-\mathcal{T}_{,k}A_{kj}^{l-1} + A_{kj,k}^{l-2}], \tag{3.38}$$

$$\begin{aligned}\ddot{G}_{kj,ki} &= \sum_{l=0}^{\infty} \mathcal{T}_{,k}\mathcal{T}_{,i}A^l_{kj} f_+^{(-5+l)}(t^2-\mathcal{T}) - \mathcal{T}_{,k}A^l_{kj,i} f_+^{(-4+l)}(t^2-\mathcal{T}) \\ &- \mathcal{T}_{,i}A^l_{kj,k} f_+^{(-4+l)}(t^2-\mathcal{T}) - \mathcal{T}_{,ki}A^l_{kj} f_+^{(-4+l)}(t^2-\mathcal{T}) + A^l_{kj,ki} f_+^{(-3+l)}(t^2-\mathcal{T}) \\ &= \sum_{l=0}^{\infty} f_+^{(-5+l)}(t^2-\mathcal{T})[\mathcal{T}_{,k}\mathcal{T}_{,i}A^l_{kj} - \mathcal{T}_{,k}A^{l-1}_{kj,i} - \mathcal{T}_{,i}A^{l-1}_{kj,k} - \mathcal{T}_{,ki}A^{l-1}_{kj} + A^{l-2}_{kj,ki}],\end{aligned} \tag{3.39}$$

$$\ddot{G}_{ij,kk} = \sum_{l=0}^{\infty} f_+^{(-5+l)}(t^2-\mathcal{T})[\mathcal{T}_{,k}\mathcal{T}_{,k}A^l_{ij} - \mathcal{T}_{,k}A^{l-1}_{ij,k} - \mathcal{T}_{,k}A^{l-1}_{ij,k} - \mathcal{T}_{,kk}A^{l-1}_{ij} + A^{l-2}_{ij,kk}]. \tag{3.40}$$

Inserting above derivatives into (3.34) and according to the meaning of an asymptotic series being zero, we vanish the coefficients of $f_+^{(-5+l)}$ successively to obtain

$$\begin{aligned}0 =& 4\rho\mathcal{T}A^l_{ij} - (\lambda+\mu)\mathcal{T}_{,k}\mathcal{T}_{,i}A^l_{kj} - \mu\mathcal{T}_{,k}\mathcal{T}_{,k}A^l_{ij} \\ &+ 2\rho(2l-9)A^{l-1}_{ij} + (\lambda+\mu)\mathcal{T}_{,k}A^{l-1}_{kj,i} + (\lambda+\mu)\mathcal{T}_{,i}A^{l-1}_{kj,k} + (\lambda+\mu)\mathcal{T}_{,ki}A^{l-1}_{kj} \\ &+ 2\mu\mathcal{T}_{,k}A^{l-1}_{ij,k} + \mu\mathcal{T}_{,kk}A^{l-1}_{ij} + \lambda_{,i}\mathcal{T}_{,k}A^{l-1}_{kj} + \mu_{,k}\mathcal{T}_{,k}A^{l-1}_{ij} + \mu_{,k}\mathcal{T}_{,i}A^{l-1}_{kj} \\ &- (\lambda+\mu)A^{l-2}_{kj,ki} - \mu A^{l-2}_{ij,kk} - \lambda_{,i}A^{l-2}_{kj,k} - \mu_{,k}A^{l-2}_{ij,k} - \mu_{,k}A^{l-2}_{kj,i}.\end{aligned} \tag{3.41}$$

Setting $l=0$ in (3.41) and remembering that A^l_{ij} is zero for $l<0$, we obtain

$$4\rho\mathcal{T}A^0_{ij} - (\lambda+\mu)\mathcal{T}_{,k}\mathcal{T}_{,i}A^0_{kj} - \mu\mathcal{T}_{,k}\mathcal{T}_{,k}A^0_{ij} = 0, \tag{3.42}$$

or in vector notation

$$(4\rho\mathcal{T} - \mu|\nabla\mathcal{T}|^2)\boldsymbol{A}^0_j = (\lambda+\mu)\nabla\mathcal{T}(\nabla\mathcal{T}\cdot\boldsymbol{A}^0_j). \tag{3.43}$$

Here $\boldsymbol{A}^0_j$ denotes the j-th column of the coefficient matrix $\boldsymbol{A}^0$, which means $\boldsymbol{A}^0 = (\boldsymbol{A}^0_1, \boldsymbol{A}^0_2, \boldsymbol{A}^0_3)$.

Two cases arise, and we call them case I and case II.

Case I, both sides of (3.43) are zero. Since $\boldsymbol{A}_j^0$ for $1 \leq j \leq 3$ is assumed to be non-zero, we have

$$\nabla \mathcal{T} \cdot \boldsymbol{A}_j^0 = 0, \text{ and } 4\rho\mathcal{T} - \mu|\nabla\mathcal{T}|^2 = 0, \tag{3.44}$$

or

Case II, both sides of (3.43) are non-zero, then we have

$$\boldsymbol{A}_j^0 \parallel \nabla\mathcal{T}, \text{ and } 4\rho\mathcal{T} - (\lambda + 2\mu)|\nabla\mathcal{T}|^2 = 0, \tag{3.45}$$

which can be seen from taking the scalar product of (3.43) with $\nabla\mathcal{T}$.

3.3 Case I, the S wave: $\nabla\mathcal{T} \cdot \boldsymbol{A}_j^0 = 0$ and $4\rho\mathcal{T} - \mu|\nabla\mathcal{T}|^2 = 0$

Here

$$|\nabla\mathcal{T}|^2 = \frac{4\rho\mathcal{T}}{\mu}. \tag{3.46}$$

Let us set $\mathcal{T} = \tau^2$. Then we see that

$$|\nabla\tau|^2 = \frac{\rho}{\mu}, \tag{3.47}$$

the usual eikonal equation for the S-wave traveltime, and so $\mathcal{T}$ is the square of the S traveltime τ. The rays are obtained in the process of solving (3.46) or (3.47) by the method of characteristics, which gives

$$\frac{dx_i}{p_i} = \frac{d\tau}{\frac{\rho}{\mu}} = \frac{dp_i}{\frac{1}{2}(\frac{\rho}{\mu})_{,i}}, \tag{3.48}$$

where $p_i = \tau_i$ and from (3.47),

$$\frac{1}{2}(|p|^2 - \frac{\rho}{\mu}) = 0. \tag{3.49}$$

In our development whenever convenient we shall use $\mathcal{T}$ rather than the more usual τ. The advantage is that the argument $\Gamma = t^2 - \mathcal{T} = t^2 - \tau^2$ is linear in $\mathcal{T}$ but quadratic in τ so that in using $\mathcal{T}$, differentiation with respect to x_j does not generate factors of 2 and τ, leaving the resulting formula easier to read.

For reference here we repeat (3.41), omitting the first and third terms as they cancel by (3.46). Thus

$$\begin{aligned}
0 = &- (\lambda+\mu)\mathcal{T}_{,k}\mathcal{T}_{,i}A^l_{kj} \\
&+ 2\rho(2l-9)A^{l-1}_{ij} + (\lambda+\mu)\mathcal{T}_{,k}A^{l-1}_{kj,i} + (\lambda+\mu)\mathcal{T}_{,i}A^{l-1}_{kj,k} + (\lambda+\mu)\mathcal{T}_{,ki}A^{l-1}_{kj} \\
&+ 2\mu\mathcal{T}_{,k}A^{l-1}_{ij,k} + \mu\mathcal{T}_{,kk}A^{l-1}_{ij} + \lambda_{,i}\mathcal{T}_{,k}A^{l-1}_{kj} + \mu_{,k}\mathcal{T}_{,k}A^{l-1}_{ij} + \mu_{,k}\mathcal{T}_{,i}A^{l-1}_{kj} \\
&- (\lambda+\mu)A^{l-2}_{kj,ki} - \mu A^{l-2}_{ij,kk} - \lambda_{,i}A^{l-2}_{kj,k} - \mu_{,k}A^{l-2}_{ij,k} - \mu_{,k}A^{l-2}_{kj,i}.
\end{aligned} \tag{3.50}$$

3.3.1 S-wave transport equations for $\boldsymbol{A}^0$ and $\boldsymbol{A}^1$

First, we derive the governing equation for $\boldsymbol{A}^0$. Setting $l = 1$ in (3.50) and knowing that $A^{-1}_{ij} = 0$, we get

$$\begin{aligned}
0 = &- (\lambda+\mu)\mathcal{T}_{,k}\mathcal{T}_{,i}A^1_{kj} - 14\rho A^0_{ij} + (\lambda+\mu)\mathcal{T}_{,i}A^0_{kj,k} \\
&+ 2\mu\mathcal{T}_{,k}A^0_{ij,k} + \mu\mathcal{T}_{,kk}A^0_{ij} + \mu_{,k}\mathcal{T}_{,k}A^0_{ij} + \mu_{,k}\mathcal{T}_{,i}A^0_{kj},
\end{aligned} \tag{3.51}$$

where we have made use of $\mathcal{T}_{,k}A^0_{kj} = 0$ by $\nabla\mathcal{T}\cdot\boldsymbol{A}^0_j = 0$, and its derivative

$$(\mathcal{T}_{,k}A^0_{kj})_{,i} = \mathcal{T}_{,k}A^0_{kj,i} + \mathcal{T}_{,ki}A^0_{kj} = 0.$$

Form the scalar product of (3.51) with $\mathcal{T}_{,i}$ to get

$$0 = -(\lambda+\mu)\mathcal{T}_{,i}\mathcal{T}_{,i}\mathcal{T}_{,k}A^1_{kj} + (\lambda+\mu)\mathcal{T}_{,i}\mathcal{T}_{,i}A^0_{kj,k} + 2\mu\mathcal{T}_{,k}\mathcal{T}_{,i}A^0_{ij,k} + \mu_{,k}\mathcal{T}_{,i}\mathcal{T}_{,i}A^0_{kj}. \tag{3.52}$$

But

$$\begin{aligned} 0 = 2(\mathcal{T}_{,k}\mathcal{T}_{,i}A^0_{ij})_{,k} =& 2(\mathcal{T}_{,kk}\mathcal{T}_{,i}A^0_{ij} + \mathcal{T}_{,k}\mathcal{T}_{,ik}A^0_{ij} + \mathcal{T}_{,k}\mathcal{T}_{,i}A^0_{ij,k}) \\ =& (\mathcal{T}_{,k}\mathcal{T}_{,k})_{,i}A^0_{ij} + 2\mathcal{T}_{,k}\mathcal{T}_{,i}A^0_{ij,k} \\ =& \left(\frac{4\rho\mathcal{T}}{\mu}\right)_{,i}A^0_{ij} + 2\mathcal{T}_{,k}\mathcal{T}_{,i}A^0_{ij,k}, \end{aligned} \tag{3.53}$$

so that

$$2\mu\mathcal{T}_{,i}\mathcal{T}_{,k}A^0_{ij,k} = -\mu\left(\frac{4\rho\mathcal{T}}{\mu}\right)_{,i}A^0_{ij}. \tag{3.54}$$

Thus (3.52) becomes

$$\begin{aligned} (\lambda+\mu)\frac{4\rho\mathcal{T}}{\mu}\mathcal{T}_{,k}A^1_{kj} =& (\lambda+\mu)\frac{4\rho\mathcal{T}}{\mu}A^0_{kj,k} - \mu\left(\frac{4\rho\mathcal{T}}{\mu}\right)_{,i}A^0_{ij} + \mu_{,k}\frac{4\rho\mathcal{T}}{\mu}A^0_{kj} \\ =& (\lambda+\mu)\frac{4\rho\mathcal{T}}{\mu}A^0_{kj,k} - \mu^2\left(\frac{4\rho\mathcal{T}}{\mu^2}\right)_{,k}A^0_{kj}, \end{aligned} \tag{3.55}$$

so that we can obtain the following relationship between A^0_{kj} and $\mathcal{T}_{,k}A^1_{kj}$,

$$\mathcal{T}_{,k}A^1_{kj} = A^0_{kj,k} - \frac{\mu^3}{\rho(\lambda+\mu)}\left(\frac{\rho}{\mu^2}\right)_{,k} A^0_{kj}. \tag{3.56}$$

Inserting (3.56) into (3.51) results in the following transport equation for A^0_{ij},

$$\mathcal{T}_{,k}A^0_{ij,k} + \frac{1}{2\mu}((\mu\mathcal{T}_{,k})_{,k} - 14\rho)A^0_{ij} + \frac{\mu}{2\rho}(\frac{\rho}{\mu})_{,k}A^0_{kj}\mathcal{T}_{,i} = 0. \tag{3.57}$$

Or, in vector notation,

$$(\nabla\mathcal{T}\cdot\nabla)\boldsymbol{A}^0 + \frac{1}{2\mu}(\nabla\cdot(\mu\nabla\mathcal{T}) - 14\rho)\boldsymbol{A}^0 + \frac{\mu}{2\rho}\nabla\mathcal{T}[\nabla(\frac{\rho}{\mu})\cdot\boldsymbol{A}^0] = 0, \tag{3.58}$$

where $\nabla(\frac{\rho}{\mu})\cdot\boldsymbol{A}^0 = ((\frac{\rho}{\mu})_{,i}A^0_{i1}, (\frac{\rho}{\mu})_{,i}A^0_{i2}, (\frac{\rho}{\mu})_{,i}A^0_{i3})$ results in a row vector.

Next, we will derive the governing equation for the amplitude coefficient $\boldsymbol{A}^1$. Setting $l = 2$ in (3.50), all terms exist, so that we can get a relationship between $\nabla\mathcal{T}\cdot\mathbf{A}^2$, $\mathbf{A}^1$ and $\mathbf{A}^0$,

$$\begin{aligned} 0 =&(\lambda+\mu)(-\mathcal{T}_{,k}A^2_{kj} + A^1_{kj,k})\mathcal{T}_{,i} - 10\rho A^1_{ij} + (\lambda+\mu)(\mathcal{T}_{,k}A^1_{kj})_{,i} \\ &+ 2\mu\mathcal{T}_{,k}A^1_{ij,k} + \mu\mathcal{T}_{,kk}A^1_{ij} + \lambda_{,i}\mathcal{T}_{,k}A^1_{kj} + \mu_{,k}\mathcal{T}_{,k}A^1_{ij} + \mu_{,k}\mathcal{T}_{,i}A^1_{kj} \\ &- (\lambda+\mu)A^0_{kj,ki} - \mu A^0_{ij,kk} - \lambda_{,i}A^0_{kj,k} - \mu_{,k}A^0_{ij,k} - \mu_{,k}A^0_{kj,i}. \end{aligned} \tag{3.59}$$

To make our formulas easy to read, we introduce some notations. Let

$$a^0_j = \mathcal{T}_{,k}A^1_{kj} = A^0_{kj,k} - \frac{\mu^3}{\rho(\lambda+\mu)}(\frac{\rho}{\mu^2})_{,k}A^0_{kj}, \tag{3.60}$$

so that $\boldsymbol{a}^0 = (a_1^0, a_2^0, a_3^0)$ is a row vector depending only on A_{kj}^0, and

$$B_{ij}^0 = (\lambda+\mu)A_{kj,ki}^0 + \mu A_{ij,kk}^0 + \lambda_{,i}A_{kj,k}^0 + \mu_{,k}A_{ij,k}^0 + \mu_{,k}A_{kj,i}^0. \tag{3.61}$$

Next we take the scalar product of (3.59) with $\mathcal{T}_{,i}$ to get

$$\begin{aligned} 0 =&(\lambda+\mu)(-\mathcal{T}_{,k}A_{kj}^2 + A_{kj,k}^1)\mathcal{T}_{,i}\mathcal{T}_{,i} - 10\rho a_j^0 + (\lambda+\mu)a_{j,i}^0\mathcal{T}_{,i} \\ &+ 2\mu\mathcal{T}_{,k}A_{ij,k}^1\mathcal{T}_{,i} + \mu\mathcal{T}_{,kk}a_j^0 + \lambda_{,i}a_j^0\mathcal{T}_{,i} + \mu_{,k}\mathcal{T}_{,k}a_j^0 + \mu_{,k}\mathcal{T}_{,i}A_{kj}^1\mathcal{T}_{,i} - B_{ij}^0\mathcal{T}_{,i}. \end{aligned} \tag{3.62}$$

Let

$$b_j^0 = 10\rho a_j^0 - (\lambda+\mu)\mathcal{T}_{,i}a_{j,i}^0 - \mu\mathcal{T}_{,kk}a_j^0 - \lambda_{,i}\mathcal{T}_{,i}a_j^0 - \mu_{,i}\mathcal{T}_{,i}a_j^0 + B_{ij}^0\mathcal{T}_{,i}, \tag{3.63}$$

where $\boldsymbol{b}^0 = (b_1^0, b_2^0, b_3^0)$ is also a row vector. Consequently, equation (3.62) becomes

$$\begin{aligned} 0 =&(\lambda+\mu)(-\mathcal{T}_{,k}A_{kj}^2)\mathcal{T}_{,i}\mathcal{T}_{,i} + (\lambda+\mu)A_{kj,k}^1\mathcal{T}_{,i}\mathcal{T}_{,i} \\ &+ 2\mu\mathcal{T}_{,k}A_{ij,k}^1\mathcal{T}_{,i} + \mu_{,k}\mathcal{T}_{,i}A_{kj}^1\mathcal{T}_{,i} - b_j^0. \end{aligned} \tag{3.64}$$

Inserting (3.64) into (3.59) and employing the following relationship,

$$2\mu\mathcal{T}_{,k}A_{ij,k}^1\mathcal{T}_{,i} = 2\mu\mathcal{T}_{,k}(\mathcal{T}_{,i}A_{ij}^1)_{,k} - 4\rho\mathcal{T}_{,i}A_{ij}^1 - 4\mu\mathcal{T}(\frac{\rho}{\mu})_{,i}A_{ij}^1, \tag{3.65}$$

we obtain the following transport equation for A_{ij}^1,

$$\mathcal{T}_{,k}A_{ij,k}^1 + \frac{1}{2\mu}((\mu\mathcal{T}_{,k})_{,k} - 10\rho)A_{ij}^1 + \frac{\mu}{2\rho}A_{kj}^1\left(\frac{\rho}{\mu}\right)_{,k}\mathcal{T}_{,i} = R_{ij}^0, \tag{3.66}$$

where

$$R_{ij}^0 = -\frac{a_j^0 \mathcal{T}_{,i}}{2\mathcal{T}} + \frac{\mu}{4\rho\mathcal{T}} a_{j,k}^0 \mathcal{T}_{,k} \mathcal{T}_{,i} - \frac{b_j^0 \mathcal{T}_{,i}}{8\rho\mathcal{T}} - \frac{(\lambda+\mu) a_{j,i}^0}{2\mu} - \frac{\lambda_{,i} a_j^0}{2\mu} + \frac{B_{ij}^0}{2\mu}. \tag{3.67}$$

Or, in vector notation,

$$(\nabla\mathcal{T}\cdot\nabla)\boldsymbol{A}^1 + \frac{1}{2\mu}[\nabla\cdot(\mu\nabla\mathcal{T}) - 10\rho]\boldsymbol{A}^1 + \frac{\mu}{2\rho}\nabla\mathcal{T}[\nabla\left(\frac{\rho}{\mu}\right)\cdot\boldsymbol{A}^1] = \boldsymbol{R}^0, \tag{3.68}$$

where

$$\boldsymbol{R}^0 = -\frac{\nabla\mathcal{T}\boldsymbol{a}^0}{2\mathcal{T}} + \frac{\mu}{4\rho\mathcal{T}}\nabla\mathcal{T}[(\nabla\mathcal{T}\cdot\nabla)\boldsymbol{a}^0] - \frac{\nabla\mathcal{T}\boldsymbol{b}^0}{8\rho\mathcal{T}} - \frac{\nabla\lambda\boldsymbol{a}^0}{2\mu} - \frac{(\lambda+\mu)\nabla\boldsymbol{a}^0}{2\mu} + \frac{\boldsymbol{B}^0}{2\mu}. \tag{3.69}$$

Here $\nabla\mathcal{T}\boldsymbol{a}^0 = (\mathcal{T}_{,i}a_j^0)_{3\times3}$ and $\nabla\boldsymbol{a}^0 = (a_{j,i}^0)_{3\times3}$ are 3 by 3 matrices.

3.3.2 S-wave transport equations for general $\boldsymbol{A}^l$

By proceeding in a similar manner as above, we can derive the governing equations for other $\boldsymbol{A}^l$ when $l \geq 2$. Hence we may conclude that the general amplitude coefficients $\boldsymbol{A}^l$ satisfy

$$(\nabla\mathcal{T}\cdot\nabla)\boldsymbol{A}^l + \frac{1}{2\mu}[\nabla\cdot(\mu\nabla\mathcal{T}) + (4l-14)\rho]\boldsymbol{A}^l + \frac{\mu}{2\rho}\nabla\mathcal{T}[\nabla\left(\frac{\rho}{\mu}\right)\cdot\boldsymbol{A}^l] = \boldsymbol{R}^{l-1}, \tag{3.70}$$

where

$$\begin{aligned}\boldsymbol{R}^{l-1} = &-\frac{\nabla\mathcal{T}\boldsymbol{a}^{l-1}}{2\mathcal{T}} + \frac{\mu}{4\rho\mathcal{T}}\nabla\mathcal{T}[(\nabla\mathcal{T}\cdot\nabla)\boldsymbol{a}^{l-1}] - \frac{\nabla\mathcal{T}\boldsymbol{b}^{l-1}}{8\rho\mathcal{T}} - \frac{\nabla\lambda\boldsymbol{a}^{l-1}}{2\mu} \\ &- \frac{(\lambda+\mu)\nabla\boldsymbol{a}^{l-1}}{2\mu} + \frac{\boldsymbol{B}^{l-1}}{2\mu}.\end{aligned} \tag{3.71}$$

Here $\boldsymbol{B}^{l-1}$, $\boldsymbol{a}^{l-1}$, and $\boldsymbol{b}^{l-1}$ are given by

$$\begin{aligned}\boldsymbol{B}^{l-1} =&(\lambda+\mu)\nabla(\nabla\cdot\boldsymbol{A}^{l-1})+\mu\nabla^2\boldsymbol{A}^{l-1}+\nabla\lambda(\nabla\cdot\boldsymbol{A}^{l-1})\\ &+\nabla\mu\times(\nabla\times\boldsymbol{A}^{l-1})+2(\nabla\mu\cdot\nabla)\boldsymbol{A}^{l-1},\end{aligned} \tag{3.72}$$

$$\begin{aligned}\boldsymbol{a}^{l-1} =&\nabla\mathcal{T}\cdot\boldsymbol{A}^{l}\\ =&\nabla\cdot\boldsymbol{A}^{l-1}+\frac{1}{\lambda+\mu}\nabla\mu\cdot\boldsymbol{A}^{l-1}+\frac{2\mu^2}{(\lambda+\mu)4\rho\mathcal{T}}\nabla\mathcal{T}[(\nabla\mathcal{T}\cdot\nabla)\boldsymbol{A}^{l-1}]-\frac{\mu\boldsymbol{b}^{l-2}}{(\lambda+\mu)4\rho\mathcal{T}},\end{aligned} \tag{3.73}$$

$$\begin{aligned}\boldsymbol{b}^{l-1} =&2\rho(-2l+7)\boldsymbol{a}^{l-1}-(\lambda+\mu)(\nabla\mathcal{T}\cdot\nabla)\boldsymbol{a}^{l-1}-\mu\nabla^2\mathcal{T}\boldsymbol{a}^{l-1}\\ &-(\nabla\mathcal{T}\cdot\nabla\lambda)\boldsymbol{a}^{l-1}-(\nabla\mathcal{T}\cdot\nabla\mu)\boldsymbol{a}^{l-1}+\nabla\mathcal{T}\cdot\boldsymbol{B}^{l-1},\end{aligned} \tag{3.74}$$

where $\boldsymbol{b}^{l}$, $\boldsymbol{a}^{l}$, $\boldsymbol{B}^{l}$ and $\boldsymbol{R}^{l}$ are zero for all $l<0$.

3.3.3 S wave: verification in a homogeneous medium

In a homogeneous medium, the parameters ρ, λ and μ are constants so that we have the exact solution (3.28) for the S-wave, which we rewrite here as

$$\ddot{G}_{ij}^{S}=\frac{\gamma^{S^3}}{\rho\pi}[2\gamma^{S^2}r^2(\delta_{ij}-t_it_j)f_+^{(-3)}(t^2-\gamma^{S^2}r^2)-2\delta_{ij}f_+^{(-2)}(t^2-\gamma^{S^2}r^2)]. \tag{3.75}$$

To simplify the derivation, we assume that $\boldsymbol{r}_0=\boldsymbol{0}$ in this subsection. From the exact solution we know that

$$A_{ij}^{0}=2\frac{\gamma^{S^3}}{\rho\pi}\gamma^{S^2}r^2(\delta_{ij}-t_it_j), \tag{3.76}$$

$$A_{ij}^{1}=-2\frac{\gamma^{S^3}}{\rho\pi}\delta_{ij}. \tag{3.77}$$

In this case, the last term of (3.58) disappears, and also, since in a homogeneous medium $\mathcal{T} = \gamma^{S^2} r^2 = \frac{\rho}{\mu} r^2$, we see that $\nabla \cdot (\mu \nabla \mathcal{T}) = 6\rho$. Hence (3.57) reduces to

$$\mathcal{T}_{,k} A^0_{ij,k} - 4\frac{\rho}{\mu} A^0_{ij} = 0. \tag{3.78}$$

From the exact formula for A^0_{ij} in (3.76), we see that

$$\begin{aligned}
\mathcal{T}_{,k} A^0_{ij,k} &= 2\frac{\rho}{\mu} x_k \left(2\frac{\gamma^{S^3}}{\rho\pi} \gamma^{S^2} r^2 (\delta_{ij} - t_i t_j) \right)_{,k} \\
&= 2\frac{\rho}{\mu} x_k 2\frac{\gamma^{S^3}}{\rho\pi} \gamma^{S^2} (2x_k \delta_{ij} - x_j \delta_{ik} - x_i \delta_{jk}) \\
&= 2\frac{\rho}{\mu} 4\frac{\gamma^{S^3}}{\rho\pi} \gamma^{S^2} r^2 (\delta_{ij} - t_i t_j) \\
&= 4\frac{\rho}{\mu} A^0_{ij}.
\end{aligned} \tag{3.79}$$

This verifies equation (3.57).

Now we verify (3.56) in a homogeneous medium, i.e. $\mathcal{T}_{,i} A^1_{ij} = A^0_{ij,i}$. We have

$$\begin{aligned}
A^0_{ij,i} &= \left(2\frac{\gamma^{S^5}}{\rho\pi} r^2 (\delta_{ij} - t_i \, t_j) \right)_{,i} \\
&= 2\frac{\gamma^{S^5}}{\rho\pi} (r^2 \delta_{ij} - x_i x_j)_{,i} \\
&= 2\frac{\gamma^{S^5}}{\rho\pi} (2x_i \delta_{ij} - 3x_j - x_j) \\
&= -4\frac{\gamma^{S^5}}{\rho\pi} x_j.
\end{aligned} \tag{3.80}$$

Again using $\mathcal{T} = \frac{\rho}{\mu} r^2$ and $\mathcal{T}_{,i} = 2\frac{\rho}{\mu} x_i$, we obtain

$$\mathcal{T}_{,i} A^1_{ij} = -4\frac{\gamma^{S^5}}{\rho\pi} x_j, \tag{3.81}$$

which is the same as (3.80), thus verifying (3.56).

Finally we may check the governing equation (3.68) for $\boldsymbol{A}^1$ in a homogeneous medium. Using formulas (3.76) and (3.80), we obtain

$$a^0_j = -4\frac{\gamma^{S^5}}{\rho\pi} x_j, \tag{3.82}$$

$$a^0_{j,k} = -4\frac{\gamma^{S^5}}{\rho\pi} \delta_{jk}, \tag{3.83}$$

$$B^0_{ij} = -4\frac{(\lambda+\mu)\gamma^{S^5}}{\rho\pi} \delta_{ij} + \frac{8\mu\gamma^{S^5}}{\rho\pi} \delta_{ij}. \tag{3.84}$$

Also using the fact that $\mathcal{T} = \frac{\rho}{\mu} r^2$, $\mathcal{T}_{,i} = 2\frac{\rho}{\mu} x_i$, and $\mathcal{T}_{,kk} = 6\frac{\rho}{\mu}$, we can get

$$\begin{aligned} b^0_j &= 10\rho a^0_j - (\lambda+\mu)\mathcal{T}_{,i} a^0_{j,i} - \mu \mathcal{T}_{,kk} a^0_j + B^0_{ij} \mathcal{T}_{,i} \\ &= -\frac{40\gamma^{S^5}}{\pi} x_j + \frac{8(\lambda+\mu)\gamma^{S^5} x_j}{\mu\pi} + \frac{24\gamma^{S^5} x_j}{\pi} - \frac{8(\lambda+\mu)\gamma^{S^5} x_j}{\mu\pi} + \frac{16\gamma^{S^5} x_j}{\pi} \\ &= 0. \end{aligned} \tag{3.85}$$

Hence we can obtain R^0_{ij} as the following,

$$\begin{aligned} R^0_{ij} &= -\frac{a^0_j \mathcal{T}_{,i}}{2\mathcal{T}} + \frac{\mu}{4\rho\mathcal{T}} a^0_{j,k} \mathcal{T}_{,k} \mathcal{T}_{,i} - \frac{b^0_j \mathcal{T}_{,i}}{8\rho\mathcal{T}} - \frac{(\lambda+\mu) a^0_{j,i}}{2\mu} + \frac{B^0_{ij}}{2\mu} \\ &= 4\frac{\gamma^{S^5} x_i x_j}{\rho\pi r^2} - 4\frac{\gamma^{S^5} x_i x_j}{\rho\pi r^2} + 2\frac{(\lambda+\mu)\gamma^{S^5}\delta_{ij}}{\mu\rho\pi} - 2\frac{(\lambda+\mu)\gamma^{S^5}\delta_{ij}}{\mu\rho\pi} + 4\frac{\gamma^{S^5}\delta_{ij}}{\rho\pi} \\ &= 4\frac{\gamma^{S^5}\delta_{ij}}{\rho\pi}. \end{aligned} \tag{3.86}$$

For the left hand side of (3.68), we use formula (3.77) to get

$$\mathcal{T}_{,k}A^1_{ij,k} + \frac{1}{2\mu}((\mu\mathcal{T}_{,k})_{,k} - 10\rho)A^1_{ij} = -2\frac{\rho}{\mu}A^1_{ij} = 4\frac{\gamma^{S^5}}{\rho\pi}\delta_{ij}, \tag{3.87}$$

which is the same as R^0_{ij} derived above. Similarly, we can also verify the amplitude coefficients $A^l_{ij} = 0$ for $l \geq 2$ in a homogeneous medium.

3.3.4 S wave: governing equations for desingularizing $\boldsymbol{A}^l$

We enforce the condition that $\boldsymbol{A}^l$ is bounded at the source for all $l \geq 0$, which may not be amenable to numerical computation. Therefore, we define new dyadic coefficients to be

$$\tilde{\boldsymbol{A}}^l = \boldsymbol{A}^l\tau^{2l} \tag{3.88}$$

so that

$$\boldsymbol{A}^l = O(1) \text{ as } \boldsymbol{r} \to \boldsymbol{r}_0,$$
$$\tilde{\boldsymbol{A}}^l = O(\tau^{2l}) \text{ as } \boldsymbol{r} \to \boldsymbol{r}_0.$$

We introduce $\tilde{\boldsymbol{A}}^l$ here since $\boldsymbol{A}^l$ may not be smooth at the source $\boldsymbol{r}_0$ for an inhomogeneous medium; this can be seen from the initial conditions (3.150)-(3.153). It is easy to derive governing equations for $\tilde{\boldsymbol{A}}^l$ from those for $\boldsymbol{A}^l$ for $l = 0, 1$ as the following,

$$(\nabla\mathcal{T}\cdot\nabla)\tilde{\boldsymbol{A}}^0 + \frac{1}{2\mu}[\nabla\cdot(\mu\nabla\mathcal{T}) - 14\rho]\tilde{\boldsymbol{A}}^0 + \frac{\mu}{2\rho}\nabla\mathcal{T}\left[\nabla\left(\frac{\rho}{\mu}\right)\cdot\tilde{\boldsymbol{A}}^0\right] = 0, \tag{3.89}$$
$$(\nabla\mathcal{T}\cdot\nabla)\tilde{\boldsymbol{A}}^1 + \frac{1}{2\mu}[\nabla\cdot(\mu\nabla\mathcal{T}) - 18\rho]\tilde{\boldsymbol{A}}^1 + \frac{\mu}{2\rho}\nabla\mathcal{T}\left[\nabla\left(\frac{\rho}{\mu}\right)\cdot\tilde{\boldsymbol{A}}^1\right] = \tilde{\boldsymbol{R}}^0, \tag{3.90}$$

where

$$\tilde{\boldsymbol{R}}^0 \equiv -\frac{\nabla\mathcal{T}\tilde{\boldsymbol{a}}^0}{2} + \frac{\mu\nabla\mathcal{T}[(\nabla\mathcal{T}\cdot\nabla)\tilde{\boldsymbol{a}}^0]}{4\rho} - \frac{\nabla\mathcal{T}\tilde{\boldsymbol{b}}^0}{8\rho} - \frac{\mathcal{T}\nabla\lambda\tilde{\boldsymbol{a}}^0}{2\mu} - \frac{(\lambda+\mu)\mathcal{T}\nabla\tilde{\boldsymbol{a}}^0}{2\mu} + \frac{\mathcal{T}\tilde{\boldsymbol{B}}^0}{2\mu}. \quad (3.91)$$

Here $\tilde{\boldsymbol{B}}^0$, $\tilde{\boldsymbol{a}}^0$, and $\tilde{\boldsymbol{b}}^0$ are given by

$$\begin{aligned}
\tilde{\boldsymbol{B}}^0 &\equiv (\lambda+\mu)\nabla(\nabla\cdot\tilde{\boldsymbol{A}}^0) + \mu\nabla^2\tilde{\boldsymbol{A}}^0 + \nabla\lambda(\nabla\cdot\tilde{\boldsymbol{A}}^0) \\
&\quad +\nabla\mu\times(\nabla\times\tilde{\boldsymbol{A}}^0) + 2(\nabla\mu\cdot\nabla)\tilde{\boldsymbol{A}}^0, \qquad (3.92)\\
\tilde{\boldsymbol{a}}^0 &\equiv \nabla\cdot\tilde{\boldsymbol{A}}^0 + \frac{1}{\lambda+\mu}\nabla\mu\cdot\tilde{\boldsymbol{A}}^0 + \frac{2\mu}{(\lambda+\mu)|\nabla\mathcal{T}|^2}\nabla\mathcal{T}[(\nabla\mathcal{T}\cdot\nabla)\tilde{\boldsymbol{A}}^0], \qquad (3.93)\\
\tilde{\boldsymbol{b}}^0 &\equiv 10\rho\tilde{\boldsymbol{a}}^0 - (\lambda+\mu)(\nabla\mathcal{T}\cdot\nabla)\tilde{\boldsymbol{a}}^0 - \mu\nabla^2\mathcal{T}\tilde{\boldsymbol{a}}^0 \\
&\quad -(\nabla\mathcal{T}\cdot\nabla\lambda)\tilde{\boldsymbol{a}}^0 - (\nabla\mathcal{T}\cdot\nabla\mu)\tilde{\boldsymbol{a}}^0 + \nabla\mathcal{T}\cdot\tilde{\boldsymbol{B}}^0. \qquad (3.94)
\end{aligned}$$

The governing equations for general $\tilde{\boldsymbol{A}}^l$ for $l \geq 2$ are

$$(\nabla\mathcal{T}\cdot\nabla)\tilde{\boldsymbol{A}}^l + \frac{1}{2\mu}[\nabla\cdot(\mu\nabla\mathcal{T}) - (4l+14)\rho]\tilde{\boldsymbol{A}}^l + \frac{\mu}{2\rho}\nabla\mathcal{T}\left[\nabla\left(\frac{\rho}{\mu}\right)\cdot\tilde{\boldsymbol{A}}^l\right] = \tilde{\boldsymbol{R}}^{l-1}, \quad (3.95)$$

where

$$\begin{aligned}
\tilde{\boldsymbol{R}}^{l-1} &\equiv -\frac{\nabla\mathcal{T}\tilde{\boldsymbol{a}}^{l-1}}{2}\mathcal{T}^{l-1} + \frac{\mu\nabla\mathcal{T}[(\nabla\mathcal{T}\cdot\nabla)\tilde{\boldsymbol{a}}^{l-1}]}{4\rho}\mathcal{T}^{l-1} - \frac{\nabla\mathcal{T}\tilde{\boldsymbol{b}}^{l-1}}{8\rho}\mathcal{T}^{l-1} - \frac{\nabla\lambda\tilde{\boldsymbol{a}}^{l-1}}{2\mu}\mathcal{T}^l \\
&\quad -\frac{(\lambda+\mu)\nabla\tilde{\boldsymbol{a}}^{l-1}}{2\mu}\mathcal{T}^l + \frac{\tilde{\boldsymbol{B}}^{l-1}}{2\mu}\mathcal{T}^l. \qquad (3.96)
\end{aligned}$$

Here the explicit formulas for $\tilde{\boldsymbol{B}}^{l-1}$, $\tilde{\boldsymbol{a}}^{l-1}$, and $\tilde{\boldsymbol{b}}^{l-1}$ are given in Appendix A.

3.4 Case II, P wave: $\boldsymbol{A}^0_j \parallel \nabla\mathcal{T}$ and $4\rho\mathcal{T}-(\lambda+2\mu)|\nabla\mathcal{T}|^2=0$

Let us repeat (3.41) here for reference,

$$\begin{aligned}
0 =&4\rho\mathcal{T}A^l_{ij} - (\lambda+\mu)\mathcal{T}_{,k}\mathcal{T}_{,i}A^l_{kj} - \mu\mathcal{T}_{,k}\mathcal{T}_{,k}A^l_{ij}\\
&+ 2\rho(2l-9)A^{l-1}_{ij} + (\lambda+\mu)\mathcal{T}_{,k}A^{l-1}_{kj,i} + (\lambda+\mu)\mathcal{T}_{,i}A^{l-1}_{kj,k} + (\lambda+\mu)\mathcal{T}_{,ki}A^{l-1}_{kj}\\
&+ 2\mu\mathcal{T}_{,k}A^{l-1}_{ij,k} + \mu\mathcal{T}_{,kk}A^{l-1}_{ij} + \lambda_{,i}\mathcal{T}_{,k}A^{l-1}_{kj} + \mu_{,k}\mathcal{T}_{,k}A^{l-1}_{ij} + \mu_{,k}\mathcal{T}_{,i}A^{l-1}_{kj}\\
&- (\lambda+\mu)A^{l-2}_{kj,ki} - \mu A^{l-2}_{ij,kk} - \lambda_{,i}A^{l-2}_{kj,k} - \mu_{,k}A^{l-2}_{ij,k} - \mu_{,k}A^{l-2}_{kj,i}.
\end{aligned} \tag{3.97}$$

Rewriting the first line using the fact that in case II,

$$-\mu\mathcal{T}_{,k}\mathcal{T}_{,k}A^l_{ij} = (\lambda+\mu)\mathcal{T}_{,k}\mathcal{T}_{,k}A^l_{ij} - 4\rho\mathcal{T}A^l_{ij}, \tag{3.98}$$

we have

$$\begin{aligned}
0 =&(\lambda+\mu)(\mathcal{T}_{,k}\mathcal{T}_{,k}A^l_{ij} - \mathcal{T}_{,k}\mathcal{T}_{,i}A^l_{kj})\\
&+ 2\rho(2l-9)A^{l-1}_{ij} + (\lambda+\mu)\mathcal{T}_{,k}A^{l-1}_{kj,i} + (\lambda+\mu)\mathcal{T}_{,i}A^{l-1}_{kj,k} + (\lambda+\mu)\mathcal{T}_{,ki}A^{l-1}_{kj}\\
&+ 2\mu\mathcal{T}_{,k}A^{l-1}_{ij,k} + \mu\mathcal{T}_{,kk}A^{l-1}_{ij} + \lambda_{,i}\mathcal{T}_{,k}A^{l-1}_{kj} + \mu_{,k}\mathcal{T}_{,k}A^{l-1}_{ij} + \mu_{,k}\mathcal{T}_{,i}A^{l-1}_{kj}\\
&- (\lambda+\mu)A^{l-2}_{kj,ki} - \mu A^{l-2}_{ij,kk} - \lambda_{,i}A^{l-2}_{kj,k} - \mu_{,k}A^{l-2}_{ij,k} - \mu_{,k}A^{l-2}_{kj,i}.
\end{aligned} \tag{3.99}$$

3.4.1 P-wave transport equations for $\boldsymbol{A}^0$ and $\boldsymbol{A}^1$

First, we derive the governing equation for $\boldsymbol{A}^0$. We set $l = 1$ in (3.99) and then take the scalar product of (3.99) with $\mathcal{T}_{,i}$ to obtain

$$\begin{aligned} 0 =& -14\rho\mathcal{T}_{,i}A^0_{ij} + (\lambda+\mu)\mathcal{T}_{,i}\mathcal{T}_{,k}A^0_{kj,i} + (\lambda+\mu)\mathcal{T}_{,i}\mathcal{T}_{,i}A^0_{kj,k} + (\lambda+\mu)\mathcal{T}_{,i}\mathcal{T}_{,ki}A^0_{kj} \\ &+ 2\mu\mathcal{T}_{,i}\mathcal{T}_{,k}A^0_{ij,k} + \mu\mathcal{T}_{,i}\mathcal{T}_{,kk}A^0_{ij} + \lambda_{,i}\mathcal{T}_{,i}\mathcal{T}_{,k}A^0_{kj} + \mu_{,k}\mathcal{T}_{,i}\mathcal{T}_{,k}A^0_{ij} + \mu_{,k}\mathcal{T}_{,i}\mathcal{T}_{,i}A^0_{kj}, \end{aligned} \tag{3.100}$$

where we have made use of the eikonal equation, $4\rho\mathcal{T} = (\lambda+2\mu)\mathcal{T}_{,i}\mathcal{T}_{,i}$. Also the last line does not contribute since $A^{-1}_{ij} = 0$.

Since $\boldsymbol{A}^0_j$ is parallel to $\nabla\mathcal{T}$ for $1 \le j \le 3$, we may write it as

$$A^0_{ij} = \alpha^0_j\mathcal{T}_{,i}, \tag{3.101}$$

where $\boldsymbol{\alpha}^0 = (\alpha^0_1, \alpha^0_2, \alpha^0_3)$ is a row vector.

Inserting (3.101) into (3.100), we get

$$\begin{aligned} 0 =& -14\rho\mathcal{T}_{,i}\alpha^0_j\mathcal{T}_{,i} + 2(\lambda+2\mu)\mathcal{T}_{,i}\mathcal{T}_{,i}\alpha^0_{j,k}\mathcal{T}_{,k} + 2(\lambda+2\mu)\mathcal{T}_{,i}\mathcal{T}_{,k}\alpha^0_j\mathcal{T}_{,ik} \\ &+ (\lambda+2\mu)\mathcal{T}_{,i}\mathcal{T}_{,i}\mathcal{T}_{,kk}\alpha^0_j + (\lambda_{,k}+2\mu_{,k})\mathcal{T}_{,k}\mathcal{T}_{,i}\mathcal{T}_{,i}\alpha^0_j. \end{aligned} \tag{3.102}$$

Employing the following relations

$$[(\lambda+2\mu)\mathcal{T}_{,i}\mathcal{T}_{,i}]_{,k}\mathcal{T}_{,k} = (\lambda+2\mu)_{,k}\mathcal{T}_{,i}\mathcal{T}_{,i}\mathcal{T}_{k} + 2(\lambda+2\mu)\mathcal{T}_{,i}\mathcal{T}_{,ik}\mathcal{T}_{,k}, \tag{3.103}$$

$$(4\rho\mathcal{T})_{,k}\mathcal{T}_{,k} = 4\rho_{,k}\mathcal{T}_{,k}\mathcal{T} + 4\rho\mathcal{T}_{,i}\mathcal{T}_{,i}, \tag{3.104}$$

we can get

$$\begin{aligned} 0 = &- 14\rho\alpha_j^0\mathcal{T}_{,i}\mathcal{T}_{,i} + 2(\lambda+2\mu)\mathcal{T}_{,i}\mathcal{T}_{,i}\mathcal{T}_{,k}\alpha_{j,k}^0 + (\lambda+2\mu)\alpha^0\mathcal{T}_{,kk}\mathcal{T}_{,i}\mathcal{T}_{,i} \\ &+ 4\rho_{,k}\mathcal{T}_{,k}\mathcal{T}\alpha_j^0 + 4\rho\mathcal{T}_{,k}\mathcal{T}_{,k}\alpha_j^0. \end{aligned} \tag{3.105}$$

Simplifying the result, we obtain

$$\mathcal{T}_{,i}\alpha_{j,i}^0 + \left[\frac{1}{2\rho}(\rho\mathcal{T}_{,i})_{,i} - \frac{5\rho}{\lambda+2\mu}\right]\alpha_j^0 = 0. \tag{3.106}$$

Next, we can derive the governing equation for $\boldsymbol{A}^1$. To determine $\boldsymbol{A}^1$, we set $l = 1$ in (3.99) and form the cross product of the resulting equation with $\nabla\mathcal{T}$,

$$\begin{aligned} 0 =&(-4\rho\mathcal{T} + \mu|\nabla\mathcal{T}|^2)\nabla\mathcal{T}\times\boldsymbol{A}^1 - (\lambda+\mu)\nabla\mathcal{T}\times\nabla(\nabla\mathcal{T}\cdot\boldsymbol{A}^0) \\ &- 2\mu\nabla\mathcal{T}\times[(\nabla\mathcal{T}\cdot\nabla)\boldsymbol{A}^0] - (\nabla\mathcal{T}\times\nabla\lambda)(\nabla\mathcal{T}\cdot\boldsymbol{A}^0). \end{aligned} \tag{3.107}$$

To go further, we need to use the following relations which can be verified directly,

$$\nabla\mathcal{T}\times[(\nabla\mathcal{T}\cdot\nabla)\boldsymbol{A}^0] = 2\mathcal{T}\nabla\mathcal{T}\times\left(\nabla\left(\frac{\rho}{\lambda+2\mu}\right)\boldsymbol{\alpha}^0\right), \tag{3.108}$$

and

$$\nabla\mathcal{T}\times\nabla(\nabla\mathcal{T}\cdot\boldsymbol{A}^0) = \frac{4\rho\mathcal{T}}{\lambda+2\mu}\nabla\mathcal{T}\times\nabla\boldsymbol{\alpha}^0 + 4\mathcal{T}\nabla\mathcal{T}\times\left(\nabla\left(\frac{\rho}{\lambda+2\mu}\right)\boldsymbol{\alpha}^0\right). \tag{3.109}$$

Inserting the above two relations into (3.107), we can obtain

$$\nabla\mathcal{T}\times\left(\boldsymbol{A}^1+\nabla\boldsymbol{\alpha}^0+\frac{(\lambda+2\mu)^2}{\rho(\lambda+\mu)}\nabla\left(\frac{\rho}{\lambda+2\mu}\right)\boldsymbol{\alpha}^0+\frac{\nabla\lambda\boldsymbol{\alpha}^0}{\lambda+\mu}\right)=0. \tag{3.110}$$

From (3.110) we may conclude that

$$\boldsymbol{A}^1=\boldsymbol{C}^0+\nabla\mathcal{T}\boldsymbol{\alpha}^1. \tag{3.111}$$

where $\boldsymbol{\alpha}^1=(\alpha_1^1,\alpha_2^1,\alpha_3^1)$ is a row vector to be determined, and

$$\boldsymbol{C}^0=-\nabla\boldsymbol{\alpha}^0-\frac{(\lambda+2\mu)^2}{\rho(\lambda+\mu)}\nabla\left(\frac{\rho}{\lambda+2\mu}\right)\boldsymbol{\alpha}^0-\frac{\nabla\lambda\boldsymbol{\alpha}^0}{\lambda+\mu}. \tag{3.112}$$

To find $\boldsymbol{\alpha}^1$, we set $l=2$ in (3.99) and form the scalar product of the resulting equation with $\nabla\mathcal{T}$, yielding

$$\begin{aligned}
0=&10\rho(\nabla\mathcal{T}\cdot\boldsymbol{A}^1)-(\lambda+\mu)\nabla\mathcal{T}\cdot\nabla(\nabla\mathcal{T}\cdot\boldsymbol{A}^1)-(\lambda+\mu)|\nabla\mathcal{T}|^2(\nabla\cdot\boldsymbol{A}^1)\\
&-2\mu\nabla\mathcal{T}\cdot[(\nabla\mathcal{T}\cdot\nabla)\boldsymbol{A}^1]-\mu\nabla^2\mathcal{T}(\nabla\mathcal{T}\cdot\boldsymbol{A}^1)-(\nabla\lambda\cdot\nabla\mathcal{T})(\nabla\mathcal{T}\cdot\boldsymbol{A}^1)\\
&-(\nabla\mu\cdot\boldsymbol{A}^1)|\nabla\mathcal{T}|^2-(\nabla\mu\cdot\nabla\mathcal{T})(\nabla\mathcal{T}\cdot\boldsymbol{A}^1)\\
&+(\lambda+\mu)\nabla\mathcal{T}\cdot\nabla(\nabla\cdot\boldsymbol{A}^0)+\mu\nabla\mathcal{T}\cdot(\nabla^2\boldsymbol{A}^0)\\
&+(\nabla\lambda\cdot\nabla\mathcal{T})(\nabla\cdot\boldsymbol{A}^0)+\nabla\mathcal{T}\cdot[\nabla\mu\times(\nabla\times\boldsymbol{A}^0)]+2\nabla\mathcal{T}\cdot[(\nabla\mu\cdot\nabla)\boldsymbol{A}^0].
\end{aligned} \tag{3.113}$$

Inserting (3.111) into (3.113), we obtain

$$\begin{aligned}0 =&[10\rho - \mu\nabla^2\mathcal{T} - \nabla\mathcal{T}\cdot\nabla(\lambda+\mu)]|\nabla\mathcal{T}|^2\boldsymbol{\alpha}^1 - (\lambda+\mu)\nabla\mathcal{T}\cdot\nabla(|\nabla\mathcal{T}|^2\boldsymbol{\alpha}^1)\\ &- (\lambda+\mu)|\nabla\mathcal{T}|^2\nabla\cdot(\nabla\mathcal{T}\boldsymbol{\alpha}^1) - 2\mu\nabla\mathcal{T}\cdot[(\nabla\mathcal{T}\cdot\nabla)(\nabla\mathcal{T}\boldsymbol{\alpha}^1)] - (\nabla\mu\cdot\nabla\mathcal{T})|\nabla\mathcal{T}|^2\boldsymbol{\alpha}^1\\ &+ [10\rho - \mu\nabla^2\mathcal{T} - \nabla\mathcal{T}\cdot\nabla(\lambda+\mu)](\nabla\mathcal{T}\cdot\boldsymbol{C}^0) - (\lambda+\mu)\nabla\mathcal{T}\cdot\nabla(\nabla\mathcal{T}\cdot\boldsymbol{C}^0)\\ &- (\lambda+\mu)|\nabla\mathcal{T}|^2(\nabla\cdot\boldsymbol{C}^0) - 2\mu\nabla\mathcal{T}\cdot[(\nabla\mathcal{T}\cdot\nabla)\boldsymbol{C}^0] - (\nabla\mu\cdot\boldsymbol{C}^0)|\nabla\mathcal{T}|^2 + \boldsymbol{d}^0, \qquad (3.114)\end{aligned}$$

where

$$\begin{aligned}\boldsymbol{d}^0 =&(\lambda+\mu)\nabla\mathcal{T}\cdot\nabla(\nabla\cdot\boldsymbol{A}^0) + \mu\nabla\mathcal{T}\cdot\nabla^2\boldsymbol{A}^0 + (\nabla\lambda\cdot\nabla\mathcal{T})(\nabla\cdot\boldsymbol{A}^0)\\ &+ \nabla\mathcal{T}\cdot[\nabla\mu\times(\nabla\times\boldsymbol{A}^0)] + 2\nabla\mathcal{T}\cdot[(\nabla\mu\cdot\nabla)\boldsymbol{A}^0]. \qquad (3.115)\end{aligned}$$

Using the following relations

$$\nabla\mathcal{T}\cdot[(\nabla\mathcal{T}\cdot\nabla)(\nabla\mathcal{T}\boldsymbol{\alpha}^1)] = (\nabla\mathcal{T}\cdot\nabla\boldsymbol{\alpha}^1)|\nabla\mathcal{T}|^2 + \frac{1}{2}\nabla\mathcal{T}\cdot\nabla(|\nabla\mathcal{T}|^2)\boldsymbol{\alpha}^1 \qquad (3.116)$$

and

$$\nabla\cdot(\nabla\mathcal{T}\boldsymbol{\alpha}^1) = \nabla\mathcal{T}\cdot\nabla\boldsymbol{\alpha}^1 + \nabla^2\mathcal{T}\boldsymbol{\alpha}^1, \qquad (3.117)$$

we may simplify (3.114) into

$$\nabla\mathcal{T}\cdot\nabla\boldsymbol{\alpha}^1 + [\frac{1}{2\rho}\nabla\cdot(\rho\nabla\mathcal{T}) - \frac{3\rho}{\lambda+2\mu}]\boldsymbol{\alpha}^1 = \boldsymbol{c}^0, \qquad (3.118)$$

where $\boldsymbol{c}^0$ is defined to be

$$\begin{aligned}\boldsymbol{c}^0 =&\frac{1}{8\rho\mathcal{T}}\{[10\rho-\mu\nabla^2\mathcal{T}-\nabla\mathcal{T}\cdot\nabla(\lambda+\mu)](\nabla\mathcal{T}\cdot\boldsymbol{C}^0)-(\lambda+\mu)\nabla\mathcal{T}\cdot\nabla(\nabla\mathcal{T}\cdot\boldsymbol{C}^0)\\&-(\lambda+\mu)|\nabla\mathcal{T}|^2(\nabla\cdot\boldsymbol{C}^0)-2\mu\nabla\mathcal{T}\cdot[(\nabla\mathcal{T}\cdot\nabla)\boldsymbol{C}^0]-(\nabla\mu\cdot\boldsymbol{C}^0)|\nabla\mathcal{T}|^2+\boldsymbol{d}^0\}.\end{aligned}\tag{3.119}$$

3.4.2 P-wave transport equations for general $\boldsymbol{A}^l$

Similarly, we can derive governing equations for $\boldsymbol{A}^l$ when $l \geq 2$, which are stated as the following,

$$\boldsymbol{A}^l = \boldsymbol{C}^{l-1} + \nabla\mathcal{T}\boldsymbol{\alpha}^l, \tag{3.120}$$

where $\boldsymbol{\alpha}^l$ is to be determined, and $\boldsymbol{C}^{l-1}$ is available from already computed quantities by using the following formula,

$$\begin{aligned}\boldsymbol{C}^{l-1} \equiv&\frac{1}{(\lambda+\mu)|\nabla\mathcal{T}|^2}\{-\rho(4l-18)\boldsymbol{A}^{l-1}\\&-(\lambda+\mu)\nabla(\nabla\mathcal{T}\cdot\boldsymbol{A}^{l-1})-2\mu(\nabla\mathcal{T}\cdot\nabla)\boldsymbol{A}^{l-1}-\mu\nabla^2\mathcal{T}\boldsymbol{A}^{l-1}\\&-\nabla\lambda(\nabla\mathcal{T}\cdot\boldsymbol{A}^{l-1})-(\nabla\mu\cdot\nabla\mathcal{T})\boldsymbol{A}^{l-1}+(\lambda+\mu)\nabla(\nabla\cdot\boldsymbol{A}^{l-2})\\&+\mu\nabla^2\boldsymbol{A}^{l-2}+\nabla\lambda(\nabla\cdot\boldsymbol{A}^{l-2})+\nabla\mu\times(\nabla\times\boldsymbol{A}^{l-2})+2(\nabla\mu\cdot\nabla)\boldsymbol{A}^{l-2}\}.\end{aligned}\tag{3.121}$$

Accordingly, we can derive the recursive equations for $\boldsymbol{\alpha}^l$

$$\nabla\mathcal{T}\cdot\nabla\boldsymbol{\alpha}^l+\left[\frac{1}{2\rho}\nabla\cdot(\rho\nabla\mathcal{T})+\frac{(2l-5)\rho}{\lambda+2\mu}\right]\boldsymbol{\alpha}^l=\boldsymbol{c}^{l-1},\tag{3.122}$$

where $\boldsymbol{c}^{l-1}$ satisfies

$$\begin{aligned}\boldsymbol{c}^{l-1} \equiv & \frac{1}{8\rho\mathcal{T}}\{[(14-4l)\rho-\mu\nabla^2\mathcal{T}-\nabla\mathcal{T}\cdot\nabla(\lambda+\mu)](\nabla\mathcal{T}\cdot\boldsymbol{C}^{l-1}) \\ & -(\lambda+\mu)\nabla\mathcal{T}\cdot\nabla(\nabla\mathcal{T}\cdot\boldsymbol{C}^{l-1})-(\lambda+\mu)|\nabla\mathcal{T}|^2(\nabla\cdot\boldsymbol{C}^{l-1}) \\ & -2\mu\nabla\mathcal{T}\cdot[(\nabla\mathcal{T}\cdot\nabla)\boldsymbol{C}^{l-1}]-(\nabla\mu\cdot\boldsymbol{C}^{l-1})|\nabla\mathcal{T}|^2 \\ & +(\lambda+\mu)\nabla\mathcal{T}\cdot\nabla(\nabla\cdot\boldsymbol{A}^{l-1})+\mu\nabla\mathcal{T}\cdot\nabla^2\boldsymbol{A}^{l-1}+(\nabla\lambda\cdot\nabla\mathcal{T})(\nabla\cdot\boldsymbol{A}^{l-1}) \\ & +\nabla\mathcal{T}\cdot[\nabla\mu\times(\nabla\times\boldsymbol{A}^{l-1})]+2\nabla\mathcal{T}\cdot[(\nabla\mu\cdot\nabla)\boldsymbol{A}^{l-1}]\}, \end{aligned} \tag{3.123}$$

with $\boldsymbol{C}^l=0$ and $\boldsymbol{c}^l=0$ for $l<0$.

3.4.3 P wave: verification in a homogeneous medium

In a homogeneous medium, the parameters ρ, λ and μ are constants. In this case, (3.106) reduces to

$$\mathcal{T}_{,i}\alpha^0_{j,i}-\frac{2\rho}{\lambda+2\mu}\alpha^0_j=0. \tag{3.124}$$

Here we have $\mathcal{T}=\gamma^{P^2}r^2=\frac{\rho}{\lambda+2\mu}r^2$ in a homogeneous medium. We have the exact Green's function for the P wave, which we rewrite here as

$$\ddot{G}^P_{ij}=\frac{\gamma^{P^3}}{\rho\pi}[2\gamma^{P^2}r^2t_it_jf_+^{(-3)}(t^2-\gamma^{P^2}r^2)-\delta_{ij}f_+^{(-2)}(t^2-\gamma^{P^2}r^2)]. \tag{3.125}$$

To simplify the derivation, we assume that the source is at the origin in this subsection. From this, we obtain $A^0_{ij}=2\frac{\gamma^{P^5}}{\rho\pi}x_ix_j$ and $A^1_{ij}=-\frac{\gamma^{P^3}}{\rho\pi}\delta_{ij}$. So for any $1\le j\le 3$, $A^0_{ij}=\frac{\gamma^{P^3}}{\rho\pi}\mathcal{T}_{,i}x_j$,

and the corresponding $\alpha_j^0 = \frac{\gamma P^3}{\rho\pi} x_j$. Since $\alpha_{j,i}^0 = \frac{\gamma P^3}{\rho\pi}\delta_{ij}$, we have

$$\mathcal{T}_{,i}\alpha_{j,i}^0 - \frac{2\rho}{\lambda+2\mu}\alpha_j^0 = 2\frac{\gamma P^5}{\rho\pi}x_i\delta_{ij} - 2\frac{\gamma P^5}{\rho\pi}x_j = 0, \tag{3.126}$$

which verifies equation (3.124).

Now we verify (3.111) in a uniform medium, i.e. $A_{ij}^1 = C_{ij}^0 + \alpha_j^1\mathcal{T}_{,i}$. From equation (3.112), we have

$$C_{ij}^0 = -\alpha_{j,i}^0 = -\frac{\gamma P^3}{\rho\pi}\delta_{ij}, \tag{3.127}$$

yielding

$$A_{ij}^1 - C_{ij}^0 = -\frac{\gamma P^3}{\rho\pi}\delta_{ij} + \frac{\gamma P^3}{\rho\pi}\delta_{ij} = 0, \tag{3.128}$$

which implies that $\alpha_j^1 = 0$.

To see that $\alpha_j^1 = 0$ satisfies equation (3.118) in a homogeneous medium, we just need to check that c_j^0 defined in equation (3.119) vanishes,

$$c_j^0 = \frac{1}{8\rho\mathcal{T}}\{(10\rho - \mu\mathcal{T}_{,kk})C_{ij}^0\mathcal{T}_{,i} - (\lambda+\mu)\mathcal{T}_{,i}(C_{kj}^0\mathcal{T}_{,k})_{,i} + d_j^0\}. \tag{3.129}$$

First we find that $\boldsymbol{d}^0$ in equation (3.115) is given by

$$\begin{aligned} d_j^0 &= (\lambda+\mu)\mathcal{T}_{,i}A_{kj,ki}^0 + \mu\mathcal{T}_{,i}A_{ij,kk}^0 \\ &= 16(\lambda+\mu)\frac{\gamma P^7}{\rho\pi}x_j + 8\mu\frac{\gamma P^7}{\rho\pi}x_j. \end{aligned} \tag{3.130}$$

Inserting this into (3.129), we can obtain

$$\begin{aligned} c_j^0 &= \frac{1}{8\rho\mathcal{T}}\left\{-\frac{20\gamma P^5 x_j}{\pi}+\frac{12\mu\gamma P^7 x_j}{\rho\pi}+\frac{4(\lambda+\mu)\gamma P^7 x_j}{\rho\pi}+\frac{16(\lambda+\mu)\gamma P^7 x_j}{\rho\pi}+\frac{8\mu\gamma P^7 x_j}{\rho\pi}\right\} \\ &= 0. \end{aligned} \tag{3.131}$$

Similarly, we can verify that the coefficients A_{ij}^l are 0 for $l \geq 2$ in a homogeneous medium.

3.4.4 P wave: governing equations for desingularized $\boldsymbol{A}^l$

Although we enforce the condition that $\boldsymbol{A}^l$ are $O(1)$ near the source for all $l \geq 0$, they are not necessarily smooth at the source $\boldsymbol{r}_0$ in an inhomogeneous medium; this can be seen from the initial conditions (3.182)-(3.185). Therefore, we desingularize $\boldsymbol{A}^l$ by introducing a new set of dyadic coefficients,

$$\tilde{\boldsymbol{A}}^l = \boldsymbol{A}^l \tau^{2l}, \tag{3.132}$$

so that

$$\boldsymbol{A}^l = O(1) \text{ as } \boldsymbol{r} \to \boldsymbol{r}_0,$$

$$\tilde{\boldsymbol{A}}^l = O(\tau^{2l}) \text{ as } \boldsymbol{r} \to \boldsymbol{r}_0.$$

According to (3.120) and (3.132), we can set

$$\tilde{\boldsymbol{A}}^l = \tilde{\boldsymbol{C}}^{l-1} + \nabla\mathcal{T}\tilde{\boldsymbol{\alpha}}^l, \tag{3.133}$$

where $\tilde{\boldsymbol{C}}^{l-1} = \boldsymbol{C}^{l-1}\mathcal{T}^l$ and $\tilde{\boldsymbol{\alpha}}^l = \boldsymbol{\alpha}^l\mathcal{T}^l$. Hence, we can derive transport equations for $\tilde{\boldsymbol{\alpha}}^l$

from transport equations for $\boldsymbol{\alpha}^l$ for $l = 0, 1$ as the following,

$$\nabla\mathcal{T}\cdot\nabla\tilde{\boldsymbol{\alpha}}^0 + [\frac{1}{2\rho}\nabla\cdot(\rho\nabla\mathcal{T}) - \frac{5\rho}{\lambda+2\mu}]\tilde{\boldsymbol{\alpha}}^0 = 0, \tag{3.134}$$

$$\nabla\mathcal{T}\cdot\nabla\tilde{\boldsymbol{\alpha}}^1 + [\frac{1}{2\rho}\nabla\cdot(\rho\nabla\mathcal{T}) - \frac{7\rho}{\lambda+2\mu}]\tilde{\boldsymbol{\alpha}}^1 = \tilde{\boldsymbol{c}}^0, \tag{3.135}$$

where $\tilde{\boldsymbol{c}}^0$ can be computed by the following formula,

$$\begin{aligned}\tilde{\boldsymbol{c}}^0 \equiv&\frac{1}{8\rho}\{10\rho - \mu\nabla^2\mathcal{T} - \nabla\mathcal{T}\cdot\nabla(\lambda+\mu)](\nabla\mathcal{T}\cdot\boldsymbol{C}^0) - (\lambda+\mu)\nabla\mathcal{T}\cdot\nabla(\nabla\mathcal{T}\cdot\boldsymbol{C}^0)\\ &- (\lambda+\mu)|\nabla\mathcal{T}|^2(\nabla\cdot\boldsymbol{C}^0) - 2\mu\nabla\mathcal{T}\cdot[(\nabla\mathcal{T}\cdot\nabla)\boldsymbol{C}^0] - (\nabla\mu\cdot\boldsymbol{C}^0)|\nabla\mathcal{T}|^2 + \boldsymbol{d}^0\},\end{aligned} \tag{3.136}$$

where $\boldsymbol{C}^0$ and $\boldsymbol{d}^0$ are defined in (3.112) and (3.115) since $\tilde{\boldsymbol{A}}^0 = \boldsymbol{A}^0$.

For general $l \geq 2$, we can similarly derive the following governing equations,

$$\nabla\mathcal{T}\cdot\nabla\tilde{\boldsymbol{\alpha}}^l + \left[\frac{1}{2\rho}\nabla\cdot(\rho\nabla\mathcal{T}) - \frac{(2l+5)\rho}{\lambda+2\mu}\right]\tilde{\boldsymbol{\alpha}}^l = \tilde{\boldsymbol{c}}^{l-1}, \tag{3.137}$$

where $\tilde{\boldsymbol{c}}^{l-1} = \mathcal{T}^l\boldsymbol{c}^{l-1}$, and $\boldsymbol{c}^{l-1}$ is the same as (3.123). The detailed formula for $\tilde{\boldsymbol{c}}^{l-1}$ is given in Appendix A.

3.5 Initial conditions for the traveltime and amplitudes

3.5.1 Initial conditions for S-wave

In this section, we shall initialize those amplitude coefficients $\boldsymbol{A}^l$ and $\tilde{\boldsymbol{A}}^l$ for the S wave at the source $\boldsymbol{r}_0$ in the three dimensional space. In a center-deleted neighborhood of $\boldsymbol{r}_0$, say $0 < |\boldsymbol{r} - \boldsymbol{r}_0| < x_0$, where x_0 is a positive constant, we propose the following matching

condition

$$(\ddot{\boldsymbol{G}}^S(\boldsymbol{r};t) - \ddot{\boldsymbol{G}}^S_{hom}(\boldsymbol{r};t))t^n \in L^1(\{t;(0,T)\}) \tag{3.138}$$

over any finite time period $(0,T)$ for any non-negative integer n, where

$$\ddot{\boldsymbol{G}}^S_{hom} = \frac{{\gamma_0^S}^3}{\rho_0\pi}[2\gamma_0^S r^2(\boldsymbol{I} - \boldsymbol{t}\boldsymbol{t}^T)f_+^{(-3)}(t^2 - \gamma_0^S r^2) - 2\boldsymbol{I}f_+^{(-2)}(t^2 - \gamma_0^S r^2)], \tag{3.139}$$

with $\boldsymbol{t} = \frac{\boldsymbol{r}-\boldsymbol{r}_0}{|\boldsymbol{r}-\boldsymbol{r}_0|}$ being the unit tangent vector to the S ray. Here $\boldsymbol{t}\boldsymbol{t}^T = (t_i t_j)_{3\times 3}$ is a matrix. And $\gamma_0^S = \sqrt{\frac{\rho_0}{\mu_0}}$ is the slowness for the S wave with $\rho_0 = \rho(\boldsymbol{r}_0)$ and $\mu_0 = \mu(\boldsymbol{r}_0)$.

Since $f_+^{(-3+l)}(t^2 - \mathcal{T}) \in L^1(\{t;(0,T)\})$ for $l \geq 3$, the above matching condition can be reduced to

$$\begin{aligned}
\ddot{\boldsymbol{G}}^n_{\text{diff}} &= [\ddot{\boldsymbol{G}}^S(\boldsymbol{r};t) - \ddot{\boldsymbol{G}}^S_{hom}(\boldsymbol{r};t)]t^n \\
&= \boldsymbol{A}^0 f_+^{(-3)}(t^2 - \mathcal{T}(\boldsymbol{r}))t^n + \boldsymbol{A}^1 f_+^{(-2)}(t^2 - \mathcal{T}(\boldsymbol{r}))t^n \\
&\quad + \boldsymbol{A}^2 f_+^{(-1)}(t^2 - \mathcal{T}(\boldsymbol{r}))t^n - \ddot{\boldsymbol{G}}^S_{hom}t^n \\
&= \boldsymbol{A}^0\delta^{(2)}(t^2 - \mathcal{T}(\boldsymbol{r}))t^n + \boldsymbol{A}^1\delta^{(1)}(t^2 - \mathcal{T}(\boldsymbol{r}))t^n + \boldsymbol{A}^2\delta(t^2 - \mathcal{T}(\boldsymbol{r}))t^n \\
&\quad - \frac{{\gamma_0^S}^3}{\rho_0\pi}[2\gamma_0^S r^2(\boldsymbol{I} - \boldsymbol{t}\boldsymbol{t}^T)\delta^{(2)}(t^2 - {\gamma^S}^2 r^2) - 2\boldsymbol{I}\delta^{(1)}(t^2 - \gamma_0^S r^2)]t^n \\
&\in L^1(\{t;(0,T)\}),
\end{aligned} \tag{3.140}$$

for any $\boldsymbol{r}$ satisfying $0 < |\boldsymbol{r} - \boldsymbol{r}_0| < x_0$.

For $\boldsymbol{r}$ sufficiently close to $\boldsymbol{r}_0$ such that all δ-related functions do not vanish, one gets

$$\begin{aligned}\int_0^T \delta^{(k)}[t^2-\mathcal{T}(\boldsymbol{r})]t^n dt &= \int_{-\mathcal{T}(\boldsymbol{r})}^{T^2-\mathcal{T}(\boldsymbol{r})} \delta^{(k)}(\tilde{t})\frac{1}{2}(\tilde{t}+\mathcal{T}(\boldsymbol{r}))^{\frac{n}{2}-\frac{1}{2}}d\tilde{t} \\ &= \frac{(-1)^k}{2}[(\tilde{t}+\mathcal{T}(\boldsymbol{r}))^{\frac{n-1}{2}}]^{(k)}|_{\tilde{t}=0} \\ &= \frac{(-1)^k}{2}\prod_{j=0}^{k-1}(\frac{n}{2}-\frac{1}{2}-j)[\mathcal{T}(\boldsymbol{r})]^{\frac{n}{2}-\frac{1}{2}-k}.\end{aligned} \tag{3.141}$$

Since k is at most 2 in our situation, $\frac{n}{2}-\frac{1}{2}-k \geq 0$ for $n \geq 5$ so that we are concerned about the five cases $n = 0, 1, 2, 3, 4$ only. Therefore, we enforce

$$\begin{aligned}\int_0^T \ddot{\boldsymbol{G}}^0_{\text{diff}}dt &= \frac{3}{8}\left[\frac{\boldsymbol{A}^0}{\mathcal{T}(\boldsymbol{r})^{\frac{5}{2}}}-\frac{2\gamma_0^{S^5}r^2}{\rho_0\pi(\gamma_0^S r)^5}(\boldsymbol{I}-\boldsymbol{t}\boldsymbol{t}^T)\right] \\ &\quad+\frac{1}{4}\left[\frac{\boldsymbol{A}^1}{\mathcal{T}(\boldsymbol{r})^{\frac{3}{2}}}+\frac{2\gamma_0^{S^3}}{\rho_0\pi(\gamma_0^S r)^3}\boldsymbol{I}\right]+\frac{\boldsymbol{A}^2}{2\mathcal{T}(\boldsymbol{r})^{\frac{1}{2}}} \\ &= \frac{3}{8}\frac{\boldsymbol{A}^0}{\mathcal{T}(\boldsymbol{r})^{\frac{5}{2}}}+\frac{1}{4}\frac{\boldsymbol{A}^1}{\mathcal{T}(\boldsymbol{r})^{\frac{3}{2}}}+\frac{\boldsymbol{A}^2}{2\mathcal{T}(\boldsymbol{r})^{\frac{1}{2}}}-\frac{1}{4\rho_0\pi r^3}(\boldsymbol{I}-3\boldsymbol{t}\boldsymbol{t}^T)=O(1),\end{aligned} \tag{3.142}$$

$$\int_0^T \ddot{\boldsymbol{G}}^1_{\text{diff}}dt = \frac{\boldsymbol{A}^2}{2}=O(1), \tag{3.143}$$

$$\begin{aligned}\int_0^T \ddot{\boldsymbol{G}}^2_{\text{diff}}dt &= -\frac{1}{8}\left[\frac{\boldsymbol{A}^0}{\mathcal{T}(\boldsymbol{r})^{\frac{3}{2}}}-\frac{2\gamma_0^{S^5}r^2}{\rho_0\pi(\gamma_0^S r)^3}(\boldsymbol{I}-\boldsymbol{t}\boldsymbol{t}^T)\right] \\ &\quad-\frac{1}{4}\left[\frac{\boldsymbol{A}^1}{\mathcal{T}(\boldsymbol{r})^{\frac{1}{2}}}+\frac{2\gamma_0^{S^3}}{\rho_0\pi(\gamma_0^S r)}\boldsymbol{I}\right]+\frac{\boldsymbol{A}^2}{2}\mathcal{T}(\boldsymbol{r})^{\frac{1}{2}} \\ &= -\frac{1}{8}\frac{\boldsymbol{A}^0}{\mathcal{T}(\boldsymbol{r})^{\frac{3}{2}}}-\frac{1}{4}\frac{\boldsymbol{A}^1}{\mathcal{T}(\boldsymbol{r})^{\frac{1}{2}}}+\frac{\boldsymbol{A}^2}{2}\mathcal{T}(\boldsymbol{r})^{\frac{1}{2}}-\frac{\gamma_0^{S^2}}{4\rho_0\pi r}(\boldsymbol{I}+\boldsymbol{t}\boldsymbol{t}^T)=O(1),\end{aligned} \tag{3.144}$$

$$\int_0^T \ddot{\boldsymbol{G}}^3_{\text{diff}} dt = -\frac{1}{2}\left[\boldsymbol{A}^1 + \frac{2\gamma_0^{S^3}\boldsymbol{I}}{\rho_0\pi}\right] + \frac{1}{2}\boldsymbol{A}^2\mathcal{T}(\boldsymbol{r}) = O(1), \tag{3.145}$$

$$\begin{aligned}\int_0^T \ddot{\boldsymbol{G}}^4_{\text{diff}} dt &= \frac{3}{8}\left[\frac{\boldsymbol{A}^0}{\mathcal{T}(\boldsymbol{r})^{\frac{1}{2}}} - \frac{2\gamma_0^{S^5} r^2}{\rho_0\pi(\gamma_0^S r)}(\boldsymbol{I} - \boldsymbol{t}\boldsymbol{t}^T)\right] \\ &\quad - \frac{3}{4}\left[\boldsymbol{A}^1\mathcal{T}(\boldsymbol{r})^{\frac{1}{2}} + \frac{2\gamma_0^{S^3}}{\rho_0\pi}(\gamma_0^S r)\boldsymbol{I}\right] + \frac{\boldsymbol{A}^2}{2}\mathcal{T}(\boldsymbol{r})^{\frac{3}{2}} \\ &= \frac{3}{8}\frac{\boldsymbol{A}^0}{\mathcal{T}(\boldsymbol{r})^{\frac{1}{2}}} - \frac{3}{4}\boldsymbol{A}^1\mathcal{T}(\boldsymbol{r})^{\frac{1}{2}} + \frac{\boldsymbol{A}^2}{2}\mathcal{T}(\boldsymbol{r})^{\frac{3}{2}} - \frac{3\gamma_0^{S^4} r}{4\rho_0\pi}(3\boldsymbol{I} - \boldsymbol{t}\boldsymbol{t}^T) = O(1),\end{aligned} \tag{3.146}$$

for $0 < |\boldsymbol{r} - \boldsymbol{r}_0| < x_0$.

Hiding $O(1)$ terms above, we get

$$\frac{3}{8}\frac{\boldsymbol{A}^0}{\mathcal{T}(\boldsymbol{r})^{\frac{5}{2}}} + \frac{1}{4}\frac{\boldsymbol{A}^1}{\mathcal{T}(\boldsymbol{r})^{\frac{3}{2}}} + \frac{\boldsymbol{A}^2}{2\mathcal{T}(\boldsymbol{r})^{\frac{1}{2}}} - \frac{1}{4\rho_0\pi r^3}(\boldsymbol{I} - 3\boldsymbol{t}\boldsymbol{t}^T) = O(1), \tag{3.147}$$

$$-\frac{1}{8}\frac{\boldsymbol{A}^0}{\mathcal{T}(\boldsymbol{r})^{\frac{3}{2}}} - \frac{1}{4}\frac{\boldsymbol{A}^1}{\mathcal{T}(\boldsymbol{r})^{\frac{1}{2}}} - \frac{\gamma_0^{S^2}}{4\rho_0\pi r}(\boldsymbol{I} + \boldsymbol{t}\boldsymbol{t}^T) = O(1), \tag{3.148}$$

$$\frac{3}{8}\frac{\boldsymbol{A}^0}{\mathcal{T}(\boldsymbol{r})^{\frac{1}{2}}} = O(1). \tag{3.149}$$

Considering (3.147)$\times\mathcal{T}(\boldsymbol{r})$+(3.148), we can obtain the initial condition for $\boldsymbol{A}^0$ as $\boldsymbol{r} \to \boldsymbol{r}_0$,

$$\boldsymbol{A}^0 = \frac{\mathcal{T}^{\frac{5}{2}}}{\rho_0\pi r^3}(\boldsymbol{I} - 3\boldsymbol{t}\boldsymbol{t}^T) + \frac{\gamma_0^{S^2}\mathcal{T}^{\frac{3}{2}}}{\rho_0\pi r}(\boldsymbol{I} + \boldsymbol{t}\boldsymbol{t}^T) + O(\mathcal{T}^{\frac{3}{2}}). \tag{3.150}$$

Moreover, since τ is the traveltime from the source $\boldsymbol{r}_0$ to $\boldsymbol{r}$ which is proportional to $r = |\boldsymbol{r} - \boldsymbol{r}_0|$, $\mathcal{T} = \tau^2$ is proportional to r^2 as $\boldsymbol{r} \to \boldsymbol{r}_0$, leading to $\boldsymbol{A}^0 = O(1)$ as $\boldsymbol{r} \to \boldsymbol{r}_0$.

Next (3.147) $\times 4\mathcal{T}(\boldsymbol{r})^{\frac{3}{2}}$ gives rise to the initial condition for $\boldsymbol{A}^1$ as $\boldsymbol{r} \to \boldsymbol{r}_0$,

$$\begin{aligned}\boldsymbol{A}^1 =& -\frac{3}{2}\frac{\boldsymbol{A}^0}{\mathcal{T}} + \frac{\mathcal{T}^{\frac{3}{2}}}{\rho_0 \pi r^3}(\boldsymbol{I} - 3\boldsymbol{t}\boldsymbol{t}^T) + 2\boldsymbol{A}^2\mathcal{T}(\boldsymbol{x}) + O(\mathcal{T}^{\frac{3}{2}}) \\ =& -\frac{3}{2}\frac{\boldsymbol{A}^0}{\mathcal{T}} + \frac{\mathcal{T}^{\frac{3}{2}}}{\rho_0 \pi r^3}(\boldsymbol{I} - 3\boldsymbol{t}\boldsymbol{t}^T) + O(\mathcal{T}). \end{aligned} \tag{3.151}$$

Substituting (3.150) into (3.151), we could obtain

$$\boldsymbol{A}^1 = -\frac{1}{2}\frac{\mathcal{T}^{\frac{3}{2}}}{\rho_0 \pi r^3}(\boldsymbol{I} - 3\boldsymbol{t}\boldsymbol{t}^T) - \frac{3}{2}\frac{\gamma_0^{S^2}\mathcal{T}^{\frac{1}{2}}}{\rho_0 \pi r}(\boldsymbol{I} + \boldsymbol{t}\boldsymbol{t}^T) + O(\mathcal{T}^{\frac{1}{2}}). \tag{3.152}$$

Similar to the case for $\boldsymbol{A}^0$, we may conclude that $\boldsymbol{A}^1 = O(1)$ as $\boldsymbol{r} \to \boldsymbol{r}_0$.

Finally, (3.147) $\times 2\mathcal{T}(\boldsymbol{r})^{\frac{1}{2}}$ gives rise to the initial condition for $\boldsymbol{A}^2$ as $\boldsymbol{r} \to \boldsymbol{r}_0$,

$$\boldsymbol{A}^2 = -\frac{3}{4}\frac{\boldsymbol{A}^0}{\mathcal{T}^2} - \frac{1}{2}\frac{\boldsymbol{A}^1}{\mathcal{T}} + \frac{\mathcal{T}^{\frac{1}{2}}}{2\rho_0 \pi r^3}(\boldsymbol{I} - 3\boldsymbol{t}\boldsymbol{t}^T) + O(\mathcal{T}^{\frac{1}{2}}). \tag{3.153}$$

When substituting (3.151) into (3.153), the first three terms on the right hand side of (3.153) will be canceled. Hence we may conclude that $\boldsymbol{A}^2 = O(1)$ as $\boldsymbol{r} \to \boldsymbol{r}_0$ which is also consistent with (3.143).

Similarly we can obtain the following initial conditions for $\tilde{\boldsymbol{A}}^l$

$$\tilde{\boldsymbol{A}}^0 = \frac{\mathcal{T}^{\frac{5}{2}}}{\rho_0 \pi r^3}(\boldsymbol{I} - 3\boldsymbol{t}\boldsymbol{t}^T) + \frac{\gamma_0^{S^2}\mathcal{T}^{\frac{3}{2}}}{\rho_0 \pi r}(\boldsymbol{I} + \boldsymbol{t}\boldsymbol{t}^T) + O(\mathcal{T}^{\frac{3}{2}}), \tag{3.154}$$

$$\tilde{\boldsymbol{A}}^1 = -\frac{3}{2}\tilde{\boldsymbol{A}}^0 + \frac{\mathcal{T}^{\frac{5}{2}}}{\rho_0 \pi r^3}(\boldsymbol{I} - 3\boldsymbol{t}\boldsymbol{t}^T) + O(\mathcal{T}^2), \tag{3.155}$$

$$\tilde{\boldsymbol{A}}^2 = -\frac{3}{4}\tilde{\boldsymbol{A}}^0 - \frac{1}{2}\tilde{\boldsymbol{A}}^1 + \frac{\mathcal{T}^{\frac{5}{2}}}{2\rho_0 \pi r^3}(\boldsymbol{I} - 3\boldsymbol{t}\boldsymbol{t}^T) + O(\mathcal{T}^{\frac{5}{2}}). \tag{3.156}$$

Next, we give details to initialize the general $\tilde{\boldsymbol{A}}^l$ from the governing equations (3.95) and

the initial conditions (3.154)-(3.156) for $\tilde{\boldsymbol{A}}^l$ with $0 \le l \le 2$.

In an isotropic medium, the travel time function $\tau(\cdot;\boldsymbol{r}_0)$ solving the eikonal equation $|\nabla\tau(\boldsymbol{r};\boldsymbol{r}_0)| = \gamma^S(\boldsymbol{r})$ is locally smooth near the source except at the source point $\boldsymbol{r}_0$ itself [52, 71].

Assuming that the refractive index $\gamma^{S^2}(\boldsymbol{r})$ is analytic, $\gamma^{S^2}(\boldsymbol{r})$ can be written as the following power series centered at the source point,

$$\gamma^{S^2}(\boldsymbol{r}) = \sum_{k=0}^{\infty} \Phi_k(\boldsymbol{r};\boldsymbol{r}_0), \tag{3.157}$$

where Φ_k is the homogeneous polynomial of degree-k term in the Taylor expansion of γ^{S^2} about the source $\boldsymbol{r}_0$ and $\Phi_0 = \gamma_0^{S^2}$ with $\gamma_0^S = \gamma^S(\boldsymbol{r}_0)$.

Assuming that $\mathcal{T} = \tau^2$ is analytic, we have in the source neighborhood [44]

$$\tau^2 - \left(\Phi_0 + \frac{1}{2}\Phi_1 + \frac{1}{3}\Phi_2 - \frac{1}{48\Phi_0}|\nabla\Phi_1|^2 r^2\right) r^2 = O(r^5). \tag{3.158}$$

This in fact gives rise to the following estimate: for any $k \in \boldsymbol{R}$, as $r \to 0$,

$$\left(\frac{\tau}{\gamma_0^S r}\right)^k = 1 + \frac{k}{2\Phi_0}\left(\frac{\Phi_1}{2} + \frac{\Phi_2}{3} - \frac{|\nabla\Phi_1|^2}{48\Phi_0} r^2\right) + \frac{k}{4}\left(\frac{k}{2} - 1\right)\frac{\Phi_1^2}{4\Phi_0^2} + O(r^3). \tag{3.159}$$

Then using formulas (3.158) and (3.159), we can rewrite (3.154)-(3.156) as follows.

(a) The sequence $\{\tilde{\boldsymbol{A}}_{0k}\}$ is initialized by

$$\tilde{\boldsymbol{A}}_{00} = 0,\ \tilde{\boldsymbol{A}}_{01} = 0,\ \tilde{\boldsymbol{A}}_{02} = \frac{2\gamma_0^{S^5} r^2}{\rho_0 \pi}(\boldsymbol{I} - \boldsymbol{t}\boldsymbol{t}^T). \tag{3.160}$$

(b) The sequence $\{\tilde{\boldsymbol{A}}_{1k}\}$ is initialized by

$$\tilde{\boldsymbol{A}}_{10} = 0,\ \tilde{\boldsymbol{A}}_{11} = 0,\ \tilde{\boldsymbol{A}}_{12} = -\frac{2\gamma_0^{S^5} r^2}{\rho_0 \pi}\boldsymbol{I}, \tag{3.161}$$
$$\tilde{\boldsymbol{A}}_{13} = -\frac{3}{2}\tilde{\boldsymbol{A}}_{03} + \frac{5\gamma_0^{S^3}\Phi_1 r^2}{4\rho_0\pi}(\boldsymbol{I} - 3\boldsymbol{t}\boldsymbol{t}^T).$$

(c) The sequence $\{\tilde{\boldsymbol{A}}_{2k}\}$ is initialized by

$$\tilde{\boldsymbol{A}}_{20} = 0,\ \tilde{\boldsymbol{A}}_{21} = 0, \tilde{\boldsymbol{A}}_{22} = 0,\ \tilde{\boldsymbol{A}}_{23} = 0, \tag{3.162}$$
$$\tilde{\boldsymbol{A}}_{24} = -\frac{3}{4}\tilde{\boldsymbol{A}}_{04} - \frac{1}{2}\tilde{\boldsymbol{A}}_{14} + \frac{\gamma_0^{S^3}}{2\rho_0\pi}(\boldsymbol{I} - 3\boldsymbol{t}\boldsymbol{t}^T)\left[\frac{5\Phi_2}{6}r^2 + \frac{15\Phi_1^2}{32\Phi_0}r^2 - \frac{5|\nabla\Phi_1|^2}{96\Phi_0}r^4\right].$$

If we further assume that $\log\mu(\boldsymbol{r})$, $\tilde{\boldsymbol{A}}^l$, and $\tilde{\boldsymbol{R}}^{l-1}$ for all $l \geq 0$ are analytic at the source $\boldsymbol{r}_0$, then those asymptotic behaviors (3.154)-(3.156) for $\tilde{\boldsymbol{A}}^0$, $\tilde{\boldsymbol{A}}^1$, and $\tilde{\boldsymbol{A}}^2$ respectively, can be further clarified, and the exact solutions of $\tilde{\boldsymbol{A}}^l$ for general l near the source can be constructed recursively.

We first expand these ingredients as Taylor series about the source as:

$$\log\mu(\boldsymbol{r}) = \sum_{k=0}^{\infty} U_k(\boldsymbol{r}), \tag{3.163}$$
$$\tilde{\boldsymbol{A}}^l(\boldsymbol{r}) = \sum_{k=0}^{\infty} \tilde{\boldsymbol{A}}_{lk}(\boldsymbol{r}), \tag{3.164}$$
$$\tilde{\boldsymbol{R}}^{l-1}(\boldsymbol{r}) = \sum_{k=0}^{\infty} \tilde{\boldsymbol{R}}_{l-1,k}(\boldsymbol{r}), \tag{3.165}$$

where the term with subscript k denotes a homogeneous polynomial of degree k. As $\mathcal{T} = \tau^2$

is analytic near the source neighborhood, we denote its Taylor series as

$$\mathcal{T}(\boldsymbol{r}) = \tau^2(\boldsymbol{r}) = \sum_{k=0}^{\infty} T_k(\boldsymbol{r}). \tag{3.166}$$

We see from the eikonal equation that $T_0 = T_1 = 0$, and $T_2 = \Phi_0 r^2$. Thus the transport equation (3.95) for the S wave can be rewritten as

$$\begin{aligned}
&\sum_{k=0}^{\infty} \Phi_k(\boldsymbol{r}) \left(\sum_{k=2}^{\infty} \nabla T_k(\boldsymbol{r}) \cdot \nabla \right) \sum_{k=0}^{\infty} \tilde{\boldsymbol{A}}_{lk}(\boldsymbol{r}) + \frac{1}{2} \sum_{k=2}^{\infty} \nabla T_k(\boldsymbol{r}) \left[\sum_{k=0}^{\infty} \nabla \Phi_k(\boldsymbol{r}) \cdot \sum_{k=0}^{\infty} \tilde{\boldsymbol{A}}_{lk}(\boldsymbol{r}) \right] \\
&+ \sum_{k=0}^{\infty} \Phi_k(\boldsymbol{r}) \left[\frac{1}{2} \sum_{k=2}^{\infty} \Delta T_k(\boldsymbol{r}) + \frac{1}{2} \sum_{k=2}^{\infty} \nabla T_k(\boldsymbol{r}) \cdot \sum_{k=0}^{\infty} \nabla U_k(\boldsymbol{r}) \right] \sum_{k=0}^{\infty} \tilde{\boldsymbol{A}}_{lk}(\boldsymbol{r}) \\
&+ \sum_{k=0}^{\infty} \Phi_k(\boldsymbol{r}) \left[-(2l+7) \sum_{k=0}^{\infty} \Phi_k(\boldsymbol{r}) \right] \sum_{k=0}^{\infty} \tilde{\boldsymbol{A}}_{lk}(\boldsymbol{r}) \\
&= \sum_{k=0}^{\infty} \Phi_k(\boldsymbol{r}) \sum_{k=0}^{\infty} \tilde{\boldsymbol{R}}_{l-1,k}(\boldsymbol{r}).
\end{aligned} \tag{3.167}$$

Comparing the q-th degree polynomial of both sides, we have

$$\begin{aligned}
0 &= \Phi_0(\nabla T_2 \cdot \nabla) \tilde{\boldsymbol{A}}_{lq} + \Phi_0(\frac{1}{2}\Delta T_2 - (2l+7)\Phi_0) \tilde{\boldsymbol{A}}_{lq} \\
&+ \frac{1}{2} \sum_{s=0}^{q-1} \sum_{j+k=q-s, j,k \geq 0} \nabla T_{2+k} (\nabla \Phi_j \cdot \tilde{\boldsymbol{A}}_{ls}) + \sum_{s=0}^{q-1} \sum_{j+k=q-s, j,k \geq 0} \Phi_j (\nabla T_{2+k} \cdot \nabla) \tilde{\boldsymbol{A}}_{ls} \\
&+ \sum_{s=0}^{q-1} \sum_{j+k=q-s, j,k \geq 0} \Phi_j \left(\frac{\Delta T_{2+k}}{2} + \frac{1}{2} \sum_{m+n=k, m,n \geq 0} \nabla T_{2+m} \cdot \nabla U_n - (2l+7)\Phi_k \right) \tilde{\boldsymbol{A}}_{ls} \\
&- \sum_{j+k=q, j,k \geq 0} \Phi_j \tilde{\boldsymbol{R}}_{l-1,k}.
\end{aligned} \tag{3.168}$$

Using the fact that $(\nabla T_2 \cdot \nabla)\tilde{\boldsymbol{A}}_{lq} = 2q\Phi_0\tilde{\boldsymbol{A}}_{lq}$ and $\Delta T_2 = 6\Phi_0$, we get

$$
\begin{aligned}
0 &= (2q - (2l+4))\Phi_0^2\tilde{\boldsymbol{A}}_{lq} \\
&+ \frac{1}{2}\sum_{s=0}^{q-1}\sum_{j+k=q-s,j,k\geq 0}\nabla T_{2+k}(\nabla\Phi_j\cdot\tilde{\boldsymbol{A}}_{ls}) + \sum_{s=0}^{q-1}\sum_{j+k=q-s,j,k\geq 0}\Phi_j(\nabla T_{2+k}\cdot\nabla)\tilde{\boldsymbol{A}}_{ls} \\
&+ \sum_{s=0}^{q-1}\sum_{j+k=q-s,j,k\geq 0}\Phi_j\left(\frac{\Delta T_{2+k}}{2} + \frac{1}{2}\sum_{m+n=k,m,n\geq 0}\nabla T_{2+m}\cdot\nabla U_n - (2l+7)\Phi_k\right)\tilde{\boldsymbol{A}}_{ls} \\
&- \sum_{j+k=q,j,k\geq 0}\Phi_j\tilde{\boldsymbol{R}}_{l-1,k}. \qquad (3.169)
\end{aligned}
$$

Hence we obtain a recursive formula to compute the q-th degree polynomial $\tilde{\boldsymbol{A}}_{lq}$ of the l-th amplitude coefficient $\tilde{\boldsymbol{A}}^l$.

It is clear that (3.169) is not valid for computing $\tilde{\boldsymbol{A}}_{lq^*}$ when $q^* = l+2$, since the coefficient of $\tilde{\boldsymbol{A}}_{lq^*}$ becomes 0. However, in this case, we first notice that when $l \geq 3$, $\tilde{\boldsymbol{A}}^l$ has been assumed to be $O(\mathcal{T}^l) = O(r^{2l}) = o(r^{l+2})$ due to $2l \geq l+2$, so that $\tilde{\boldsymbol{A}}_{lq^*} = 0$ when $q^* = l+2$. In addition, we have three special cases: (1) $l = 0$ so that $q^* = 2$, but $\tilde{\boldsymbol{A}}_{02}$ has been initialized according to (3.160); (2) $l = 1$ so that $q^* = 3$, but $\tilde{\boldsymbol{A}}_{13}$ has been initialized according to (3.161); (3) $l = 2$ so that $q^* = 4$, but $\tilde{\boldsymbol{A}}_{24}$ has been initialized according to (3.162).

In the recursive formula (3.169), $\tilde{\boldsymbol{R}}_{l-1,k}$ depends on $\tilde{\boldsymbol{A}}^{l-1}$ but does not depend on $\tilde{\boldsymbol{A}}^l$; therefore, the power series of $\tilde{\boldsymbol{A}}^l$ is computable via (3.169) once $\tilde{\boldsymbol{A}}^{l-1}$ is available near the source.

3.5.2 Initial conditions for P-wave

In this section, we shall initialize those amplitude coefficients $\boldsymbol{A}^l$ and $\tilde{\boldsymbol{A}}^l$for the P wave at the source $\boldsymbol{r}_0$ in the three dimensional space. In a center-deleted neighborhood of $\boldsymbol{r}_0$, say $0 < |\boldsymbol{r} - \boldsymbol{r}_0| < x_0$, where x_0 is a positive constant, we propose the following matching condition,

$$(\ddot{\boldsymbol{G}}^P(\boldsymbol{r};t) - \ddot{\boldsymbol{G}}^P_{hom}(\boldsymbol{r};t))t^n \in L^1(\{t;(0,T)\}), \tag{3.170}$$

over any finite time period $(0,T)$ for any non-negative integer n, where

$$\ddot{\boldsymbol{G}}^P_{hom} = \frac{{\gamma_0^P}^3}{\rho_0\pi}\left[2{\gamma_0^P}^2 r^2 \boldsymbol{t}\boldsymbol{t}^T f_+^{(-3)}(t^2 - {\gamma_0^P}^2 r^2) - \boldsymbol{I} f_+^{(-2)}(t^2 - {\gamma_0^P}^2 r^2)\right], \tag{3.171}$$

with $\boldsymbol{t} = \frac{\boldsymbol{r}-\boldsymbol{r}_0}{|\boldsymbol{r}-\boldsymbol{r}_0|}$ being the unit tangent vector to the P ray. Here $\boldsymbol{t}\boldsymbol{t}^T = (t_i t_j)_{3\times 3}$ is a matrix. And $\gamma_0^P = \sqrt{\frac{\rho_0}{\lambda_0+2\mu_0}}$ is the slowness for the P wave with $\rho_0 = \rho(\boldsymbol{r}_0)$, $\mu_0 = \mu(\boldsymbol{r}_0)$ and $\lambda_0 = \lambda(\boldsymbol{r}_0)$.

Since $f_+^{(-3+l)}(t^2 - \mathcal{T}) \in L^1(\{t;(0,T)\})$ for $l \geq 3$, the above matching condition can be

reduced to

$$\begin{aligned}
\ddot{\boldsymbol{G}}^n_{\rm diff} &= [\ddot{\boldsymbol{G}}^P(\boldsymbol{r};t) - \ddot{\boldsymbol{G}}^P_{hom}(\boldsymbol{r};t)]t^n \\
&= \boldsymbol{A}^0 f_+^{(-3)}(t^2-\mathcal{T}(\boldsymbol{r}))t^n + \boldsymbol{A}^1 f_+^{(-2)}(t^2-\mathcal{T}(\boldsymbol{r}))t^n \\
&\quad + \boldsymbol{A}^2 f_+^{(-1)}(t^2-\mathcal{T}(\boldsymbol{r}))t^n - \ddot{\boldsymbol{G}}^P_{hom}t^n \\
&= \boldsymbol{A}^0\delta^{(2)}(t^2-\mathcal{T}(\boldsymbol{r}))t^n + \boldsymbol{A}^1\delta^{(1)}(t^2-\mathcal{T}(\boldsymbol{r}))t^n + \boldsymbol{A}^2\delta(t^2-\mathcal{T}(\boldsymbol{r}))t^n \\
&- \frac{\gamma_0^{P3}}{\rho_0\pi}[2\gamma_0^{P2}r^2\boldsymbol{t}\boldsymbol{t}^T\delta^{(2)}(t^2-\gamma_0^{P2}r^2) - \boldsymbol{I}\delta^{(1)}(t^2-\gamma_0^{P2}r^2)]t^n \\
&\in L^1(\{t;(0,T)\}),
\end{aligned} \tag{3.172}$$

for any $\boldsymbol{r}$ satisfying $0 < |\boldsymbol{r}-\boldsymbol{r}_0| < x_0$.

For $\boldsymbol{r}$ sufficiently close to $\boldsymbol{r}_0$ such that all δ-related functions do not vanish, one gets

$$\begin{aligned}
\int_0^T \delta^{(k)}[t^2-\mathcal{T}(\boldsymbol{r})]t^n dt &= \int_{-\mathcal{T}(\boldsymbol{r})}^{T^2-\mathcal{T}(\boldsymbol{r})} \delta^{(k)}(\tilde{t})\frac{1}{2}(\tilde{t}+\mathcal{T}(\boldsymbol{r}))^{\frac{n}{2}-\frac{1}{2}}d\tilde{t} \\
&= \frac{(-1)^k}{2}\prod_{j=0}^{k-1}(\frac{n}{2}-\frac{1}{2}-j)[\mathcal{T}(\boldsymbol{r})]^{\frac{n}{2}-\frac{1}{2}-k}.
\end{aligned} \tag{3.173}$$

Since k is at most 2 in our situation, $\frac{n}{2}-\frac{1}{2}-k \geq 0$ for $n \geq 5$ so that we are concerned about the five cases $n = 0, 1, 2, 3, 4$ only. Therefore, we enforce

$$\begin{aligned}
\int_0^T \ddot{\boldsymbol{G}}^0_{\rm diff}dt &= \frac{3}{8}\left[\frac{\boldsymbol{A}^0}{\mathcal{T}(\boldsymbol{r})^{\frac{5}{2}}} - \frac{2\gamma_0^{P5}r^2}{\rho_0\pi(\gamma_0^P r)^5}\boldsymbol{t}\boldsymbol{t}^T\right] \\
&\quad + \frac{1}{4}\left[\frac{\boldsymbol{A}^1}{\mathcal{T}(\boldsymbol{r})^{\frac{3}{2}}} + \frac{\gamma_0^{P3}}{\rho_0\pi(\gamma_0^P r)^3}\boldsymbol{I}\right] + \frac{\boldsymbol{A}^2}{2\mathcal{T}(\boldsymbol{r})^{\frac{1}{2}}} \\
&= \frac{3}{8}\frac{\boldsymbol{A}^0}{\mathcal{T}(\boldsymbol{r})^{\frac{5}{2}}} + \frac{1}{4}\frac{\boldsymbol{A}^1}{\mathcal{T}(\boldsymbol{r})^{\frac{3}{2}}} + \frac{\boldsymbol{A}^2}{2\mathcal{T}(\boldsymbol{r})^{\frac{1}{2}}} + \frac{1}{4\rho_0\pi r^3}(\boldsymbol{I}-3\boldsymbol{t}\boldsymbol{t}^T) = O(1),
\end{aligned} \tag{3.174}$$

$$\int_0^T \ddot{\boldsymbol{G}}^1_{\rm diff} dt = \frac{\boldsymbol{A}^2}{2} = O(1), \tag{3.175}$$

$$\begin{aligned}\int_0^T \ddot{\boldsymbol{G}}^2_{\rm diff} dt &= -\frac{1}{8}\left[\frac{\boldsymbol{A}^0}{\mathcal{T}(\boldsymbol{r})^{\frac{3}{2}}} - \frac{2\gamma_0^{P5} r^2}{\rho_0 \pi (\gamma_0^P r)^3}\boldsymbol{t}\boldsymbol{t}^T\right] \\ &\quad - \frac{1}{4}\left[\frac{\boldsymbol{A}^1}{\mathcal{T}(\boldsymbol{r})^{\frac{1}{2}}} + \frac{\gamma_0^{P3}}{\rho_0 \pi (\gamma_0^P r)}\boldsymbol{I}\right] + \frac{\boldsymbol{A}^2}{2}\mathcal{T}(\boldsymbol{r})^{\frac{1}{2}} \\ &= -\frac{1}{8}\frac{\boldsymbol{A}^0}{\mathcal{T}(\boldsymbol{r})^{\frac{3}{2}}} - \frac{1}{4}\frac{\boldsymbol{A}^1}{\mathcal{T}(\boldsymbol{r})^{\frac{1}{2}}} + \frac{\boldsymbol{A}^2}{2}\mathcal{T}(\boldsymbol{r})^{\frac{1}{2}} - \frac{\gamma_0^{P2}}{4\rho_0 \pi r}(\boldsymbol{I} - \boldsymbol{t}\boldsymbol{t}^T) = O(1),\end{aligned} \tag{3.176}$$

$$\int_0^T \ddot{\boldsymbol{G}}^3_{\rm diff} dt = -\frac{1}{2}\left[\boldsymbol{A}^1 + \frac{\gamma_0^{P3}}{\rho_0 \pi}\right] + \frac{1}{2}\boldsymbol{A}^2 \mathcal{T}(\boldsymbol{r}) = O(1), \tag{3.177}$$

$$\begin{aligned}\int_0^T \ddot{\boldsymbol{G}}^4_{\rm diff} dt &= \frac{3}{8}\left[\frac{\boldsymbol{A}^0}{\mathcal{T}(\boldsymbol{r})^{\frac{1}{2}}} - \frac{2\gamma_0^{P5} r^2}{\rho_0 \pi (\gamma_0^P r)}\boldsymbol{t}\boldsymbol{t}^T\right] \\ &\quad - \frac{3}{4}\left[\boldsymbol{A}^1 \mathcal{T}(\boldsymbol{r})^{\frac{1}{2}} + \frac{\gamma_0^{P3}}{\rho_0 \pi}(\gamma_0^P r)\boldsymbol{I}\right] + \frac{\boldsymbol{A}^2}{2}\mathcal{T}(\boldsymbol{r})^{\frac{3}{2}} \\ &= \frac{3}{8}\frac{\boldsymbol{A}^0}{\mathcal{T}(\boldsymbol{r})^{\frac{1}{2}}} - \frac{3}{4}\boldsymbol{A}^1 \mathcal{T}(\boldsymbol{r})^{\frac{1}{2}} + \frac{\boldsymbol{A}^2}{2}\mathcal{T}(\boldsymbol{r})^{\frac{3}{2}} - \frac{3\gamma_0^{P4} r}{4\rho_0 \pi}(\boldsymbol{I} + \boldsymbol{t}\boldsymbol{t}^T) = O(1),\end{aligned} \tag{3.178}$$

for $0 < |\boldsymbol{r} - \boldsymbol{r}_0| < x_0$.

Hiding $O(1)$ terms above, we get

$$\frac{3}{8}\frac{\boldsymbol{A}^0}{\mathcal{T}(\boldsymbol{r})^{\frac{5}{2}}}+\frac{1}{4}\frac{\boldsymbol{A}^1}{\mathcal{T}(\boldsymbol{r})^{\frac{3}{2}}}+\frac{\boldsymbol{A}^2}{2\mathcal{T}(\boldsymbol{r})^{\frac{1}{2}}}+\frac{1}{4\rho_0\pi r^3}(\boldsymbol{I}-3\boldsymbol{t}\boldsymbol{t}^T)=O(1), \tag{3.179}$$

$$-\frac{1}{8}\frac{\boldsymbol{A}^0}{\mathcal{T}(\boldsymbol{r})^{\frac{3}{2}}}-\frac{1}{4}\frac{\boldsymbol{A}^1}{\mathcal{T}(\boldsymbol{r})^{\frac{1}{2}}}-\frac{\gamma_0^{P^2}}{4\rho_0\pi r}(\boldsymbol{I}-\boldsymbol{t}\boldsymbol{t}^T)=O(1), \tag{3.180}$$

$$\frac{3}{8}\frac{\boldsymbol{A}^0}{\mathcal{T}(\boldsymbol{r})^{\frac{1}{2}}}=O(1). \tag{3.181}$$

Considering (3.179)$\times\mathcal{T}(\boldsymbol{r})$+(3.180), we can obtain the initial condition for $\boldsymbol{A}^0$ as $\boldsymbol{r}\to\boldsymbol{r}_0$,

$$\boldsymbol{A}^0=-\frac{\mathcal{T}^{\frac{5}{2}}}{\rho_0\pi r^3}(\boldsymbol{I}-3\boldsymbol{t}\boldsymbol{t}^T)+\frac{\gamma_0^{P^2}\mathcal{T}^{\frac{3}{2}}}{\rho_0\pi r}(\boldsymbol{I}-\boldsymbol{t}\boldsymbol{t}^T)+O(\mathcal{T}^{\frac{3}{2}}). \tag{3.182}$$

Moreover, since τ is the traveltime from the source $\boldsymbol{r}_0$ to $\boldsymbol{r}$ which is proportional to $r=|\boldsymbol{r}-\boldsymbol{r}_0|$, $\mathcal{T}=\tau^2$ is proportional to r^2 as $\boldsymbol{r}\to\boldsymbol{r}_0$, leading to $\boldsymbol{A}^0=O(1)$ as $\boldsymbol{r}\to\boldsymbol{r}_0$.

Next, (3.179) $\times\, 4\mathcal{T}(\boldsymbol{r})^{\frac{3}{2}}$ gives rise to the initial condition for $\boldsymbol{A}^1$ as $\boldsymbol{r}\to\boldsymbol{r}_0$,

$$\begin{aligned}\boldsymbol{A}^1=&-\frac{3}{2}\frac{\boldsymbol{A}^0}{\mathcal{T}}-\frac{\mathcal{T}^{\frac{3}{2}}}{\rho_0\pi r^3}(\boldsymbol{I}-3\boldsymbol{t}\boldsymbol{t}^T)+2\boldsymbol{A}^2\mathcal{T}+O(\mathcal{T}^{\frac{3}{2}})\\ =&-\frac{3}{2}\frac{\boldsymbol{A}^0}{\mathcal{T}}-\frac{\mathcal{T}^{\frac{3}{2}}}{\rho_0\pi r^3}(\boldsymbol{I}-3\boldsymbol{t}\boldsymbol{t}^T)+O(\mathcal{T}).\end{aligned} \tag{3.183}$$

Substituting (3.182) into (3.183), we will get

$$\boldsymbol{A}^1=\frac{1}{2}\frac{\mathcal{T}^{\frac{3}{2}}}{\rho_0\pi r^3}(\boldsymbol{I}-3\boldsymbol{t}\boldsymbol{t}^T)-\frac{3}{2}\frac{\gamma_0^{P^2}\mathcal{T}^{\frac{1}{2}}}{\rho_0\pi r}(\boldsymbol{I}-\boldsymbol{t}\boldsymbol{t}^T)+O(\mathcal{T}^{\frac{1}{2}}). \tag{3.184}$$

Similar to the case for $\boldsymbol{A}^0$, we have $\boldsymbol{A}^1=O(1)$ as $\boldsymbol{r}\to\boldsymbol{r}_0$.

Finally, (3.179) $\times 2\mathcal{T}(\boldsymbol{r})^{\frac{1}{2}}$ gives rise to the initial condition for $\boldsymbol{A}^2$ as $\boldsymbol{r} \to \boldsymbol{r}_0$,

$$\boldsymbol{A}^2 = -\frac{3}{4}\frac{\boldsymbol{A}^0}{\mathcal{T}^2} - \frac{1}{2}\frac{\boldsymbol{A}^1}{\mathcal{T}} - \frac{\mathcal{T}^{\frac{1}{2}}}{2\rho_0\pi r^3}(\boldsymbol{I} - 3\boldsymbol{t}\boldsymbol{t}^T) + O(\mathcal{T}^{\frac{1}{2}}). \tag{3.185}$$

When substituting (3.183) into (3.185), the first three terms on the right hand side of (3.185) will be canceled. So we have $\boldsymbol{A}^2 = O(1)$ as $\boldsymbol{r} \to \boldsymbol{r}_0$ which is also consistent with (3.175).

Similarly, we can get the following initial condition for $\tilde{\boldsymbol{A}}^l$,

$$\tilde{\boldsymbol{A}}^0 = -\frac{\mathcal{T}^{\frac{5}{2}}}{\rho_0\pi r^3}(\boldsymbol{I} - 3\boldsymbol{t}\boldsymbol{t}^T) + \frac{{\gamma^P}^2\mathcal{T}^{\frac{3}{2}}}{\rho_0\pi r}(\boldsymbol{I} - \boldsymbol{t}\boldsymbol{t}^T) + O(\mathcal{T}^{\frac{3}{2}}), \tag{3.186}$$

$$\tilde{\boldsymbol{A}}^1 = -\frac{3}{2}\tilde{\boldsymbol{A}}^0 - \frac{\mathcal{T}^{\frac{5}{2}}}{\rho_0\pi r^3}(\boldsymbol{I} - 3\boldsymbol{t}\boldsymbol{t}^T) + O(\mathcal{T}^2), \tag{3.187}$$

$$\tilde{\boldsymbol{A}}^2 = -\frac{3}{4}\tilde{\boldsymbol{A}}^0 - \frac{1}{2}\tilde{\boldsymbol{A}}^1 - \frac{\mathcal{T}^{\frac{5}{2}}}{2\rho_0\pi r^3}(\boldsymbol{I} - 3\boldsymbol{t}\boldsymbol{t}^T) + O(\mathcal{T}^{\frac{5}{2}}). \tag{3.188}$$

Assuming that the refractive index ${\gamma^P}^2(\boldsymbol{r})$ is analytic, ${\gamma^P}^2(\boldsymbol{r})$ can be written as the following power series

$${\gamma^P}^2(\boldsymbol{r}) = \sum_{k=0}^{\infty} \Psi_k(\boldsymbol{r}; \boldsymbol{r}_0), \tag{3.189}$$

where Ψ_k are homogeneous polynomials of degree k in the Taylor expansion of ${\gamma^P}^2$ about the source $\boldsymbol{r}_0$ and $\Psi_0 = {\gamma_0^P}^2$ with $\gamma_0^P = \gamma^P(\boldsymbol{r}_0)$.

In an isotropic medium, when γ^P is smooth, the travel time function $\tau(\cdot; \boldsymbol{r}_0)$ solving the eikonal equation $|\nabla\tau(\boldsymbol{r}; \boldsymbol{r}_0)| = \gamma^P(\boldsymbol{r})$ is locally smooth in the source neighborhood except at the source itself [52, 71]. Therefore, we may assume that τ^2 is analytic, so that we have in the source neighborhood [44],

$$\tau^2 - \left(\Psi_0 + \frac{1}{2}\Psi_1 + \frac{1}{3}\Psi_2 - \frac{1}{48\Psi_0}|\nabla\Psi_1|^2 r^2\right) r^2 = O(r^5). \tag{3.190}$$

Similar to the case for the S wave, we can derive the initial conditions for the first three dyadic coefficients.

(a) The sequence $\{\tilde{\boldsymbol{A}}_{0k}\}$ is initialized by

$$\tilde{\boldsymbol{A}}_{00} = 0,\ \tilde{\boldsymbol{A}}_{01} = 0,\ \tilde{\boldsymbol{A}}_{02} = \frac{2\gamma_0^{P^5} r^2}{\rho_0 \pi} \boldsymbol{t}\boldsymbol{t}^T. \tag{3.191}$$

(b) The sequence $\{\tilde{\boldsymbol{A}}_{1k}\}$ is initialized by

$$\begin{aligned} \tilde{\boldsymbol{A}}_{10} &= 0,\ \tilde{\boldsymbol{A}}_{11} = 0,\ \tilde{\boldsymbol{A}}_{12} = -\frac{\gamma_0^{P^5} r^2}{\rho_0 \pi} \boldsymbol{I}, \\ \tilde{\boldsymbol{A}}_{13} &= -\frac{3}{2}\tilde{\boldsymbol{A}}_{03} - \frac{5\gamma_0^{P^3} \Psi_1 r^2}{4\rho_0 \pi}(\boldsymbol{I} - 3\boldsymbol{t}\boldsymbol{t}^T). \end{aligned} \tag{3.192}$$

(c) The sequence $\{\tilde{\boldsymbol{A}}_{2k}\}$ is initialized by

$$\tilde{\boldsymbol{A}}_{20} = 0,\ \tilde{\boldsymbol{A}}_{21} = 0, \tilde{\boldsymbol{A}}_{22} = 0,\ \tilde{\boldsymbol{A}}_{23} = 0, \tag{3.193}$$

$$\tilde{\boldsymbol{A}}_{24} = -\frac{3}{4}\tilde{\boldsymbol{A}}_{04} - \frac{1}{2}\tilde{\boldsymbol{A}}_{14} - \frac{\gamma_0^{P^3}}{2\rho_0 \pi}(\boldsymbol{I} - 3\boldsymbol{t}\boldsymbol{t}^T) \left[\frac{5\Psi_2}{6} r^2 + \frac{15\Psi_1^2}{32\Psi_0} r^2 - \frac{5|\nabla \Psi_1|^2}{96\Psi_0} r^4 \right].$$

If we further assume that $\log \rho(\boldsymbol{r})$, $\tilde{\boldsymbol{\alpha}}^l$, $\tilde{\boldsymbol{C}}^{l-1}$ and $\tilde{\boldsymbol{c}}^{l-1}$ for $l \geq 0$ are all analytic in a

neighborhood of the source $\boldsymbol{r}_0$, we can expand these functions as Taylor series at the source,

$$\log \rho(\boldsymbol{r}) = \sum_{k=0}^{\infty} P_k(\boldsymbol{r}), \tag{3.194}$$

$$\tilde{\boldsymbol{\alpha}}^l(\boldsymbol{r}) = \sum_{k=0}^{\infty} \tilde{\boldsymbol{\alpha}}_{lk}(\boldsymbol{r}), \tag{3.195}$$

$$\tilde{\boldsymbol{C}}^{l-1}(\boldsymbol{r}) = \sum_{k=0}^{\infty} \tilde{\boldsymbol{C}}_{l-1,k}(\boldsymbol{r}), \tag{3.196}$$

$$\tilde{\boldsymbol{c}}^{l-1}(\boldsymbol{r}) = \sum_{k=0}^{\infty} \tilde{\boldsymbol{c}}_{l-1,k}(\boldsymbol{r}), \tag{3.197}$$

where the term with subscript k denotes a homogeneous polynomial of degree k.

As $\mathcal{T} = \tau^2$ is analytic near the source neighborhood, we denote its Taylor series as

$$\mathcal{T}(\boldsymbol{r}) = \tau^2(\boldsymbol{r}) = \sum_{k=0}^{\infty} T_k(\boldsymbol{r}). \tag{3.198}$$

Moreover, from the formula (3.133), $\tilde{\boldsymbol{\alpha}}^l$ can be expanded

$$\sum_{k=0}^{\infty} \tilde{\boldsymbol{A}}_{lk} = \sum_{k=0}^{\infty} \tilde{\boldsymbol{C}}_{l-1,k} + \sum_{k=0}^{\infty} \nabla\mathcal{T}_k \sum_{k=0}^{\infty} \tilde{\boldsymbol{\alpha}}_{lk}. \tag{3.199}$$

Equating the $(q+1)$th degree polynomials of both sides, we can get

$$\nabla\mathcal{T}_2 \tilde{\boldsymbol{\alpha}}_{lq} = \tilde{\boldsymbol{A}}_{l,q+1} - \tilde{\boldsymbol{C}}_{l-1,q+1} - \sum_{k=0}^{q-1} \nabla\mathcal{T}_{q+2-k} \tilde{\boldsymbol{\alpha}}_{lk}, \tag{3.200}$$

and forming the dot product of the above with $\nabla\mathcal{T}_2$ yields

$$\tilde{\boldsymbol{\alpha}}_{lq} = \frac{1}{4\Psi_0^2 r^2} \left(\nabla\mathcal{T}_2 \cdot \tilde{\boldsymbol{A}}_{l,q+1} - \nabla\mathcal{T}_2 \cdot \tilde{\boldsymbol{C}}_{l-1,q+1} - \sum_{k=0}^{q-1} (\nabla\mathcal{T}_2 \cdot \nabla\mathcal{T}_{q+2-k}) \tilde{\boldsymbol{\alpha}}_{lk} \right), \tag{3.201}$$

which is useful for initializing the computation of $\tilde{\boldsymbol{\alpha}}_l$.

On the other hand, the transport equations (3.137) for $\tilde{\boldsymbol{\alpha}}^l$ can be expanded,

$$\begin{aligned}
&\sum_{k=2}^{\infty} \nabla T_k(\boldsymbol{r}) \cdot \sum_{k=0}^{\infty} \nabla \tilde{\boldsymbol{\alpha}}_{lk}(\boldsymbol{r}) \\
&+ \left[\frac{1}{2} \sum_{k=2}^{\infty} \Delta T_k(\boldsymbol{r}) + \frac{1}{2} \sum_{k=2}^{\infty} \nabla T_k(\boldsymbol{r}) \sum_{k=0}^{\infty} \nabla P_k(\boldsymbol{r}) - (2l+5) \sum_{k=0}^{\infty} \Psi_k(\boldsymbol{r}) \right] \sum_{k=0}^{\infty} \tilde{\boldsymbol{\alpha}}_{lk}(\boldsymbol{r}) \\
&= \sum_{k=0}^{\infty} \tilde{\boldsymbol{c}}_{l-1,k}(\boldsymbol{r}).
\end{aligned} \tag{3.202}$$

Equating q-th degree polynomials of both sides, we have

$$\begin{aligned}
(2q-2l-2)\Psi_0 \tilde{\boldsymbol{\alpha}}_{lq} =& \tilde{\boldsymbol{c}}_{l-1,q} - \sum_{k=1}^{q-1} \nabla T_{2+q-k} \cdot \nabla \tilde{\boldsymbol{\alpha}}_{lk} - \frac{1}{2} \sum_{k=0}^{q-1} \Delta T_{2+q-k} \tilde{\boldsymbol{\alpha}}_{lk} \\
&+ (2l+5) \sum_{k=0}^{q-1} \Psi_{q-k} \tilde{\boldsymbol{\alpha}}_{lk} - \frac{1}{2} \sum_{k=0}^{q-1} \tilde{\boldsymbol{\alpha}}_{lk} \left(\sum_{j=1}^{q-k} \nabla T_{2+q-j-k} \cdot \nabla P_j \right).
\end{aligned} \tag{3.203}$$

Hence we obtain a recursive formula to compute the q-th degree polynomial $\tilde{\boldsymbol{\alpha}}_{lq}$. It is clear that (3.203) is not valid for computing $\tilde{\boldsymbol{\alpha}}_{lq^*}$ for $q^* = l+1$ since the coefficient of $\tilde{\boldsymbol{\alpha}}_{lq^*}$ vanishes. Two cases arise here: Case (a) for $l \geq 3$ and Case (b) for $0 \leq l \leq 2$.

Consider Case (a) for $l \geq 3$ first; in this case, $\tilde{\boldsymbol{A}}^l$ have been assumed to be $O(\mathcal{T}^l) = O(r^{2l})$. From the formula (3.133), it implies that $\tilde{\boldsymbol{\alpha}}^l$ behaves at least $O(r^{2l-1}) = o(r^{l+1})$ due to $2l \geq l+2$, and we further have that $\tilde{\boldsymbol{\alpha}}_{lq^*} = 0$ for $q^* = l+1$.

Next, consider Case (b) for $0 \leq l \leq 2$; in this case, $\tilde{\boldsymbol{\alpha}}_{01}$, $\tilde{\boldsymbol{\alpha}}_{12}$ and $\tilde{\boldsymbol{\alpha}}_{23}$ can be directly initialized from initial conditions (3.191)-(3.193) and the recursive formula (3.201), respectively.

In the recursive formula (3.203), $\tilde{\boldsymbol{c}}_{l-1,q}$ depends on $\tilde{\boldsymbol{\alpha}}^{l-1}$ but does not depend on $\tilde{\boldsymbol{\alpha}}^l$;

therefore, the power series of $\tilde{\boldsymbol{\alpha}}^l$ is computable via (3.203) once $\tilde{\boldsymbol{\alpha}}^{l-1}$ is obtained near the source.

3.6 Hadamard-Babich ansatz in the frequency domain

The Fourier transform of (3.30) in time yields the FDPS elastic wave equations (3.1) with

$$\boldsymbol{G}(\boldsymbol{r};\boldsymbol{r}_0)=\int_0^\infty \boldsymbol{G}(\boldsymbol{r},t;\boldsymbol{r}_0)e^{i\omega t}dt, \tag{3.204}$$

so that by (3.30), (3.88), and (3.132), we get the following frequency-domain asymptotic ansatz,

$$\boldsymbol{G}(\boldsymbol{r};\boldsymbol{r}_0)=\sum_{l=0}^{\infty}\frac{\tilde{\boldsymbol{A}}^l(\boldsymbol{r};\boldsymbol{r}_0)}{-\omega^2\mathcal{T}^l}\int_0^\infty e^{i\omega t}f_+^{(-3+l)}(t^2-\tau^2(\boldsymbol{r};\boldsymbol{r}_0))dt. \tag{3.205}$$

The integral in (3.205) has the following closed form [46],

$$\int_\tau^\infty e^{i\omega t}f_+^{(\nu-\frac{1}{2})}(t^2-\tau^2(\boldsymbol{r};\boldsymbol{r}_0))dt=\frac{1}{2}i\sqrt{\pi}\left(\frac{2\tau}{\omega}\right)^\nu e^{i\omega\nu}H_\nu^{(1)}(\omega\tau)\equiv f_\nu(\omega,\tau), \tag{3.206}$$

where $f_\nu(\omega,\tau)$ is exactly the basis function used in Babich's ansatz [3].

By (3.205) and (3.206), we immediately find that the frequency-domain Hadamard's ansatz should be

$$\boldsymbol{G}(\boldsymbol{r};\boldsymbol{r}_0)=\sum_{l=0}^{\infty}\frac{\tilde{\boldsymbol{A}}^l(\boldsymbol{r};\boldsymbol{r}_0)}{-\omega^2\mathcal{T}^l}f_{-3+l+\frac{1}{2}}(\omega,\tau(\boldsymbol{r};\boldsymbol{r}_0)), \tag{3.207}$$

which we refer to as the Hadamard-Babich ansatz.

3.7 Numerical implementation

3.7.1 Numerical computation for S waves

Numerically, it is impossible to construct $\{\tilde{\boldsymbol{A}}^l\}$ for all $l \geq 0$ so that we have to truncate the ansatz in our implementation. To make sure that this truncated ansatz is at least capable of reproducing the homogeneous fundamental solution (3.27), we truncate the formula to obtain the following ansatz,

$$\boldsymbol{G}^S(\boldsymbol{r};\boldsymbol{r}_0) = \frac{\tilde{\boldsymbol{A}}^0(\boldsymbol{r};\boldsymbol{r}_0)}{-\omega^2} f_{-3+\frac{1}{2}}(\omega,\tau(\boldsymbol{r};\boldsymbol{r}_0)) + \frac{\tilde{\boldsymbol{A}}^1(\boldsymbol{r};\boldsymbol{r}_0)}{-\omega^2\mathcal{T}(\boldsymbol{r};\boldsymbol{r}_0)} f_{-2+\frac{1}{2}}(\omega,\tau(\boldsymbol{r};\boldsymbol{r}_0)). \tag{3.208}$$

Therefore, we have to compute τ, $\tilde{\boldsymbol{A}}^0$ and $\tilde{\boldsymbol{A}}^1$ to approximate the Green's function $\boldsymbol{G}^S$.

For the sake of convenience, we restate the governing equations for τ_S, $\tilde{\boldsymbol{A}}^0$ and $\tilde{\boldsymbol{A}}^1$ along with their initial conditions. We have that τ_S satisfies

$$|\nabla\tau_S| = \gamma^S \tag{3.209}$$

with the initial condition $\tau_S(\boldsymbol{r}_0;\boldsymbol{r}_0) = 0$.

We have that $\tilde{\boldsymbol{A}}^0$ satisfies

$$(\nabla\mathcal{T}\cdot\nabla)\tilde{\boldsymbol{A}}^0 + \frac{1}{2\mu}[\nabla\cdot(\mu\nabla\mathcal{T}) - 14\rho]\tilde{\boldsymbol{A}}^0 + \frac{\mu}{2\rho}\nabla\mathcal{T}\left[\nabla\left(\frac{\rho}{\mu}\right)\cdot\tilde{\boldsymbol{A}}^0\right] = 0 \tag{3.210}$$

with the initial condition

$$\tilde{\boldsymbol{A}}^0 = \frac{\mathcal{T}^{\frac{5}{2}}}{\rho_0\pi r^3}(\boldsymbol{I} - 3\boldsymbol{t}\boldsymbol{t}^T) + \frac{\gamma_0^{S^2}\mathcal{T}^{\frac{3}{2}}}{\rho_0\pi r}(\boldsymbol{I} + \boldsymbol{t}\boldsymbol{t}^T) + O(\mathcal{T}^{\frac{3}{2}}), \tag{3.211}$$

where $\boldsymbol{t}$ is the unit tangent vector to the S ray.

We also have that $\tilde{\boldsymbol{A}}^1$ satisfies

$$(\nabla\mathcal{T}\cdot\nabla)\tilde{\boldsymbol{A}}^1+\frac{1}{2\mu}[\nabla\cdot(\mu\nabla\mathcal{T})-18\rho]\tilde{\boldsymbol{A}}^1+\frac{\mu}{2\rho}\nabla\mathcal{T}\left[\nabla\left(\frac{\rho}{\mu}\right)\cdot\tilde{\boldsymbol{A}}^1\right]=\tilde{\boldsymbol{R}}^0, \tag{3.212}$$

with the initial condition

$$\tilde{\boldsymbol{A}}^1=-\frac{3}{2}\tilde{\boldsymbol{A}}^0+\frac{\mathcal{T}^{\frac{5}{2}}}{\rho_0\pi r^3}(\boldsymbol{I}-3\boldsymbol{t}\boldsymbol{t}^T)+O(\mathcal{T}^2), \tag{3.213}$$

where

$$\tilde{\boldsymbol{R}}^0=-\frac{\nabla\mathcal{T}\tilde{\boldsymbol{a}}^0}{2}+\frac{\mu\nabla\mathcal{T}[(\nabla\mathcal{T}\cdot\nabla)\tilde{\boldsymbol{a}}^0]}{4\rho}-\frac{\nabla\mathcal{T}\tilde{\boldsymbol{b}}^0}{8\rho}-\frac{\mathcal{T}\nabla\lambda\tilde{\boldsymbol{a}}^0}{2\mu}-\frac{(\lambda+\mu)\mathcal{T}\nabla\tilde{\boldsymbol{a}}^0}{2\mu}+\frac{\mathcal{T}\tilde{\boldsymbol{B}}^0}{2\mu}. \tag{3.214}$$

Here $\tilde{\boldsymbol{B}}^0$, $\tilde{\boldsymbol{a}}^0$, and $\tilde{\boldsymbol{b}}^0$ are given by

$$\begin{aligned}\tilde{\boldsymbol{B}}^0 &= (\lambda+\mu)\nabla(\nabla\cdot\tilde{\boldsymbol{A}}^0)+\mu\nabla^2\tilde{\boldsymbol{A}}^0+\nabla\lambda(\nabla\cdot\tilde{\boldsymbol{A}}^0)\\ &\quad+\nabla\mu\times(\nabla\times\tilde{\boldsymbol{A}}^0)+2(\nabla\mu\cdot\nabla)\tilde{\boldsymbol{A}}^0, \qquad (3.215)\\ \tilde{\boldsymbol{a}}^0 &= \nabla\cdot\tilde{\boldsymbol{A}}^0+\frac{1}{\lambda+\mu}\nabla\mu\cdot\tilde{\boldsymbol{A}}^0+\frac{2\mu}{(\lambda+\mu)|\nabla\mathcal{T}|^2}\nabla\mathcal{T}[(\nabla\mathcal{T}\cdot\nabla)\tilde{\boldsymbol{A}}^0], \qquad (3.216)\\ \tilde{\boldsymbol{b}}^0 &= 10\rho\tilde{\boldsymbol{a}}^0-(\lambda+\mu)(\nabla\mathcal{T}\cdot\nabla)\tilde{\boldsymbol{a}}^0-\mu\nabla^2\mathcal{T}\tilde{\boldsymbol{a}}^0\\ &\quad-(\nabla\mathcal{T}\cdot\nabla\lambda)\tilde{\boldsymbol{a}}^0-(\nabla\mathcal{T}\cdot\nabla\mu)\tilde{\boldsymbol{a}}^0+\nabla\mathcal{T}\cdot\tilde{\boldsymbol{B}}^0. \qquad (3.217)\end{aligned}$$

To compute (3.208) numerically, we need to solve the eikonal equation to obtain τ_S, and the vectorial transport equations (3.210)-(3.212) to obtain $\tilde{\boldsymbol{A}}^0$ and $\tilde{\boldsymbol{A}}^1$ for S waves. To obtain a first-order accurate approximation of $\tilde{\boldsymbol{A}}^1$, we have to achieve a third-order accurate

approximation of $\tilde{\boldsymbol{A}}^0$ due to the term $\Delta\tilde{\boldsymbol{A}}^0$ appearing in (3.212). However, to obtain a third-order accurate approximation of $\tilde{\boldsymbol{A}}^0$, we need a fifth-order accurate τ as $\Delta\tau^2$ appearing in (3.210) for $\tilde{\boldsymbol{A}}^0$. Therefore, we employ fifth-order weighted essentially non-oscillatory (WENO) [53, 41, 31] Lax-Friedrichs fast sweeping schemes developed in [34, 69, 87, 88, 63, 45] to solve the eikonal equation (3.209), where the upwind source singularity at the source point is treated by the factorization idea [54, 85, 20, 50, 63, 45]. As for $\tilde{\boldsymbol{A}}^0$ and $\tilde{\boldsymbol{A}}^1$, their components are coupled in the transport equations, and we cannot directly employ high-order Lax-Friedrichs schemes developed [63, 45]. However, since the transport equations for $\tilde{\boldsymbol{A}}^l$ are analogous to those of Maxwell's equations in [44], we will directly use the method developed in [44] to transform these strongly coupled systems into decoupled scalar equations and then use high-order Lax-Friedrichs WENO schemes to compute those solutions accordingly.

3.7.2 Numerical computation for P waves

Similarly, to compute the Green's function for P waves, we can also truncate the formula to obtain the following ansatz

$$\boldsymbol{G}^P(\boldsymbol{r};\boldsymbol{r}_0) = \frac{\tilde{\boldsymbol{A}}^0(\boldsymbol{r};\boldsymbol{r}_0)}{-\omega^2} f_{-3+\frac{1}{2}}(\omega,\tau(\boldsymbol{r};\boldsymbol{r}_0)) + \frac{\tilde{\boldsymbol{A}}^1(\boldsymbol{r};\boldsymbol{r}_0)}{-\omega^2\mathcal{T}(\boldsymbol{r};\boldsymbol{r}_0)} f_{-2+\frac{1}{2}}(\omega,\tau(\boldsymbol{r};\boldsymbol{r}_0)). \tag{3.218}$$

Therefore, we also have to compute τ, $\tilde{\boldsymbol{A}}^0$ and $\tilde{\boldsymbol{A}}^1$ to approximate the Green's function $\boldsymbol{G}^P$.

However, in the P-wave case, we can decouple related transport equations easily due to the propagation property of P waves. Here we restate the governing equations in the following,

$$|\nabla\tau_P| = \gamma^P \tag{3.219}$$

with the initial condition $\tau_S(\boldsymbol{r}_0;\boldsymbol{r}_0)=0$;

$$\nabla\mathcal{T}\cdot\nabla\tilde{\boldsymbol{\alpha}}^0+[\frac{1}{2\rho}\nabla\cdot(\rho\nabla\mathcal{T})-\frac{5\rho}{\lambda+2\mu}]\tilde{\boldsymbol{\alpha}}^0=0 \tag{3.220}$$

with the initial condition $\tilde{\boldsymbol{\alpha}}^0=\frac{\gamma_0^P}{\rho\pi}\boldsymbol{r}$ as $\boldsymbol{r}\to\boldsymbol{r}_0$;

$$\nabla\mathcal{T}\cdot\nabla\tilde{\boldsymbol{\alpha}}^1+[\frac{1}{2\rho}\nabla\cdot(\rho\nabla\mathcal{T})-\frac{7\rho}{\lambda+2\mu}]\tilde{\boldsymbol{\alpha}}^1=\tilde{\boldsymbol{c}}^0 \tag{3.221}$$

with the initial condition $\tilde{\boldsymbol{\alpha}}^1=0$ as $\boldsymbol{r}\to\boldsymbol{r}_0$, where $\tilde{\boldsymbol{c}}^0$ is

$$\begin{aligned}\tilde{\boldsymbol{c}}^0=&\frac{1}{8\rho}\{10\rho-\mu\nabla^2\mathcal{T}-\nabla\mathcal{T}\cdot\nabla(\lambda+\mu)](\nabla\mathcal{T}\cdot\tilde{\boldsymbol{C}}^0)-(\lambda+\mu)\nabla\mathcal{T}\cdot\nabla(\nabla\mathcal{T}\cdot\tilde{\boldsymbol{C}}^0)\\&-(\lambda+\mu)|\nabla\mathcal{T}|^2(\nabla\cdot\tilde{\boldsymbol{C}}^0)-2\mu\nabla\mathcal{T}\cdot[(\nabla\mathcal{T}\cdot\nabla)\tilde{\boldsymbol{C}}^0]-(\nabla\mu\cdot\tilde{\boldsymbol{C}}^0)|\nabla\mathcal{T}|^2+\tilde{\boldsymbol{d}}^0\},\end{aligned} \tag{3.222}$$

and $\tilde{\boldsymbol{C}}^0$ is the same as (3.112).

Numerically, we apply similar considerations as those for computing S waves to compute the ingredients of constructing P waves, and we omit details here.

3.8 Numerical examples

In this section, we will study several numerical examples. To obtain a reference solution, if necessary, we apply the finite-difference time-domain (FDTD) method directly to the time-domain elastic wave equations to obtain a numerical solution in time, and then take the Fourier transform in time to obtain a numerical solution in the frequency domain.

In the following, $\boldsymbol{G}_1$ and $\boldsymbol{G}_2$ indicate the one-term and the two-term truncation of the Hadamard-Babich ansatz, respectively.

3.8.1 Example 1: Constant model

We take $\lambda = 1$, $\mu = 1$, and $\rho = 1$. The computational setup for our asymptotic method is the following:

- The computational domain is $[0, 0.5] \times [0, 0.5] \times [0, 0.5]$.
- The mesh size is $51 \times 51 \times 51$ with grid size $h = 0.01$.
- The angular frequency $\omega = 16\pi$ or $\omega = 32\pi$.
- The source point is $(0.25, 0.25, 0.25)^T$.

In this example, since all elastic parameters are constants, we use the exact solution to check the accuracy of our numerical solutions.

We first compare the results at $\omega = 16\pi$. Figure 3.1 shows the contour plots of the yy-component of $\boldsymbol{G}_1$, $\boldsymbol{G}_2$, and $\boldsymbol{G}_{hom}$ at $x = 0.25$. Figure 3.2 shows the detailed comparisons along three different lines. These results clearly show that the two-term ansatz can correctly capture singularities near the source.

Next, we consider frequency $\omega = 32\pi$ so that there are roughly eight waves propagating in the computational domain and about five to six points are used per wavelength. Figure 3.3 shows the zz-component of $\boldsymbol{G}_1$, $\boldsymbol{G}_2$, and $\boldsymbol{G}_{hom}$ at $y = 0.25$. Figure 3.4 shows the detailed comparisons along three different lines. Therefore, in a homogeneous medium, the two-term approximation is able to faithfully reproduce source singularities of the exact solution.

In Table 3.1, we list numerical errors in the L^2-norm between our new ansatz based solutions and exact solutions for the component G_{yy} in the computational domain excluding a neighborhood of the source at which the Green's functions $\boldsymbol{G}$ is singular. In terms of G_{yy}, although the one-term ansatz based solution approximates the exact solution asymptotically

in terms of $O(1/\omega)$, our two-term ansatz based solution approximates the exact solution not only asymptotically in terms of $O(1/\omega)$ but also with very high accuracy.

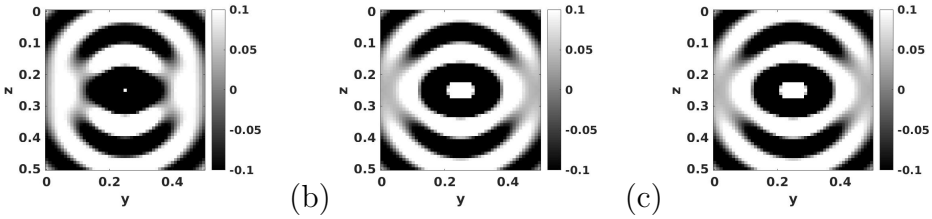

(a) (b) (c)

Figure 3.1: Example 1 with $\boldsymbol{r}_0 = (0.25, 0.25, 0.25)^T$ and $\omega = 16\pi$. The real part of the yy-component of $\boldsymbol{G}(\boldsymbol{r}; \boldsymbol{r}_0)$ at $x = 0.25$ computed via (a) one-term ansatz $\boldsymbol{G}_1$; (b) two-term ansatz $\boldsymbol{G}_2$; (c) exact solution $\boldsymbol{G}_{hom}$.

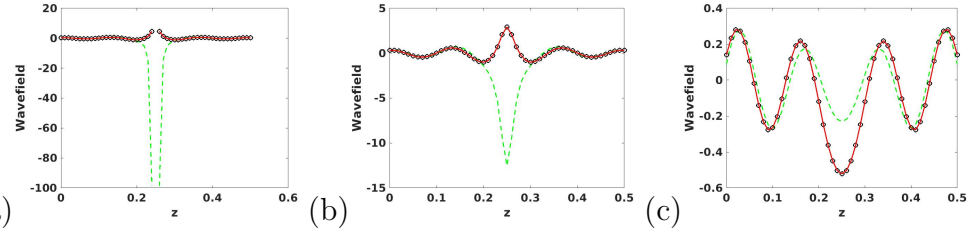

(a) (b) (c)

Figure 3.2: Example 1 with $\boldsymbol{r}_0 = (0.25, 0.25, 0.25)^T$ and $\omega = 16\pi$. The real part of the yy-component of $\boldsymbol{G}(\boldsymbol{r}; \boldsymbol{r}_0)$ at $x = 0.25$ and at (a) $y = 0.25$; (b) $y = 0.23$; (c) $y = 0.15$. Green dash line: $\boldsymbol{G}_1$; black circle line: $\boldsymbol{G}_2$; red solid line: exact solution $\boldsymbol{G}_{hom}$.

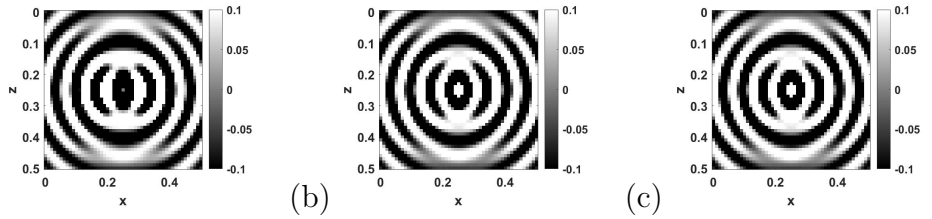

(a) (b) (c)

Figure 3.3: Example 1 with $\boldsymbol{r}_0 = (0.25, 0.25, 0.25)^T$ and $\omega = 32\pi$. The real part of the zz-component of $\boldsymbol{G}(\boldsymbol{r}; \boldsymbol{r}_0)$ at $y = 0.25$ computed via (a) one-term ansatz $\boldsymbol{G}_1$; (b) two-term ansatz $\boldsymbol{G}_2$; (c) exact solution $\boldsymbol{G}_{hom}$.

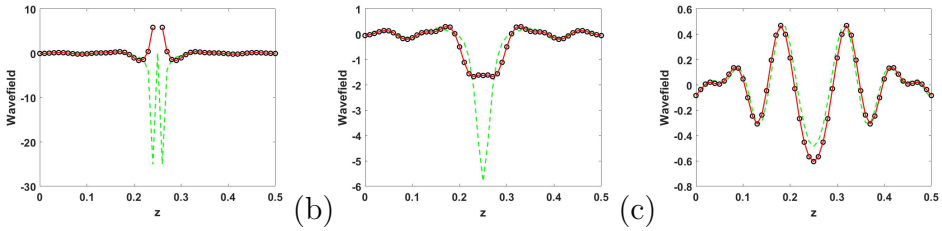

Figure 3.4: Example 1 with $\boldsymbol{r}_0 = (0.25, 0.25, 0.25)^T$ and $\omega = 32\pi$. The real part of the zz-component of $\boldsymbol{G}(\boldsymbol{r}; \boldsymbol{r}_0)$ at $y = 0.25$ and at (a) $x = 0.25$; (b) $x = 0.23$; (c) $x = 0.15$. Green dash line: $\boldsymbol{G}_1$; black circle line: $\boldsymbol{G}_2$; red solid line: exact solution $\boldsymbol{G}_{hom}$.

ω	8π	16π	32π	64π
$1/\omega$	4E-2	2E-2	1E-2	5E-3
one-term $L^2_{G_{yy}}$ error	3.4E-2	1.6E-2	8.9E-3	4.3E-3
two-term $L^2_{G_{yy}}$ error	3.2E-9	1.6E-9	8.3E-10	4.3E-10

Table 3.1: Example 1: L^2-norm errors between the new ansatz based solutions and the FDTD solution in a region excluding a neighborhood of the source.

3.8.2 Example 2: A variable density model

We take $\lambda = 1$ and $\mu = 1$ but variable ρ:

$$\rho = \frac{1}{(0.5 - (y - 0.25))^2}.$$

In this case, the exact solution is not available, so we compute the FDTD-based solution to check the accuracy of our method.

The computational setup for our asymptotic methods is the following:

- The computational domain is $[0, 0.5] \times [0, 0.5] \times [0, 0.5]$.
- The mesh size is $51 \times 51 \times 51$ with grid size $h = 0.01$.
- The angular frequency $\omega = 8\pi$ or $\omega = 16\pi$.
- The source point is $(0.25, 0.25, 0.25)^T$.

We first compare the results at frequency $\omega = 8\pi$. Figure 3.5 shows the contour plots of the yy-component of $\boldsymbol{G}_1$, $\boldsymbol{G}_2$ and $\boldsymbol{G}_{\text{FDTD}}$ at $x = 0.25$. Figure 3.6 shows the detailed comparisons along three different lines. We can see that $\boldsymbol{G}_2$ matches $\boldsymbol{G}_{\text{FDTD}}$ much better than $\boldsymbol{G}_1$.

Next, we compare the results at frequency $\omega = 16\pi$. Figure 3.7 shows the contour plots of the yy-component of $\boldsymbol{G}_1$, $\boldsymbol{G}_2$, and $\boldsymbol{G}_{\text{FDTD}}$ at $x = 0.25$. Figure 3.8 shows the detailed comparisons along three different lines. At high frequencies, the discrepancy between $\boldsymbol{G}_1$ and $\boldsymbol{G}_{\text{FDTD}}$ concentrates near the source, and such discrepancy disappears between two-term solution $\boldsymbol{G}_2$ and $\boldsymbol{G}_{\text{FDTD}}$. Therefore, in an inhomogeneous medium the two-term approximation is able to faithfully reproduce source singularities of the exact solution and yields a uniform asymptotic expansion in the region of space containing the point source but no caustics.

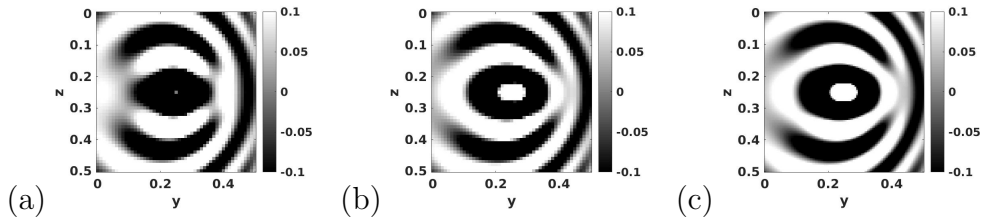

(a) (b) (c)

Figure 3.5: Example 2 with $\boldsymbol{r}_0 = (0.25, 0.25, 0.25)^T$ and $\omega = 8\pi$. The real part of the yy-component of $\boldsymbol{G}(\boldsymbol{r}; \boldsymbol{r}_0)$ at $x = 0.25$ computed via (a) one-term ansatz $\boldsymbol{G}_1$; (b) two-term ansatz $\boldsymbol{G}_2$; (c) FDTD method.

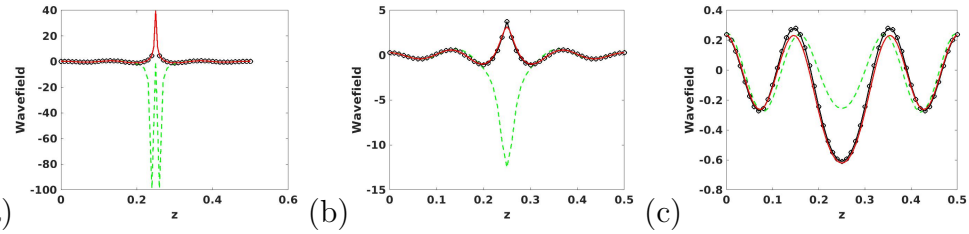

(a) (b) (c)

Figure 3.6: Example 2 with $\boldsymbol{r}_0 = (0.25, 0.25, 0.25)^T$ and $\omega = 8\pi$. The real part of the yy-component of $\boldsymbol{G}(\boldsymbol{r}; \boldsymbol{r}_0)$ at $x = 0.25$ and at (a) $y = 0.25$; (b) $y = 0.23$; (c) $y = 0.15$. Green dash line: $\boldsymbol{G}_1$; black circle line: $\boldsymbol{G}_2$; red solid line: FDTD-based solution.

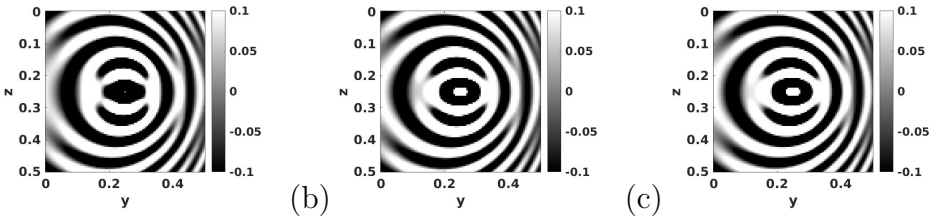

(a) (b) (c)

Figure 3.7: Example 2 with $\boldsymbol{r}_0 = (0.25, 0.25, 0.25)^T$ and $\omega = 16\pi$. The real part of the yy-component of $\boldsymbol{G}(\boldsymbol{r}; \boldsymbol{r}_0)$ at $x = 0.25$ computed via (a) one-term ansatz $\boldsymbol{G}_1$; (b) two-term ansatz $\boldsymbol{G}_2$; (c) FDTD method.

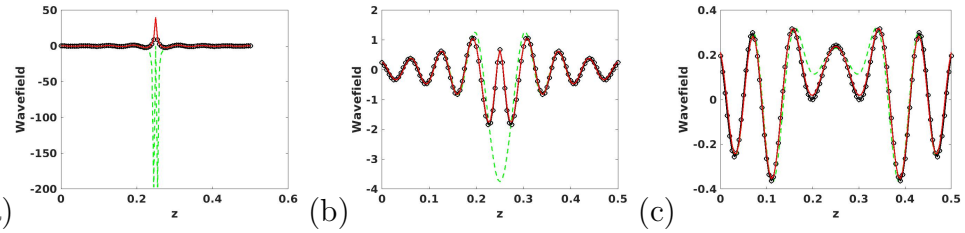

(a) (b) (c)

Figure 3.8: Example 2 with $\boldsymbol{r}_0 = (0.25, 0.25, 0.25)^T$ and $\omega = 16\pi$. The real part of the yy-component of $\boldsymbol{G}(\boldsymbol{r}; \boldsymbol{r}_0)$ at $x = 0.25$ and at (a) $y = 0.25$; (b) $y = 0.23$; (c) $y = 0.15$. Green dash line: $\boldsymbol{G}_1$; black circle line: $\boldsymbol{G}_2$; red solid line: FDTD-based solution.

3.8.3 Example 3: A Gaussian model

We take $\rho = 9$ but variable λ and μ. Here we set $\lambda = \mu$ and

$$\mu = \left(3.0 - 1.75 e^{-\frac{(x-0.25)^2 + (y-0.25)^2 + (z-0.125)^2}{0.125}} \right)^2.$$

In this example, we compute the FDTD-based solution to check the accuracy of our method.

The computational setup for our asymptotic methods is the following:

- The computational domain is $[0, 0.5] \times [0, 0.5] \times [0, 0.5]$.
- The mesh size is $51 \times 51 \times 51$ with grid size $h = 0.01$.
- The angular frequency $\omega = 16\pi$ or $\omega = 32\pi$.
- The source point is $(0.25, 0.25, 0.25)^T$.

We compare the results at frequency $\omega = 16\pi$. Figures 3.9 and 3.10 show the solutions of the zz-component of $\boldsymbol{G}_1$, $\boldsymbol{G}_2$, and $\boldsymbol{G}_{\text{FDTD}}$ at $y = 0.25$. Figures 3.11 and 3.12 show the solutions of the yy-component of $\boldsymbol{G}_1$, $\boldsymbol{G}_2$, and $\boldsymbol{G}_{\text{FDTD}}$ at $x = 0.25$.

Table 3.2 shows numerical differences between our two-term ansatz based solution and the FDTD solution for the two particular components, $\boldsymbol{G}_{xy}$ and $\boldsymbol{G}_{yy}$. Since the computed FDTD solution is a numerical rather than "exact" solution which is not accurate enough, the numerical comparison did not indicate a clear asymptotic convergence pattern in terms of $O(1/\omega)$, but we can still conclude that our numerical solutions agree well with the FDTD solution with accuracy in the order of $O(1/\omega)$.

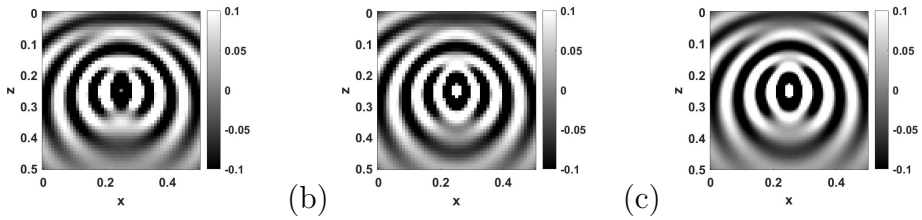

Figure 3.9: Example 3 with $\boldsymbol{r}_0 = (0.25, 0.25, 0.25)^T$ and $\omega = 16\pi$. The real part of the zz-component of $\boldsymbol{G}(\boldsymbol{r}; \boldsymbol{r}_0)$ at $y = 0.25$ computed via (a) one-term ansatz $\boldsymbol{G}_1$; (b) two-term ansatz $\boldsymbol{G}_2$; (c) FDTD method. Mesh in (a) and (b): $51 \times 51 \times 51$; mesh in (c): $101 \times 101 \times 101$.

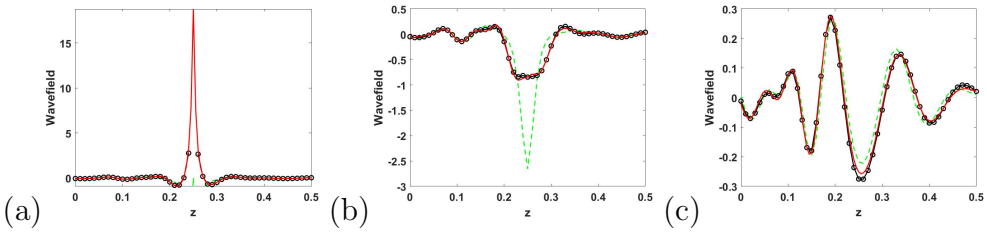

Figure 3.10: Example 3 with $\boldsymbol{r}_0 = (0.25, 0.25, 0.25)^T$ and $\omega = 16\pi$. The real part of the zz-component of $\boldsymbol{G}(\boldsymbol{r}; \boldsymbol{r}_0)$ at $y = 0.25$ and at (a) $x = 0.25$; (b) $x = 0.23$; (c) $x = 0.15$. Green dash line: $\boldsymbol{G}_1$; black circle line: $\boldsymbol{G}_2$; red solid line: FDTD-based solution.

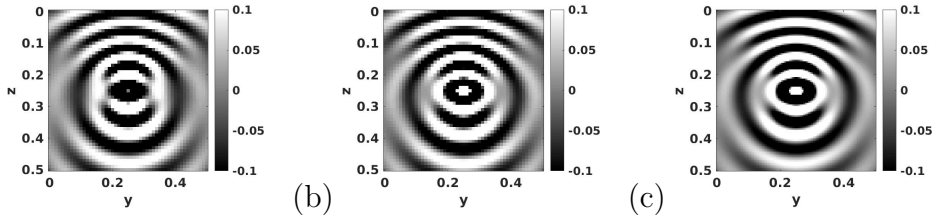

Figure 3.11: Example 3 with $\boldsymbol{r}_0 = (0.25, 0.25, 0.25)^T$ and $\omega = 16\pi$. The real part of the yy-component of $\boldsymbol{G}(\boldsymbol{r}; \boldsymbol{r}_0)$ at $x = 0.25$ computed via (a) one-term ansatz $\boldsymbol{G}_1$; (b) two-term ansatz $\boldsymbol{G}_2$; (c) FDTD method. Mesh in (a) and (b): $51 \times 51 \times 51$; mesh in (c): $101 \times 101 \times 101$.

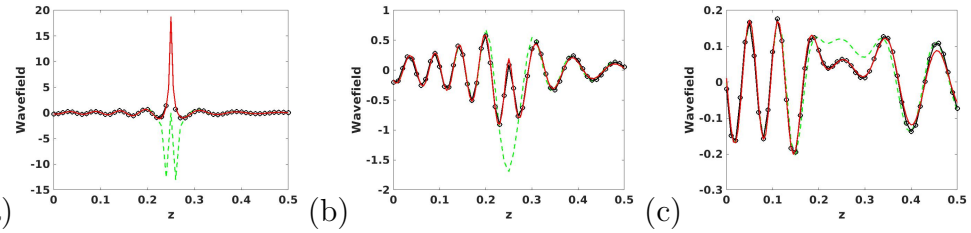

Figure 3.12: Example 3 with $\boldsymbol{r}_0 = (0.25, 0.25, 0.25)^T$ and $\omega = 16\pi$. The real part of the yy-component of $\boldsymbol{G}(\boldsymbol{r}; \boldsymbol{r}_0)$ at $x = 0.25$ and at (a) $y = 0.25$; (b) $y = 0.23$; (c) $y = 0.15$. Green dash line: $\boldsymbol{G}_1$; black circle line: $\boldsymbol{G}_2$; red solid line: FDTD-based solution.

ω	8π	16π	32π
$1/\omega$	4E-2	2E-2	1E-2
$L^2_{G_{xy}}$	2.4E-3	2.4E-3	2.9E-3
$L^2_{G_{yy}}$	6.3E-3	3.6E-3	6.3E-3

Table 3.2: Example 3: L^2-norm errors between the two-term ansatz solution and the FDTD solution in a region excluding a neighborhood of the source.

Chapter 4

Fast Huygens' sweeping method for time-harmonic high-frequecy elastic wave equations in inhomogeneous media

This chapter is based on a modified version of the published work in [59]. We have developed Hadamard-Babich ansatz for point-source elastic wave equations. The new ansatz is capable of producing accurate asymptotic solutions in the region of space containing the point source but no other caustics. However, like the classical geometrica-optics ansatz, this new ansatz could not resolve the issue with caustics which occur with high possibility for wave propagation in an inhomogeneous medium. Because the eikonal equation is a first-order nonlinear partial differential equation, and in general it does not have a globally defined solution. The concept of viscosity solution was invented to single out the unique weak solution among the possible generalized solutions for a first-order nonlinear partial differential equations and in general the viscosity solution is continuous everywhere but not differentiable everywhere. Computationally, nevertheless, high order schemes may be applied to compute the traveltime and amplitudes. But when we compare the resulting asymptotic solution with the direct so-

lution from the Helmholtz equation, we find that the two solutions are different globally. This difference may be traced back to the multivaluedness of traveltime and related caustics [6], which can be detected by applying the method of characteristics to the eikonal equation with appropriate initial condition.

However, it has been showed in [50, 45, 44, 58], the squared eikonal solution is smooth in the neighborhood of point source in isotropic media. This implies that there is a neighborhood of point source which is free of caustics so that the Hadamard-Babich ansatz could generate locally valid asymptotic solutions. To treat caustics away from this neighborhood, we will use the Huygens secondary source principle. By constructing locally valid asymptotic Green's functions in small neighborhood of secondary sources layer by layer, we can construct the globally valid Green's functions in the whole computational domain, so that the caustics can be treated automatically. The key idea is to use the Huygens-Kirchhoff integral to integrate many locally valid asymptotic Green's functions which build the relation between secondary sources and corresponding layers.

To motivate our method, we first introduce the H-B ansatz [58] of the Green's function $\boldsymbol{G}$ for the frequency-domain point-source elastic wave equation:

$$\boldsymbol{G}(\boldsymbol{r};\boldsymbol{r}_0) = \sum_{l=0}^{\infty} \frac{\tilde{\boldsymbol{A}}^l(\boldsymbol{r};\boldsymbol{r}_0)}{-\omega^2 \mathcal{T}^l(\boldsymbol{r};\boldsymbol{r}_0)} f_{-3+l+\frac{1}{2}}(\omega, \tau(\boldsymbol{r};\boldsymbol{r}_0)). \tag{4.1}$$

where $\mathcal{T}(\boldsymbol{r};\boldsymbol{r}_0) = \tau^2(\boldsymbol{r};\boldsymbol{r}_0)$, and $\tau(\boldsymbol{r};\boldsymbol{r}_0)$ is the traveltime from the source $\boldsymbol{r}_0$ to $\boldsymbol{r}$. We shall define $\boldsymbol{A}^l(\boldsymbol{r};\boldsymbol{r}_0) \equiv 0$ for $l < 0$. Here we have from [46]

$$f_\nu(\omega,\tau) := \int_\tau^\infty e^{i\omega t} f_+^{(\nu-\frac{1}{2})}(t^2 - \tau^2(\boldsymbol{r};\boldsymbol{r}_0))dt = \frac{1}{2} i\sqrt{\pi} \left(\frac{2\tau}{\omega}\right)^\nu e^{i\omega\nu} H_\nu^{(1)}(\omega\tau), \tag{4.2}$$

where $H_\nu^{(1)}$ denotes the Hankel function of the first kind of order ν.

The governing equations and initial conditions for amplitudes $\tilde{\boldsymbol{A}}^l$ for both S- and P-waves are also derived in [58], and we will show these equations for the truncated H-B ansatz later on.

In order to distinguish the two wave modes, S-wave and P-wave, we introduce the following wave-mode specific Green's tensors for the two modes,

$$\boldsymbol{G}^S(\boldsymbol{r};\boldsymbol{r}_0) = \sum_{l=0}^{\infty} \frac{\tilde{\boldsymbol{A}}^{Sl}(\boldsymbol{r};\boldsymbol{r}_0)}{-\omega^2 {\tau^S}^{2l}(\boldsymbol{r};\boldsymbol{r}_0)} f_{-3+l+\frac{1}{2}}(\omega, \tau^S(\boldsymbol{r};\boldsymbol{r}_0)), \tag{4.3}$$

$$\boldsymbol{G}^P(\boldsymbol{r};\boldsymbol{r}_0) = \sum_{l=0}^{\infty} \frac{\tilde{\boldsymbol{A}}^{Pl}(\boldsymbol{r};\boldsymbol{r}_0)}{-\omega^2 {\tau^P}^{2l}(\boldsymbol{r};\boldsymbol{r}_0)} f_{-3+l+\frac{1}{2}}(\omega, \tau^P(\boldsymbol{r};\boldsymbol{r}_0)). \tag{4.4}$$

Since we are in the high-frequency regime and are dealing with a smooth elastic medium, we have

$$\boldsymbol{G}(\boldsymbol{r};\boldsymbol{r}_0) = \boldsymbol{G}^S(\boldsymbol{r};\boldsymbol{r}_0) + \boldsymbol{G}^P(\boldsymbol{r};\boldsymbol{r}_0). \tag{4.5}$$

4.1 Numerics for the truncated H-B ansatz

4.1.1 Truncating the ansatz for the S-wave

Since, numerically, it is impossible to construct $\tilde{\boldsymbol{A}}^{Sl}$ for all $l \geq 0$, we need to truncate the ansatz in implementation. In order to at least reproduce the fundamental solution in a homogeneous medium, we truncate the formula (4.3) to keep only two terms,

$$\boldsymbol{G}^S(\boldsymbol{r};\boldsymbol{r}_0) = \frac{\tilde{\boldsymbol{A}}^{S0}(\boldsymbol{r};\boldsymbol{r}_0)}{-\omega^2} f_{-3+\frac{1}{2}}(\omega, \tau^S(\boldsymbol{r};\boldsymbol{r}_0)) + \frac{\tilde{\boldsymbol{A}}^{S1}(\boldsymbol{r};\boldsymbol{r}_0)}{-\omega^2 \mathcal{T}(\boldsymbol{r};\boldsymbol{r}_0)} f_{-2+\frac{1}{2}}(\omega, \tau^S(\boldsymbol{r};\boldsymbol{r}_0)), \tag{4.6}$$

where the superscript S refers to the S-wave and $\mathcal{T} = \tau^{S^2}$.

In [58] we have verified that keeping the first two terms is sufficient to capture the S-wave source singularity. Here we summarize the governing equations from [58] for τ^S, $\tilde{\boldsymbol{A}}^{S0}$, and $\tilde{\boldsymbol{A}}^{S1}$ for the S-wave.

We have the eikonal equation for τ^S,

$$|\nabla \tau^S| = \gamma^S \tag{4.7}$$

with the initial condition $\tau^S(\boldsymbol{r}_0; \boldsymbol{r}_0) = 0$, where γ^S is the S-wave slowness function, $\gamma^S = \sqrt{\frac{\rho}{\mu}}$.

We have the transport equation for the leading H-B coefficient $\tilde{\boldsymbol{A}}^{S0}$,

$$(\nabla \mathcal{T} \cdot \nabla)\tilde{\boldsymbol{A}}^{S0} + \frac{1}{2\mu}[\nabla \cdot (\mu \nabla \mathcal{T}) - 14\rho]\tilde{\boldsymbol{A}}^{S0} + \frac{\mu}{2\rho}\nabla \mathcal{T}\left[\nabla\left(\frac{\rho}{\mu}\right) \cdot \tilde{\boldsymbol{A}}^{S0}\right] = 0, \tag{4.8}$$

with the initial condition

$$\tilde{\boldsymbol{A}}^{S0} = \frac{\mathcal{T}^{\frac{5}{2}}}{\rho_0 \pi r^3}(\boldsymbol{I} - 3\tilde{\boldsymbol{r}}\tilde{\boldsymbol{r}}^T) + \frac{\gamma_0^{S^2}\mathcal{T}^{\frac{3}{2}}}{\rho_0 \pi r}(\boldsymbol{I} + \tilde{\boldsymbol{r}}\tilde{\boldsymbol{r}}^T) + O(\mathcal{T}^{\frac{3}{2}}), \tag{4.9}$$

where $\gamma_0^S = \gamma^S(\boldsymbol{r}_0)$ and $\rho_0 = \rho(\boldsymbol{r}_0)$.

We have the transport equation for the second H-B coefficient $\tilde{\boldsymbol{A}}^{S1}$,

$$(\nabla \mathcal{T} \cdot \nabla)\tilde{\boldsymbol{A}}^{S1} + \frac{1}{2\mu}[\nabla \cdot (\mu \nabla \mathcal{T}) - 18\rho]\tilde{\boldsymbol{A}}^{S1} + \frac{\mu}{2\rho}\nabla \mathcal{T}\left[\nabla\left(\frac{\rho}{\mu}\right) \cdot \tilde{\boldsymbol{A}}^{S1}\right] = \tilde{\boldsymbol{R}}^0, \tag{4.10}$$

where

$$\tilde{\boldsymbol{R}}^0 = -\frac{\nabla \mathcal{T}\tilde{\boldsymbol{a}}^0}{2} + \frac{\mu \nabla \mathcal{T}[(\nabla \mathcal{T} \cdot \nabla)\tilde{\boldsymbol{a}}^0]}{4\rho} - \frac{\nabla \mathcal{T}\tilde{\boldsymbol{b}}^0}{8\rho} - \frac{\mathcal{T}\nabla\lambda\tilde{\boldsymbol{a}}^0}{2\mu} - \frac{(\lambda+\mu)\mathcal{T}\nabla\tilde{\boldsymbol{a}}^0}{2\mu} + \frac{\mathcal{T}\tilde{\boldsymbol{B}}^0}{2\mu}. \tag{4.11}$$

Here $\tilde{\boldsymbol{B}}^0$, the row vector $\tilde{\boldsymbol{a}}^0$, and the row vector $\tilde{\boldsymbol{b}}^0$ are given by

$$\begin{aligned}
\tilde{\boldsymbol{B}}^0 &= (\lambda+\mu)\nabla(\nabla\cdot\tilde{\boldsymbol{A}}^{S0}) + \mu\nabla^2\tilde{\boldsymbol{A}}^{S0} + \nabla\lambda(\nabla\cdot\tilde{\boldsymbol{A}}^{S0}) \\
&\quad +\nabla\mu\times(\nabla\times\tilde{\boldsymbol{A}}^{S0}) + 2(\nabla\mu\cdot\nabla)\tilde{\boldsymbol{A}}^{S0}, \qquad (4.12)\\
\tilde{\boldsymbol{a}}^0 &= \nabla\cdot\tilde{\boldsymbol{A}}^{S0} + \frac{1}{\lambda+\mu}\nabla\mu\cdot\tilde{\boldsymbol{A}}^{S0} + \frac{2\mu}{(\lambda+\mu)|\nabla\mathcal{T}|^2}\nabla\mathcal{T}[(\nabla\mathcal{T}\cdot\nabla)\tilde{\boldsymbol{A}}^{S0}], \qquad (4.13)\\
\tilde{\boldsymbol{b}}^0 &= 10\rho\tilde{\boldsymbol{a}}^0 - (\lambda+\mu)(\nabla\mathcal{T}\cdot\nabla)\tilde{\boldsymbol{a}}^0 - \mu\nabla^2\mathcal{T}\tilde{\boldsymbol{a}}^0 \\
&\quad -(\nabla\mathcal{T}\cdot\nabla\lambda)\tilde{\boldsymbol{a}}^0 - (\nabla\mathcal{T}\cdot\nabla\mu)\tilde{\boldsymbol{a}}^0 + \nabla\mathcal{T}\cdot\tilde{\boldsymbol{B}}^0. \qquad (4.14)
\end{aligned}$$

And the initial condition for $\tilde{\boldsymbol{A}}^{S1}$ is

$$\tilde{\boldsymbol{A}}^{S1} = -\frac{3}{2}\tilde{\boldsymbol{A}}^{S0} + \frac{\mathcal{T}^{\frac{5}{2}}}{\rho_0\pi r^3}(\boldsymbol{I} - 3\tilde{\boldsymbol{r}}\tilde{\boldsymbol{r}}^T) + O(\mathcal{T}^2). \qquad (4.15)$$

Because these governing equations are weakly coupled to each other, we need to design appropriate schemes to solve these equations up to suitable orders of accuracy. To obtain a first-order accurate approximation of $\tilde{\boldsymbol{A}}^{S1}$ by solving the corresponding transport equation, we need a third-order accurate approximation of $\tilde{\boldsymbol{A}}^{S0}$, since equation (4.10) involves the second-order derivative of $\tilde{\boldsymbol{A}}^{S0}$ in its right-hand side. Moreover, a third-order accurate $\tilde{\boldsymbol{A}}^{S0}$ requires a fifth-order accurate τ^S due to the appearance of $\Delta\mathcal{T}$ in (4.8). For the eikonal equation (4.7), we can employ Lax-Friedrichs (LxF) high-order weighted essentially non-oscillatory (WENO) based sweeping schemes developed in [53, 41, 32, 31, 61, 34, 88, 87, 69, 64]. Since the governing equations for $\tilde{\boldsymbol{A}}^{S0}$ and $\tilde{\boldsymbol{A}}^{S1}$ are linear, we can also apply LxF-WENO based schemes directly to the linear system. But since the S-wave is analogous to the electromagnetic wave satisfying the Maxwell's equations, we employ the schemes developed in [44] to decouple the components of $\tilde{\boldsymbol{A}}^{S0}$. Namely, instead of computing the

nine components of $\tilde{\boldsymbol{A}}^{S0}$ directly, we decouple the governing transport equation so that we are able to compute $\tilde{\boldsymbol{A}}^{S0}$ more efficiently.

4.1.1.1 Computing take-off directions

In our computational algorithm, we frequently need to use the so-called take-off direction, and we derive the related transport equation for computing this quantity.

Suppose that $\mathcal{T} = \tau^{S2}$ is available. According to the method of characteristics, a geodesic ray tracing out from $\boldsymbol{r}_0$ to $\boldsymbol{r}$ is governed by

$$\boldsymbol{t}^{(1)}(\boldsymbol{r};\boldsymbol{r}_0) := \dot{\boldsymbol{r}} = \frac{d\boldsymbol{r}}{ds} = \frac{\nabla\tau^S(\boldsymbol{r}(s))}{\gamma^S}, \tag{4.16}$$

where the s parameter is the arc length parameter and the $\dot{}$ indicates the derivative in s.

The unit take-off vector at a given spatial position $\boldsymbol{r}$ is defined as

$$\boldsymbol{t}^{(0)}(\boldsymbol{r};\boldsymbol{r}_0) := \lim_{\boldsymbol{r}'\to\boldsymbol{r}_0} \boldsymbol{t}^{(1)}(\boldsymbol{r}';\boldsymbol{r}_0), \tag{4.17}$$

where $\boldsymbol{r}'$ approaches $\boldsymbol{r}_0$ along the geodesic ray from $\boldsymbol{r}_0$ to $\boldsymbol{r}$. It is clear that $\boldsymbol{t}^{(0)}$ is invariant along each geodesic ray so that it is governed by the following advection equation,

$$\dot{\boldsymbol{t}}^{(0)}(\boldsymbol{r};\boldsymbol{r}_0) = \frac{\nabla\tau^S\cdot\nabla}{\gamma^S}\boldsymbol{t}^{(0)} = \boldsymbol{0}, \tag{4.18}$$

with the initial condition

$$\lim_{\boldsymbol{r}\to\boldsymbol{r}_0}(\boldsymbol{t}^{(0)}(\boldsymbol{r};\boldsymbol{r}_0) - \tilde{\boldsymbol{r}}) = 0, \tag{4.19}$$

where $\tilde{\boldsymbol{r}} = \frac{\boldsymbol{r}-\boldsymbol{r}_0}{|\boldsymbol{r}-\boldsymbol{r}_0|}$.

4.1.1.2 Computing $\tilde{\boldsymbol{A}}^{S0}$

Following [44], we first write $\tilde{\boldsymbol{A}}^{S0} = A\boldsymbol{P}^{(1)}$, where A is a scalar amplitude function and $\boldsymbol{P}^{(1)} = (\boldsymbol{P}_1^{(1)}, \boldsymbol{P}_2^{(1)}, \boldsymbol{P}_3^{(1)})$ is the 3 by 3 polarization dyad, and we then insert this into equation (4.8) to obtain

$$(\nabla\mathcal{T}\cdot\nabla A)\boldsymbol{P}^{(1)} + A(\nabla\mathcal{T}\cdot\nabla)\boldsymbol{P}^{(1)} + A\frac{1}{2\mu}[\nabla\cdot(\mu\nabla\mathcal{T}) - 14\rho]\boldsymbol{P}^{(1)} + \frac{\mu}{2\rho}A\nabla\mathcal{T}\left[\nabla\left(\frac{\rho}{\mu}\right)\cdot\boldsymbol{P}^{(1)}\right] = 0. \tag{4.20}$$

By property of the S-wave, we know that $\nabla\mathcal{T}$ is orthogonal to the two-dimensional subspace spanned by the columns of $\boldsymbol{P}^{(1)}$, and we further assume that the norm of the polarization vector $\boldsymbol{P}_j^{(1)}$, $1 \le j \le 3$, is invariant along a ray $\boldsymbol{r}(s)$; consequently, $\frac{d}{ds}\boldsymbol{P}_j^{(1)} \cdot \boldsymbol{P}_j^{(1)} = 0$ so that we have

$$\boldsymbol{P}_j^{(1)}\cdot(\nabla\mathcal{T}\cdot\nabla)\boldsymbol{P}_j^{(1)} = 0, \tag{4.21}$$

where we have used the property that $\frac{d}{ds} = \frac{\nabla\tau S\cdot\nabla}{\gamma S}$ along a ray with s the arc length parameter.

Taking the dot product of equation (4.20) with $\boldsymbol{P}_j^{(1)}$ in terms of individual columns, we can obtain

$$\nabla\mathcal{T}\cdot\nabla A + \frac{1}{2\mu}[\nabla\cdot(\mu\nabla\mathcal{T}) - 14\rho]A = 0. \tag{4.22}$$

Inserting equation (4.22) into equation (4.20), we get the following equation for $\boldsymbol{P}_j^{(1)}$:

$$(\nabla\mathcal{T}\cdot\nabla)\boldsymbol{P}_j^{(1)}+\frac{\mu}{2\rho}\nabla\mathcal{T}\left[\nabla\left(\frac{\rho}{\mu}\right)\cdot\boldsymbol{P}_j^{(1)}\right]=0, \tag{4.23}$$

so that $\frac{d}{ds}\boldsymbol{P}_j^{(1)}$ is parallel to $\nabla\mathcal{T}$. The above decomposition is analogous to that in [44] which introduces a variable v_0 satisfying that $\tilde{\boldsymbol{A}}^{S0}=v_0\mathcal{T}\boldsymbol{P}^{(1)}$.

Since, in a small neighborhood of the primary source $\boldsymbol{r}_0$, $\gamma^S(\boldsymbol{r})$ and $\rho(\boldsymbol{r})$ approximately equal γ_0^S and ρ_0, respectively, we expect that $\tilde{\boldsymbol{A}}^{S0}$ is consistent with $\frac{2\gamma_0^{S^5}|\boldsymbol{r}-\boldsymbol{r}_0|^2}{\rho_0\pi}(\boldsymbol{I}-\tilde{\boldsymbol{r}}\tilde{\boldsymbol{r}}^T)$ in this neighborhood according to the S-wave Green's tensor. Therefore, we enforce the following initial conditions

$$\lim_{\boldsymbol{r}\to\boldsymbol{r}_0}\left(A(\boldsymbol{r};\boldsymbol{r}_0)-\frac{2\gamma_0^{S^5}|\boldsymbol{r}-\boldsymbol{r}_0|^2}{\rho_0\pi}\right)=0, \tag{4.24}$$

$$\lim_{\boldsymbol{r}\to\boldsymbol{r}_0}\left(\boldsymbol{P}^{(1)}(\boldsymbol{r};\boldsymbol{r}_0)-(\boldsymbol{I}-\tilde{\boldsymbol{r}}\tilde{\boldsymbol{r}}^T)\right)=0, \tag{4.25}$$

where the limit $\boldsymbol{r}\to\boldsymbol{r}_0$ should be understood in the sense that $\boldsymbol{r}$ approaches $\boldsymbol{r}_0$ along its ray $\boldsymbol{r}(s)$ as $s\to 0^+$.

Now by writing $A=v_0\mathcal{T}$, we can derive the governing equation for v_0,

$$\nabla\mathcal{T}\cdot\nabla v_0+\frac{1}{2\mu}[\nabla\cdot(\mu\nabla\mathcal{T})-6\rho]v_0=0, \tag{4.26}$$

with the initial condition $v_0(\boldsymbol{r};\boldsymbol{r}_0)=\frac{2\gamma_0^{S^3}}{\rho_0\pi}$. Following [44], the above transport equation has the following solution along the unique ray connecting $\boldsymbol{r}$ and $\boldsymbol{r}_0$,

$$v_0(\tau^S)=\frac{2\gamma_0^{S^3}}{\rho_0\pi}\exp\left(-\int_0^{\tau^S}\frac{\nabla\cdot(\mu\nabla\tau'^2)-6\rho}{4\tau'\mu\gamma^{S^2}}d\tau'\right). \tag{4.27}$$

If we define $\boldsymbol{P}^{(0)} = \left(\boldsymbol{I} - \boldsymbol{t}^{(0)}\boldsymbol{t}^{(0)^T}\right)$, then we can derive the following relations by using equation (4.18),

$$\dot{\boldsymbol{P}}^{(0)} = 0, \tag{4.28}$$

$$\boldsymbol{t}^{(0)} \cdot \boldsymbol{P}^{(0)} = 0, \tag{4.29}$$

with the initial condition

$$\boldsymbol{P}^{(0)}(\boldsymbol{r}; \boldsymbol{r}_0) - (\boldsymbol{I} - \tilde{\boldsymbol{r}}\tilde{\boldsymbol{r}}^T) = O(r) \quad \text{as} \quad \boldsymbol{r} \to \boldsymbol{r}_0 \tag{4.30}$$

due to equation (4.19).

We use the method proposed in [44] to compute A and $\boldsymbol{P}^{(1)}$ with desired order of accuracy, since this method is very efficient in computing the nine components of $\tilde{\boldsymbol{A}}^{S0}$; we omit the details here.

4.1.1.3 Computing $\tilde{\boldsymbol{A}}^{S1}$

We first notice that, in equation (4.10), the term $\nabla\mathcal{T}(\nabla(\frac{\rho}{\mu})\cdot\tilde{\boldsymbol{A}}^{S1})$ entangles with $\tilde{\boldsymbol{A}}^{S1}$. Since we know that $\tilde{\boldsymbol{A}}_j^{S0}$, $1 \le j \le 3$, are orthogonal to $\nabla\mathcal{T}$, we take the scalar product of equation (4.10) columnwise with $\tilde{\boldsymbol{A}}_j^{S0}$ so that we can obtain a decoupled governing equation.

Thus, we have

$$\begin{aligned}(\nabla\mathcal{T}\cdot\nabla)g_{kj} &+ \frac{1}{\mu}[\nabla\cdot(\mu\nabla\mathcal{T}) - 16\rho]g_{kj} \\ &= \tilde{\boldsymbol{R}}_k^0 \cdot \tilde{\boldsymbol{A}}_j^{S0} - \frac{\mu}{2\rho}\mathcal{T}\left(\nabla\left(\frac{\rho}{\mu}\right)\cdot\tilde{\boldsymbol{A}}_j^{S0}\right)\left(\nabla\cdot\tilde{\boldsymbol{A}}_k^{S0} - \frac{\mu^3}{\rho(\lambda+\mu)}\nabla\left(\frac{\rho}{\mu^2}\right)\cdot\tilde{\boldsymbol{A}}_k^{S0}\right),\end{aligned} \tag{4.31}$$

where $g_{kj} = \tilde{\boldsymbol{A}}_k^{S1} \cdot \tilde{\boldsymbol{A}}_j^{S0}$, and we have used the relation [58]

$$\nabla \mathcal{T} \cdot \tilde{\boldsymbol{A}}_k^{S1} = \mathcal{T} \nabla \cdot \tilde{\boldsymbol{A}}_k^{S0} - \frac{\mu^3 \mathcal{T}}{\rho(\lambda+\mu)} \nabla \left(\frac{\rho}{\mu^2} \right) \cdot \tilde{\boldsymbol{A}}_k^{S0}. \tag{4.32}$$

Since $\tilde{\boldsymbol{A}}^{S0} = O(r^2)$ and $\tilde{\boldsymbol{A}}^{S1} = O(r^2)$, $g_{kj} = O(r^4)$ are very close to 0 near $\boldsymbol{r}_0$, making numerical errors quite sensitive to the initialization and inducing numerical instabilities. To remedy the situation, we define new variables

$$\tilde{g}_{kj} := g_{kl}/\mathcal{T}. \tag{4.33}$$

Hence we get the following governing equations

$$\begin{aligned} (\nabla \mathcal{T} \cdot \nabla) \tilde{g}_{kj} \quad &+ \quad \frac{1}{\mu} [\nabla \cdot (\mu \nabla \mathcal{T}) - 12\rho] \tilde{g}_{kj} \qquad (4.34) \\ &= \quad \frac{\tilde{\boldsymbol{R}}_k^0 \cdot \tilde{\boldsymbol{A}}_j^{S0}}{\mathcal{T}} - \frac{\mu}{2\rho} \left(\nabla \left(\frac{\rho}{\mu} \right) \cdot \tilde{\boldsymbol{A}}_j^{S0} \right) \left(\nabla \cdot \tilde{\boldsymbol{A}}_k^{S0} - \frac{\mu^3}{\rho(\lambda+\mu)} \nabla \left(\frac{\rho}{\mu^2} \right) \cdot \tilde{\boldsymbol{A}}_k^{S0} \right), \end{aligned}$$

with the initial condition

$$\tilde{g}_{kj} = -\frac{4\gamma_0^{S^8} r^2}{\rho_0^2 \pi^2} (\boldsymbol{I} - \tilde{\boldsymbol{r}} \tilde{\boldsymbol{r}}^T)_{kj}. \tag{4.35}$$

Then the LxF WENO-based schemes can be used to compute $\tilde{g}_{kj}$. Once all $\tilde{g}_{kj}$ are available, we can obtain the dyadic coefficients $\tilde{\boldsymbol{A}}^{S1}$ by using the method proposed in [44] and we omit details here.

4.1.2 Truncating the ansatz for the P-wave

We truncate formula (4.4) to keep only two terms,

$$\boldsymbol{G}^P(\boldsymbol{r};\boldsymbol{r}_0) = \frac{\tilde{\boldsymbol{A}}^{P0}(\boldsymbol{r};\boldsymbol{r}_0)}{-\omega^2} f_{-3+\frac{1}{2}}(\omega,\tau^P(\boldsymbol{r};\boldsymbol{r}_0)) + \frac{\tilde{\boldsymbol{A}}^{P1}(\boldsymbol{r};\boldsymbol{r}_0)}{-\omega^2\mathcal{T}(\boldsymbol{r};\boldsymbol{r}_0)} f_{-2+\frac{1}{2}}(\omega,\tau^P(\boldsymbol{r};\boldsymbol{r}_0)), \quad (4.36)$$

where the superscript P refers to the P-wave and $\mathcal{T} = {\tau^P}^2$.

We have the following eikonal equation for the P-wave,

$$|\nabla\tau^P| = \gamma^P, \quad (4.37)$$

with the initial condition $\tau^P(\boldsymbol{r}_0;\boldsymbol{r}_0) = 0$, where $\gamma^P = \sqrt{\frac{\rho}{\lambda+2\mu}}$.

For the P-wave we have the following relation for $\tilde{\boldsymbol{A}}^{P0}$ and $\tilde{\boldsymbol{A}}^{P1}$ [58],

$$\tilde{\boldsymbol{A}}^{P0} = \nabla\mathcal{T}\tilde{\boldsymbol{\alpha}}^0, \quad (4.38)$$

$$\tilde{\boldsymbol{A}}^{P1} = \tilde{\boldsymbol{C}}^0 + \nabla\mathcal{T}\tilde{\boldsymbol{\alpha}}^1, \quad (4.39)$$

where $\tilde{\boldsymbol{\alpha}}^0 = (\tilde{\alpha}_1^0, \tilde{\alpha}_2^0, \tilde{\alpha}_3^0)$ and $\tilde{\boldsymbol{\alpha}}^1 = (\tilde{\alpha}_1^1, \tilde{\alpha}_2^1, \tilde{\alpha}_3^1)$ are row vectors, which are governed by some transport equations.

According to [58], the governing equations for $\tilde{\boldsymbol{\alpha}}^0$ are

$$\nabla\mathcal{T}\cdot\nabla\tilde{\boldsymbol{\alpha}}^0 + [\frac{1}{2\rho}\nabla\cdot(\rho\nabla\mathcal{T}) - \frac{5\rho}{\lambda+2\mu}]\tilde{\boldsymbol{\alpha}}^0 = 0, \quad (4.40)$$

with the initial condition

$$\tilde{\boldsymbol{\alpha}}^0 = \frac{\gamma_0^{P^3}}{\rho_0\pi}(\boldsymbol{r}-\boldsymbol{r}_0) + O(r^2) \quad \text{as} \quad \boldsymbol{r}\to\boldsymbol{r}_0. \quad (4.41)$$

Similarly, according to [58], the governing equations for $\tilde{\boldsymbol{\alpha}}^1$ are

$$\nabla\mathcal{T}\cdot\nabla\tilde{\boldsymbol{\alpha}}^1+[\frac{1}{2\rho}\nabla\cdot(\rho\nabla\mathcal{T})-\frac{7\rho}{\lambda+2\mu}]\tilde{\boldsymbol{\alpha}}^1=\tilde{\boldsymbol{c}}^0, \tag{4.42}$$

with the initial condition $\tilde{\boldsymbol{\alpha}}^1=O(r^2)$ as $\boldsymbol{r}\to\boldsymbol{r}_0$, where $\tilde{\boldsymbol{c}}^0$ is

$$\begin{aligned}\tilde{\boldsymbol{c}}^0 &= \frac{1}{8\rho}\{10\rho-\mu\nabla^2\mathcal{T}-\nabla\mathcal{T}\cdot\nabla(\lambda+\mu)](\nabla\mathcal{T}\cdot\tilde{\boldsymbol{C}}^0)-(\lambda+\mu)\nabla\mathcal{T}\cdot\nabla(\nabla\mathcal{T}\cdot\tilde{\boldsymbol{C}}^0)\\ &\quad -(\lambda+\mu)|\nabla\mathcal{T}|^2(\nabla\cdot\tilde{\boldsymbol{C}}^0)-2\mu\nabla\mathcal{T}\cdot[(\nabla\mathcal{T}\cdot\nabla)\tilde{\boldsymbol{C}}^0]-(\nabla\mu\cdot\tilde{\boldsymbol{C}}^0)|\nabla\mathcal{T}|^2+\tilde{\boldsymbol{d}}^0\}\end{aligned} \tag{4.43}$$

Here $\tilde{\boldsymbol{C}}^0$ and $\tilde{\boldsymbol{d}}^0$ are defined to be

$$\tilde{\boldsymbol{C}}^0 \equiv -\nabla\tilde{\boldsymbol{\alpha}}^0-\frac{(\lambda+2\mu)^2}{\rho(\lambda+\mu)}\nabla\left(\frac{\rho}{\lambda+2\mu}\right)\tilde{\boldsymbol{\alpha}}^0-\frac{\nabla\lambda\tilde{\boldsymbol{\alpha}}^0}{\lambda+\mu}, \tag{4.44}$$

$$\begin{aligned}\tilde{\boldsymbol{d}}^0 &\equiv (\lambda+\mu)\nabla\mathcal{T}\cdot\nabla(\nabla\cdot\tilde{\boldsymbol{A}}^{P0})+\mu\nabla\mathcal{T}\cdot\nabla^2\tilde{\boldsymbol{A}}^{P0}+(\nabla\lambda\cdot\nabla\mathcal{T})(\nabla\cdot\tilde{\boldsymbol{A}}^{P0})\\ &\quad +\nabla\mathcal{T}\cdot[\nabla\mu\times(\nabla\times\tilde{\boldsymbol{A}}^{P0})]+2\nabla\mathcal{T}\cdot[(\nabla\mu\cdot\nabla)\tilde{\boldsymbol{A}}^{P0}].\end{aligned} \tag{4.45}$$

To evaluate the formula (4.36) numerically, we need to solve the eikonal equation (4.37) to obtain τ^P, and the governing equations (4.40) and (4.42) to obtain $\tilde{\boldsymbol{A}}^{P0}$ and $\tilde{\boldsymbol{A}}^{P1}$, respectively. To obtain a first-order accurate $\boldsymbol{G}^P$, we need a fifth-order accurate τ^P, a third-order accurate $\tilde{\boldsymbol{\alpha}}^0$, and a first-order accurate $\tilde{\boldsymbol{\alpha}}^1$. For the eikonal equation (4.37), we can employ fifth-order LxF WENO-based schemes developed in [64] to compute τ^P. Since the governing equations (4.40) and (4.42) are decoupled, we can also apply high-order schemes in [64] to compute $\tilde{\boldsymbol{\alpha}}^0$ and $\tilde{\boldsymbol{\alpha}}^1$ with desired oder of accuracy.

4.2 Huygens' principle based globally valid Green's functions

In previous work [58], we have implemented the Hadamard-Babich ansatz to approximate the Green's tensor by assuming that no caustic occurs in the region of space containing the point source. However, caustics occur with high possibility in a generic inhomogeneous medium [79]. And the viscosity solution of traveltime is a single valued solution which does not contain later-arriving traveltimes [47, 51, 50]. Hence the constructed asymptotic Green's tensor does not contain the interference effects due to the multivaluedness of traveltime and is only valid before the occurrence of caustics. Therefore, inspired by the work [49, 44, 56], we develop the Huygens-Kirchhoff formula for elastic wave fields to construct a globally valid wave fields.

4.2.1 Huygens-Kirchhoff formula for elastic wave fields

Assuming that the wave field $\boldsymbol{u}(\boldsymbol{r};\boldsymbol{r}_0)$ due to the primary source $\boldsymbol{r}_0$ is known for $\boldsymbol{r} \in \Omega$ in a domain Ω enclosing the primary source $\boldsymbol{r_0}$, we would like to extrapolate this wave field to obtain the wave field $\boldsymbol{u}(\boldsymbol{r};\boldsymbol{r}_0)$ for $\boldsymbol{r} \in \Omega_{\text{ext}}$ in the exterior domain Ω_{ext}; see Figure 4.1.

As illustrated in Figure 4.1, the elastic wave field $\boldsymbol{u}(\boldsymbol{r};\boldsymbol{r}_0)$ in Ω_{ext} excited by the source $\boldsymbol{r}_0$ satisfies the following equation,

$$\rho(\boldsymbol{r})\omega^2 u_k(\boldsymbol{r};\boldsymbol{r}_0) + \partial_j[\lambda(\boldsymbol{r})\delta_{kj}\partial_m u_m(\boldsymbol{r};\boldsymbol{r}_0) + \mu(\partial_k u_j(\boldsymbol{r};\boldsymbol{r}_0) + \partial_j u_k(\boldsymbol{r};\boldsymbol{r}_0))] = 0, \quad \boldsymbol{r} \in \Omega_{ext}. \tag{4.46}$$

Here ∂_k represents the x_k-derivative, u_k is the kth component of $\boldsymbol{u}$ and the Einstein sum-

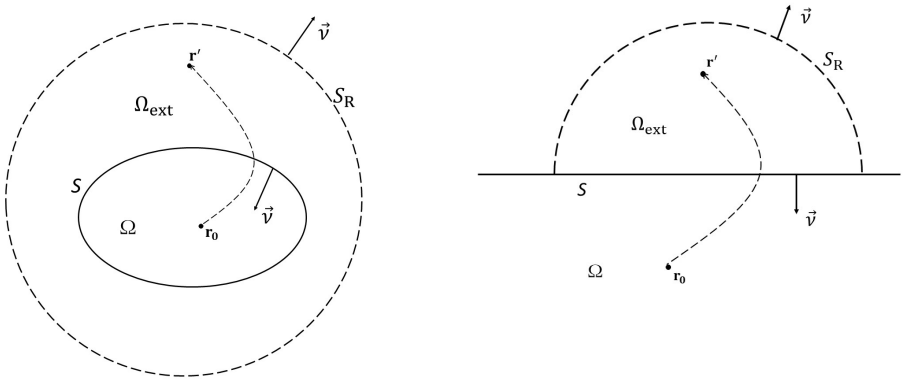

(a) (b)

Figure 4.1: Huygens-Kirchhoff formula for wave field extrapolation. (a) Spherical domains. (b) Planar domains.

mation convention is applied. The (k,l)th element of the Green's tensor $\boldsymbol{G}(\boldsymbol{r};\boldsymbol{r'})$ excited by the $\boldsymbol{r'} \in \Omega_{ext}$, satisfies

$$\rho(\boldsymbol{r})\omega^2 G_{kl}(\boldsymbol{r};\boldsymbol{r'}) + \partial_j[\lambda(\boldsymbol{r})\delta_{kj}\partial_m G_{ml}(\boldsymbol{r};\boldsymbol{r'}) + \mu(\boldsymbol{r})(\partial_k G_{jl}(\boldsymbol{r};\boldsymbol{r'}) + \partial_j G_{kl}(\boldsymbol{r};\boldsymbol{r'}))] \qquad (4.47)$$
$$= -\delta_{kl}\delta(\boldsymbol{r}-\boldsymbol{r'})$$

for $1 \le k,l \le 3$, where δ_{kl} is the kronecker delta. Thus, we have for the lth element of u,

$$\begin{aligned} -u_l(\boldsymbol{r'};\boldsymbol{r}_0) &= \int_{\Omega_{ext}} -\delta_{kl}\delta(\boldsymbol{r}-\boldsymbol{r'})u_k(\boldsymbol{r};\boldsymbol{r}_0)d\boldsymbol{r} \qquad (4.48)\\ &= \int_{\Omega_{ext}} \big\{\rho\omega^2 G_{kl} + \partial_j[\lambda\delta_{kj}\partial_m G_{ml} + \mu(\partial_k G_{jl} + \partial_j G_{kl})]\big\}u_k d\boldsymbol{r} \\ &= \int_{\Omega_{ext}} \big\{\partial_j[\lambda\delta_{kj}\partial_m G_{ml} + \mu(\partial_k G_{jl} + \partial_j G_{kl})]u_k \\ &\qquad - \partial_j[\lambda\delta_{kj}\partial_m u_m + \mu(\partial_k u_j + \partial_j u_k)]G_{kl}\big\}d\boldsymbol{r}. \end{aligned}$$

Integrating by parts, we get

$$
\begin{aligned}
u_l(\boldsymbol{r}';\boldsymbol{r}_0) = \int_{\Omega_{ext}} \big\{ & [\lambda\delta_{kj}\partial_m G_{ml} + \mu(\partial_k G_{jl} + \partial_j G_{kl})]\partial_j u_k \\
& - [\lambda\delta_{kj}\partial_m u_m + \mu(\partial_k u_j + \partial_j u_k)]\partial_j G_{kl}\big\} d\boldsymbol{r} \\
- \int_{S+S_R} \big\{ & [\lambda\delta_{kj}\partial_m G_{ml} + \mu(\partial_k G_{jl} + \partial_j G_{kl})]u_k \\
& - [\lambda\delta_{kj}\partial_m u_m + \mu(\partial_k u_j + \partial_j u_k)]G_{kl}\big\}\nu_j dS(\boldsymbol{r}) \\
= - \int_S \big\{ & \lambda[\partial_m G_{ml} u_j \nu_j - \partial_m u_m G_{jl}\nu_j] \\
& + \mu\nu_j[(\partial_k G_{jl} + \partial_j G_{kl})u_k - (\partial_k u_j + \partial_j u_k)G_{kl}]\big\} dS(\boldsymbol{r})
\end{aligned}
\tag{4.49}
$$

for $l = 1, 2, 3$, where $\boldsymbol{\nu} = (\nu_1, \nu_2, \nu_3)^T$ is the unit normal vector directing outward Ω_{ext}. The last equality holds since by letting $R \to \infty$, the integration on S_R vanishes by virtue of Sommerfeld radiation condition.

Consequently, in vector notation, we have obtained the folllowing equivalence of Huygens-Kirchhoff formula

$$
\begin{aligned}
\boldsymbol{u}(\boldsymbol{r}';\boldsymbol{r}_0) = \int_S \big\{ & \lambda[-(\nabla\cdot\boldsymbol{G})(\boldsymbol{u}\cdot\boldsymbol{\nu}) + (\nabla\cdot\boldsymbol{u})(\boldsymbol{G}\cdot\boldsymbol{\nu})] \\
& + \mu[(\boldsymbol{\nu}\cdot\nabla)\boldsymbol{u}\cdot\boldsymbol{G} - (\boldsymbol{\nu}\cdot\nabla)\boldsymbol{G}\cdot\boldsymbol{u}] \\
& + \mu[(\boldsymbol{G}\cdot\nabla)\boldsymbol{u}\cdot\boldsymbol{\nu} - (\boldsymbol{u}\cdot\nabla)\boldsymbol{G}\cdot\boldsymbol{\nu}]\big\} dS(\boldsymbol{r}),
\end{aligned}
\tag{4.50}
$$

on the boundary S of the domain Ω enclosing $\boldsymbol{r}_0$. The formula indicates that if the wave fields $\boldsymbol{u}(\boldsymbol{r};\boldsymbol{r}_0)$ and the Green's tensor $\boldsymbol{G}(\boldsymbol{r};\boldsymbol{r}')$ are known on the boundary S, then the wave fields $\boldsymbol{u}(\boldsymbol{r}';\boldsymbol{r}_0)$ away from S can be constructed.

In particular, we are interested in the case when the boundary S is the plane at $z = z_0$,

and the wave field is known in $z \leq z_0$. In other words, we need to determine $\boldsymbol{u}$ in $\Omega_{ext} := \{\boldsymbol{r} = (x, y, z) | z > z_0\}$ and hence in this case $\boldsymbol{\nu} = (0, 0, -1)^T$. Therefore, equation (4.49) reduces to

$$\begin{aligned} u_l(\boldsymbol{r}'; \boldsymbol{r}_0) = \int_{z=z_0} \big\{ & \lambda(\boldsymbol{r})[\partial_m G_{ml}(\boldsymbol{r}; \boldsymbol{r}') u_3(\boldsymbol{r}; \boldsymbol{r}_0) - \partial_m u_m(\boldsymbol{r}; \boldsymbol{r}_0) G_{3l}(\boldsymbol{r}; \boldsymbol{r}')] \\ & + \mu(\boldsymbol{r})(\partial_k G_{3l}(\boldsymbol{r}; \boldsymbol{r}') + \partial_3 G_{kl}(\boldsymbol{r}; \boldsymbol{r}')) u_k(\boldsymbol{r}; \boldsymbol{r}_0) \\ & - \mu(\boldsymbol{r})(\partial_k u_3(\boldsymbol{r}; \boldsymbol{r}_0) + \partial_3 u_k(\boldsymbol{r}; \boldsymbol{r}_0)) G_{kl}(\boldsymbol{r}; \boldsymbol{r}') \big\} dxdy. \end{aligned} \tag{4.51}$$

Consequently, to obtain for computing the (l, n)th element of the Green's tensor $\boldsymbol{G}(\boldsymbol{r}'; \boldsymbol{r}_0)$, $G_{ln}(\boldsymbol{r}'; \boldsymbol{r}_0)$, we can replace u_l with G_{ln} in the equation (4.51). Then the corresponding Huygens-Kirchhoff formula for the Green's tensor $\boldsymbol{G}(\boldsymbol{r}'; \boldsymbol{r}_0)$ is

$$\begin{aligned} G_{ln}(\boldsymbol{r}'; \boldsymbol{r}_0) = \int_{z=z_0} \big\{ & \lambda(\boldsymbol{r})[\partial_m G_{ml}(\boldsymbol{r}; \boldsymbol{r}') G_{3n}(\boldsymbol{r}; \boldsymbol{r}_0) - \partial_m G_{mn}(\boldsymbol{r}; \boldsymbol{r}_0) G_{3l}(\boldsymbol{r}; \boldsymbol{r}')] \\ & + \mu(\boldsymbol{r})(\partial_k G_{3l}(\boldsymbol{r}; \boldsymbol{r}') + \partial_3 G_{kl}(\boldsymbol{r}; \boldsymbol{r}')) G_{kn}(\boldsymbol{r}; \boldsymbol{r}_0) \\ & - \mu(\boldsymbol{r})(\partial_k G_{3n}(\boldsymbol{r}; \boldsymbol{r}_0) + \partial_3 G_{kn}(\boldsymbol{r}; \boldsymbol{r}_0)) G_{kl}(\boldsymbol{r}; \boldsymbol{r}') \big\} dxdy \end{aligned} \tag{4.52}$$

for $1 \leq l, n \leq 3$.

Numerically, it is expensive to compute the Green's tensor $\boldsymbol{G}(\boldsymbol{r}; \boldsymbol{r}')$ excited by $\boldsymbol{r}' \in \Omega_{ext}$ since the manifold Ω_{ext} is one dimension higher than S. However, the following reciprocal relations are satisfied

$$\tau(\boldsymbol{r}; \boldsymbol{r}') = \tau(\boldsymbol{r}'; \boldsymbol{r}), \quad \boldsymbol{G}(\boldsymbol{r}; \boldsymbol{r}') = \boldsymbol{G}^T(\boldsymbol{r}'; \boldsymbol{r}). \tag{4.53}$$

Hence, we can interchange the two arguments $\boldsymbol{r}$ and $\boldsymbol{r}'$ in $\boldsymbol{G}(\boldsymbol{r}'; \boldsymbol{r})$ in (4.52) and use the

relation above to get

$$G_{ln}(\boldsymbol{r}';\boldsymbol{r}_0) = \int_{z=z_0} \big\{\lambda(\boldsymbol{r})[\partial_m G_{lm}(\boldsymbol{r}';\boldsymbol{r})G_{3n}(\boldsymbol{r};\boldsymbol{r}_0) - \partial_m G_{mn}(\boldsymbol{r};\boldsymbol{r}_0)G_{l3}(\boldsymbol{r}';\boldsymbol{r})] \tag{4.54}$$
$$+ \mu(\boldsymbol{r})(\partial_k G_{l3}(\boldsymbol{r}';\boldsymbol{r}) + \partial_3 G_{lk}(\boldsymbol{r}';\boldsymbol{r}))G_{kn}(\boldsymbol{r};\boldsymbol{r}_0)$$
$$- \mu(\boldsymbol{r})(\partial_k G_{3n}(\boldsymbol{r};\boldsymbol{r}_0) + \partial_3 G_{kn}(\boldsymbol{r};\boldsymbol{r}_0))G_{lk}(\boldsymbol{r}';\boldsymbol{r})\big\}dxdy,$$

We can rewrite above formula (4.54) as

$$G_{ln}(\boldsymbol{r}',\boldsymbol{r}_0) = \int_{z=z_0} \{\lambda(\boldsymbol{r}) \sum_{m=1}^{3} [\partial_m G_{lm}(\boldsymbol{r}';\boldsymbol{r})G_{3n}(\boldsymbol{r};\boldsymbol{r}_0) - \partial_m G_{mn}(\boldsymbol{r};\boldsymbol{r}_0)G_{l3}(\boldsymbol{r}';\boldsymbol{r})] \tag{4.55}$$
$$+ \mu(\boldsymbol{r})(\partial_1 G_{l3}(\boldsymbol{r}';\boldsymbol{r}) + \partial_3 G_{l1}(\boldsymbol{r}';\boldsymbol{r}))G_{1n}(\boldsymbol{r};\boldsymbol{r}_0)$$
$$+ \mu(\boldsymbol{r})(\partial_2 G_{l3}(\boldsymbol{r}';\boldsymbol{r}) + \partial_3 G_{l2}(\boldsymbol{r}';\boldsymbol{r}))G_{2n}(\boldsymbol{r};\boldsymbol{r}_0)$$
$$+ \mu(\boldsymbol{r})(\partial_3 G_{l3}(\boldsymbol{r}';\boldsymbol{r}) + \partial_3 G_{l3}(\boldsymbol{r}';\boldsymbol{r}))G_{3n}(\boldsymbol{r};\boldsymbol{r}_0)$$
$$- \mu(\boldsymbol{r})(\partial_1 G_{3n}(\boldsymbol{r};\boldsymbol{r}_0) + \partial_3 G_{1n}(\boldsymbol{r};\boldsymbol{r}_0))G_{l1}(\boldsymbol{r}';\boldsymbol{r})$$
$$- \mu(\boldsymbol{r})(\partial_2 G_{3n}(\boldsymbol{r};\boldsymbol{r}_0) + \partial_3 G_{2n}(\boldsymbol{r};\boldsymbol{r}_0))G_{l2}(\boldsymbol{r}';\boldsymbol{r})$$
$$- \mu(\boldsymbol{r})(\partial_3 G_{3n}(\boldsymbol{r};\boldsymbol{r}_0) + \partial_3 G_{3n}(\boldsymbol{r};\boldsymbol{r}_0))G_{l3}(\boldsymbol{r}';\boldsymbol{r})\}dxdy,$$

As can be seen, the only unknowns in (4.55) are $\boldsymbol{G}(\boldsymbol{r}';\boldsymbol{r})$ and its spatial derivatives. Specifically, $\boldsymbol{G}(\boldsymbol{r}';\boldsymbol{r})$ is assumed to have no caustics in Ω_{ext}. By (4.6) and (4.36), we may

approximate

$$
\begin{aligned}
G_{kj}(\boldsymbol{r}';\boldsymbol{r}) =& G^S_{kj}(\boldsymbol{r}';\boldsymbol{r}) + G^P_{kj}(\boldsymbol{r}';\boldsymbol{r}) \\
\approx& \frac{\tilde{A}^{S0}_{kj}(\boldsymbol{r}';\boldsymbol{r})}{-\omega^2} f_{-3+\frac{1}{2}}(\omega,\tau^S(\boldsymbol{r}';\boldsymbol{r})) + \frac{\tilde{A}^{S1}_{kj}(\boldsymbol{r}';\boldsymbol{r})}{-\omega^2\tau^{S2}} f_{-2+\frac{1}{2}}(\omega,\tau^S(\boldsymbol{r}';\boldsymbol{r})) \\
&+ \frac{\tilde{A}^{P0}_{kj}(\boldsymbol{r}';\boldsymbol{r})}{-\omega^2} f_{-3+\frac{1}{2}}(\omega,\tau^P(\boldsymbol{r}';\boldsymbol{r})) + \frac{\tilde{A}^{P1}_{kj}(\boldsymbol{r}';\boldsymbol{r})}{-\omega^2\tau^{P2}} f_{-2+\frac{1}{2}}(\omega,\tau^P(\boldsymbol{r}';\boldsymbol{r})).
\end{aligned} \tag{4.56}
$$

Then based on the formula (3.206) and the properties of Hankel functions, we can derive the spatial derivative of $\boldsymbol{G}(\boldsymbol{r}';\boldsymbol{r})$ with respect to $\boldsymbol{r}$ as follows

$$
\begin{aligned}
\partial_{x_i} G^S_{kj}(\boldsymbol{r}';\boldsymbol{r}) \approx& \frac{2\tau^S \partial_{x_i}\tau^S \tilde{A}^{S0}_{kj}(\boldsymbol{r}';\boldsymbol{r})}{\omega^2} f_{-4+\frac{1}{2}}(\omega,\tau^S(\boldsymbol{r}';\boldsymbol{r})) \\
&+ \left[\frac{\partial_{x_i}\tilde{A}^{S0}_{kj}(\boldsymbol{r}';\boldsymbol{r})}{-\omega^2} + \frac{2\partial_{x_i}\tau^S \tilde{A}^{S1}_{kj}(\boldsymbol{r}';\boldsymbol{r})}{\omega^2\tau^S}\right] f_{-3+\frac{1}{2}}(\omega,\tau^S(\boldsymbol{r}';\boldsymbol{r})) \\
&+ \partial_{x_i}\left[\frac{\tilde{A}^{S1}_{kj}(\boldsymbol{r}';\boldsymbol{r})}{-\omega^2\tau^{S2}}\right] f_{-2+\frac{1}{2}}(\omega,\tau^S(\boldsymbol{r}';\boldsymbol{r})),
\end{aligned} \tag{4.57}
$$

and the same can be applied to $\boldsymbol{G}^P(\boldsymbol{r}';\boldsymbol{r})$ to obtain $\partial_{x_i}\boldsymbol{G}^P(\boldsymbol{r}';\boldsymbol{r})$.

Since $f_{-3+l+\frac{1}{2}}(\omega,\tau) = O(\omega^{-l+2})$ as $\omega \to \infty$, retaining the only leading order terms, i.e. the $O(1)$ terms in (4.56) and $O(\omega)$ terms in (4.57), then we have the the following approximation

$$
G^S_{kj}(\boldsymbol{r}';\boldsymbol{r}) \approx \frac{\tilde{A}^{S0}_{kj}(\boldsymbol{r}';\boldsymbol{r})}{8\tau^{S3}(\boldsymbol{r}';\boldsymbol{r})} e^{i\omega\tau^S(\boldsymbol{r}';\boldsymbol{r})}, \tag{4.58}
$$

$$
\partial_{x_i} G^S_{kj}(\boldsymbol{r}';\boldsymbol{r}) \approx \frac{i\omega\partial_{x_i}\tau^S(\boldsymbol{r}';\boldsymbol{r})\tilde{A}^{S0}_{kj}(\boldsymbol{r}';\boldsymbol{r})}{8\tau^{S3}(\boldsymbol{r}';\boldsymbol{r})} e^{i\omega\tau^S(\boldsymbol{r}';\boldsymbol{r})}, \tag{4.59}
$$

and the same approximation for P-wave can be obtained similarly.

Noticing that such approximations are adequately accurate for computing $\boldsymbol{G}(\boldsymbol{r}';\boldsymbol{r}_0)$ since

the formula (4.55) is in general $O(\omega)$ and becomes $O(1)$ only when $\partial_{x_i}\boldsymbol{G}(\boldsymbol{r'};\boldsymbol{r}) = O(1)$ and $\boldsymbol{G}(\boldsymbol{r'};\boldsymbol{r}) = O(1/\omega)$ since $\partial_{x_i}\boldsymbol{G}(\boldsymbol{r};\boldsymbol{r}_0) = O(\omega)$. Hence the approximation lose accuracy only when the approximations we choose for both $\partial_{x_i}\boldsymbol{G}(\boldsymbol{r'};\boldsymbol{r})$ and $\boldsymbol{G}(\boldsymbol{r'};\boldsymbol{r})$ becomes 0 simultaneously, the points with such property constitute only a set of measure 0 and will not affect the value of $\boldsymbol{G}(\boldsymbol{r'};\boldsymbol{r}_0)$ in (4.55).

As can be seen, the only unkowns in (4.58) and (4.59) are τ^S, $\tilde{\boldsymbol{A}}^{S0}$ and $\nabla_{\boldsymbol{r}}\tau^S(\boldsymbol{r'};\boldsymbol{r})$. Hence in order to obtain the Green's tensor $\boldsymbol{G}(\boldsymbol{r'};\boldsymbol{r}_0)$, we need to compute the asymptotic ingredients: τ^S, $\tilde{\boldsymbol{A}}^{S0}$ and $\nabla_{\boldsymbol{r}}\tau^S(\boldsymbol{r'};\boldsymbol{r})$ for S-wave and τ^P, $\tilde{\boldsymbol{A}}^{P0}$ and $\nabla_{\boldsymbol{r}}\tau^P(\boldsymbol{r'};\boldsymbol{r})$ for P-wave. In previous section, we have introduced how to compute the traveltimes and dyadic coefficients for both the S-wave and P-wave up to a suitable order of accuracy. The same methods can be used here for all secondary sources. Since that $\nabla_{\boldsymbol{r}}\tau(\boldsymbol{r'};\boldsymbol{r})$ is opposite to the take-off direction $\boldsymbol{t}^{(0)}(\boldsymbol{r'},\boldsymbol{r})$ along the ray from $\boldsymbol{r}$ to $\boldsymbol{r'}$, where $\boldsymbol{t}^{(0)}(\boldsymbol{r'},\boldsymbol{r})$ is governed by the following equation

$$(\nabla_{\boldsymbol{r'}}\tau(\boldsymbol{r'};\boldsymbol{r})\cdot\nabla_{\boldsymbol{r'}})\boldsymbol{t}^{(0)}(\boldsymbol{r'},\boldsymbol{r}) = 0, \tag{4.60}$$

with the initial condition

$$\lim_{\boldsymbol{r'}\to\boldsymbol{r}}\left[\boldsymbol{t}^{(0)}(\boldsymbol{r'};\boldsymbol{r}) - \frac{\boldsymbol{r'}-\boldsymbol{r}}{|\boldsymbol{r'}-\boldsymbol{r}|}\right] = 0, \tag{4.61}$$

the high order LxF-WENO schemes [45, 44] can be applied to compute $\boldsymbol{t}^{(0)}$ for both the S- and P-waves, yielding $\nabla_{\boldsymbol{r}}\tau(\boldsymbol{r'};\boldsymbol{r})$ accordingly.

4.2.2 Huygens principle based sweeping method

Based on the Huygens-Kirchhoff formula, we now develop a layer-by-layer sweeping method to construct the globally valid Green's functions.

The Green's tensor $\boldsymbol{G}$ as constructed by the ansatz (4.1) is valid only in a local neighborhood of $\boldsymbol{r}_0$ where no caustics occur since the computed ingredients in (4.1) are single-valued viscosity solutions. Therefore the integration formula (4.55) can only be used in a narrow layer where the Green's functions $\boldsymbol{G}$ excited by every selected secondary source point $\boldsymbol{r} \in S$ is valid. However, since caustics will not develop close to a source in an isotropic medium, we can construct the elastic wave fields from a point source to a global domain in a layer-by-layer manner.

Given the primary source $\boldsymbol{r}_0$, we can first construct asymptotic Green's functions $\boldsymbol{G}(\boldsymbol{r}; \boldsymbol{r}_0)$ by substituting the computed ingredients into the ansatz (4.1), which is valid in a local neighborhood Ω_1 containing the source $\boldsymbol{r}_0$; consequently, the Green's functions $\boldsymbol{G}(\boldsymbol{r}; \boldsymbol{r}_0)$ and their gradients $\nabla \boldsymbol{G}(\boldsymbol{r}; \boldsymbol{r}_0)$ are known on the boundary of Ω_1, denoted by S_1. Letting Ω_1 be the first layer, we can set up secondary point sources on the boundary S_1, and identify a narrow layer, denoted by Ω_2, where the Green's functions $\boldsymbol{G}(\boldsymbol{r}'; \boldsymbol{r})$ ($\boldsymbol{r} \in S_1$, $\boldsymbol{r}' \in \Omega_2$) is valid. The method of identifying the narrow will be addressed later. Then we can apply the integration formula (4.55) to construct the Green's function $\boldsymbol{G}(\boldsymbol{r}'; \boldsymbol{r}_0)$ in the layer Ω_2, so that $\boldsymbol{G}(\boldsymbol{r}'; \boldsymbol{r}_0)$ and $\nabla \boldsymbol{G}(\boldsymbol{r}'; \boldsymbol{r}_0)$ are available on $S_2 = \partial\Omega_2$. The process can be repeated so that the Green's functions can be constructed everywhere by sweeping through the whole domain in a layer-by-layer fashion.

As addressed in [49, 56], the method of partitioning the whole computational domain into layers is based on the first-arrival traveltime solutions for the eikonal equations with

point source for both S-wave and P-wave. Suppose that the traveltime solutions, $\tau^S(\boldsymbol{r};\boldsymbol{r}_0)$ and $\tau^P(\boldsymbol{r};\boldsymbol{r}_0)$, are computed in the whole domain, we can determine the first layer Ω_1 as the neighborhood of $\boldsymbol{r}_0$ where both $\tau^S(\boldsymbol{r};\boldsymbol{r}_0)$ and $\tau^P(\boldsymbol{r};\boldsymbol{r}_0)$ are smooth. Then we can set up a few secondary-source points on the boundary S_1 of the first layer, compute the first-arrival traveltimes for both S-wave and P-wave for each individual point and determine a local neighborhood where all traveltimes are smooth. This is the second narrow layer Ω_2. The process can be repeated so that the whole domain will be covered by all such layers.

The asymptotic Green's functions are singular at the point source, hence we will use the Huygens-Kirchhoff formula (4.55) to compute the Green's functions $\boldsymbol{G}$ at the observation points away from the secondary source surface. To well separate the receiver domain and the secondary source surface, we can move the secondary source surface slightly closer to the primary source. The missing portion of the Green's functions is already computed by either using the primary source or using the previous layer. In practice, we are interested in designing methods with efficiency independent of frequency. We will set a fixed distance $d_f \geq 0$ to separate the secondary source surface and the receiver domain since when the frequency parameter ω is big enough, the asymptotic Green's functions become accurate roughly away from the source by this distance.

4.2.3 Planer-layer based Huygens sweeping

To better illustrate the sweeping process, we consider the wave fields direct along the positive z direction. As showed in Figure 4.2, the computational domain is partitioned into some non-overlapping layers Ω_j, all secondary-source surfaces S_j are planar and perpendicular to the z-direction, and this partition satisfies the properties discussed above. The planar-based sweeping method can be summarized as the following.

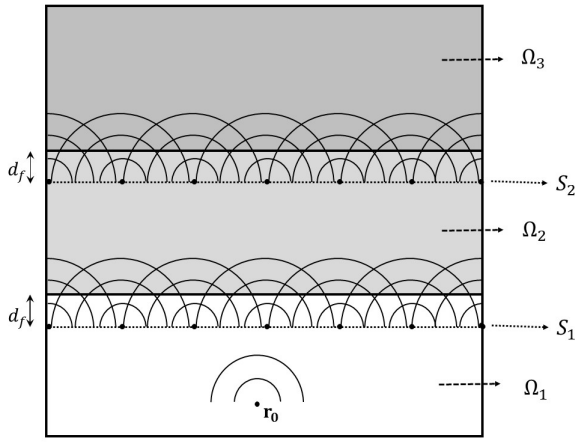

Figure 4.2: The computational domain is partitioned into three layers: Ω_1, Ω_2, and Ω_3. The first layer Ω_1 contains the primary source $\boldsymbol{r}_0$; the source plane S_1 is placed in Ω_1 and is d_f wide away from Ω_2; the source plane S_2 is d_f wide away from Ω_3 and locates in Ω_2.

- **Stage 1.** Precomputing asymptotic ingredients.
  - The computation domain are partitioned into layers Ω_j and identify secondary source planes S_j so that the sources and receivers are well sperated.
  - For each secondary source plane S_j, the tables of traveltime, amplitudes and take-off directions are computed at each secondary source on a coarse mesh in the layer Ω_{j+1}. Then the tables on a dense set of secondary sources can be obtained by interpolating the coarse tables.
  - The tables for the coarse set of secondary sources are stored (on a hard drive) and can be used to construct the wave fields for all high frequencies and for arbitrary point source.
- **Stage 2.** Given a free-space frequency ω, constructing the wave fields layer by layer.
  - For each secondary source plane S_j, the tables of the traveltimes, amplitudes and

take-off directions for both S-wave and P-wave are loaded from the hard drive to construct the Green's function $\boldsymbol{G}(\boldsymbol{r};\boldsymbol{r}_0)$ in the corresponding layer Ω_{j+1}.

- For each table, the data is first interpolated onto a finer mesh to resolve the highly osillatory nature of $\boldsymbol{G}$ and then compute $\boldsymbol{G}(\boldsymbol{r};\boldsymbol{r}_0)$ by Huygens-Kirchhoff formula with a quadrature rule.
- For the given frequency ω, we can interpolate the tables from the given source locations onto the region bounded by these source locations to obtain the data for the desired dense sources. This is feasible because asymptotic ingredients are continuous functions of source location.

To implement the above algorithm, we need to overcome some obstacles. The first obstacle is how to store the data tables generated in stage 1 since there are many sources in the source plane S_j and also we are dealing with nine-element Green's functions for 3-D elastic wave equations. The second obstacle is how to efficiently carry out the matrix-vector products induced by the discretization of the Huygens-Kirchhoff integral (4.55). We will address these two issues in the following subsections.

4.2.4 Data tables and compression

To reduce data storage, we will follow the approach in [49, 57] to compress each data table into a linear combination of tensor product based multivariate Chebyshev polynomials so that information in each table is enclosed into a small number of Chebyshev coefficients. In our implement, we need to compress the data tables for both the S-wave and P-wave separately.

To efficiently reconstruct the information from those compressed tables, we will follow

the method in [49] which is based on the product fo low-rank matrices. The approach is also equivalent to the Orszag partial summation method [10].

4.2.5 Discretization of Huygens-Kirchhoff integral

In numerical implementation, it is difficult to evaluate the (k, j)-entry of the electric Green's functions $\boldsymbol{G}(\boldsymbol{r}; \boldsymbol{r}_0)$ by the equation(4.55) for $k, j = 1, 2, 3$, when the secondary source plane is unbounded. Hence, first we need to truncate the unbounded integration domain S to a finite, bounded domain $\tilde{S}$ according to the specified computational domain for elastic wave equations. Since the expansion (4.1) automatically exhibits outgoing wave behavior and satisfies the Sommerfeld radiation condition at infinity, such a truncation may slightly affects the accuracy of the wave field near the boundary of $\tilde{S}$ only.

After truncation, the bounded domain $\tilde{S}$ can be discretized so that the quadrature rule can be applied to approximate the integral in (4.55). Since we are interested in computing highly oscillatory solution, we have to specify sufficient mesh points to sample the overall solution. In principle, the optimal number of sampling points is arguably four to six mesh points per wavelength in each direction. However, in the high frequency regime, the direct methods such as finite difference or finite-element methods require many more points per wavelength so as to yield accurate numerical solutions due to pollution or dispersion errors [5, 4]. On the other hand, the Hadamard-Babich ansatz based method requires only four to six mesh points per wavelength to resolve the overall solution in the high-frequency regime and this has been verified in [49, 45, 56] and in the following examples.

Since given the index of refraction γ and the frequency parameter ω, the smallest wavelength in the computational domain can be estimated to be $\lambda_{\max} = \frac{2\pi}{\omega\gamma_{\max}}$, where $\gamma_{\max}$ is the largest value of γ^S and γ^P for both S-wave and P-wave in the computational domain,

and we specify 4 to 6 points per wavelength in each direction accordingly. We remark that because all the ingredients in Hadamard-Babich ansatz are independent of frequency, one can compute these asymptotic ingredients on much coarser meshes with number of points independent of frequency rather than on this very fine mesh. Only when we construct the overall wave fields do we need to interpolate those ingredients onto the fine meshes so as to capture each wave accurately.

Based on above considerations, we are ready to discretize the integral (4.55). Assume the primary point source $\boldsymbol{r}_0$ is given, and the truncated rectangular region $\tilde{S}$ is discretized into a set of $M_s = M_x \times M_y$ uniform grid points with the same mesh size h in both x- and y-directions so that the above sampling requirement of four to six points per wavelength is satisfied. We apply the trapezoidal rule to approximate the integral over $\tilde{S}$ and obtain

$$
\begin{aligned}
G_{kj}(\boldsymbol{r}', \boldsymbol{r}_0) \approx & h^2 \sum_{m=1}^{Mx}{}'' \sum_{n=1}^{My}{}'' \\
& \big[\lambda(\boldsymbol{s}_{mn}) \sum_{m=1}^{3} (\partial_m G_{km}(\boldsymbol{r}'; \boldsymbol{s}_{mn}) G_{3j}(\boldsymbol{s}_{mn}; \boldsymbol{r}_0) \\
& - \lambda(\boldsymbol{s}_{mn}) \sum_{m=1}^{3} \partial_m G_{mj}(\boldsymbol{s}_{mn}; \boldsymbol{r}_0) G_{k3}(\boldsymbol{r}'; \boldsymbol{s}_{mn})) \\
& + \mu(\boldsymbol{s}_{mn})(\partial_1 G_{k3}(\boldsymbol{r}'; \boldsymbol{s}_{mn}) + \partial_3 G_{k1}(\boldsymbol{r}'; \boldsymbol{s}_{mn})) G_{1j}(\boldsymbol{s}_{mn}; \boldsymbol{r}_0) \\
& + \mu(\boldsymbol{s}_{mn})(\partial_2 G_{k3}(\boldsymbol{r}'; \boldsymbol{s}_{mn}) + \partial_3 G_{k2}(\boldsymbol{r}'; \boldsymbol{s}_{mn})) G_{2j}(\boldsymbol{s}_{mn}; \boldsymbol{r}_0) \\
& + \mu(\boldsymbol{s}_{mn})(\partial_3 G_{k3}(\boldsymbol{r}'; \boldsymbol{s}_{mn}) + \partial_3 G_{k3}(\boldsymbol{r}'; \boldsymbol{s}_{mn})) G_{3j}(\boldsymbol{s}_{mn}; \boldsymbol{r}_0) \\
& - \mu(\boldsymbol{s}_{mn})(\partial_1 G_{3j}(\boldsymbol{s}_{mn}; \boldsymbol{r}_0) + \partial_3 G_{1j}(\boldsymbol{s}_{mn}; \boldsymbol{r}_0)) G_{k1}(\boldsymbol{r}'; \boldsymbol{s}_{mn}) \\
& - \mu(\boldsymbol{s}_{mn})(\partial_2 G_{3j}(\boldsymbol{s}_{mn}; \boldsymbol{r}_0) + \partial_3 G_{2j}(\boldsymbol{s}_{mn}; \boldsymbol{r}_0)) G_{k2}(\boldsymbol{r}'; \boldsymbol{s}_{mn}) \\
& - \mu(\boldsymbol{s}_{mn})(\partial_3 G_{3j}(\boldsymbol{s}_{mn}; \boldsymbol{r}_0) + \partial_3 G_{3j}(\boldsymbol{s}_{mn}; \boldsymbol{r}_0)) G_{k3}(\boldsymbol{r}'; \boldsymbol{s}_{mn})\big]
\end{aligned}
\tag{4.62}
$$

for $k, j = 1, 2, 3$, where $\sum''$ denotes that the first and last term have a factor $1/2$. Notice that partial derivatives of $\boldsymbol{G}(\boldsymbol{s}_{mn}; \boldsymbol{r}_0)$ are estimated by numerical differentiation since the Green's functions $\boldsymbol{G}(\boldsymbol{r}; \boldsymbol{r}_0)$ are already computed from last step. M_x and M_y are the number of grid points in the x- and y- directions, respectively; $\{\boldsymbol{s}_{mn}\}$ are the M_s mesh points on the source plane $\tilde{S}$, and are re-enumerated as $\{\boldsymbol{s}_m\}_{m=1}^{M_s}$. According to the partition strategy, we are interested in evaluating (4.62) for all observation points in a narrow layer which is about d_f far away from the source plane and we enumerate those mesh points as $\{\boldsymbol{r}_n\}_{n=1}^{N_r}$. Then we obtain

$$\begin{aligned} \boldsymbol{g}_{kj} =& \boldsymbol{U}_{k1}\boldsymbol{f}_{1j} + \boldsymbol{U}_{k2}\boldsymbol{f}_{2j} + \boldsymbol{U}_{k3}\boldsymbol{f}_{3j} + \boldsymbol{U}_{k4}\boldsymbol{f}_{4j} \\ & \boldsymbol{U}_{k5}\boldsymbol{f}_{5j} + \boldsymbol{U}_{k6}\boldsymbol{f}_{6j} + \boldsymbol{U}_{k7}\boldsymbol{f}_{7j} + \boldsymbol{U}_{k8}\boldsymbol{f}_{8j} \end{aligned} \tag{4.63}$$

for $k, j = 1, 2, 3$, where

$$\boldsymbol{g}_{kj} = [G_{kj}(\boldsymbol{r}_1; \boldsymbol{r}_0), G_{kj}(\boldsymbol{r}_2; \boldsymbol{r}_0), \cdots, G_{kj}(\boldsymbol{r}_{N_r}; \boldsymbol{r}_0)]^T,$$

$$\boldsymbol{U}_{k1} = [\sum_{l=1}^{3} \partial_l G_{kl}(\boldsymbol{r}_n; \boldsymbol{s}_m)]_{1 \le n \le N_r, 1 \le m \le M_s},$$

$$\boldsymbol{U}_{k2} = [G_{k3}(\boldsymbol{r}_n; \boldsymbol{s}_m)]_{1 \le n \le N_r, 1 \le m \le M_s},$$

$$\boldsymbol{U}_{k3} = [\partial_1 G_{k3}(\boldsymbol{r}_n; \boldsymbol{s}_n) + \partial_3 G_{k1}(\boldsymbol{r}_n; \boldsymbol{s}_m)]_{1 \le n \le N_r, 1 \le m \le M_s},$$

$$\boldsymbol{U}_{k4} = [\partial_2 G_{k3}(\boldsymbol{r}_n; \boldsymbol{s}_m) + \partial_3 G_{k2}(\boldsymbol{r}_n; \boldsymbol{s}_m)]_{1 \le n \le N_r, 1 \le m \le M_s},$$

$$\boldsymbol{U}_{k5} = [\partial_3 G_{k3}(\boldsymbol{r}_n; \boldsymbol{s}_m) + \partial_3 G_{k3}(\boldsymbol{r}_n; \boldsymbol{s}_m)]_{1 \le n \le N_r, 1 \le m \le M_s},$$

$$\boldsymbol{U}_{k6} = [G_{k1}(\boldsymbol{r}_n; \boldsymbol{s}_m)]_{1 \le n \le N_r, 1 \le m \le M_s},$$

$$\boldsymbol{U}_{k7} = [G_{k2}(\boldsymbol{r}_n; \boldsymbol{s}_m)]_{1 \le n \le N_r, 1 \le m \le M_s},$$

$$\boldsymbol{U}_{k8} = [G_{k3}(\boldsymbol{r}_n; \boldsymbol{s}_m)]_{1 \le n \le N_r, 1 \le m \le M_s},$$

$$\boldsymbol{f}_{1j} = [\lambda(\boldsymbol{s}_1) G_{3j}(\boldsymbol{s}_1; \boldsymbol{r}_0), \cdots, \lambda(\boldsymbol{s}_{M_s}) G_{3j}(\boldsymbol{s}_{M_s}; \boldsymbol{r}_0)]^T,$$

$$\boldsymbol{f}_{2j} = -[\lambda(\boldsymbol{s}_1) \sum_{l=1}^{3} \partial_l G_{lj}(\boldsymbol{s}_1; \boldsymbol{r}_0), \cdots, \lambda(\boldsymbol{s}_{M_s}) \sum_{l=1}^{3} \partial_l G_{lj}(\boldsymbol{s}_{M_s}; \boldsymbol{r}_0)]^T,$$

$$\boldsymbol{f}_{3j} = [\mu(\boldsymbol{s}_1) G_{1j}(\boldsymbol{s}_1; \boldsymbol{r}_0), \cdots \mu(\boldsymbol{s}_{M_s}) G_{1j}(\boldsymbol{s}_{M_s}; \boldsymbol{r}_0)]^T,$$

$$\boldsymbol{f}_{4j} = [\mu(\boldsymbol{s}_1) G_{2j}(\boldsymbol{s}_1; \boldsymbol{r}_0), \cdots \mu(\boldsymbol{s}_{M_s}) G_{2j}(\boldsymbol{s}_{M_s}; \boldsymbol{r}_0)]^T,$$

$$\boldsymbol{f}_{5j} = [\mu(\boldsymbol{s}_1) G_{3j}(\boldsymbol{s}_1; \boldsymbol{r}_0), \cdots \mu(\boldsymbol{s}_{M_s}) G_{3j}(\boldsymbol{s}_{M_s}; \boldsymbol{r}_0)]^T,$$

$$\boldsymbol{f}_{6j} = [-\mu(\boldsymbol{s}_1)(\partial_1 G_{3j}(\boldsymbol{s}_1; \boldsymbol{r}_0) + \partial_3 G_{1j}(\boldsymbol{s}_1; \boldsymbol{r}_0)), \cdots, -\mu(\boldsymbol{s}_{M_s})(\partial_1 G_{3j}(\boldsymbol{s}_{M_s}; \boldsymbol{r}_0) + \partial_3 G_{1j}(\boldsymbol{s}_{M_s}; \boldsymbol{r}_0))]^T,$$

$$\boldsymbol{f}_{7j} = [-\mu(\boldsymbol{s}_1)(\partial_2 G_{3j}(\boldsymbol{s}_1; \boldsymbol{r}_0) + \partial_3 G_{2j}(\boldsymbol{s}_1; \boldsymbol{r}_0)), \cdots, -\mu(\boldsymbol{s}_{M_s})(\partial_2 G_{3j}(\boldsymbol{s}_{M_s}; \boldsymbol{r}_0) + \partial_3 G_{2j}(\boldsymbol{s}_{M_s}; \boldsymbol{r}_0))]^T,$$

$$\boldsymbol{f}_{8j} = [-\mu(\boldsymbol{s}_1)(\partial_3 G_{3j}(\boldsymbol{s}_1; \boldsymbol{r}_0) + \partial_3 G_{3j}(\boldsymbol{s}_1; \boldsymbol{r}_0)), \cdots, -\mu(\boldsymbol{s}_{M_s})(\partial_3 G_{3j}(\boldsymbol{s}_{M_s}; \boldsymbol{r}_0) + \partial_3 G_{3j}(\boldsymbol{s}_{M_s}; \boldsymbol{r}_0))]^T,$$

In numerical implementation, we will uniformly and coarsely sample the secondary sources so that the asymptotic ingredients for those coarsely sampled sources are efficiently precomputed. In the high frequency regime, we need to sample enough points on the source plane with finer meshes so as to obtain the desired accuracy. The asymptotic ingredients on those finer meshes can be obtained by interpolation.

To evaluate (4.63), we need to carry out total 72 matrix-vector multiplications for nine components of $\boldsymbol{G}$. In practice, M_s and N_r could be extremely large for high frequencies so that the direct evaluation of (4.63) with complexity $O(M_s \times N_r)$ is expensive and impractical. To accelerate the evaluation process, we will use a multilevel matrix decomposition based butterfly algorithm in [84, 11, 18, 49, 56].

4.2.6 A butterfly algorithm

We can reformulate (4.63) as the following:

$$g_{kj}(\boldsymbol{r}) = \sum_{q=1}^{8} \sum_{\boldsymbol{s} \in \boldsymbol{X}_s} U_{kq}(\boldsymbol{r}; \boldsymbol{s}) f_{qj}(\boldsymbol{s}), \quad \boldsymbol{r} \in \boldsymbol{X}_r \subset \Omega_r, \, \boldsymbol{s} \in \boldsymbol{X}_s \subset \Omega_s, \tag{4.64}$$

and $1 \leq k, j \leq 3$. Here the set of sources $\boldsymbol{X}_s$ is in the domain Ω_s, and the set of receivers is in the domain Ω_r. Ω_s and Ω_r are d_f apart from each other. f_{qj} is the representative function of $\boldsymbol{f}_{qj}$ in the sense that $f_{qj}(\boldsymbol{s}_m)$ is the mth element of $\boldsymbol{f}_{qj}$ for $1 \leq m \leq M_s$. $U_{kq}(\boldsymbol{r}; \boldsymbol{s})$ is the representative function of $\boldsymbol{U}_{kq}$.

Noticing in (4.63) that for each secondary source $\boldsymbol{s}_m$ and receiver $\boldsymbol{r}_n$, $1 \leq m \leq M_s, 1 \leq n \leq N_r$, the Green's tensor $\boldsymbol{G}(\boldsymbol{r}_n; \boldsymbol{s}_m)$ has the decomposition $\boldsymbol{G}(\boldsymbol{r}_n; \boldsymbol{s}_m) = \boldsymbol{G}^S(\boldsymbol{r}_n; \boldsymbol{s}_m) +$

$\boldsymbol{G}^P(\boldsymbol{r}_n;\boldsymbol{s}_m)$. Hence the representative function $U_{kq}(\boldsymbol{r};\boldsymbol{s})$ can be decomposed as the following

$$U_{kq}(\boldsymbol{r};\boldsymbol{s}) = U^S_{kq}(\boldsymbol{r};\boldsymbol{s}) + U^P_{kq}(\boldsymbol{r};\boldsymbol{s}) = A^S_{kq}(\boldsymbol{r};\boldsymbol{s})e^{i\omega\tau^S(\boldsymbol{r};\boldsymbol{s})} + A^P_{kq}(\boldsymbol{r};\boldsymbol{s})e^{i\omega\tau^P(\boldsymbol{r};\boldsymbol{s})} \tag{4.65}$$

where the amplitude $A^S_{kq}(\boldsymbol{r};\boldsymbol{s})$ and the traveltime $\tau^S(\boldsymbol{r};\boldsymbol{s})$ for S-wave are available from (4.58) and (4.59). $A^P_{kq}(\boldsymbol{r};\boldsymbol{s})$ and $\tau^P(\boldsymbol{r};\boldsymbol{s})$ for P-wave can be obtained in the same way. Then it is clear that we have

$$g_{kj}(\boldsymbol{r}) = g^S_{kj}(\boldsymbol{r}) + g^P_{kj}(\boldsymbol{r}) \tag{4.66}$$

with

$$g^S_{kj}(\boldsymbol{r}) = \sum_{q=1}^{8}\sum_{\boldsymbol{s}\in\boldsymbol{X}_s} U^S_{kq}(\boldsymbol{r};\boldsymbol{s})f_{qj}(\boldsymbol{s}), \quad g^P_{kj}(\boldsymbol{r}) = \sum_{q=1}^{8}\sum_{\boldsymbol{s}\in\boldsymbol{X}_s} U^P_{kq}(\boldsymbol{r};\boldsymbol{s})f_{qj}(\boldsymbol{s}) \tag{4.67}$$

Based on such decomposition (4.65), we can follow the work in [11, 50, 56] to adopt the low-rank-separation−based butterfly algorithm to speed up the matrix-vector multiplication for both g^S_{kj} and g^P_{kj}. In implementation, we can first use the butterfly algorithm to compute g^S_{kj} and then g^P_{kj}. Next, we can add g^S_{kj} and g^P_{kj} together to obtain g_{kj}. For the sake of convenience, we will no longer use the superscripts S and P since the following methodology works the same for computing g^S_{kj} and g^P_{kj}.

To begin with, we first introduce the multi-dimensional Lagrange basis with respect to Chebyshev nodes. For a given integer $p > 0$, the Chebyshev nodes of order p on [-1,1] are

defined as

$$X = \left\{ x_j = \cos\left(\frac{(j-1)\pi}{p-1} \right) \right\}_{j=1}^{p}. \tag{4.68}$$

The jth Lagrange basis function at $x \in [-1,1]$ with nodes X is denoted as $L_X(x; x_j)$ which takes 1 at x_j and 0 else where in X, for $j = 1, \cdots, p$. Then the Chebyshev nodes of order p on d-dimensional box $[-1,1]^d$ are d tensor products of X as

$$X^d = \{x_{j_1}^1\}_{j_1=1}^p \times \cdots \times \{x_{j_d}^d\}_{j_d=1}^p. \tag{4.69}$$

Thus, the $\boldsymbol{j}$th , $\boldsymbol{j} = (j_1, \cdots, j_d)$, Lagrange basis function with nodes X^d at $\boldsymbol{x} = (x^1, \cdots, x^d)^T \in [-1,1]^d$ is given as a tensor product

$$L_{X^d}^d(\boldsymbol{x}; \boldsymbol{x_j}) = L_X(x^1; x_{j_1}^1) \cdots L_X(x^d; x_{j_d}^d), \tag{4.70}$$

where $\boldsymbol{x_j} = (x_{j_1}^1, \cdots, x_{j_d}^1)^T$.

For general one-dimensional interval $[a,b]$, the Chebyshev nodes of order p satisfy

$$Y = \left\{ y_j = \frac{b-a}{a} x_j + \frac{b+a}{2} \right\}_{j=1}^{p}, \tag{4.71}$$

Hence the jth Lagrange basis function at $y \in [a,b]$ with nodes Y is denoted as $L_Y(y; y_j)$, for $j = 1, \cdots, p$. Similarly, the Chebyshev nodes of order p are d tensor products

$$\boldsymbol{Y} = Y_1 \times \cdots \times Y_d \tag{4.72}$$

with

$$Y_i = \left\{ y_{j_i}^i = \frac{b-a}{a} x_{j_i}^i + \frac{b+a}{2} \right\}_{j_i=1}^{p}. \tag{4.73}$$

Thus, the $\boldsymbol{j}$th Lagrange basis function with nodes at $\boldsymbol{y} = (y^1, \cdots, y^d)^T \in [-1,1]^d$ is given as

$$L_{\boldsymbol{Y}}^d(\boldsymbol{y}; \boldsymbol{y}_{\boldsymbol{j}}) = L_{Y_1}(y^1; y_{j_1}^1) \cdots \times L_{Y_d}(y^d; y_{j_d}^d). \tag{4.74}$$

In the following, we will denote by $\boldsymbol{C}^B$ the set of p^d d-dimensional Chebyshev nodes in a d-dimensional box B. Following closely the butterfly algorithm in [50, 56], we present algorithm as follows.

1. **Construct** the cluster trees for both receivers and sources. Assume that the domain of receivers is a cube $\Omega_r = [\mathcal{L}_{min}^r, \mathcal{L}_{max}^r]^3$, and the domain of sources is a square $\Omega_s = [\mathcal{L}_{min}^s, \mathcal{L}_{max}^s]^2$. The domain is discretized such that the number of sampling points per wavelength is fixed, such as 4 to 6 points per wavelength. The cluster tree for receivers and sources are an octree and a quadtree, respectively.

   At the loot level (denote as level 0), the boxes for both the source and receiver cluster trees are assigned to the corresponding domain directly. Then the tree construction goes by dyadically subdividing the boxes: for an octree (quadtree), each box is divided into 8 (4) boxes. The construction reaches or stops at leaf level (denote as level L) where the size of each box is about 2 minimum wavelengths so that approximately $O(p)$ sampling points are used along each dimension with p the order of Chebyshev nodes. Hence except for the leaf level, each box B of an octree (quadtree) has 8(4)

children boxes, denoted as B^c, and except for the root level, each box B has a parent box, denoted as B^p. We denote the resulting two trees as T_s (the source tree) and T_r (the receiver tree), respectively. From now on, we will use the superscript $(\cdot)^B$ to denote the dependence on the box B.

The butterfly algorithm traverses through the two cluster trees in the following way: for $l = L \cdots, 0$, visit level l in T_s and level $L-l$ in T_r by considering each pair $\{B_r, B_s\}$ with $B_r \in T^r$ and $B_s \in T^s$, $l(B_s) = l$ and $l(B^r) = L - l$, where $l(B)$ indicates the level of B in a tree.

Moreover at the root level of receiver and at the leaf level of source, each pair $\{B_r, B_s\}$ satisfies

$$\mathrm{w}(B_r)\mathrm{w}(B_s) = (\mathcal{L}^r_{\max} - \mathcal{L}^r_{\min})O(2\lambda_{\min}) = O\left(\frac{4\pi(\mathcal{L}^r_{\max} - \mathcal{L}^r_{\min})}{\omega\gamma_{\max}}\right) = O\left(\frac{1}{\omega}\right), \tag{4.75}$$

where $\mathrm{w}(B)$ is the size of box B and $\gamma_{\max} = \max(\gamma^S_{\max}, \gamma^P_{\max})$. $\gamma^S_{\max}$ and $\gamma^P_{\max}$ are the maximum refraction indexes for S-wave and P-wave, respectively. As moving downward the receiver tree by one level and simultaneously moving upward the source tree by one level, $\mathrm{w}(B_r)$ is divided by 2 while $\mathrm{w}(B_s)$ is multiplied by 2 so that $\mathrm{w}(B_r)\mathrm{w}(B_s) = O(\frac{1}{\omega})$ is automatically satisfied.

2. The **Upward Pass** starts at the leaf level (level L) of the source tree T_s and ends at the level (denoted as L_s) where the size of the boxes $\mathrm{w}(B_s) \geq O(\frac{1}{\sqrt{\omega}})$. Correspondingly, the level of the receiver tree T_r varies from root level (level 0) to the level $L_r \equiv L - L_s$.

   (1) **Initialization:** For each pair $\{B_r, B_s\}$ with B_r traversing all boxes at the root

level of the receiver tree and B_s traversing all boxes at the leaf level of the source tree, interpolate 24 equivalent densities $\{\bar{f}_{qj}^{B_r,B_s}\}$ for $1 \le q \le 8$ and $1 \le j \le 3$ at the equivalent sources $\boldsymbol{C}^{B_s} = \{\boldsymbol{s}_n^{B_s}\}_{n=1}^{p^2}$ in B_s from the given 24 densities $\{f_{qj}\}$ at all sources in $B_s \cap \boldsymbol{X}_s$:

$$\bar{f}_{qj}^{B_r,B_s}(\boldsymbol{s}_n^{B_s}) = \sum_{\boldsymbol{s} \in B_s \cap \boldsymbol{X}_s} e^{-i\omega\tau(\boldsymbol{r}_c^{B_r};\boldsymbol{s}_n^{B_s})} L^2_{\boldsymbol{C}^{B_s}}(\boldsymbol{s};\boldsymbol{s}_n^{B_s}) e^{i\omega\tau(\boldsymbol{r}_c^{B_r};\boldsymbol{s})} f_{qj}(\boldsymbol{s}), \quad (4.76)$$

where $\boldsymbol{r}_c^{B_r}$ is the center of the receiver box B_r.

(2) For l from $L-1$ to L_s, for each pair $\{B_r, B_s\}$ with B_r traversing all boxes at the level $L-l$ of the receiver tree and B_s traversing all boxes at the level l of the source tree, interpolate 24 equivalent densities $\{\bar{f}_{qj}^{B_r,B_s}\}$ at the equivalent sources $\boldsymbol{C}^{B_s} = \{\boldsymbol{s}_n^{B_s}\}_{n=1}^{p^2}$ in B_s from the equivalent densities $\{\bar{f}_{qj}^{B_r^p,B_s^c}\}$ at equivalent sources $\boldsymbol{C}^{B_s^c} = \{\boldsymbol{s}_m^{B_s^c}\}_{m=1}^{p^2}$ of all the children cluster of B_s and the parent cluster of B_r:

$$\bar{f}_{qj}^{B_r,B_s}(\boldsymbol{s}_n^{B_s}) = \sum_{B_s^c} \sum_{m=1}^{P^2} e^{-i\omega\tau(\boldsymbol{r}_c^{B_r};\boldsymbol{s}_n^{B_s})} L^2_{\boldsymbol{C}^{B_s}}(\boldsymbol{s}_m^{B_s^c};\boldsymbol{s}_n^{B_s}) e^{i\omega\tau(\boldsymbol{r}_c^{B_r};\boldsymbol{s}_m^{B_s^c})} \bar{f}_{qj}^{B_r^p,B_s^c}(\boldsymbol{s}_m^{B_s^c}), \quad (4.77)$$

for $1 \le q \le 8$ and $1 \le j \le 3$.

3. **Switch** at the level where the upward pass has ended (Level L_s of the source tree and level L_r of the receiver tree). For each pair $\{B_r, B_s\}$ with B_r traversing all boxes at the level L_r of the receiver tree and B_s traversing all boxes at the level L_s of the source tree, compute 9 equivalent fields $\{\bar{g}_{kj}^{B_r,B_s}\}$ at equivalent points $\boldsymbol{C}^{B_r} = \{\boldsymbol{r}_m^{B_r}\}_{m=1}^{p^3}$ from

equivalent densities $\{\bar{f}_{qj}^{B_r,B_s}\}$ at equivalent sources $\boldsymbol{C}^{B_s} = \{\boldsymbol{s}_n^{B_s}\}_{n=1}^{p^2}$:

$$\bar{g}_{qj}^{B_r,B_s}(\boldsymbol{r}_m^{B_s}) = \sum_{q=1}^{8}\sum_{n=1}^{P^2} U_{kq}(\boldsymbol{r}_m^{B_r}, \boldsymbol{s}_n^{B_s})\bar{f}_{qj}^{B_r,B_s}(\boldsymbol{s}_n^{B_s}), \tag{4.78}$$

for $1 \le k, j \le 3$.

4. The **Downward Pass** starts at the level L_r of the receiver tree T_r where the **Upward Pass** has ended and ends at level L of the receiver tree. Meanwhile, the level of the source tree varies from L_s to 0.

   (1) For l from L_r to $L-2$, for each pair $\{B_r, B_s\}$ with B_r traversing all boxes at the level $l+1$ of the receiver tree and B_s traversing all boxes at the level $L-l-1$ of the source tree, interpolate the equivalent fields $\{\bar{g}_{kj}^{B_r,B_s}\}$ at the equivalent sources $\boldsymbol{C}^{B_r} = \{\boldsymbol{r}_m^{B_r}\}_{m=1}^{p^3}$ from the equivalent densities $\{\bar{g}_{kj}^{B_r^p,B_s^c}\}$ at equivalent sources $\boldsymbol{C}^{B_r^p} = \{\boldsymbol{r}_n^{B_r^p}\}_{n=1}^{p^3}$ of all the children cluster of B_s and the parent cluster of B_r:

$$\bar{g}_{kj}^{B_r,B_s}(\boldsymbol{r}_m^{B_r}) = \sum_{B_s^c}\sum_{n=1}^{P^3} e^{i\omega\tau(\boldsymbol{r}_m^{B_r};\boldsymbol{s}_c^{B_s^c})} L_{\boldsymbol{C}^{B_r}}(\boldsymbol{r}_m^{B_r};\boldsymbol{r}_n^{B_r^p}) e^{-i\omega\tau(\boldsymbol{r}_n^{B_r^p};\boldsymbol{s}_c^{B_s^c})} \bar{g}_{kj}^{B_r^p,B_s^c}(\boldsymbol{r}_n^{B_r^p}), \tag{4.79}$$

   for $1 \le k, j \le 3$, where $\boldsymbol{s}_c^{B_s^c}$ is the center of the receiver box B_s^c.

   (2) For each pair $\{B_r, B_s\}$ with B_r traversing all boxes at the leaf level of the receiver tree and B_s traversing all boxes at the root level of the source tree, interpolate equivalent fields $\{\bar{g}_{kj}^{B_r,B_s}\}$ at $\boldsymbol{r} \in B_r \cap \boldsymbol{X}_r$ from the equivalent fields $\{\bar{g}_{kj}^{B_r^p,B_s^c}\}$ at equivalent sources $\boldsymbol{C}^{B_r^p} = \{\boldsymbol{r}_n^{B_r^p}\}_{n=1}^{p^3}$ of all the children level 1 of source tree and

the parent level $L-1$ of receiver tree:

$$\bar{g}_{kj}^{B_r,B_s}(\boldsymbol{r}) = \sum_{B_s^c} \sum_{n=1}^{P^3} e^{i\omega\tau(\boldsymbol{r};\boldsymbol{s}_c^{B_s^c})} L_{C^{B_r}}(\boldsymbol{r};\boldsymbol{r}_n^{B_r^p}) e^{-i\omega\tau(\boldsymbol{r}_n^{B_r^p};\boldsymbol{s}_c^{B_s^c})} \bar{g}_{kj}^{B_r^p,B_s^c}(\boldsymbol{r}_n^{B_r^p}), \tag{4.80}$$

for $1 \le k, j \le 3$.

5. **Termination.** For each box B_r at the leaf level of the receiver tree, sum up the equivalent fields over all the boxes of the source tree at the root level, and according to equation (4.63) compute the representative function g_{kj} at $\boldsymbol{r} \in B_r \cap \boldsymbol{X}_r$:

$$g_{kj}(\boldsymbol{r}) = \sum_{B_s} \bar{g}_{kj}^{B_r,B_s}(\boldsymbol{r}), \tag{4.81}$$

for $1 \le k, j \le 3$.

To analyze the complexity of the butterfly algorithm, we follow closely the complexity analysis of the that in [50, 56]. Assume that p Chebyshev nodes are chosen in each dimension and also $O(n) = O(2^L)$ points are sampled in each dimension. Then the total complexity of Algorithm 2 is

$$O(24p^4n^{5/2} + 72p^5n^{5/2} + 9p^4n^3 + n^3\log n).$$

4.2.7 Complexity analysis of the overall algorithm

In above section, we see that the overall algorithm consists of two stages. The first stage is preprocessing in which the asymptotic ingredients: traveltimes, dyadic coefficients, and take-off directions for both the S-wave and P-wave, are computed and they are further

encoded into a set of tables of Chebyshev coefficients. The second stage is postprocessing in which globally valid Green's functions are constructed for a given primary source $\boldsymbol{r}_0$ and an arbitrary frequency ω. The two stages can be done on different meshes and are independent of each other, hence we can analyze the computational complexities of the two stages separately.

In the following analysis, we will assume that the computational domain is partitioned into $P+1$ layers and P secondary-source planes are set up. In the layer containing the primary source, we just need to compute the asymptotic ingredients once. Hence we focus on analyzing the computational complexity of layers in which we need to compute the asymptotic ingredients for all the secondary sources on the secondary-source plane and carry out the matrix-vector products.

4.2.7.1 Preprocessing: computing asymptotic ingredients

Noticing that the asymptotic ingredients are independent of the frequency ω, we can compute them on very coarse meshes. Moreover, these ingredients are not only continuous functions away from the source but also continuous functions of the source itself. Therefore, interpolation not only can be used later to generate asymptotic ingredients on a finer mesh of observation points, but also can be applied to compute asymptotic ingredients for densely sampled secondary sources.

Assuming that the computational domain in three dimension is uniformly and coarsely discretized by m^3 grid point, which amounts to m sampling points in each dimension. Since the computational domain is partitioned into $P+1$ layers, there are roughly $O(\frac{m^3}{P+1})$ for each layer. And for each plane of P secondary source planes, m^2 source points are evenly sampled. Then for each secondary source on that plane, we have to compute the asymptotic

ingredients in the corresponding layer. According to [50, 56], we can apply higher-order Lax−Friedriches sweeping method to compute the asymptotic ingredients for both the S-wave and P-wave. Thus the computational cost for those asymptotic ingredients at each secondary source is $O(\frac{m^3}{P+1}\log m)$. Totally, there are P secondary source planes with m^2 sampled points on each plane. Therefore, the overall computational complexity at the whole m^2P secondary sources is

$$O\left(\frac{m^3}{P+1}\log m \cdot m^2 P\right) = O(m^5 \log m).$$

Although, the computational complexity seems to be high, these computed asymptotic ingredients can be stored and reused for different frequencies and different primary sources. And in fact, it is this feature that makes our method appealing to many applications. Also, the asymptotic ingredients for each secondary source are independent of each other, we can use MPI in C code to compute different groups of secondary sources simultaneously.

On the other hand, to construct the Greens' functions, the whole computational domain is uniformly discretized by n points in each direction. Thus, we need to recover the tables of asymptotic ingredients on roughly $O(\frac{n^3}{P+1})$ points in each layer for some specified secondary sources. And this requires complexity of $O(\frac{n^3}{P+1})$ for each layer and each secondary source; see details in [50].

4.2.7.2 Postprocessing: constructing global Green's functions

Given a primary source $\boldsymbol{r}_0$ and a frequency parameter ω, a fine mesh is required to capture the highly oscillatory Green's functions. To estimate the mesh points in each direction, first we need to approximate the minimum wavelength for both S-wave and P-wave by the given

refractive indexes and frequency so that the total number of waves can be estimated. Then we need to sample 4-6 points per wave in order to capture the oscillations. Certainly, it does not hurt to take more points per wavelength. Hence the number of mesh points can be chosen to satisfy the above consideration, and it is assumed to be $N = n^3$ with n points in each direction. Correspondingly, the number of points on each secondary source plane can be chosen to be roughly n^2 with n points in each direction.

Once those asymptotic ingredients are available on this specified mesh inside each layer, the Green's functions can be constructed by the butterfly algorithm. Given the accuracy $\epsilon > 0$, according to [11], we may choose $p = p_\epsilon < O(\log^2(\frac{1}{\epsilon}))$ for the order of one-dimension Chebyshev nodes in the butterfly algorithm so that the algorithm for computing the summation achieves the accuracy ϵ in $O(\frac{N}{P+1}\log N)$ in each layer, where the prefactor depends only on ϵ and is independent of ω. Therefore, the overall complexity of constructing the Green's function is by the butterfly algorithm in P layers is $O(\frac{P}{P+1}N\log N) = O(N\log N)$ for a given primary source and a given frequency. To speed up the construction, we use the 'build-in' parfor (parallel for) loop in our MATLAB implementation, see details in [56].

4.3 Numerical examples

In the following examples, we first compute the asymptotic ingredients: traveltimes, amplitudes, and take-off directions for both S-wave and P-wave in the domain near the primary source on a coarse mesh. When the corresponding mesh is used for computing the asymptotic ingredients at secondary sources, this coarse mesh will be restricted to a neighborhood of each secondary source. Then the ingredients are compressed into tables represented as Chebyshev coefficients. Thus for all numerical experiments, the asymptotic ingredients are

given as the compressed data, and they are recovered onto the finer mesh by the Chebyshev partial summation when needed. The computational domain is discretized into mesh points with roughly 5 points per wavelength in each direction.

Unless otherwise stated, all computations were executed in a 20-core Intel Xeon processor with 377 Gbytes of RAM, associated with a bi-processor Intel Xeon Gold 6148 node, at High performance computing center (HPCC) of MSU. The stage 1 was implemented in C codes to obtain all the tables of the asymptotic ingredients which were computed parallelly using MPI for all secondary sources. While the stage 2 was constructed in MATLAB codes and the butterfly algorithm was carried out in parallel in 10 cores via parallel computing toolbox in MATLAB.

When the elastic parameters are not constants, the exact solutions of the Green's functions are not available. To validate the sweeping method, we obtain reference solutions by applying the FDTD method [72] directly on the time-domain elastic wave equations. However, due to the limited computing resources, we are only able to compute the FDTD-based solutions at low frequencies, so that the comparison will be only carried out for low frequencies.

4.3.1 Example 1: Constant model

In this example, we take $\rho = 1$, $\lambda = 1$, and $\mu = 1$. The computational setup for our asymptotic method is the following:

- The computational domain is $[0, 2] \times [0, 2] \times [0, 2]$.
- The coarse mesh size is $51 \times 51 \times 51$ with grid size $h = 0.04$.
- The source point is $(1.0, 1.0, 0.2)^T$.

- The computational domain is partitioned as follows: the first layer containing the primary source is $\Omega_1 = [0,2] \times [0,2] \times [0,1.4]$; one secondary source plane is placed at $z = 1.2$ and we coarsely sample 51×51 equally spaced secondary sources on truncated source domain $S_1 = [0,2] \times [0,2] \times \{z = 1.2\}$; then the corresponding receiver domain is $\Omega_2 = [0,2] \times [0,2] \times [1.4,2]$, which is $d_f = 0.2$ wide away from the secondary source plane S_1.

In this example, since all elastic parameters are constants, we use the exact solutions to check the accuracy of our numerical solutions. The data tables of the asymptotic ingredients are computed in C codes. Since the asymptotic ingredients for each source are independent of each other, we can compute these data tables for many sources efficiently by using MPI. Once the data tables are available, we construct the Green's functions in the second layer by using the butterfly algorithm in MATLAB which can be computed parallelly.

Five points per wavelength are chosen in the construction stage to capture the highly oscillatory wave in the butterfly algorithm. In Table 4.1, we compute the L_∞ error between the numerical solutions of our method, denoted as $\boldsymbol{G}_{num}$, and the exact solutions, denoted as $\boldsymbol{G}_{exa}$ for the total nine elements of $\boldsymbol{G}(\boldsymbol{r};\boldsymbol{r}_0)$ in Ω_2

$$E_\infty = ||\boldsymbol{G}_{num} - \boldsymbol{G}_{exa}||_\infty. \tag{4.82}$$

The error was obtained for different frequency Ω and different Chebyshev nodes p used in each dimension. Our numerical solutions meets the expected accuracy $O(1/\omega)$. Table 4.2 records the running times of the butterfly-algorithm based Huygens-Kirchhoff summation for computing all nine elements of $\boldsymbol{G}(\boldsymbol{r};\boldsymbol{r}_0)$ in Ω_2. The computational time meets the computational complexity $O(N \log N)$ analyzed before, where N is the number of the mesh

points in Ω_2.

Mesh in Ω_2	$31 \times 31 \times 11$	$61 \times 61 \times 21$	$121 \times 121 \times 41$	$241 \times 241 \times 81$
ω	6π	12π	24π	48π
NPW	5	5	5	5
$E_\infty(p = 9)$	3.18E-2	2.87E-2	3.46E-2	5.34E-2
$E_\infty(p = 11)$	3.18E-2	2.52E-2	1.48E-2	2.75E-2
$E_\infty(p = 13)$	3.19E-2	2.47E-2	1.18E-2	9.1E-3

Table 4.1: Example 1 for the constant parameters. L_∞-norm errors between the numerical solutions of fast Huygens sweeping method and exact solutions. ω: the frequency parameter; NPW: the number of points per wavelength; p: the Chebyshev nodes used in each dimension; E_∞: the L_∞-norm errors between solutions by two different approaches.

Mesh in Ω_2	$31 \times 31 \times 11$	$61 \times 61 \times 21$	$121 \times 121 \times 41$	$241 \times 241 \times 81$
ω	6π	12π	24π	48π
NPW	5	5	5	5
$T_M(p = 9)$	57.71	129.35	551.73	3393.2
$T_M(p = 11)$	74.36	195.0	927.02	5452.7
$T_M(p = 13)$	75.47	219.62	1414.6	8206.6

Table 4.2: Example 1 for the constant parameters. Computational time using the butterfly algorithm. ω: the frequency parameter; NPW: the number of points per wavelength; T_M (unit: s): CPU time for the construction of total nine elements of the Green's function for the S-wave in the receiver domain Ω_2 by the butterfly algorithm; p: the Chebyshev nodes used in each dimension; E_∞: the L_∞-norm errors between solutions by two different approaches.

Figures 4.3, 4.4 and 4.5 show the comparison between the numerical solutions of Huygens sweeping method with Chebyshev order $p = 13$ and the exact solution at frequency $\omega = 24\pi$. We can see that our solutions are consistent with the exact solutions.

4.3.2 Example 2: A Gaussian model

We take $\lambda = 1$ and $\mu = 1$ but variable ρ:

$$\rho = 9.0/(3.0 - 1.75e^{-\frac{(x-1)^2+(y-1)^2+(z-1)^2}{0.64}})^2.$$

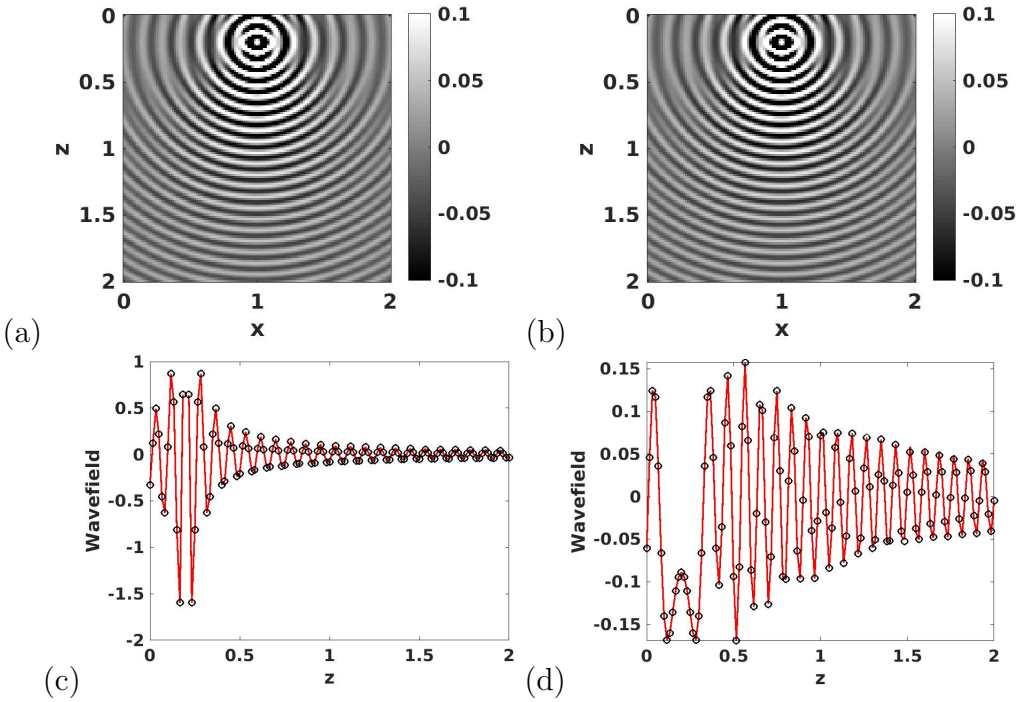

Figure 4.3: Example 1 with $\boldsymbol{r}_0 = (1.0, 1.0, 0.2)^T$ and $\omega = 24\pi$. The real part of xx-component of $\boldsymbol{G}(\boldsymbol{r}; \boldsymbol{r}_0)$ at $y = 1.0$ computed via (a) butterfly-algorithm−based Huygens sweeping method with $p = 13$; (b) exact solution. The detailed comparison of the real part of xx-component of $\boldsymbol{G}(\boldsymbol{r}; \boldsymbol{r}_0)$ at (c): line x=1.0, y=1.0 and (d): line x =0.8, y=1.0. Red solid line: exact solution; Black circle: Huygens sweeping solution. Mesh $121 \times 121 \times 121$.

In this case, the exact solution is not available, so we compute the FDTD-based solutions as the reference solutions to check the accuracy of our method.

The computational setup for our asymptotic methods is as follows:

- The computational domain is $\Omega = [0, 2] \times [0, 2] \times [0, 2]$.
- The coarse mesh size is $51 \times 51 \times 51$ with grid size $h = 0.04$.
- The source point is $(1.0, 1.0, 0.2)^T$.
- The computational domain is partitioned as follows: the first layer containing the primary source is $\Omega_1 = [0, 2] \times [0, 2] \times [0, 1.4]$; one secondary source plane is placed at $z = 1.2$ and we coarsely sample 51×51 equally spaced secondary sources on truncated

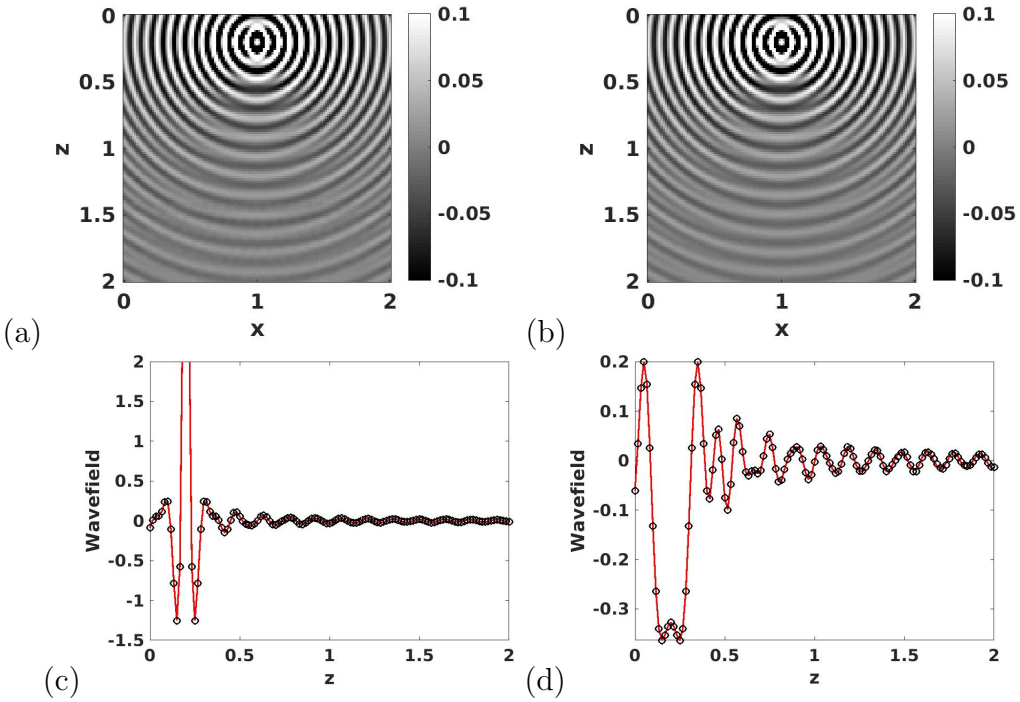

Figure 4.4: Example 1 with $\boldsymbol{r}_0 = (1.0, 1.0, 0.2)^T$ and $\omega = 24\pi$. The real part of zz-component of $\boldsymbol{G}(\boldsymbol{r}; \boldsymbol{r}_0)$ at $y = 1.0$ computed via (a) butterfly-algorithm−based Huygens sweeping method with $p = 13$; (b) exact solution. The detailed comparison of the real part of zz-component of $\boldsymbol{G}(\boldsymbol{r}; \boldsymbol{r}_0)$ at (c): line x=1.0, y=1.0 and (d): line x =0.8, y=1.0. Red solid line: exact solution; Black circle: Huygens sweeping solution. Mesh $121 \times 121 \times 121$.

source domain $S_1 = [0, 2] \times [0, 2] \times \{z = 1.2\}$; then the corresponding receiver domain is $\Omega_2 = [0, 2] \times [0, 2] \times [1.4, 2]$, which is $d_f = 0.2$ wide away from the secondary source plane S_1.

We use roughly 5 points per wavelength in the construction stage. Table 4.3 records the running time for constructing the Green's functions $\boldsymbol{G}(\boldsymbol{r}, \boldsymbol{r}_0)$ in Ω_2 using the fast Huygen's sweeping method. Different Chebyshev nodes are used in each dimension.We can see that as the mesh points are doubled in each dimension, the running time increases by about six times.

Figure 4.6 shows the comparison of the numerical solutions of the real part of xx-component of Green's function computed by two different methods: butterfly-algorithm

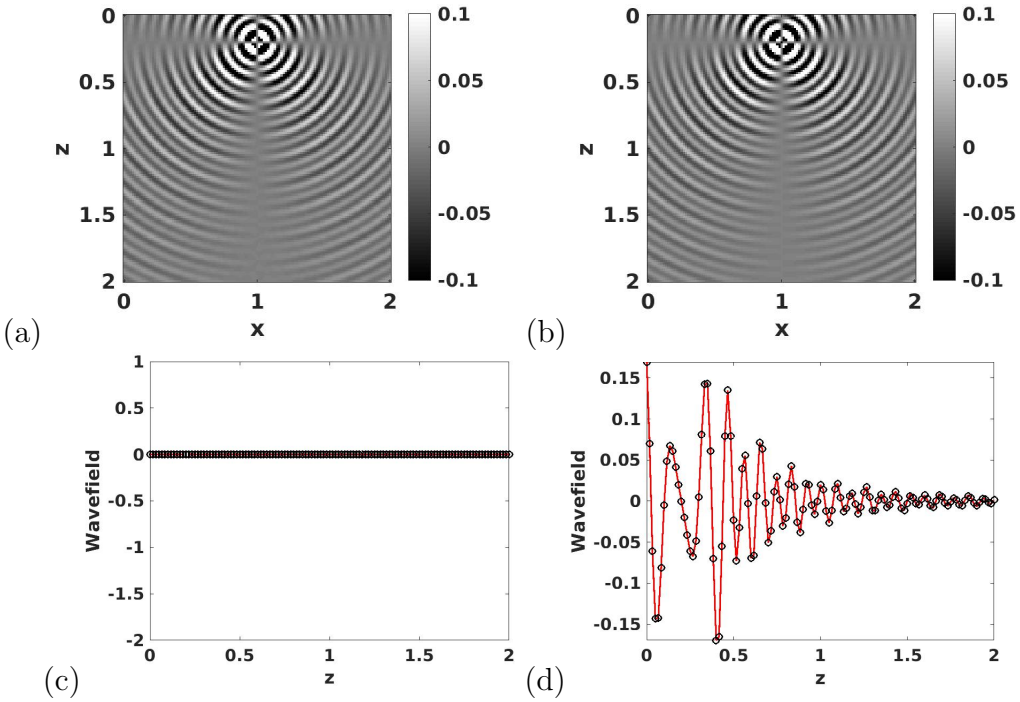

Figure 4.5: Example 1 with $\boldsymbol{r}_0 = (1.0, 1.0, 0.2)^T$ and $\omega = 24\pi$. The real part of xz-component of $\boldsymbol{G}(\boldsymbol{r}; \boldsymbol{r}_0)$ at $y = 1.0$ computed via (a) butterfly-algorithm−based Huygens sweeping method with $p = 13$; (b) exact solution. The detailed comparison of the real part of xz-component of $\boldsymbol{G}(\boldsymbol{r}; \boldsymbol{r}_0)$ at (c): line x=1.0, y=1.0 and (d): line x =0.8, y=1.0. Red solid line: exact solution; Black circle: Huygens sweeping solution. Mesh $121 \times 121 \times 121$.

based Huygens sweeping method with order $p = 13$, and the FDTD method at frequency $\omega = 10\pi$. The comparison of the numerical solutions for zz- components of the Green's functions by these two methods are shown in Figure 4.7.

In addition, we construct the Green's functions at $\omega = 20\pi$ as shown in Figure 4.8 by using fast Huygens sweeping method while the FDTD method requires finer meshes which makes it impossible to compute the solutions.

Mesh in Ω_2	$61 \times 61 \times 21$	$121 \times 121 \times 41$	$241 \times 241 \times 81$	$337 \times 337 \times 105$
ω	5π	10π	20π	$80/3\pi$
NPW	5	5	5	5
$T_M(p=9)$	176.89	649.35	3716.7	4058.7
$T_M(p=11)$	264.23	1205.3	6168.0	7460.5
$T_M(p=13)$	220.84	1369.0	7931.5	8174.2

Table 4.3: Example 2 for the Gaussian model. Computational time using the butterfly algorithm. ω: the frequency parameter; NPW: the number of points per wavelength; T_M (unit: s): CPU time for the construction of total nine elements of the Green's function for the S-wave in the receiver domain Ω_2 by the butterfly algorithm; p: the Chebyshev nodes used in each dimension; E_∞: the L_∞-norm errors between solutions by two different approaches.

4.3.3 Example 3: A Gaussian model

We take $\rho = 9$ but variable λ and μ. Here we set $\lambda = \mu$ and

$$\mu = (3.0 - 1.75e^{-\frac{(x-1.0)^2+(y-1)^2+(z-1)^2}{0.64}})^2.$$

In this example, we compute the FDTD-based solution to check the accuracy of our method.

The computational setup for our asymptotic method is as the following:

- The computational domain is $\Omega = [0,2] \times [0,2] \times [0,2]$.
- The coarse mesh size is $51 \times 51 \times 51$ with grid size $h = 0.04$.
- The source point is $(0.8, 1.0, 0.2)^T$.
- The computational domain is partitioned as follows: the first layer containing the primary source is $\Omega_1 = [0,2] \times [0,2] \times [0,1.4]$; one secondary source plane is placed at $z = 1.2$ and we coarsely sample 51×51 equally spaced secondary sources on truncated source domain $S_1 = [0,2] \times [0,2] \times \{z = 1.2\}$; then the corresponding receiver domain is $\Omega_2 = [0,2] \times [0,2] \times [1.4,2]$, which is $d_f = 0.2$ wide away from the secondary source plane S_1.

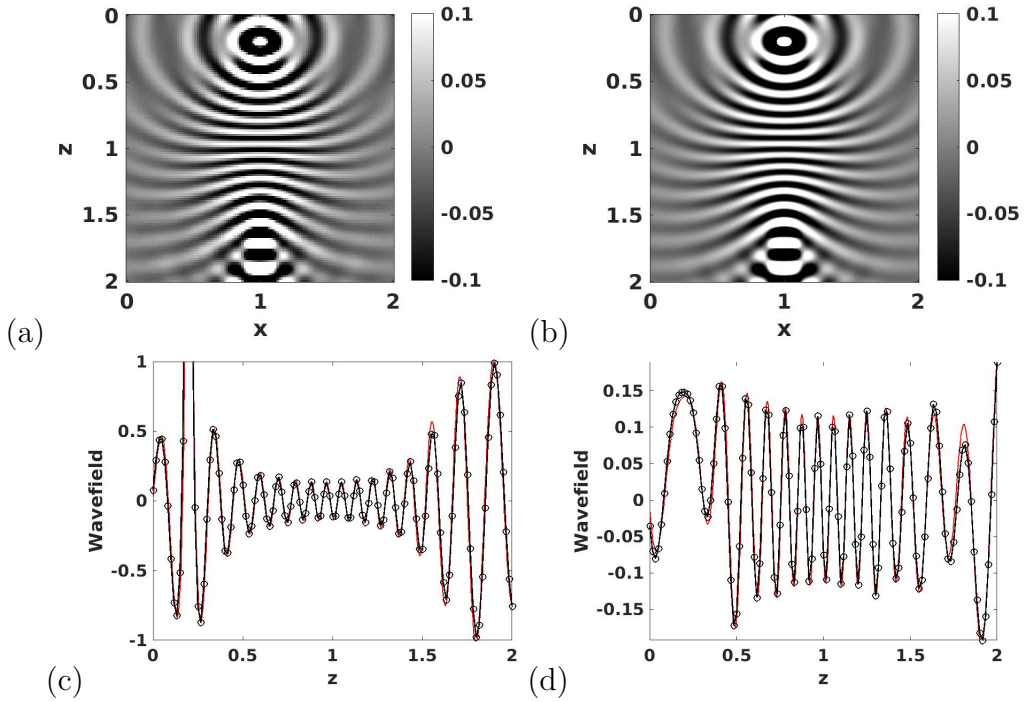

Figure 4.6: Example 2 with $\boldsymbol{r}_0 = (1.0, 1.0, 0.2)^T$ and $\omega = 10\pi$. The real part of xx-component of $\boldsymbol{G}(\boldsymbol{r}; \boldsymbol{r}_0)$ at $y = 1.0$ computed via (a) the Huygens sweeping method with $p = 13$; (b) FDTD method. The detailed comparison of the real part of xx-component of $\boldsymbol{G}(\boldsymbol{r}; \boldsymbol{r}_0)$ at (c): line x=1.0, y=1.0 and (d): line x =0.8, y=1.0. Red solid line: FDTD solution; Black circled line: solution of the Huygens sweeping method. Mesh in (a): $121 \times 121 \times 121$; mesh in (b): $401 \times 401 \times 401$.

We use four points per wavelength to capture the wave in butterfly algorithm. Figure 4.9, 4.10, and 4.11 shows the comparison of the numerical solutions of the real part of xx-, zz-, and xz- components of the Green's functions computed by two different methods: the Huygens sweeping method with order $p = 13$, and the FDTD method at frequency $\omega = 12\pi$. The numerical solutions of the Huygens sweeping method are consistent with the FDTD solutions.

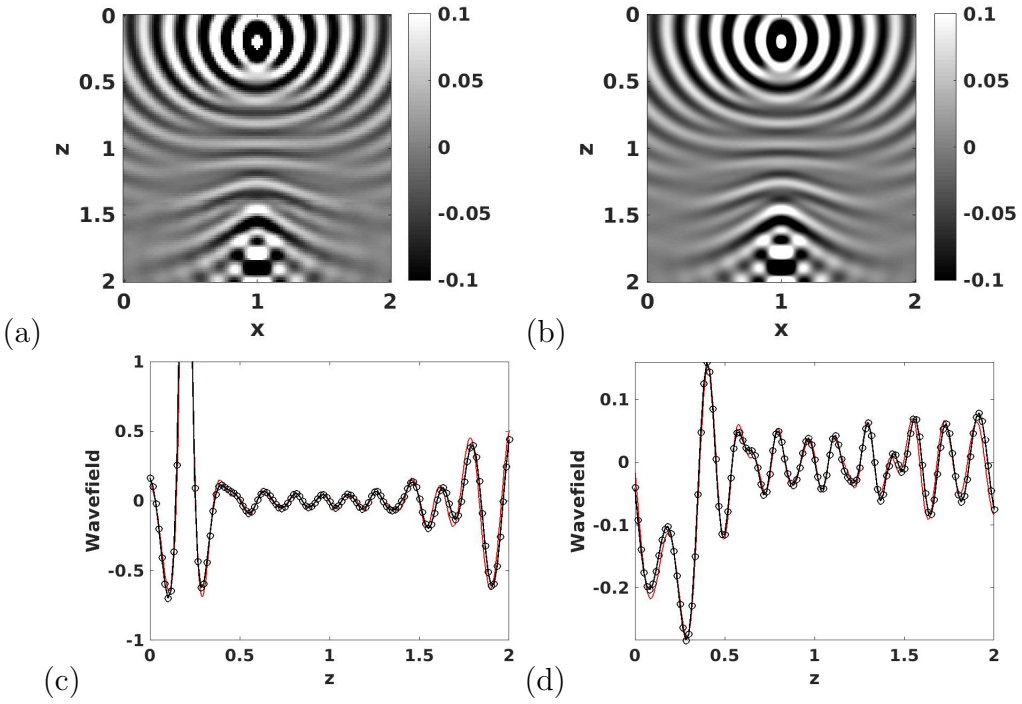

Figure 4.7: Example 2 with $\boldsymbol{r}_0 = (1.0, 1.0, 0.2)^T$ and $\omega = 10\pi$. The real part of zz-component of $\boldsymbol{G}(\boldsymbol{r}; \boldsymbol{r}_0)$ at $y = 1.0$ computed via (a) the Huygens sweeping method with $p = 13$; (b) FDTD solution. The detailed comparison of the real part of zz-component of $\boldsymbol{G}(\boldsymbol{r}; \boldsymbol{r}_0)$ at (c): line x=1.0, y=1.0 and (d): line x =0.8, y=1.0. Red solid line: FDTD solution; Black circled line: solution of the Huygens sweeping method. Mesh in (a): $121 \times 121 \times 121$; mesh in (b): $401 \times 401 \times 401$.

4.3.4 Example 4: A waveguide model

We take $\rho = 1$ but variable λ and μ. Here we set $\lambda = \mu$ and

$$\mu = \left(1.0 - 0.5e^{-6((x-1)^2+(y-1)^2)}\right)^2.$$

In this example, we have the following setup:

- The computational domain is $\Omega = [0, 2] \times [0, 2] \times [0, 1.6]$.
- The coarse mesh size is $51 \times 51 \times 41$ with grid size $h = 0.04$.
- The source point is $(1.0, 1.0, 0.2)^T$ or $(0.8, 1.0, 0.12)^T$.

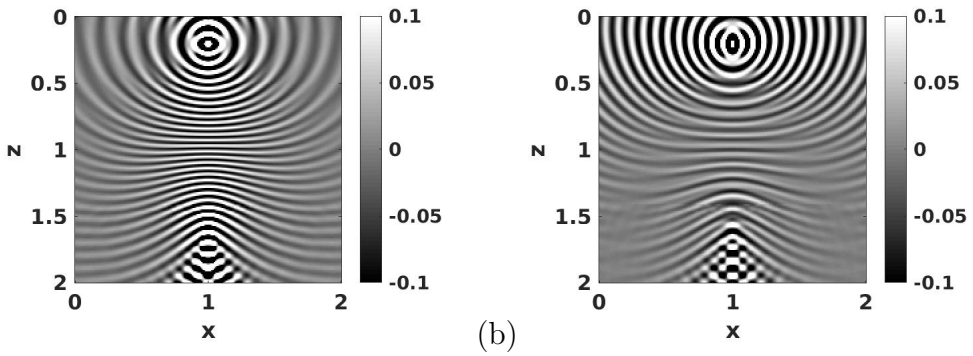

(a) (b)

Figure 4.8: Example 2 with $\boldsymbol{r}_0 = (1.0, 1.0, 0.2)^T$ and $\omega = 20\pi$. The real part of (a): xx- and (b): zz- component of $\boldsymbol{G}(\boldsymbol{r}; \boldsymbol{r}_0)$ at $y = 1.0$ computed by the Huygens sweeping method with $p = 13$. Mesh $241 \times 241 \times 241$.

- The computational domain is partitioned as follows: the first layer containing the primary source is $\Omega_1 = [0, 2] \times [0, 2] \times [0, 0.8]$; two secondary source planes are placed at $z = 0.6$ and $z = 1.0$, and we coarsely sample 51×51 equally spaced secondary sources on truncated source domains $S_1 = [0, 2] \times [0, 2] \times \{z = 0.6\}$ and $S_2 = [0, 2] \times [0, 2] \times \{z = 1.0\}$; then the corresponding receiver domains are $\Omega_2 = [0, 2] \times [0, 2] \times [0.8, 1.2]$ and $\Omega_3 = [0, 2] \times [0, 2] \times [1.2, 1.6]$ which are $d_f = 0.2$ wide away from the secondary source planes S_1 and S_2, respectively.

The exact solution for this example is not available, so we use the FDTD method to obtain a reference solution. Approximately 5 points per wavelength is used in butterfly algorithm. First, we construct the numerical solutions of the Green's functions at the source $(1.0, 1.0, 0.2)^T$ and at frequency $\omega = 10\pi$ by the fast Huygens sweeping method with order $p = 13$. The comparison with FDTD method solutions of xx- and zz- components of the Green's functions are shown in Figures 4.12 and 4.13, respectively.

Next, we use the same data tables for all secondary sources to compute the Green's functions in the receiver domain Ω_2 and Ω_3 for a different source $(0.8, 1.0, 0.2)^T$ and different frequency $\omega = 12\pi$. The comparison between the solutions of our method and FDTD

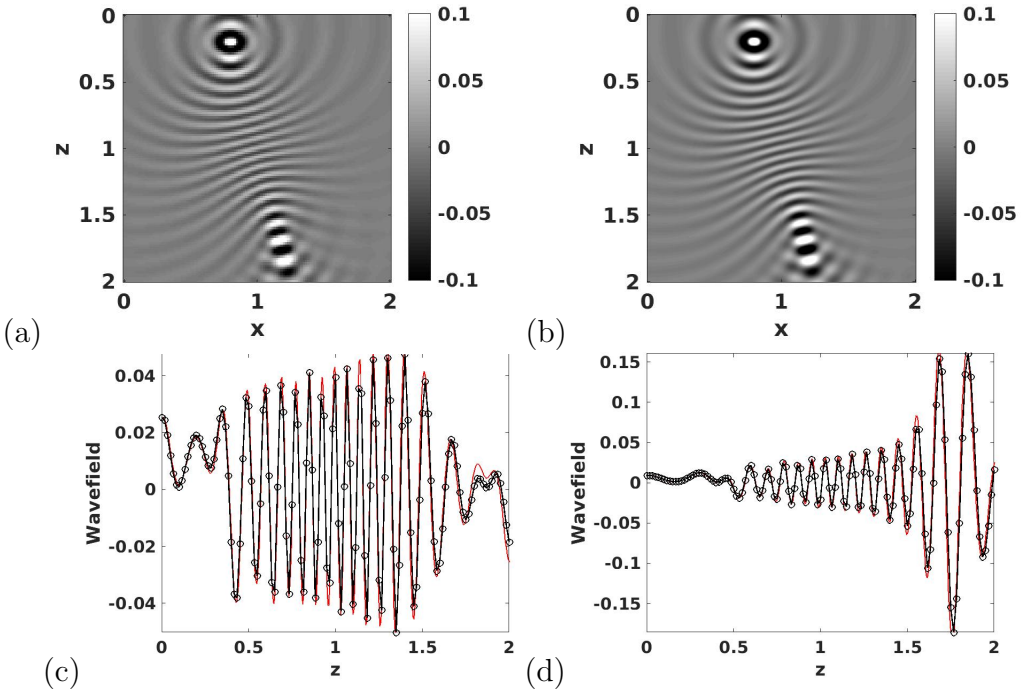

Figure 4.9: Example 3 with $\boldsymbol{r}_0 = (0.8, 1.0, 0.2)^T$ and $\omega = 12\pi$. The real part of xx-component of $\boldsymbol{G}(\boldsymbol{r}; \boldsymbol{r}_0)$ at $y = 1.0$ computed via (a) the Huygens sweeping method with $p = 13$; (b) FDTD method. The detailed comparison of the real part of xx-component of $\boldsymbol{G}(\boldsymbol{r}; \boldsymbol{r}_0)$ at (c): line x=1.0, y=1.0 and (d): line x =1.2, y=1.0. Red solid line: FDTD solution; Black circled line: solution of the Huygens sweeping method. Mesh in (a): $121 \times 121 \times 121$; mesh in (b): $401 \times 401 \times 401$.

solutions are given in Figure 4.14 and 4.15. The numerical solutions of our method are consistent with the FDTD solutions.

In addition, we construct the Green's functions at higher frequency $\omega = 20\pi$ as shown in Figure 4.8 by the Huygens sweeping method.

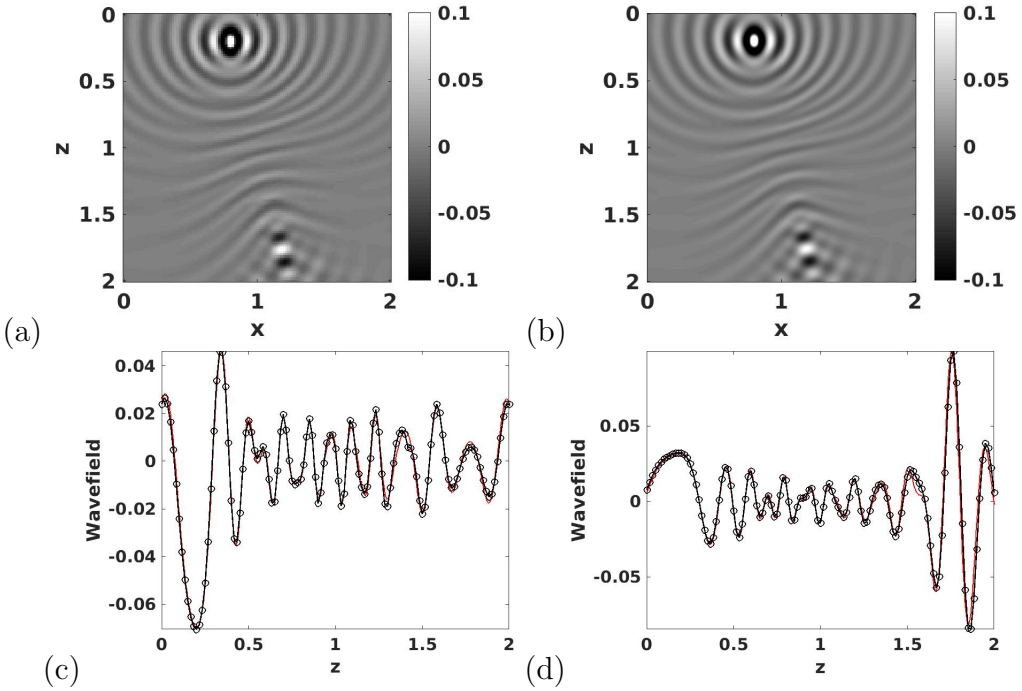

Figure 4.10: Example 3 with $\boldsymbol{r}_0 = (0.8, 1.0, 0.2)^T$ and $\omega = 12\pi$. The real part of zz-component of $\boldsymbol{G}(\boldsymbol{r}; \boldsymbol{r}_0)$ at $y = 1.0$ computed via (a) the Huygens sweeping method with $p = 13$; (b) FDTD method. The detailed comparison of the real part of zz-component of $\boldsymbol{G}(\boldsymbol{r}; \boldsymbol{r}_0)$ at (c): line x=1.0, y=1.0 and (d): line x =1.2, y=1.0. Red solid line: FDTD solution; Black circled line: solution of the Huygens sweeping method. Mesh in (a): $121 \times 121 \times 121$; mesh in (b): $401 \times 401 \times 401$.

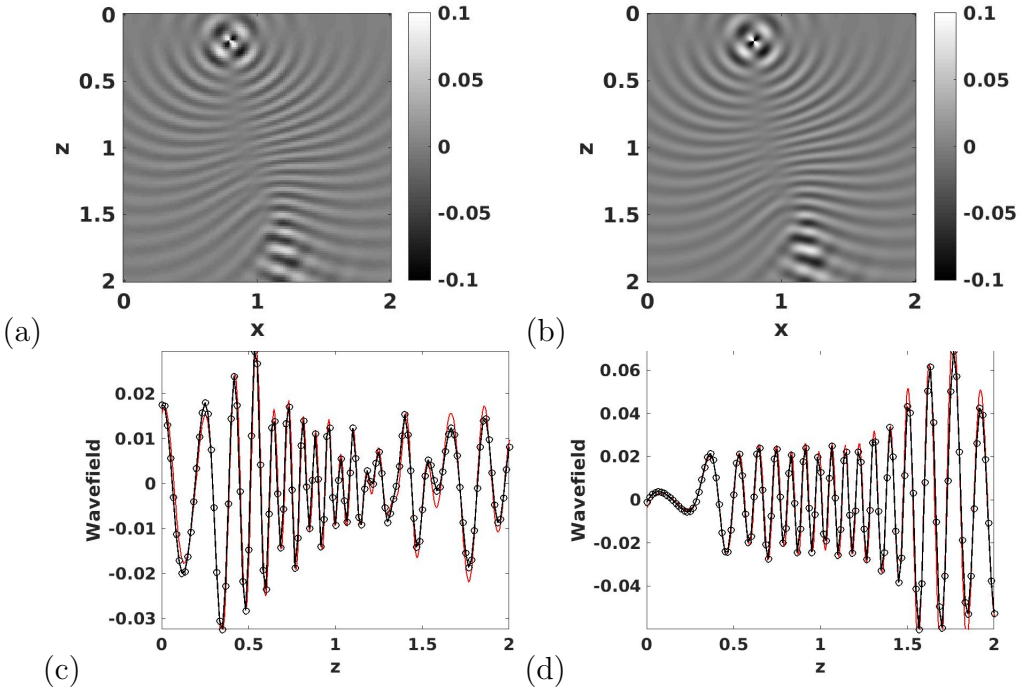

Figure 4.11: Example 3 with $\boldsymbol{r}_0 = (0.8, 1.0, 0.2)^T$ and $\omega = 12\pi$. The real part of xz-component of $\boldsymbol{G}(\boldsymbol{r}; \boldsymbol{r}_0)$ at $y = 1.0$ computed via (a) the Huygens sweeping method with $p = 13$; (b) FDTD method. The detailed comparison of the real part of xz-component of $\boldsymbol{G}(\boldsymbol{r}; \boldsymbol{r}_0)$ at (c): line x=1.0, y=1.0 and (d): line x =1.2, y=1.0. Red solid line: FDTD solution; Black circled line: solution of the Huygens sweeping method. Mesh in (a): $121 \times 121 \times 121$; mesh in (b):$401 \times 401 \times 401$.

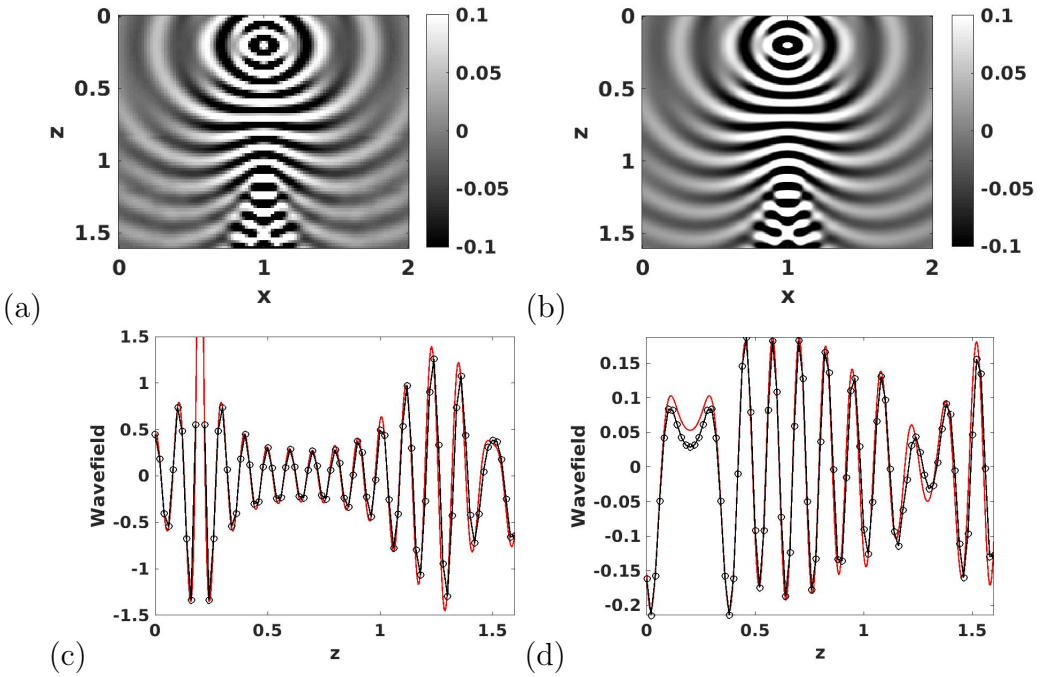

Figure 4.12: Example 4 with $\boldsymbol{r}_0 = (1.0, 1.0, 0.2)^T$ and $\omega = 10\pi$. The real part of xx-component of $\boldsymbol{G}(\boldsymbol{r}; \boldsymbol{r}_0)$ at $y = 1.0$ computed via (a) the Huygens sweeping method with $p = 13$; (b) FDTD method. The detailed comparison of the real part of xx-component of $\boldsymbol{G}(\boldsymbol{r}; \boldsymbol{r}_0)$ at (c): line x=1.0, y=1.0 and (d): line x =0.8, y=1.0. Red solid line: FDTD solution; Black circled line: solution of the Huygens sweeping method. Mesh in (a): $101 \times 101 \times 81$; mesh in (b): $401 \times 401 \times 321$.

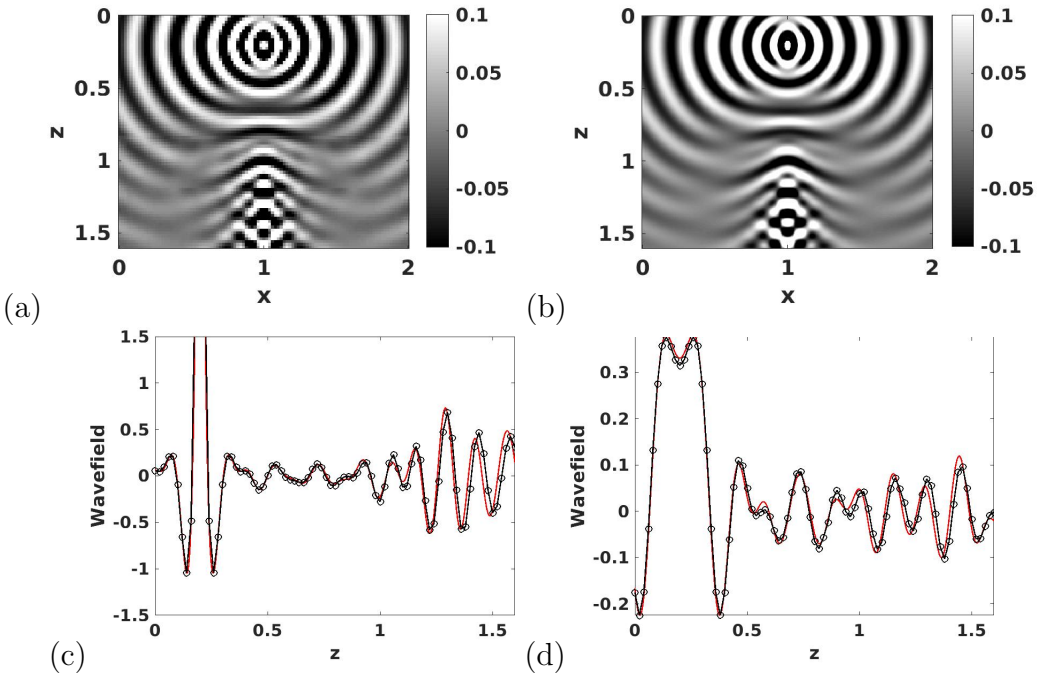

Figure 4.13: Example 4 with $\boldsymbol{r}_0 = (1.0, 1.0, 0.2)^T$ and $\omega = 10\pi$. The real part of zz-component of $\boldsymbol{G}(\boldsymbol{r}; \boldsymbol{r}_0)$ at $y = 1.0$ computed via (a) the Huygens sweeping method with $p = 13$; (b) FDTD method. The detailed comparison of the real part of zz-component of $\boldsymbol{G}(\boldsymbol{r}; \boldsymbol{r}_0)$ at (c): line x=1.0, y=1.0 an (d): line x =0.8, y=1.0. Red solid line: FDTD solution; Black circled line: solution of the Huygens sweeping method. Mesh in (a): $101 \times 101 \times 81$; mesh in (b): $401 \times 401 \times 321$.

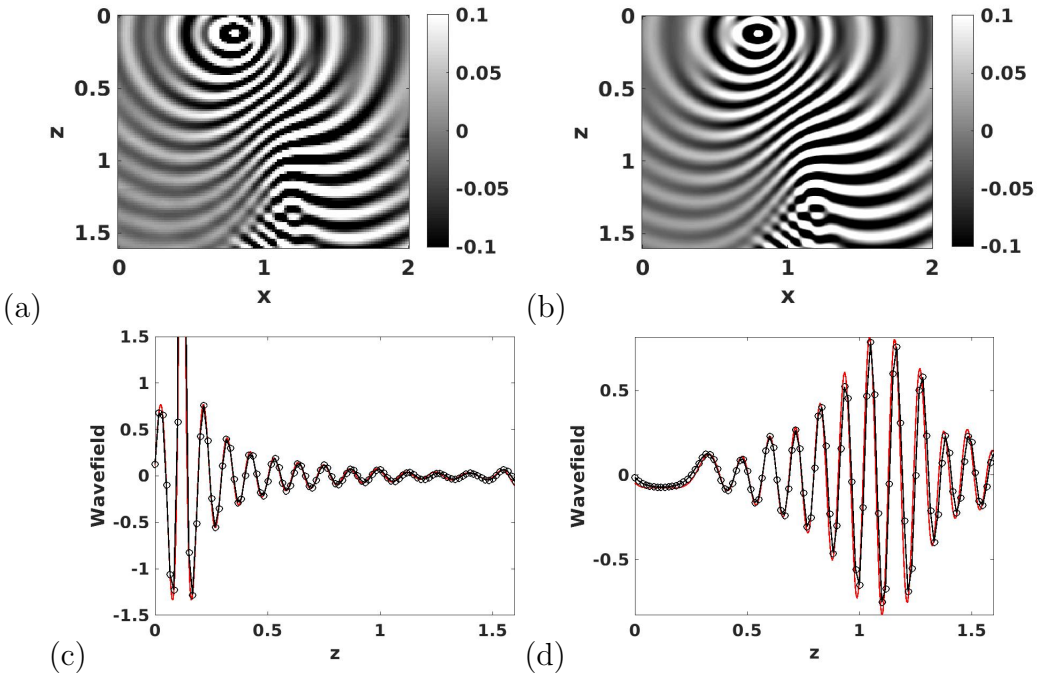

Figure 4.14: Example 4 with $\boldsymbol{r}_0 = (0.8, 1.0, 0.12)^T$ and $\omega = 12\pi$. The real part of xx-component of $\boldsymbol{G}(\boldsymbol{r}; \boldsymbol{r}_0)$ at $y = 1.0$ computed via (a) the Huygens sweeping method with $p = 13$; (b) FDTD method. The detailed comparison of the real part of xx-component of $\boldsymbol{G}(\boldsymbol{r}; \boldsymbol{r}_0)$ at (c): line x=0.8, y=1.0 and (d): line x =1.2, y=1.0. Red solid line: FDTD solution; Black circled line: solution of the Huygens sweeping method. Mesh in (a): $121 \times 121 \times 97$; mesh in (b): $401 \times 401 \times 321$.

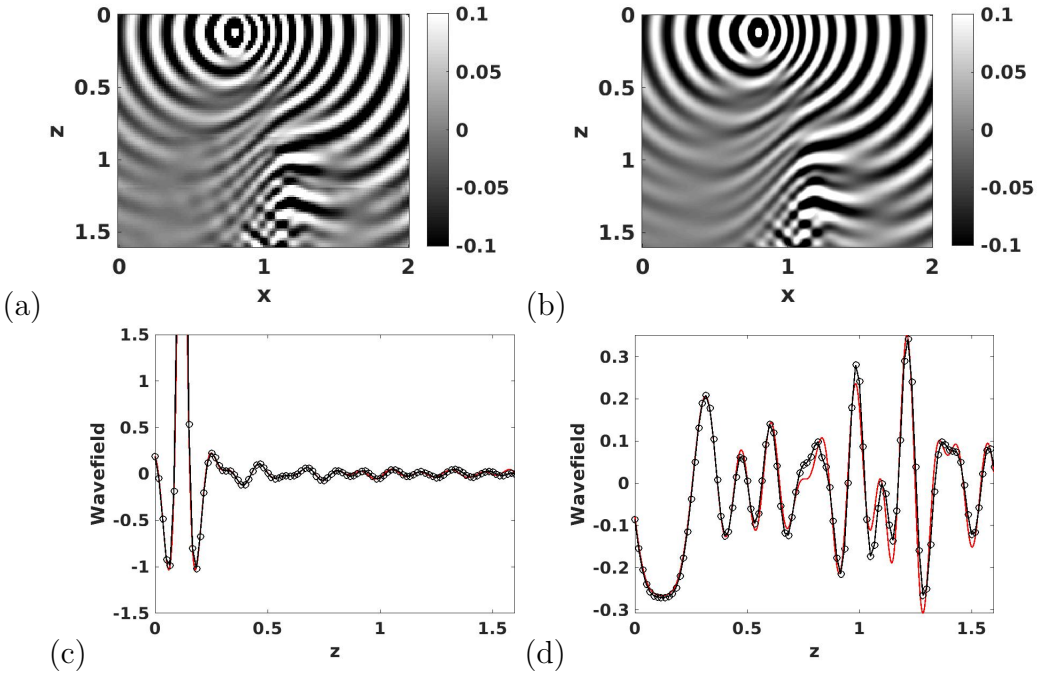

Figure 4.15: Example 4 with $\boldsymbol{r}_0 = (0.8, 1.0, 0.12)^T$ and $\omega = 12\pi$. The real part of zz-component of $\boldsymbol{G}(\boldsymbol{r}; \boldsymbol{r}_0)$ at $y = 1.0$ computed via (a) the Huygens sweeping method with $p = 13$; (b) FDTD method. The detailed comparison of the real part of zz-component of $\boldsymbol{G}(\boldsymbol{r}; \boldsymbol{r}_0)$ at (c): line x=0.8, y=1.0 an (d): line x =1.2, y=1.0. Red solid line: FDTD solution; Black circled line: solution of the Huygens sweeping method. Mesh in (a): $121 \times 121 \times 97$; mesh in (b): $401 \times 401 \times 321$.

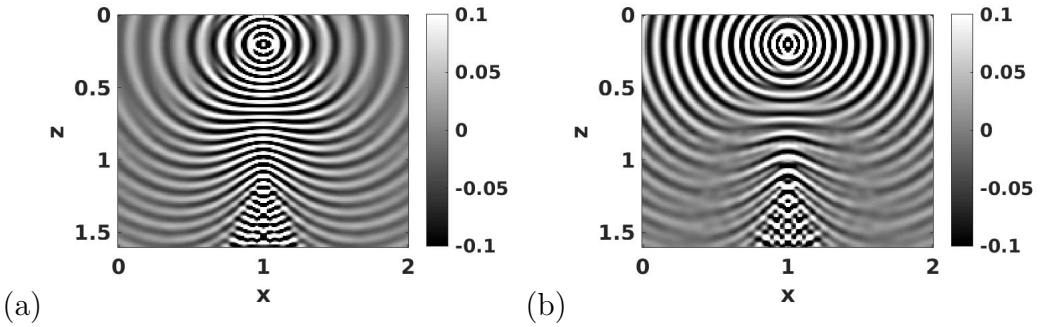

Figure 4.16: Example 4 with $\boldsymbol{r}_0 = (1.0, 1.0, 0.2)^T$ and $\omega = 20\pi$. The real part of (a): xx- and (b): zz- component of $\boldsymbol{G}(\boldsymbol{r}; \boldsymbol{r}_0)$ at $y = 1.0$ computed by the Huygens sweeping method with $p = 13$. Mesh $201 \times 201 \times 161$.

Chapter 5

Eulerian partial-differential-equation methods for complex-valued eikonals in attenuating media

This chapter is based on a modified version of the published work in [27]. We propose a unified framework to eulerianize several popular real-space Lagrangian ray-tracing methods so that we can develop efficient Eulerian partial-differential-equation methods for computing complex-valued eikonals, where the real and imaginary parts of the eikonal function describe wave propagation and attenuation effects, respectively. We first introduce the methodologies for computing the complex-valued traveltimes. Then, we apply the proposed algorithm to several attenuation models to demonstrate the performance and accuracy of the method.

5.1 High-order numerical methods for computing complex-valued traveltimes

5.1.1 Eulerian PDE framework for complex-valued traveltimes

The correspondence principle indicates that we can treat wave propagation in a viscoelastic (or viscoacoustic) medium as wave propagation through an elastic (or acoustic) medium with complex-valued elastic parameters (or a complex-valued velocity). To model wave motion in such a medium efficiently, high-frequency asymptotic approximations provide an effective alternative to direct numerical methods. One of the essential ingredients for high-frequency asymptotics of viscous wave motion is the complex-valued eikonal function. We propose a unified Eulerian framework to compute complex-valued eikonal functions for several popular high-frequency asymptotic models of viscous wave motions.

We assume that the complex-valued eikonal function τ consists of the real part T and the imaginary part T^* which satisfy the following eikonal and advection equation, respectively,

$$|\nabla T| = \frac{1}{v(\mathbf{x})}, \quad T(\mathbf{x}_s) = 0, \tag{5.1}$$

$$\nabla T \cdot \nabla T^* = \frac{1}{v^2(\mathbf{x})Q(\mathbf{x})}, \quad T^*(\mathbf{x}_s) = 0, \tag{5.2}$$

where $\mathbf{x}$ is the real-valued position vector, $v(\mathbf{x})$ is the real-valued reference velocity, and $Q(\mathbf{x})$ is a quality-factor related real-valued function.

Assuming that there is a unique ray connecting any source to any receiver, we put three popular asymptotic models into our framework. As we can see, provided that we choose an appropriate reference velocity and an appropriate quality-factor related function, our

framework is applicable to both weakly and strongly attenuating media.

5.1.2 Case (1): Viscoacoustic ray tracing and Eulerian equations

Wave motion in a viscoacoustic medium can be characterized as wave propagation through an acoustic medium with a complex-valued velocity. The complex-valued velocity is given in terms of the real acoustic velocity c_0 and the quality factor q, the latter representing the attenuation. If the attenuation is small ($q^{-1} << 1$, the weakly attenuating approximation), then an appropriate definition of the complex-valued velocity c is,

$$c(\boldsymbol{x}) = c_0(\boldsymbol{x}) \left[1 + \frac{1}{2} \frac{i}{q(\boldsymbol{x})} + \frac{1}{\pi} \ln \left(\frac{\omega}{\omega_0} \right) \right], \tag{5.3}$$

where ω is the angular frequency, ω_0 is a reference angular frequency, and the dispersive term in the real part of the velocity ensures causality of solutions to the wave equation [1].

If $q^{-1} << 1$, then to the first-order approximation in q^{-1}, the ray paths defined in the high-frequency approximation by the real acoustic velocity c_0 can be considered to be unaffected by attenuation and remain unchanged during the viscoacoustic wave motion, but the traveltime function becomes complex-valued and frequency-dependent due to the attenuation effect, which takes the following form by the Futterman's dispersion relation [22, 23, 16, 36],

$$T_c(\mathbf{x}) = T(\mathbf{x}) - \frac{1}{\pi} T^*(\mathbf{x}) \ln \left(\frac{\omega}{\omega_0} \right) - i \frac{T^*(\mathbf{x})}{2}, \tag{5.4}$$

where

$$T(\mathbf{x}) = \int_{ray} \frac{1}{c_0(\mathbf{x})} ds, \tag{5.5}$$

$$T^*(\mathbf{x}) = \int_{ray} \frac{1}{c_0(\mathbf{x}) q(\mathbf{x})} ds. \tag{5.6}$$

Here T is the traveltime in acoustic media from the source $\mathbf{x_s}$ to $\mathbf{x}$, and it satisfies the following eikonal equation,

$$|\nabla T(\mathbf{x})| = \frac{1}{c_0(\mathbf{x})}; \tag{5.7}$$

the arc-length integrations in equations (5.5) and (5.6) are over the same ray path connecting the source $\mathbf{x_s}$ to $\mathbf{x}$ defined by the real acoustic velocity c_0. The ray path can be either determined by the Fermat principle or implicitly defined by solving the eikonal equation (5.7). Since the directional derivative along the ray path defined by equation (5.7) is [45],

$$\frac{\partial}{\partial s} = c_0(\mathbf{x}) \nabla T(\mathbf{x}) \cdot \nabla, \tag{5.8}$$

we can take the directional derivative along the ray path on both sides of equation (5.6) to have the following advection equation for T^*,

$$\nabla T(\mathbf{x}) \cdot \nabla T^*(\mathbf{x}) = \frac{1}{c_0^2(\mathbf{x}) q(\mathbf{x})}. \tag{5.9}$$

This corresponds to our case that $v(\mathbf{x}) = c_0(\mathbf{x})$ and $Q(\mathbf{x}) = q(\mathbf{x})$ in equations (5.1) and (5.2).

5.1.3 Case (2): Real viscoelastic ray tracing and Eulerian equations

Wave motion in a viscoelastic medium can be described by a real-valued density ρ of the medium, complex-valued and frequency-dependent Lamé elastic coefficients λ and μ, and a real-valued angular frequency. The real parts, λ^R and μ^R, describe elastic properties of the medium, and the imaginary parts, λ^I and μ^I, describe attenuation. The velocities for P- and S- waves,

$$c_p = \sqrt{\frac{\lambda + 2\mu}{\rho}}, \qquad c_s = \sqrt{\frac{\mu}{\rho}}, \tag{5.10}$$

are complex-valued and frequency-dependent. The strength of attenuation is evaluated using the quality factor for P- and S- waves [14],

$$q_p = -\frac{\lambda^R + 2\mu^R}{\lambda^I + 2\mu^I} = -\frac{(c_p^2)^R}{(c_p^2)^I}, \qquad q_s = -\frac{\mu^R}{\mu^I} = -\frac{(c_s^2)^R}{(c_s^2)^I}. \tag{5.11}$$

[75, 76] proposed to solve the P- and S- wave complex-valued eikonal equations using real ray-tracing methods, and he derived such methods by modifying the Hamiltonians for viscoelastic media to keep rays as trajectories in real space. The resulting real viscoelastic ray tracing equations in isotropic media are [75],

$$\frac{d\mathbf{x}}{d\tau^R} = V^2\boldsymbol{p}, \quad \frac{d\boldsymbol{p}}{d\tau^R} = -\frac{1}{V}\nabla V, \quad \frac{d\tau^I}{d\tau^R} = -\frac{c^I}{c^R}, \tag{5.12}$$

where $\boldsymbol{p}$ is the slowness vector; τ^R and τ^I are the real and imaginary parts of the complex eikonal, respectively; c^R and c^I are the real and imaginary parts of the complex velocity, respectively; V is the real-valued ray velocity calculated from the complex-valued phase

velocity,

$$V = \frac{1}{(c^{-1})^R} = \frac{(c^R)^2 + (c^I)^2}{c^R}, \tag{5.13}$$

with $c = c_p$ or $c = c_s$ for the P- or S- wave, respectively.

The real part of the complex-valued eikonal, τ^R, of the ray tracing system in equation 5.12 satisfies the following eikonal equation,

$$|\nabla \tau^R| = \frac{1}{V(\mathbf{x})}. \tag{5.14}$$

The imaginary part of the complex-valued eikonal τ^I takes the following integration form,

$$\tau^I(\mathbf{x}) = \int_{ray} -\frac{c^I(\mathbf{x})}{V(\mathbf{x})c^R(\mathbf{x})} ds, \tag{5.15}$$

Similar to the viscoacoustic ray tracing case, using the directional derivative defined by equation (5.14) to take the directional derivative along the ray path on both sides of equation (5.15), we can have the following advection equation for the imaginary part of the complex-valued eikonal, τ^I,

$$\nabla \tau^R \cdot \nabla \tau^I = -\frac{c^I(\boldsymbol{x})}{V^2(\mathbf{x})c^R(\mathbf{x})}. \tag{5.16}$$

This corresponds to our case that $T = \tau^R$, $T^* = \tau^I$, $v(\mathbf{x}) = \mathbf{V}(\mathbf{x})$ and $Q(\mathbf{x}) = -\frac{\mathbf{c^R}(\mathbf{x})}{\mathbf{c^I}(\mathbf{x})}$ in equations (5.1) and (5.2).

5.1.4 Case (3): Real elastic ray tracing and Eulerian equations

In the real elastic ray-tracing theory, a viscoelastic medium is considered as the perturbation of a perfectly elastic medium so that the rays are traced in the elastic reference medium and

the effects of attenuation are calculated by first-order perturbations. The resulting real elastic ray-tracing equations are [16]

$$\frac{d\mathbf{x}}{d\tau^R} = V_0^2 \boldsymbol{p}, \quad \frac{d\boldsymbol{p}}{d\tau^R} = -\frac{1}{V_0}\nabla V_0, \quad \frac{d\tau^I}{d\tau^R} = \frac{1}{2q}, \tag{5.17}$$

where V_0 is the real-valued reference velocity in the reference elastic medium. [23] take the weakly attenuating approximation and ignore $(c^I)^2$ in equation (5.13), V_0 becomes

$$V_0 = c^R, \tag{5.18}$$

with $c^R = (c_p)^R$ and $q = q_p$ or $c^R = (c_s)^R$ and $q = q_s$ for the P- or S- wave, respectively.

Similar to the real viscoelastic ray tracing case, we can have the following eikonal and advection equations for the real part, τ^R, and the imaginary part, τ^I, of the complex-valued eikonal, respectively,

$$|\nabla \tau^R| = \frac{1}{V_0(\mathbf{x})}, \tag{5.19}$$

$$\nabla \tau^R \cdot \nabla \tau^I = \frac{1}{2q(\boldsymbol{x}) V_0^2(\mathbf{x})}. \tag{5.20}$$

This corresponds to our case that $T = \tau^R$, $T^* = \tau^I$, $v(\mathbf{x}) = \mathbf{V_0}(\mathbf{x})$ and $Q(\mathbf{x}) = \mathbf{2q}(\mathbf{x})$ in equations (5.1) and (5.2).

5.1.5 Factorized Eulerian PDEs

Finite-difference schemes to the point-source eikonal equation (5.1) is widely used [77, 73, 55, 67, 61], but without proper treatment of the point-source singularity, most of these schemes only yield low accuracy near the source point [61]. Such initial errors at the source will spread

out to the entire computational domain due to the upwind nature of these schemes [61]. Adaptive refinement near the source [61] and factorizing out the point-source singularity explicitly from the point-source eikonal [54, 85, 20, 48, 50, 45, 64] provide two effective strategies for treating this singularity. Moreover, comparing equation (5.2) to equation (5.1), we realize that the imaginary part of the complex eikonal shares a similar singularity with the real part of the complex eikonal so that we will apply the factorization idea as well to the advection equation to treat the source singularity.

We adopt a multiplicative factorization [54, 85, 20, 48, 45, 64] to the real part of the complex eikonal,

$$T(\mathbf{x}) = \tau_0(\mathbf{x})\tau_1(\mathbf{x}), \tag{5.21}$$

where τ_0 is the analytic traveltime function for a known homogeneous velocity model which captures the source singularity, and the unknown factor τ_1 is computed from a finite-difference scheme. The analytic factor τ_0 is taken to be,

$$\tau_0(\mathbf{x}) = \frac{|\mathbf{x} - \mathbf{x}_s|}{v_s}, \tag{5.22}$$

where v_s is the velocity at the source location, and this choice corresponds to the first-order factorization [64, 45]. Inserting equation 5.21 into equation (5.1), we obtain the factored eikonal equation,

$$\tau_0^2(\mathbf{x})|\nabla\tau_1(\mathbf{x})|^2 + 2\tau_0(\mathbf{x})\tau_1(\mathbf{x})\nabla\tau_0(\mathbf{x})\cdot\nabla\tau_1(\mathbf{x}) + \tau_1^2(\mathbf{x})|\nabla\tau_0(\mathbf{x})|^2 \;=\; \frac{1}{v^2(\mathbf{x})}. \tag{5.23}$$

Once the gradient of the real part of the complex eikonal, $\nabla T(\mathbf{x})$, is available, we can use it as coefficients in the advection equation to compute the imaginary part of the com-

plex eikonal. To treat the source singularity, we apply a multiplicative factorization to the imaginary part,

$$T^*(\mathbf{x}) = T(\mathbf{x})T_1^*(\mathbf{x}), \tag{5.24}$$

where T is the (just computed) real part of the complex eikonal capturing the source singularity, and the unknown perturbation factor T_1^* is computed by a finite-difference scheme. We remark in passing that, to capture the source singularity, we use T, which is solely related to the velocity, rather than Q, the reciprocal of which, Q^{-1}, may be zero near source; the reason is that the Q-based factorization may render T^* to be zero everywhere, which is ineffective. Following [64], we also derive the high order factorization in the Appendix. Here we use the first-order factorization. Inserting equation (5.24) into equation (5.2), we obtain the factored advection equation,

$$T(\mathbf{x})\nabla T(\mathbf{x}) \cdot \nabla T_1^*(\mathbf{x}) + T_1^*(\mathbf{x})(\nabla T(\mathbf{x}))^2 \;=\; \frac{1}{v^2(\mathbf{x})Q(\mathbf{x})}. \tag{5.25}$$

Once the factorized Eulerian PDEs are derived, we can design finite-difference schemes to solve these equations.

5.1.6 Third-order LxF-WENO sweeping method

We will apply a third-order LxF-WENO sweeping method [34, 87, 64] to solve the factored eikonal equation (5.23), where high-order WENO approximations [31, 64] are essential to the success of the sweeping scheme. The third-order WENO scheme will yield real parts of the complex eikonal with high-order accuracy so that the numerical gradient $\nabla T(\mathbf{x})$ is also of high-order accuracy. Once the high-order accurate real part of the complex eikonal

is obtained, we can use it as coefficients in the factored advection equation (5.25) so that a third-order LxF-WENO sweeping method can be applied to solve equation (5.25).

The LxF sweeping method [34, 87] offers a versatile and powerful approach for solving generic isotropic and anisotropic eikonal equations, such as quasi-P [60, 62] and quasi-S wave eikonal equations. To save space, we will only discuss 2-D discretizations of equation (5.25), and similar strategies apply to the discretization of equation (5.23) [64]. The extension to the 3-D case is not difficult. To apply the LxF sweeping scheme to equation (5.25), we rewrite the equation into the following form,

$$H(x, z, T_1^*, p_{1x}^*, p_{1z}^*) = f, \tag{5.26}$$

where $p_{1x}^* = \frac{\partial T_1^*}{\partial x}$, $p_{1z}^* = \frac{\partial T_1^*}{\partial z}$, and the functions H and f are defined by,

$$H(x, z, T_1^*, p_{1x}^*, p_{1z}^*) = T(\mathbf{x})\nabla T(\mathbf{x}) \cdot \nabla T_1^*(\mathbf{x}) + T_1^*(\mathbf{x})(\nabla T(\mathbf{x}))^2, \tag{5.27}$$

$$f = \frac{1}{v^2(\mathbf{x})Q(\mathbf{x})}. \tag{5.28}$$

The third-order LxF-WENO sweeping method for T_1^* is defined by the following steps.

(1) **Initialization.** The initialization is done by assigning values at a few grid points centered at the source point. In the Appendix, we provide a systematic high-order factorization for computing T_1^*. Here we use the first-order factorization to assign these values. These values are fixed during iterations.

(2) **Iterations.** Since T_1^* is computed by a third-order WENO scheme, we will use grid indexing (i.e., (i, j)) instead of spatial coordinates to demonstrate the iteration process. The LxF sweeping method computes T_1^* via Gauss-Seidel iteration with four alternating

directions,

1) $i = 1 : 1 : I$ and $j = 1 : 1 : J$; 2) $i = 1 : 1 : I$ and $j = J : -1 : 1$; 3) $i = I : -1 : 1$ and $j = 1 : 1 : J$; 4) $i = I : -1 : 1$ and $j = J : -1 : 1$,

where i and j are the indices for the x and z coordinate, respectively, and I and J are the total number of grid points in the x and z direction, respectively.

At a grid point (i, j), the Lax-Friedrichs Hamiltonian [53, 34] allows us to obtain a new value T_1^{*new} from old values T_1^{*old} in the following way,

$$\begin{aligned} T_1^{*new}(i,j) = & \left(\frac{1}{\frac{\alpha_x}{dx} + \frac{\alpha_z}{dz}}\right) \\ & \left(f(i,j) - H\left(i, j, T_1^{*old}(i,j), \frac{T_1^*(i+1,j) - T_1^*(i-1,j)}{2dx}, \frac{T_1^*(i,j+1) - T_1^*(i,j-1)}{2dz}\right)\right. \\ & \left. + \alpha_x \frac{T_1^*(i+1,j) + T_1^*(i-1,j)}{2dx} + \alpha_z \frac{T_1^*(i,j+1) + T_1^*(i,j-1)}{2dz}\right), \end{aligned} \tag{5.29}$$

where dx and dz are the grid sizes in the x and z direction, respectively, and α_x and α_z are artificial viscosities in the x and z direction, respectively. Following [87, 64, 45], we choose the following artificial viscosities,

$$\alpha_x = \max_{\Omega}\left(\left|\frac{\partial H}{\partial p_{1x}^*}\right| + \left|\frac{\partial H}{\partial T_1^*}\right|\right), \tag{5.30}$$

$$\alpha_z = \max_{\Omega}\left(\left|\frac{\partial H}{\partial p_{1z}^*}\right| + \left|\frac{\partial H}{\partial T_1^*}\right|\right), \tag{5.31}$$

where Ω is the entire computational domain. Following [87], we carry out the following replacement in equation 5.29 to introduce the third-order WENO approximation into the

sweeping iteration,

$$T_1^*(i+1,j) = T_1^{*old}(i,j) + dx(p_{1x}^*(i,j))^+, \tag{5.32}$$

$$T_1^*(i-1,j) = T_1^{*old}(i,j) - dx(p_{1x}^*(i,j))^-, \tag{5.33}$$

$$T_1^*(i,j+1) = T_1^{*old}(i,j) + dz(p_{1z}^*(i,j))^+, \tag{5.34}$$

$$T_1^*(i,j-1) = T_1^{*old}(i,j) - dz(p_{1z}^*(i,j))^-, \tag{5.35}$$

where $(p_{1x}^*(i,j))^+$ and $(p_{1x}^*(i,j))^-$ are third-order upwind WENO approximations of $p_{1x}^*(i,j)$, and $(p_{1z}^*(i,j))^+$ and $(p_{1z}^*(i,j))^-$ are third-order upwind WENO approximations of $p_{1z}^*(i,j)$ [31]. $(p_{1x}^*(i,j))^-$ and $(p_{1x}^*(i,j))^+$ are defined as the following,

$$\begin{aligned}(p_{1x}^*(i,j))^- =&(1-\beta_-)\left(\frac{T_1^*(i+1,j)-T_1^*(i-1,j)}{2dx}\right)+\\ &\beta_-\left(\frac{3T_1^{*old}(i,j)-4T_1^*(i-1,j)+T_1^*(i-2,j)}{2dx}\right),\end{aligned} \tag{5.36}$$

$$\beta_- = \frac{1}{1+2\gamma_-^2}, \quad \gamma_- = \frac{\varepsilon+(T_1^{*old}(i,j)-2T_1^*(i-1,j)+T_1^*(i-2,j))^2}{\varepsilon+(T_1^*(i+1,j)-2T_1^{*old}(i,j)+T_1^*(i-1,j))^2}, \tag{5.37}$$

$$\begin{aligned}(p_{1x}^*(i,j))^+ =&(1-\beta_+)\left(\frac{T_1^*(i+1,j)-T_1^*(i-1,j)}{2dx}\right)+\\ &\beta_+\left(\frac{-3T_1^{*old}(i,j)+4T_1^*(i+1,j)-T_1^*(i+2,j)}{2dx}\right),\end{aligned} \tag{5.38}$$

$$\beta_+ = \frac{1}{1+2\gamma_+^2}, \quad \gamma_+ = \frac{\varepsilon+(T_1^{*old}(i,j)-2T_1^*(i+1,j)+T_1^*(i+2,j))^2}{\varepsilon+(T_1^*(i+1,j)-2T_1^{*old}(i,j)+T_1^*(i-1,j))^2}; \tag{5.39}$$

similarly, we can define $(p_{1z}^*(i,j))^-$ and $(p_{1z}^*(i,j))^+$.

(3) **Convergence.** If the following condition is satisfied,

$$|T_1^{*new}(i,j) - T_1^{*old}(i,j)| \leq \delta, \tag{5.40}$$

the iteration converges and we terminate the iteration, where δ is a pre-defined threshold value.

Once T_1^* is computed, the imaginary part is available from equation 5.24. Comparing with a first-order scheme, a high-order scheme can yield corresponding numerical derivatives with high-order accuracy in the Eulerian PDEs. Therefore, to achieve a certain specified accuracy, a high-order scheme just need to use a much coarser mesh than a first-order scheme does [61, 50]; since the number of grid points is greatly reduced, the computational cost can be reduced [61, 50]. This consideration justifies our choice of using a high-order WENO scheme here.

5.2 Numerical examples

5.2.1 Eulerian examples for viscoacoustic ray tracing

To begin with, we apply our proposed algorithm to four cases of the viscoacoustic attenuating model, where the model is prescribed by a real-valued acoustic velocity and a real-valued quality factor.

For the first case, we choose a velocity v with a constant vertical gradient. The velocity model is specified by $v = 2000.0 + 0.5z$ (m/s). The Q model is homogeneous with $Q = 50$. Since [16] provides an analytic solution of the eikonal equation (5.1) for this constant-gradient velocity model, we may use this solution to validate our algorithm for the eikonal equation.

Moreover, since the Q model is homogeneous, the exact solution of the advection equation (5.2) can be obtained by dividing the exact traveltime by the Q value according to equations (5.5) and (5.6). The model dimension is 5km in depth and 5km laterally. One advantage of high-order WENO approximations is its high accuracy, which allows us to solve the eikonal and advection equations using large grid sizes. Therefore, we use a grid size of 50m in both x and z directions. The total number of grids is 101×101. We place a source at $x = 2500$m and $z = 0$m. Figures (5.1)a and (5.1)b show the computed real and imaginary parts of the complex eikonal for the first attenuating model, respectively. To validate their accuracies, we compare numerical solutions with corresponding analytic solutions, as shown in Figures (5.1)c and (5.1)d. The errors in the computed real part are of a magnitude of 10^{-6}, which is much smaller than a time sampling interval, such as 1ms of a typical seismic record. The errors in the imaginary part of the complex eikonal are of a magnitude of 10^{-7}, which also is quite accurate. This shows that the proposed method yields highly accurate complex eikonals under the weakly attenuating approximation for this case.

In the second case, the velocity model as shown in Figure (5.2)a is extracted from the BP TTI velocity model. We further construct a Q model according to the extracted velocity model: we fill the zone of low velocity in the shallow region with low Q values to simulate the gas cloud, and we set the Q value in other places to be 10000 (as shown in Figure (5.2)b). Note that in displaying Figure (5.2)b, we clip the maximum Q value to 100. The model dimension is 8km in depth and 10km laterally. The grid size is 50m in both x and z directions. The total number of grid points is 201×161. The source is located at $x = 5000$m and $z = 0$m. The proposed method is used to compute the real and imaginary parts of the complex eikonal, as shown in Figure (5.3). The imaginary part of the eikonal in Figure (5.3)b shows that only ray paths passing through the gas cloud suffer from dispersion and

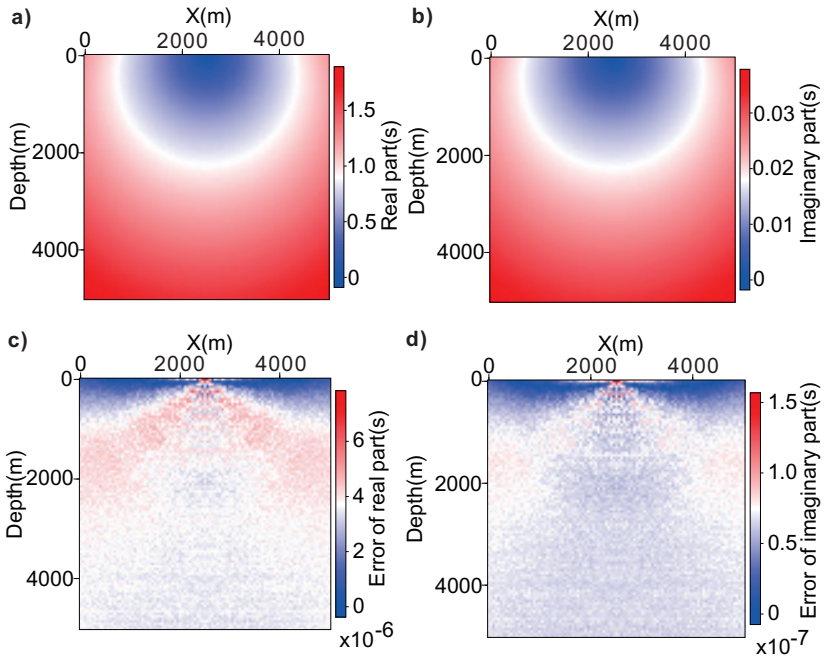

Figure 5.1: The real and imaginary parts of the complex-valued eikonal for the constant gradient velocity model. (a) Real part and (c) its difference with the analytic solution; (b) imaginary part and (d) its difference with the analytic solution under the weakly attenuating approximation.

absorption, where the maximum value of the imaginary part is about 5ms. This demonstrates the strong seismic attenuation below the gas cloud. Since in this inhomogeneous attenuating model we do not have an analytic solution to validate the result, we use the wavefield snapshot obtained by a finite-difference wavefield extrapolator to validate the real part of the complex eikonal. The wavefield snapshot is obtained on a grid with mesh size of 10m in both x and z directions. Figure (5.4) is the wavefield snapshot overlaid by the contour of the computed real part of the eikonal at 3s, where the red curve is the contour of the real part. Since the contour of the real part matches well with the first-arrival wavefront in the wavefield snapshot, this demonstrates that the real part of the eikonal is highly accurate, even though it is computed on a grid of relatively large mesh size. To validate the computed imaginary part, we carry out ray tracings with a fourth order Runge-Kutta ODE integrator to obtain imaginary parts along two ray paths, where two black curves shown in Figure (5.2)a pass

through the gas cloud. Here the ray tracing is performed on a fine grid with mesh size of 10m. We use a nonlinear interpolation method to obtain imaginary parts along these two ray paths from the result in Figure (5.3)b. The comparison between the imaginary parts obtained by the proposed method and the ray tracing method is shown in Figure (5.5), and the two results match well. This shows that the imaginary part obtained by the proposed method is highly accurate under the weakly attenuating approximation. In addition, Figure (5.5) also shows that the attenuation increases rapidly as seismic rays pass through the gas cloud.

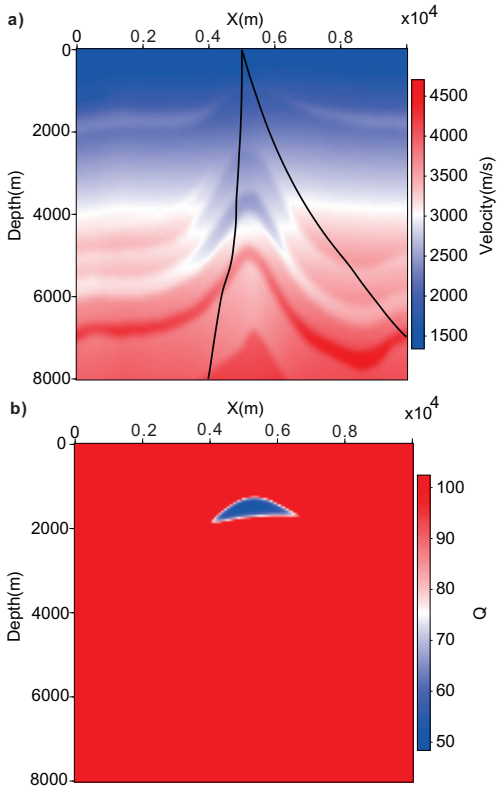

Figure 5.2: An attenuation model with gas cloud. (a) The acoustic velocity, (b) Q. Two black curves in (a) are two ray paths with takeoff angles being 0° and 20°.

In the third case, we build an attenuating model based on a land scenario, where the velocity and Q models are shown in Figure (5.6). In the Q model, the Q value is very low in the shallow area to simulate strong attenuation caused by the near-surface region.

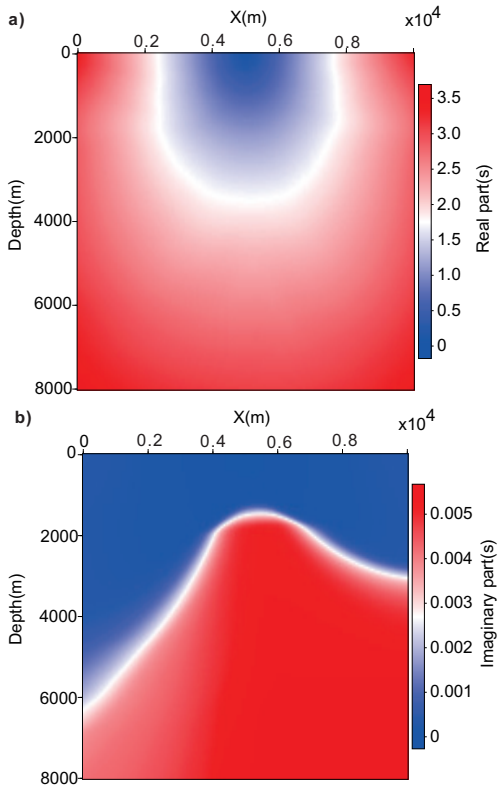

Figure 5.3: The real and imaginary parts of the complex-valued eikonal for the gas clouded attenuating model. (a) Real part; (b) Imaginary part.

The model dimension is 5km in depth and 5km laterally. The grid size is 50m in both x and z directions. The total number of mesh points is 101×101. The source is located at $x = 2500$m and $z = 0$m. Figure (5.7) shows the computed real and imaginary parts of the complex eikonal by the proposed method. The maximum value of the imaginary part in Figure (5.7)b is about 30ms, which shows a very strong attenuation due to the low Q zone in the near-surface region. To validate the result, we also use a wavefield snapshot and a ray-tracing result on a fine grid of mesh size of 10m. Figure (5.8) is the wavefield snapshot overlaid by the contour of the real part at 2s, where the contour matches well with the first-arrival wavefront in the wavefield snapshot. Figure 5.9 shows the comparison between the imaginary parts obtained by the proposed method and the ray-tracing method along two ray paths as shown in Figure (5.6)a, and these two results match well. This demonstrates that

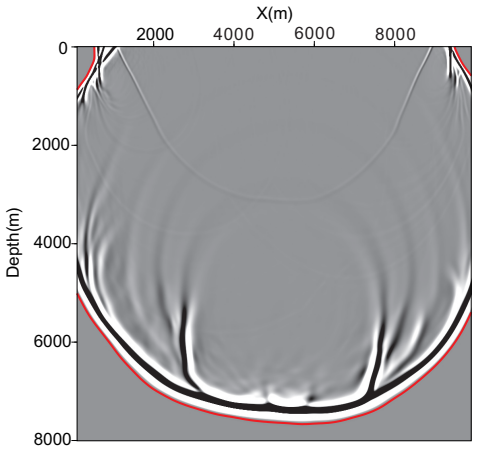

Figure 5.4: Wavefield snapshot overlaid by the contour of the real part at 3s. The red curve is the contour of the real part.

the proposed method produces highly accurate complex eikonals under weakly attenuating approximation.

In the fourth case, we show a 3-D example. We build a 3-D inhomogeneous attenuating model with velocity and Q varying vertically. The velocity and Q models are specified by $v = 1500.0 + 0.5z$ (m/s) and $Q = 50 + 0.016z$, respectively. The model dimension is 5km in the x-, y- and z- directions. The grid size is 50m in the x-, y- and z- directions. The total number of mesh points is $101 \times 101 \times 101$. The source is located at $x = 2500$m, $y = 2500$m and $z = 0$m. Figure (5.10) shows the computed real and imaginary parts of the complex eikonal by the proposed method. This demonstrates that the proposed method performs well in 3-D applications.

5.2.2 Eulerian examples for real-elastic and real-viscoelastic ray tracing

We now apply our proposed real-elastic and viscoelastic Eulerian PDE methods to a particular velocity-attenuation model in [76], which is smoothly inhomogeneous with a constant

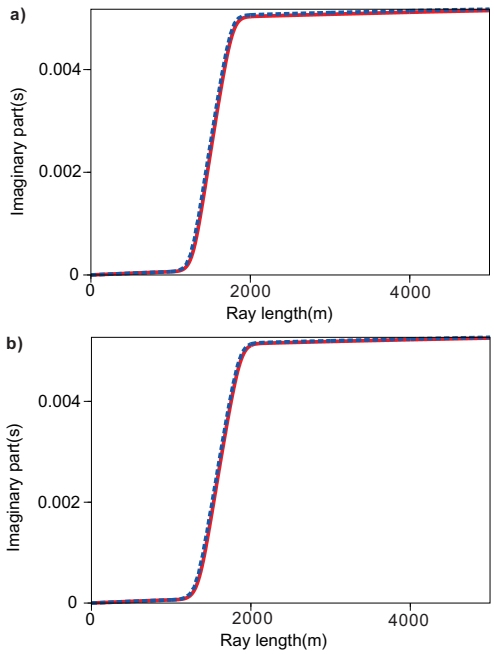

Figure 5.5: Comparison between the imaginary parts obtained by the Eulerian PDE method and the ray-tracing method for the gas clouded attenuating model. The imaginary part for rays with (a) 0° and (b) 20° takeoff angle. The red curve and blue dotted curve are the imaginary parts obtained by the ray tracing method and the Eulerian PDE method, respectively.

gradient of the square of the complex slowness. The model is specified in the following way,

$$c^{-2}(\mathbf{x}) = v_0^{-2} + A_x x + A_z z, \tag{5.41}$$

where v_0 is the background velocity, A_x and A_z are gradients in the x and z direction, respectively. This complex velocity can also be converted into v and Q in equations (5.1) and (5.2) accordingly. [76] also proposes an analytic solution of the complex eikonal to this model by using complex ray tracing.

In our computation, we set the model dimension to be 4km in depth and 10km laterally. We choose the grid size to be 50m in both x and z directions, so that the total number of mesh points is 81×201. The source is located at $x = 0$m and $z = 0$m. We consider two

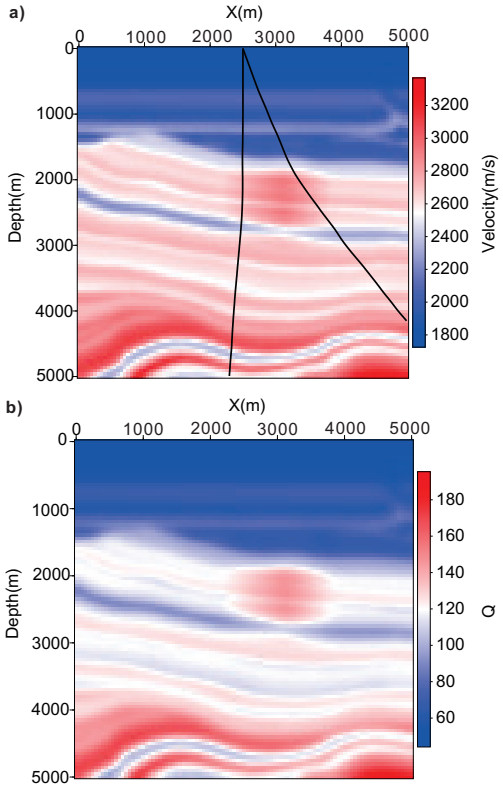

Figure 5.6: The attenuation model for a land scenario. (a) Acoustic velocity; (b) Q. Two black curves in (a) are two ray paths with takeoff angles being 0° and 20°.

cases, Case A and Case B.

In Case A, $v_0 = 1\text{km/s}$, $A_x = 0.1i$, $A_z = 0.0$, and the complex velocity is shown in Figure (5.11). This model is relatively simple with only lateral gradient along the x direction, but its quality factor can take a value as low as 1, which represents strong attenuation. Figures (5.12) and (5.13) are the real and imaginary parts of the complex eikonal computed by our real-elastic and real-viscoelastic Eulerian methods, respectively. To validate these computed results, we also compute their differences with the corresponding analytic solution. Note that we denote these differences according to the relative errors to make them comparable to those in [76]. The differences in Figures (5.12) and (5.13) show that the errors from the real-viscoelastic Eulerian method are less than 0.2%, and the real-viscoelastic Eulerian method yields higher accuracy than the real-elastic Eulerian method in this strongly attenuating

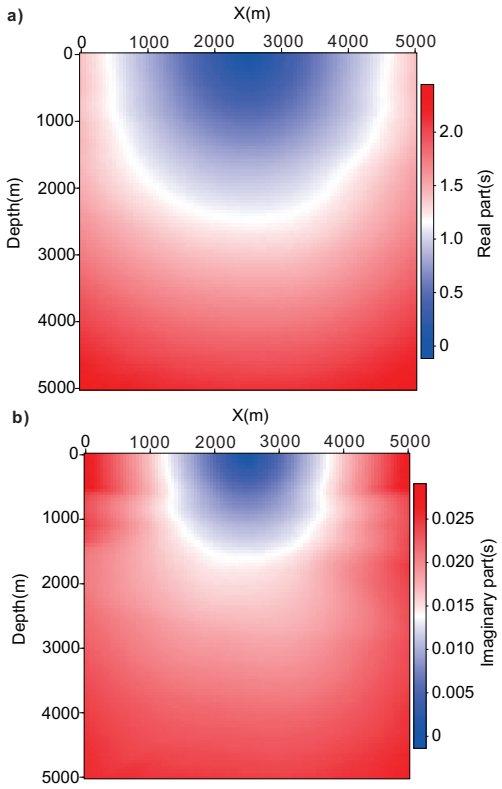

Figure 5.7: The real and imaginary parts of the complex-valued eikonal for the land attenuating model. (a) Real part and (b) Imaginary part.

model. The differences in Figures (5.12) and (5.13) are also comparable to those in [76], which show that the proposed methods can produce results comparable to those from the corresponding ray tracing methods.

In Case B, $v_0 = 1\text{km/s}$, $A_x = 0.1i$, $A_z = -0.15$, and the complex velocity is shown in Figure (5.14). This model becomes more complicated due to non-zero gradients in both x and z directions, and it also represents strong attenuation. Figures (5.15) and (5.16) show the real and imaginary parts of the complex-valued eikonal computed by the real-elastic and real-viscoelastic Eulerian methods, respectively. We also compute their differences with the corresponding analytic solutions. Similarly, in comparison with the solution provided by the exact complex ray-tracing, the real-viscoelastic Eulerian method yields higher accuracy than the real-elastic Eulerian method. Comparing the errors in Case B to those in Case A, we

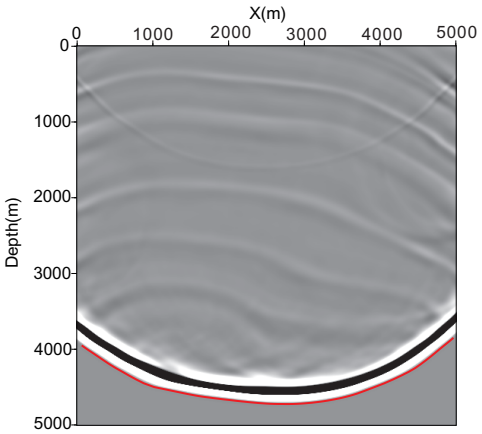

Figure 5.8: Wavefield snapshot overlaid by the contour of the real part at 2s. The red curve is the contour of the real part.

can conclude that the approximation error due to the real-space modeling increases as the model complexity in attenuation increases. The differences in Figures (5.15) and (5.16) are also comparable to those in [76], which show that the proposed methods can produce results comparable to those from the corresponding ray tracing methods.

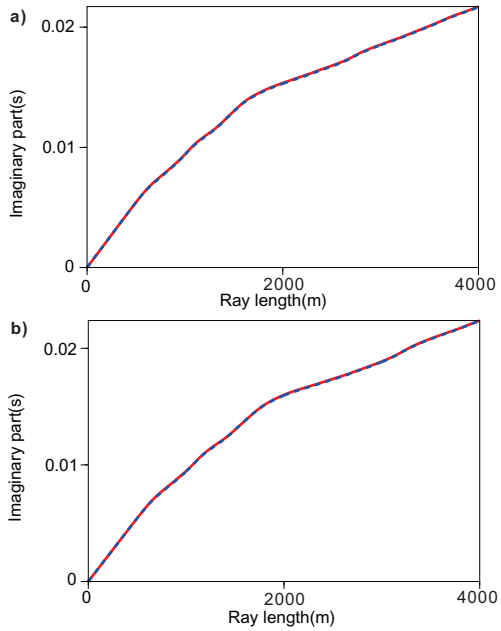

Figure 5.9: Comparison between the imaginary parts obtained by the Eulerian PDE method and the ray tracing method for the land attenuating model. The imaginary parts for rays with (a) 0° and (b) 20° takeoff angle. The red curve and blue dotted curve are the imaginary parts obtained by the ray tracing method and the Eulerian PDE method, respectively.

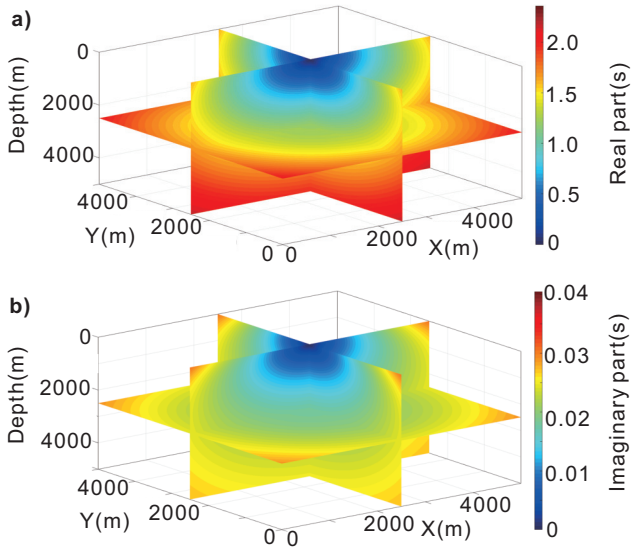

Figure 5.10: The real and imaginary parts of the complex-valued eikonal for the 3-D model. (a) Real part and (b) Imaginary part.

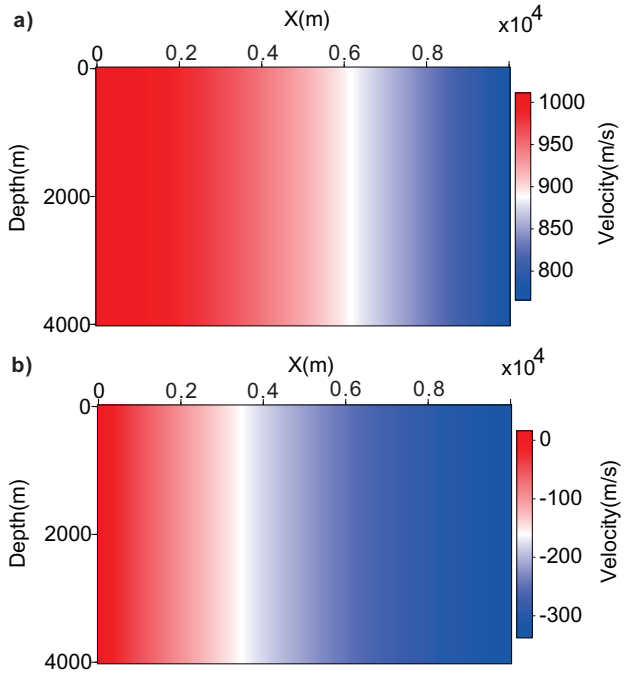

Figure 5.11: (a) Real and (b) Imaginary parts of the complex velocity in Case A.

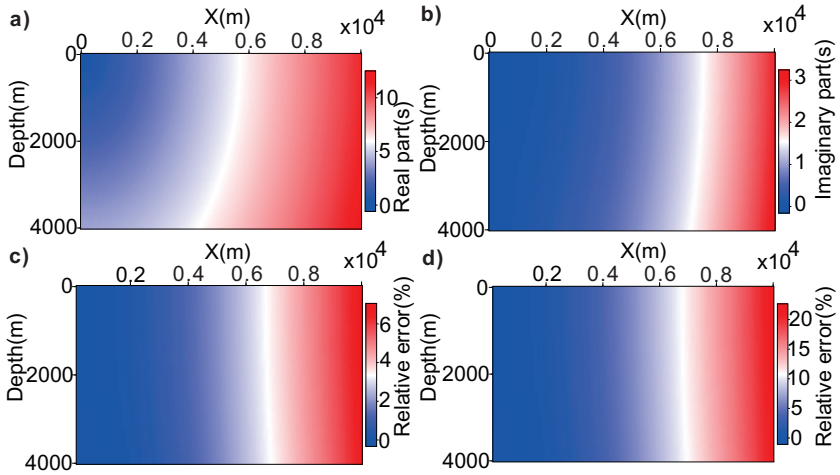

Figure 5.12: The complex-valued eikonal for the real-elastic Eulerian PDE method in Case A. (a) Real part and (c) its difference with the analytic solution; (b) imaginary part and (d) its difference with the analytic solution.

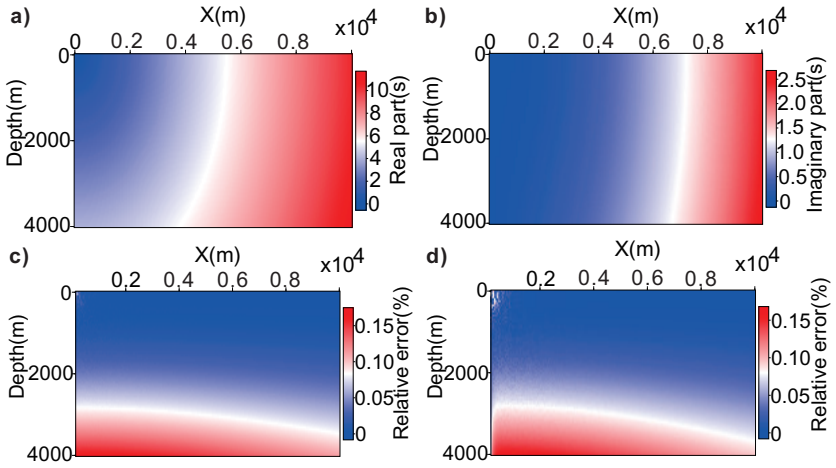

Figure 5.13: The complex-valued eikonal for the real-viscoelastic Eulerian PDE method in Case A. (a) Real part and (c) its difference with the analytic solution; (b) imaginary part and (d) its difference with the analytic solution.

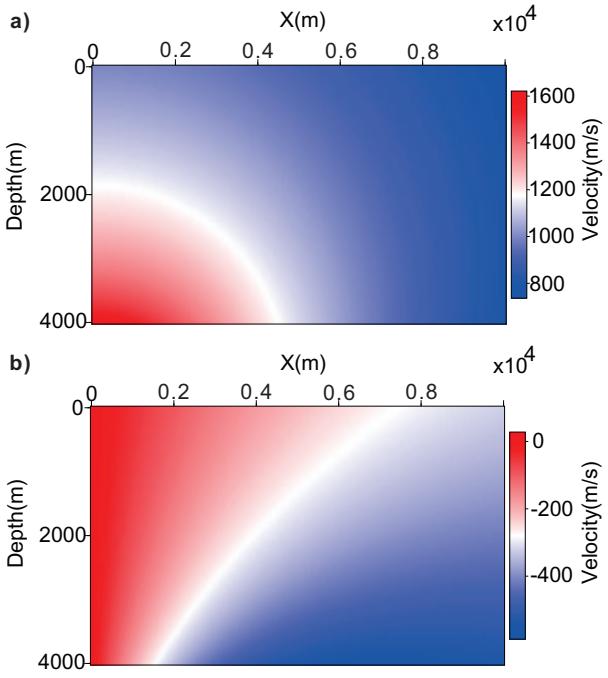

Figure 5.14: (a) Real and (b) imaginary parts of the complex velocity in Case B.

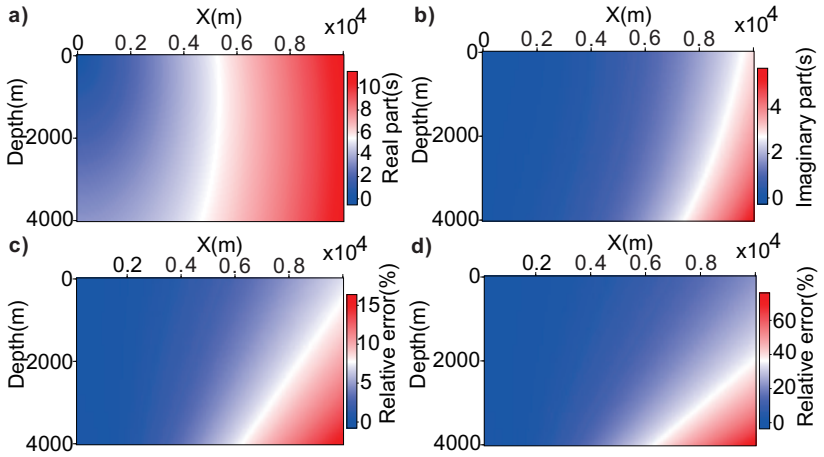

Figure 5.15: The complex-valued eikonal for the real-elastic Eulerian PDE method in Case B. (a) Real part and (c) its difference with the analytic solution; (b) imaginary part and (d) its difference with the analytic solution.

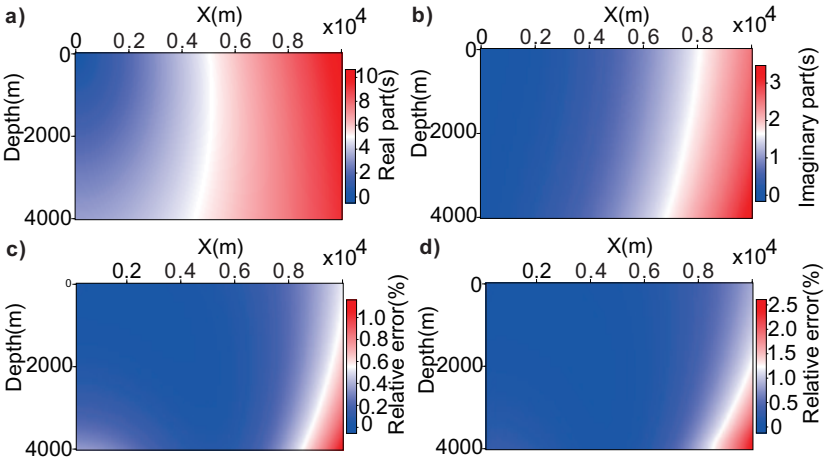

Figure 5.16: The complex-valued eikonal for the real-viscoelastic Eulerian PDE method in Case B. (a) Real part and (c) its difference with the analytic solution; (b) imaginary part and (d) its difference with the analytic solution.

Chapter 6

Conclusion

Based on Hadamard's method, we develop a novel ansatz for the vectorial three-dimensional point-source elastic wave equation in inhomogeneous media at high frequencies. We develop a new Hadamard's ansatz to form the fundamental solution of the Cauchy problem for the time-domain point-source elastic wave equations (3.4) and (3.5) in the region close to the point source. We derive the governing equations for asymptotics involved in the ansatz, such as traveltime and the dyadic coefficients. We further propose matching conditions to deduce initial conditions of amplitude coefficients at the source. Consequently, the Fourier transform of Hadamard's ansatz in time directly yields the Hadamard-Babich ansatz for the FDPS elastic wave equations (3.1). Finally, to validate our method, we truncate the ansatz after two terms and apply high-order Lax-Friedrichs WENO schemes to compute the involved asymptotic ingredients. Numerical results demonstrate that our new ansatz is capable of producing accurate asymptotic solutions in the region of space containing the point source but no other caustics.

Incorporating this new ansatz into Huygens' principle to treat caustics consists of the second project. Starting from the truncated Hadamard-Babich ansatz, we have developed a new fast Huygens sweeping method for computing the globally valid asymptotic Green's functions of elastic wave equations in an inhomogeneous medium in the high frequency regime and in the presence of caustics. The new method uses the Huygens-Kirchhoff integral to integrate

many locally valid asymptotic Green's functions into a globally valid asymptotic Green's function so that caustics can be treated automatically. To accelerate matrix-vector products induced by the Huygens-Kirchhoff integral, we have used the butterfly algorithm to speed up the multiplication process with optimal complexity. Numerical examples demonstrate the performance, efficiency, and accuracy of our new method.

Moreover, we proposed an Eulerian PDE method to compute complex-valued eikonals in attenuating media as an alternative solution to the ray-tracing method. Computing complex-valued eikonals efficiently in attenuating media is essential for seismic imaging and tomography. One major advantage of the proposed Eulerian method is that it computes complex-valued eikonals on regular grids which can be directly used by imaging and tomography methods. Our proposed method uses two Eulerian PDEs to govern the evolution of the real and imaginary parts of complex-valued eikonals. The real-space eikonal equation governs the evolution of the real part of the complex-valued eikonal, and a novel real-space advection equation governs the evolution of the imaginary part of the complex-valued eikonal. The factorization strategy is further applied to obtain factorized Eulerian PDEs to treat source singularities. Furthermore, a third-order LxF WENO sweeping method is proposed to solve these Eulerian PDEs. We applied the proposed Eulerian method to several attenuation models and have obtained satisfying results.

APPENDICES

Appendix A

Derivation of some ingredients for governing equations of S and P waves

The formula of $\tilde{\boldsymbol{R}}^{l-1}$ for the S wave in (3.95)

Let us rewrite the governing equation for $\tilde{\boldsymbol{A}}^l$ as the following,

$$(\nabla\mathcal{T}\cdot\nabla)\tilde{\boldsymbol{A}}^l+\frac{1}{2\mu}[\nabla\cdot(\mu\nabla\mathcal{T})-(4l+14)\rho]\tilde{\boldsymbol{A}}^l+\frac{\mu}{2\rho}\nabla\mathcal{T}\left[\nabla\left(\frac{\rho}{\mu}\right)\cdot\tilde{\boldsymbol{A}}^l\right]=\tilde{\boldsymbol{R}}^{l-1}, \tag{A.1}$$

where

$$\begin{aligned}\tilde{\boldsymbol{R}}^{l-1}=&-\frac{\nabla\mathcal{T}\tilde{\boldsymbol{a}}^{l-1}}{2}\mathcal{T}^{l-1}+\frac{\mu\nabla\mathcal{T}[(\nabla\mathcal{T}\cdot\nabla)\tilde{\boldsymbol{a}}^{l-1}]}{4\rho}\mathcal{T}^{l-1}-\frac{\nabla\mathcal{T}\tilde{\boldsymbol{b}}^{l-1}}{8\rho}\mathcal{T}^{l-1}-\frac{\nabla\lambda\tilde{\boldsymbol{a}}^{l-1}}{2\mu}\mathcal{T}^{l}\\&-\frac{(\lambda+\mu)\nabla\tilde{\boldsymbol{a}}^{l-1}}{2\mu}\mathcal{T}^{l}+\frac{\tilde{\boldsymbol{B}}^{l-1}}{2\mu}\mathcal{T}^{l}.\end{aligned} \tag{A.2}$$

Here $\tilde{\boldsymbol{B}}^{l-1}$, $\tilde{\boldsymbol{a}}^{l-1}$, and $\tilde{\boldsymbol{b}}^{l-1}$ are defined as,

$$\begin{aligned}
\tilde{\boldsymbol{B}}^{l-1} \equiv\ & (\lambda+\mu)\left[\frac{l(l-1)}{\mathcal{T}^{l+1}}\nabla\mathcal{T}(\nabla\mathcal{T}\cdot\tilde{\boldsymbol{A}}^{l-1})-\frac{l-1}{\mathcal{T}^{l}}\nabla(\nabla\mathcal{T}\cdot\tilde{\boldsymbol{A}}^{l-1})\right. \\
& \left.-\frac{l-1}{\mathcal{T}^{l}}\nabla\mathcal{T}(\nabla\cdot\tilde{\boldsymbol{A}}^{l-1})+\frac{1}{\mathcal{T}^{l-1}}\nabla(\nabla\cdot\tilde{\boldsymbol{A}}^{l-1})\right] \\
& +\mu\left[\frac{l(l-1)4\rho}{\mu\mathcal{T}^{l}}\tilde{\boldsymbol{A}}^{l-1}-\frac{(l-1)\nabla^2\mathcal{T}}{\mathcal{T}^{l}}\tilde{\boldsymbol{A}}^{l-1}\right. \\
& \left.-\frac{2(l-1)}{\mathcal{T}^{l}}(\nabla\mathcal{T}\cdot\nabla)\tilde{\boldsymbol{A}}^{l-1}+\frac{1}{\mathcal{T}^{l-1}}\nabla^2\tilde{\boldsymbol{A}}^{l-1}\right] \\
& +\nabla\lambda\left[\frac{-l+1}{\mathcal{T}^{l}}\nabla\mathcal{T}\cdot\tilde{\boldsymbol{A}}^{l-1}+\frac{1}{\mathcal{T}^{l-1}}\nabla\cdot\tilde{\boldsymbol{A}}^{l-1}\right] \\
& +\frac{1}{\mathcal{T}^{l-1}}\nabla\mu\times(\nabla\times\tilde{\boldsymbol{A}}^{l-1})-\frac{l-1}{\mathcal{T}^{l}}\nabla\mu\times(\nabla\mathcal{T}\times\tilde{\boldsymbol{A}}^{l-1}) \\
& +2\left[-\frac{l-1}{\mathcal{T}^{l}}(\nabla\mu\cdot\nabla\mathcal{T})\tilde{\boldsymbol{A}}^{l-1}+\frac{1}{\mathcal{T}^{l-1}}(\nabla\mu\cdot\nabla)\tilde{\boldsymbol{A}}^{l-1}\right]; \qquad \text{(A.3)} \\
\tilde{\boldsymbol{a}}^{l-1} \equiv\ & \frac{-(l-1)}{\mathcal{T}^{l}}\nabla\mathcal{T}\cdot\tilde{\boldsymbol{A}}^{l-1}+\frac{1}{\mathcal{T}^{l-1}}\nabla\cdot\tilde{\boldsymbol{A}}^{l-1}+\frac{1}{(\lambda+\mu)\mathcal{T}^{l-1}}\nabla\mu\cdot\tilde{\boldsymbol{A}}^{l-1} \\
& -\frac{2\mu(l-1)}{(\lambda+\mu)\mathcal{T}^{l}}\nabla\mathcal{T}\cdot\tilde{\boldsymbol{A}}^{l-1}+\frac{\mu^2}{(\lambda+\mu)2\rho\mathcal{T}^{l}}\nabla\mathcal{T}\cdot[(\nabla\mathcal{T}\cdot\nabla)\tilde{\boldsymbol{A}}^{l-1}]-\frac{\mu\tilde{\boldsymbol{b}}^{l-2}}{(\lambda+\mu)4\rho\mathcal{T}}; \qquad \text{(A.4)} \\
\tilde{\boldsymbol{b}}^{l-1} \equiv\ & 2\rho(-2l+7)\tilde{\boldsymbol{a}}^{l-1}-(\lambda+\mu)(\nabla\mathcal{T}\cdot\nabla)\tilde{\boldsymbol{a}}^{l-1}-\mu\nabla^2\mathcal{T}\tilde{\boldsymbol{a}}^{l-1} \\
& -(\nabla\mathcal{T}\cdot\nabla\lambda)\tilde{\boldsymbol{a}}^{l-1}-(\nabla\mathcal{T}\cdot\nabla\mu)\tilde{\boldsymbol{a}}^{l-1}+\nabla\mathcal{T}\cdot\tilde{\boldsymbol{B}}^{l-1}. \qquad \text{(A.5)}
\end{aligned}$$

The formula of $\tilde{\boldsymbol{c}}^{l-1}$ for the P wave in (3.137)

We rewrite the governing equation for $\tilde{\boldsymbol{\alpha}}^{l}$ as the following,

$$\nabla\mathcal{T}\cdot\nabla\tilde{\boldsymbol{\alpha}}^{l}+\left[\frac{1}{2\rho}\nabla\cdot(\rho\nabla\mathcal{T})-\frac{(2l+5)\rho}{\lambda+2\mu}\right]\tilde{\boldsymbol{\alpha}}^{l}=\tilde{\boldsymbol{c}}^{l-1}, \qquad \text{(A.6)}$$

and $\tilde{\boldsymbol{c}}^{l-1} = \mathcal{T}^l \boldsymbol{c}^{l-1}$, where $\boldsymbol{c}^{l-1}$ is the same as (3.123). The formula for $\tilde{\boldsymbol{c}}^{l-1}$ is

$$\begin{aligned}
\tilde{\boldsymbol{c}}^{l-1} \equiv & \frac{1}{8\rho}\{[(14-4l)\rho - \mu\nabla^2\mathcal{T} - \nabla\mathcal{T}\cdot\nabla(\lambda+\mu)]\frac{1}{\mathcal{T}}(\nabla\mathcal{T}\cdot\tilde{\boldsymbol{C}}^{l-1}) \\
& + \frac{(\lambda+\mu)4\rho l}{(\lambda+2\mu)\mathcal{T}}(\nabla\mathcal{T}\cdot\tilde{\boldsymbol{C}}^{l-1}) - \frac{(\lambda+\mu)}{\mathcal{T}}\nabla\mathcal{T}\cdot\nabla(\nabla\mathcal{T}\cdot\tilde{\boldsymbol{C}}^{l-1}) \\
& + \frac{(\lambda+\mu)4\rho l}{(\lambda+2\mu)\mathcal{T}}(\nabla\mathcal{T}\cdot\tilde{\boldsymbol{C}}^{l-1}) - \frac{(\lambda+\mu)4\rho}{(\lambda+2\mu)}(\nabla\cdot\tilde{\boldsymbol{C}}^{l-1}) \\
& + \frac{8\mu\rho l}{(\lambda+2\mu)\mathcal{T}}(\nabla\mathcal{T}\cdot\tilde{\boldsymbol{C}}^{l-1}) - \frac{2\mu}{\mathcal{T}}\nabla\mathcal{T}\cdot[(\nabla\mathcal{T}\cdot\nabla)\tilde{\boldsymbol{C}}^{l-1}] \\
& - \frac{4\rho}{\lambda+2\mu}(\nabla\mu\cdot\tilde{\boldsymbol{C}}^{l-1}) + \mathcal{T}^{l-1}\nabla\mathcal{T}\cdot\tilde{\boldsymbol{D}}^{l-1}\}, \qquad \text{(A.7)}
\end{aligned}$$

where $\tilde{\boldsymbol{C}}^{l-1} = \boldsymbol{C}^{l-1}\mathcal{T}^l$ satisfies

$$\begin{aligned}
\tilde{\boldsymbol{C}}^{l-1} \equiv & \frac{\lambda+2\mu}{(\lambda+\mu)4\rho}\{-\rho(4l-18)\tilde{\boldsymbol{A}}^{l-1} + \frac{(l-1)(\lambda+\mu)}{\mathcal{T}}\nabla\mathcal{T}(\nabla\mathcal{T}\cdot\tilde{\boldsymbol{A}}^{l-1}) \\
& - (\lambda+\mu)\nabla(\nabla\mathcal{T}\cdot\tilde{\boldsymbol{A}}^{l-1}) + \frac{8(l-1)\rho\mu}{\lambda+2\mu}\tilde{\boldsymbol{A}}^{l-1} - 2\mu(\nabla\mathcal{T}\cdot\nabla)\tilde{\boldsymbol{A}}^{l-1} \\
& - \mu\nabla^2\mathcal{T}\tilde{\boldsymbol{A}}^{l-1} - \nabla\lambda(\nabla\mathcal{T}\cdot\tilde{\boldsymbol{A}}^{l-1}) - (\nabla\mu\cdot\nabla\mathcal{T})\tilde{\boldsymbol{A}}^{l-1} + \mathcal{T}^{l-1}\tilde{\boldsymbol{D}}^{l-2}\}, \qquad \text{(A.8)}
\end{aligned}$$

and $\tilde{\boldsymbol{D}}^{l-1}$ satisfies

$$\begin{aligned}\tilde{\boldsymbol{D}}^{l-1} \equiv&(\lambda+\mu)\left[\frac{l(l-1)}{\mathcal{T}^{l+1}}\nabla\mathcal{T}(\nabla\mathcal{T}\cdot\tilde{\boldsymbol{A}}^{l-1})-\frac{l-1}{\mathcal{T}^{l}}\nabla(\nabla\mathcal{T}\cdot\tilde{\boldsymbol{A}}^{l-1})\right.\\&\left.-\frac{l-1}{\mathcal{T}^{l}}\nabla\mathcal{T}(\nabla\cdot\tilde{\boldsymbol{A}}^{l-1})+\frac{1}{\mathcal{T}^{l-1}}\nabla(\nabla\cdot\tilde{\boldsymbol{A}}^{l-1})\right]\\&+\mu\left[\frac{l(l-1)4\rho}{\mu\mathcal{T}^{l}}\tilde{\boldsymbol{A}}^{l-1}-\frac{(l-1)\nabla^2\mathcal{T}}{\mathcal{T}^{l}}\tilde{\boldsymbol{A}}^{l-1}\right.\\&\left.-\frac{2(l-1)}{\mathcal{T}^{l}}(\nabla\mathcal{T}\cdot\nabla)\tilde{\boldsymbol{A}}^{l-1}+\frac{1}{\mathcal{T}^{l-1}}\nabla^2\tilde{\boldsymbol{A}}^{l-1}\right]\\&+\nabla\lambda\left[\frac{-l+1}{\mathcal{T}^{l}}\nabla\mathcal{T}\cdot\tilde{\boldsymbol{A}}^{l-1}+\frac{1}{\mathcal{T}^{l-1}}\nabla\cdot\tilde{\boldsymbol{A}}^{l-1}\right]\\&+\frac{1}{\mathcal{T}^{l-1}}\nabla\mu\times(\nabla\times\tilde{\boldsymbol{A}}^{l-1})-\frac{l-1}{\mathcal{T}^{l}}\nabla\mu\times(\nabla\mathcal{T}\times\tilde{\boldsymbol{A}}^{l-1})\\&+2\left[-\frac{l-1}{\mathcal{T}^{l}}(\nabla\mu\cdot\nabla\mathcal{T})\tilde{\boldsymbol{A}}^{l-1}+\frac{1}{\mathcal{T}^{l-1}}(\nabla\mu\cdot\nabla)\tilde{\boldsymbol{A}}^{l-1}\right].\end{aligned}\tag{A.9}$$

Appendix B

Hadamard ansatz for anisotropic wave equations

Derivation of eikonal equations and transport equations

To develop the Hadamard's ansatz for waves in anisotropic elastic solids, we start with the fundamental equations. Hooke's law states that the stress σ_{ij} is related to the strain e_{kl} through a stiffness tensor C_{ijkl} by the relation

$$\sigma_{ij} = C_{ijkl} e_{kl}. \tag{B.1}$$

Therefore, the motion equation without body force takes the form

$$\rho \frac{\partial^2 \boldsymbol{U}}{\partial t^2} = \nabla \cdot \sigma, \tag{B.2}$$

where $\boldsymbol{U} = (U_i)$ is the displacement vector. By the relation between strain and displacement,

$$e_{kl} = \frac{1}{2}\left(\frac{\partial U_k}{\partial x_l} + \frac{\partial U_l}{\partial x_k}\right), \tag{B.3}$$

and the symmetry of the stiffness tensor, the motion equation leads to the wave equation

$$\rho\frac{\partial^2 U_j}{\partial t^2} = \frac{\partial}{\partial x_i}(C_{ijkl}\frac{\partial U_k}{\partial x_l}). \tag{B.4}$$

Inspired by our work for isotropic elastic waves, we shall seek an asymptotic solution of (B.4) in the following form,

$$\ddot{U}_i(\boldsymbol{x},t) = \sum_{l=0}^{\infty} U_i^l(\boldsymbol{x}) f_+^{(l-3)}(t^2 - \mathcal{T}(\boldsymbol{x})). \tag{B.5}$$

To derive the governing equations for the unknowns U_i^l and $\mathcal{T}$, we shall need $\partial_t^4 U_i$ and spatial derivatives of U_i. Since this is quite similar to our derivations for the isotropic elastic case, we can just use the formulas (3.35)-(3.40) directly. Inserting those formulas into the following equation

$$\rho\frac{\partial^4 U_j}{\partial t^4} = \frac{\partial}{\partial x_i}(C_{ijkl}\frac{\partial \ddot{U}_k}{\partial x_l}), \tag{B.6}$$

which is the second time derivative of (B.4).

Equating individual coefficients of $f_+^{(l-5)}$ to zero successively, we can obtain

$$\begin{aligned} 0 =& 4\rho\mathcal{T}U_j^l - C_{ijkl}\mathcal{T}_{,l}\mathcal{T}_{,i}U_k^l + 2\rho(2l-9)U_j^{l-1} + C_{ijkl,i}\mathcal{T}_{,l}U_k^{l-1} \\ &+ C_{ijkl}\mathcal{T}_{,l}U_{k,i}^{l-1} + C_{ijkl}\mathcal{T}_{,i}U_{k,l}^{l-1} + C_{ijkl}\mathcal{T}_{,li}U_k^{l-1} \\ &- C_{ijkl,i}U_{k,l}^{l-2} - C_{ijkl}U_{k,li}^{l-2}. \end{aligned} \tag{B.7}$$

Setting $l = 0$ and remembering that $\boldsymbol{U}^l = 0$ for $l < 0$, we obtain the Christoffel's equation,

$$(C_{ijkl}\mathcal{T}_{,l}\mathcal{T}_{,i} - 4\rho\mathcal{T}\delta_{jk})U_k^0 = 0, \tag{B.8}$$

which leads to the anisotropic eikonal equation for $\mathcal{T}$,

$$\det(C_{ijkl}\mathcal{T}_{,l}\mathcal{T}_{,i} - 4\rho\mathcal{T}\delta_{jk}) = 0, \tag{B.9}$$

where $\mathcal{T}(\boldsymbol{x}) = \tau^2(\boldsymbol{x})$, and τ is the traveltime. So we can obtain the eikonal equation for $\mathcal{T}$

$$\det(C_{ijkl}\mathcal{T}_{,l}\mathcal{T}_{,i} - 4\rho\mathcal{T}\delta_{jk}) = \det(a_{ijkl}p_l p_i - \delta_{jk}) = 0, \tag{B.10}$$

which is the same as the eikonal equation in [60, 62]. Here $\boldsymbol{p} = (p_i) = \nabla\tau$, $a_{ijkl} = C_{ijkl}/\rho$ are the density-normalized elastic parameters.

Next setting $l = 1$ yields

$$\begin{aligned} 0 =& 4\rho\mathcal{T}U^1_j - C_{ijkl}\mathcal{T}_{,l}\mathcal{T}_{,i}U^1_k - 14\rho U^0_j + C_{ijkl,i}\mathcal{T}_{,l}U^0_k \\ &+ C_{ijkl}\mathcal{T}_{,l}U^0_{k,i} + C_{ijkl}\mathcal{T}_{,i}U^0_{k,l} + C_{ijkl}\mathcal{T}_{,li}U^0_k. \end{aligned} \tag{B.11}$$

By equation (B.8), $\boldsymbol{U}^0$ is a multiple of the normalized eigenvector $\boldsymbol{g}$ of the matrix $(a_{ijkl}p_l p_i)$, $\boldsymbol{U}^0 = U^0\boldsymbol{g}$. By the symmetry of the stiffness tensor C_{ijkl} and equation (B.8), we can obtain the equation for the amplitude U^0,

$$\begin{aligned} 0 =& -14\rho U^0 + C_{ijkl,i}\mathcal{T}_{,l}U^0 g_k g_j \\ &+ C_{ijkl}\mathcal{T}_{,l}(U^0 g_k)_{,i}g_j + C_{ijkl}\mathcal{T}_{,i}(U^0 g_k)_{,l}g_j + C_{ijkl}\mathcal{T}_{,li}U^0 g_k g_j. \end{aligned} \tag{B.12}$$

Verification of (B.9) in an isotropic medium

When the wave propagates in an isotropic medium, the stiffness tensor C_{ijkl} has the following form,

$$C_{ijkl} = \lambda\delta_{ij}\delta_{kl} + \mu(\delta_{ik}\delta_{jl} + \delta_{il}\delta_{jk}). \tag{B.13}$$

This involves only two independent parameters, λ and μ, known as the lamé moduli. So the equation (B.8) reduces to

$$((\lambda+\mu)\mathcal{T}_{,j}\mathcal{T}_{,k} + \mu\mathcal{T}_{,l}\mathcal{T}_{,l} - 4\rho\mathcal{T}\delta_{jk})U_k^0 = 0, \tag{B.14}$$

or, in vector notation,

$$((\lambda+\mu)\nabla\mathcal{T}\nabla\mathcal{T}^T + (\mu\nabla\mathcal{T}\cdot\nabla\mathcal{T} - 4\rho\mathcal{T})\boldsymbol{I})\boldsymbol{U}^0 = 0. \tag{B.15}$$

Since $\nabla\mathcal{T}\nabla\mathcal{T}^T$ is a rank-one matrix, the eigenvalues are $\nabla\mathcal{T}\cdot\nabla\mathcal{T}$, 0 and 0. Hence if $\det((\lambda+\mu)\nabla\mathcal{T}\nabla\mathcal{T}^T + (\mu\nabla\mathcal{T}\cdot\nabla\mathcal{T} - 4\rho\mathcal{T})\boldsymbol{I}) = 0$, we can obtain two eikonal equations,

$$\mu|\nabla\mathcal{T}|^2 = 4\rho\mathcal{T}, \tag{B.16}$$

and

$$(\lambda+2\mu)|\nabla\mathcal{T}|^2 = 4\rho\mathcal{T}. \tag{B.17}$$

The corresponding eigenvectors $\boldsymbol{U}^0 \perp \nabla\mathcal{T}$ for (B.16) and $\boldsymbol{U}^0 \parallel \nabla\mathcal{T}$ for (B.17). We can see that these are actually the two cases that we find in Chapter 3. Hence we have verified equation (B.9).

Appendix C

High-order factorization for computing T^*

According to the ray theory, we have the following relation from the eikonal equation 5.1 and the advection equation 5.2,

$$\frac{dT}{ds} = \frac{1}{v}, \quad \frac{dT^*}{ds} = \frac{1}{vQ}, \tag{C.1}$$

where $\frac{d}{ds}$ corresponds to the tangential derivative along a ray path, and s is arc length.

When v and Q are constants, we can obtain the relation between T and T^*, $T^* = \frac{1}{Q}T$. Therefore, in order to compute high order approximations to T^* near the source (here set at the origin), we factorize T^* as the following:

$$T^* = TT_1^*, \tag{C.2}$$

where the singularity of T^* at the source is captured by T, and so the underlying factor T_1^* is smooth in the neighborhood of the source.

Now inserting the above factorization into equation 5.2 and multiplying both sides by

two, we can obtain the corresponding equation for T_1^*:

$$\nabla T^2 \cdot \nabla T_1^* + \frac{2}{v^2} T_1^* = \frac{2}{v^2 Q}. \tag{C.3}$$

Assuming that $\frac{1}{v^2}$ and $\frac{1}{Q}$ are smooth, we can expand T^2, T_1^*, $\frac{1}{v^2}$ and $\frac{1}{Q}$ into power series near the source as illustrated in [64]:

$$T^2 = \sum_{\nu=0}^{\infty} T_k; \quad T_1^* = \sum_{\nu=0}^{\infty} U_k; \quad \frac{1}{v^2} = \sum_{\nu=0}^{\infty} S_k; \quad \frac{1}{Q} = \sum_{\nu=0}^{\infty} Q_k. \tag{C.4}$$

T_k is given in [64], and we know that $T_0 = 0$, $T_1 = 0$ and $T_2 = S_0 \left|\boldsymbol{x}\right|^2$. Now inserting the above expansions into C.3, we can get

$$\left(\sum_{\nu=2}^{\infty} \nabla T_k\right) \cdot \left(\sum_{\nu=0}^{\infty} \nabla U_k\right) + 2\left(\sum_{\nu=0}^{\infty} S_k\right)\left(\sum_{\nu=0}^{\infty} U_k\right) = 2\left(\sum_{\nu=0}^{\infty} S_k\right)\left(\sum_{\nu=0}^{\infty} Q_k\right). \tag{C.5}$$

We can now equate the p-th degree terms to get the following recursive equation:

$$\sum_{\nu=0}^{p} \nabla T_{p-v+2} \cdot \nabla U_\nu + 2\sum_{\nu=0}^{p} S_{p-\nu} U_\nu = 2\sum_{\nu=0}^{p} S_v Q_{p-\nu}. \tag{C.6}$$

Using the relation $T_2 = S_0 \left|\boldsymbol{x}\right|^2$ and $\nabla T_2 \cdot \nabla U_p = 2pS_0 U_p$, we can obtain the following recursive formulas for $\{U_p\}$ for $p \geq 0$,

$$2(p+1)S_0 U_p = 2\sum_{\nu=0}^{p} S_v Q_{p-\nu} - \sum_{\nu=0}^{p-1} \nabla T_{p-v+2} \cdot \nabla U_\nu - 2\sum_{\nu=0}^{p-1} S_{p-\nu} U_\nu. \tag{C.7}$$

We list some special cases for $p = 0, 1, 2, 3, 4, 5$.

$$p = 0: \qquad 2S_0U_0 = 2S_0Q_0 \;\Rightarrow\; U_0 = Q_0; \tag{C.8}$$

$$p = 1: \qquad 4S_0U_1 = 2S_0Q_1 + 2S_1Q_0 - 2S_1U_0 \;\Rightarrow\; U_1 = \frac{1}{2}Q_1; \tag{C.9}$$

$$\begin{aligned} p = 2: \qquad & 6S_0U_2 = 2(S_0Q_2 + S_1Q_1 + S_2Q_0) - \nabla T_3 \cdot \nabla U_1 - 2(S_2U_0 + S_1U_1) \\ & \Rightarrow\; U_2 = \frac{Q_2}{3} + \frac{S_1Q_1}{6S_0} - \frac{\nabla T_3 \cdot \nabla Q_1}{12S_0}; \end{aligned} \tag{C.10}$$

$$\begin{aligned} p = 3: \qquad & 8S_0U_3 = 2(S_0Q_3 + S_1Q_2 + S_2Q_1 + S_3Q_0) - \nabla T_4 \cdot \nabla U_1 - \nabla T_3 \cdot \nabla U_2 \\ & -2(S_3U_0 + S_2U_1 + S_1U_2) \\ & \Rightarrow\; U_3 = \frac{Q_3}{4} + \frac{S_1Q_2}{4S_0} + \frac{S_2Q_1}{8S_0} - \frac{S_1U_2}{4S_0} - \frac{\nabla T_4 \cdot \nabla Q_1}{16S_0} - \frac{\nabla T_3 \cdot \nabla U_2}{8S_0}; \end{aligned} \tag{C.11}$$

$$\begin{aligned} p = 4: \qquad & 10S_0U_4 = 2(S_0Q_4 + S_1Q_3 + S_2Q_2 + S_3Q_1 + S_4Q_0) - \nabla T_5 \cdot \nabla U_1 - \nabla T_4 \cdot \nabla U_2 \\ & -\nabla T_3 \cdot \nabla U_3 - 2(S_4U_0 + S_3U_1 + S_2U_2 + S_1U_3) \\ & \Rightarrow\; U_4 = \frac{Q_4}{5} + \frac{S_1Q_3}{5S_0} + \frac{S_2Q_2}{5S_0} + \frac{S_3Q_1}{10S_0} - \frac{S_2U_2}{5S_0} - \frac{S_1U_3}{5S_0} \\ & -\frac{\nabla T_5 \cdot \nabla Q_1}{20S_0} - \frac{\nabla T_4 \cdot \nabla U_2}{10S_0} - \frac{\nabla T_3 \cdot \nabla U_3}{10S_0}. \end{aligned} \tag{C.12}$$

BIBLIOGRAPHY

BIBLIOGRAPHY

[1] K. Aki and P. Richards. *Quantitative seismology*. Freeman and Co., 1980.

[2] G. S. Avila and J. B. Keller. The high-frequency asymptotic field of a point source in an inhomogeneous medium. *Commun. Pure Appl. Math.*, 16:363–381, 1963.

[3] V. M. Babich. The short wave asymptotic form of the solution for the problem of a point source in an inhomogeneous medium. *USSR Computational Mathematics and Mathematical Physics*, 5(5):247–251, 1965.

[4] I. M. Babuška and S. A. Sauter. Is the pollution effect of the FEM avoidable for the Helmholtz equation considering high wave numbers? *SIAM Review*, 42:451–484, 2000.

[5] A. Bayliss, C. I. Goldstein, and E. Turkel. On accuracy conditions for the numerical computation of waves. *J. Comput. Phys.*, 59:396–404, 1985.

[6] J.-D. Benamou. Direct solution of multi-valued phase-space solutions for Hamilton-Jacobi equations. *Commun. Pure Appl. Math.*, 52:1443–1475, 1999.

[7] J. Blanch, J. Robertsson, and W. Symes. Modeling of a constant q: methodol- ogy and algorithm for an efficient and optimally inexpensive viscoelastic technique. *Geophysics*, 60:176–184, 1995.

[8] J. O. Blanch and J. O. A. Robertsson. A modified Lax-Wendroff correction for wave propagation in media described by Zener elements. *Geophys. J. Internat.*, 131:381–386, 1997.

[9] M. Born and E. Wolf. *Principles of optics*. The Macmillan Company, 1964.

[10] J. P. Boyd. *Chebyshev and Fourier Spectral Methods*. Second edition, Dover, New York, 2001.

[11] E. Candes, L. Demanet, and L. Ying. A fast butterfly algorithm for the computation of Fourier integral operators. *SIAM Multiscale Model. Simul.*, 7:1727–1750, 2009.

[12] J. M. Carcione. Staggered mesh for the anisotropic and viscoelastic wave equation. *Geophysics*, 64:1863 –1866, 1999.

[13] J. M. Carcione. Theory and modeling of constant-Q P- and S-waves using fractional time derivatives. *Geophysics*, 74(1):T1 –T11, 2009.

[14] J. M. Carcione. *Wave fields in real media: Theory and numerical simulation of wave propagation in anisotropic, anelastic, porous and electromagnetic media: Handbook of Geophysical exploration (3rd ed.)*. Elsevier, 2015.

[15] J. M. Carcione, F. Cavallini, F. Mainardi, and A. Hanyga. Time domain seismic modeling of constant-Q wave propagation using fractional derivatives. *Pure and Applied Geophysics*, 159:1719 –1736, 2002.

[16] V. Cerveny. *Seismic Ray Theory*. Cambridge University Press, Cambridge, 2001.

[17] R. Courant and D. Hilbert. *Methods of mathematical physics*, volume II. John Wiley-Sons, 1962.

[18] L. Demanet, M. Ferrara, N. Maxwell, J. Poulson, and L. Ying. A butterfly algorithm for synthetic aperture radar imaging. *SIAM J. Imaging Sci.*, 5:203–243, 2012.

[19] J. Fang, J. Qian, L. Zepeda-Nunez, and H. Zhao. A hybrid approach to solve the high-frequency Helmholtz equation with source singularity in inhomogeneous media. *J. Comp. Phys.*, 371:261–279, 2018.

[20] S. Fomel, S. Luo, and H. K. Zhao. Fast sweeping method for the factored eikonal equation. *J. Comput. Phys.*, 228:6440–6455, 2009.

[21] F. G. Friedlander. Private communication to Robert Burridge, 1966.

[22] W. Futterman. Dispersive body waves. *Journal of the Geophysical Research*, 67:5279 –5291, 1962.

[23] D. Gajewski and I. Psencik. Vector wavefields for weakly attenuating anisotropic media by the ray method. *Geophysics*, 57(1):27 –38, 1992.

[24] I.M. Gelfand and G.E. Shilov. *Generalized Functions*, volume 1. Academic Press, New York and London, 1964.

[25] J. Hadamard. *Lectures on Cauchy's Problem in Linear Partial Differential Equations*. Yale University Press; (reprinted Dover Publications, New York 1952), 1923.

[26] Q. Hao and T. Alkhalifah. An acoustic eikonal equation for attenuating transversely isotropic media with a vertical symmetry axis. *Geophysics*, 82(1):C9 –C20, 2017.

[27] J. Hu, J. Qian, J. Song, M. Ouyang, J. Cao, and Sh. Leung. Eulerian partial-differential-equation methods for complex-valued eikonals in attenuating media. *GEOPHYSICS*, 86(4):T179–T192, 2021.

[28] J. T. Hu, P. Wang, J. X. Cao, H. Z. Wang, and X. J. Wang. Frequency dependent complex traveltime computation in TI media with weak attenuation using Fermat's principle based fast marching. pages 4040–4044, 2018.

[29] X. Huang and S. Greenhalgh. Linearized formulations and approximate solutions for the complex eikonal equation in orthorhombic media and applications of complex seismic traveltime. *Geophysics*, 83(3):C115 –C136, 2018.

[30] X. Huang, J. Sun, and S. Greenhalgh. On the solution of the complex eikonal equation in acoustic VTI media: a perturbation plus optimization scheme. *Geophysical Journal International*, 214(2):907 –932, 2018.

[31] G. S. Jiang and D. Peng. Weighted ENO schemes for Hamilton-Jacobi equations. *SIAM J. Sci. Comput.*, 21:2126–2143, 2000.

[32] G. S. Jiang and C. W. Shu. Efficient implementation of weighted ENO schemes. *J. Comput. Phys.*, 126:202–228, 1996.

[33] C. Y. Kao, S. Osher, and J. Qian. Legendre transform based fast sweeping methods for static Hamilton-Jacobi equations on triangulated meshes. *J. Comput. Phys.*, 227:10209–10225, 2008.

[34] C. Y. Kao, S. J. Osher, and J. Qian. Lax-Friedrichs sweeping schemes for static Hamilton-Jacobi equations. *J. Comput. Phys.*, 196:367–391, 2004.

[35] F.C. Karal Jr. and J. B. Keller. Elastic wave propagation in homogeneous and inhomogeneous media. *J. Acoust. Soc. Am.*, 31(6):694–705, 1959.

[36] H. Keers, D. W. Vasco, and L. R. Johnson. Viscoacoustic crosswell imaging using asymptotic waveforms. *Geophysics*, 66(3):861 –870, 2001.

[37] J. Keller and R. Lewis. Asymptotic methods for partial differential equations: the reduced wave equation and Maxwell's equations. *Surv. in Appl. Math.*, 1:1–82, 1995.

[38] S. Kim and R. Cook. 3-D traveltime computation using second-order ENO scheme. *Geophysics*, 64:1867–1876, 1999.

[39] M. Klimes and L. Klimes. Perturbation expansions of complex-valued traveltime along real-valued reference rays. *Geophysical Journal International*, 186:751 –759, 2011.

[40] P. L. Lions. *Generalized solutions of Hamilton-Jacobi equations*. Pitman Advanced Publishing Program, 1982.

[41] X. D. Liu, S. J. Osher, and T. Chan. Weighted Essentially NonOscillatory schemes. *J. Comput. Phys.*, 115:200–212, 1994.

[42] Y. Liu, J. Song, R. Burridge, and J. Qian. A fast butterfly-compressed hadamard-babich integrator for high-frequency helmholtz equations in inhomogeneous media with arbitrary sources. *Multiscale Modeling and Simulation, accepted*, 2022.

[43] W. Lu, J. Qian, and R. Burridge. Babich-expansion based fast Huygens sweeping methods for point-source Helmholtz equations. In *SEG full Waveform Inversion: Depth Model Building Workshop (FWI 2015)*, pages 98–101. Society for Exploration Geophysicists, 2015.

[44] W. Lu, J. Qian, and R. Burridge. Babich-like ansatz for three-dimensional point-source Maxwell's equations in an inhomogeneous medium at high frequencies. *SIAM J. Multiscale Model. Simul.*, 14(3):1089–1122, 2016.

[45] W. Lu, J. Qian, and R. Burridge. Babich's expansion and the fast Huygens sweeping method for the Helmholtz wave equation at high frequencies. *J. Comput. Phys.*, 313:478–510, 2016.

[46] W. Lu, J. Qian, and R. Burridge. Extending Babich's ansatz for point-source Maxwell's equations using Hadamard's method. *SIAM J. Multiscale Model. Simul.*, 16:727–751, 2018.

[47] S. Luo and J. Qian. Factored singularities and high-order Lax-Friedrichs sweeping schemes for point-source traveltimes and amplitudes. *J. Comput. Phys.*, 230:4742–4755, 2011.

[48] S. Luo and J. Qian. Fast sweeping methods for factored anisotropic eikonal equations: multiplicative and additive factors. *J. Sci. Comput.*, 52:360–382, 2012.

[49] S. Luo, J. Qian, and R. Burridge. Fast Huygens sweeping methods for Helmholtz equations in inhomogeneous media in the high frequency regime. *J. Comput. Phys.*, 270:378–401, 2014.

[50] S. Luo, J. Qian, and R. Burridge. High-order factorization based high-order hybrid fast sweeping methods for point-source eikonal equations. *SIAM J. Numer. Analy.*, 52:23–44, 2014.

[51] S. Luo, J. Qian, and H.-K. Zhao. Higher-order schemes for 3-D traveltimes and amplitudes. *Geophysics*, 77:T47–T56, 2012.

[52] J. Milnor. *Morse Theory. Annals of Math., No. 51.* Princeton University Press, Princeton, New Jersey, 1973.

[53] S. J. Osher and C. W. Shu. High-order Essentially NonOscillatory schemes for Hamilton-Jacobi equations. *SIAM J. Numer. Analy.*, 28:907–922, 1991.

[54] A. Pica. Fast and accurate finite-difference solutions of the 3-D eikonal equation parameterized in celerity. In *Expanded Abstracts*, pages 1774–1777. Soc. Expl. Geophys., Tulsa, OK, 1997.

[55] P. Podvin and I. Lecomte. Finite difference computation of traveltimes in very contrasted velocity models: a massively parallel approach and its associated tools. *Geophys. J. Int.*, 105:271–284, 1991.

[56] J. Qian, W. Lu, L. Yuan, S. Luo, and R. Burridge. Eulerian geometrical optics and fast Huygens sweeping methods for three-dimensional time-harmonic high-frequency Maxwell's equations in inhomogeneous media. *SIAM J. Multiscale Modeling and Simulation*, 16:595–636, 2016.

[57] J. Qian, S. Luo, and R. Burridge. Fast Huygens sweeping methods for multi-arrival Green's functions of Helmholtz equations in the high frequency regime. *Geophysics*, 80:T91–T100, 2015.

[58] J. Qian, J. Song, W. Lu, and R. Burridge. Hadamard–babich ansatz for point-source elastic wave equations in variable media at high frequencies. *Multiscale Modeling & Simulation*, 19(1):46–86, 2021.

[59] J. Qian, J. Song, W. Lu, and R. Burridge. Truncated hadamard-babich ansatz and fast huygens sweeping methods for time-harmonic elastic wave equations in inhomogeneous media in the asymptotic regime. *Minimax Theory and its Applications, accepted*, 2022.

[60] J. Qian and W. W. Symes. Paraxial eikonal solvers for anisotropic quasi-P traveltimes. *J. Comput. Phys.*, 173:1–23, 2001.

[61] J. Qian and W. W. Symes. An adaptive finite difference method for traveltime and amplitude. *Geophysics*, 67:167–176, 2002.

[62] J. Qian and W. W. Symes. Finite-difference quasi-P traveltimes for anisotropic media. *Geophysics*, 67:147–155, 2002.

[63] J. Qian, L. Yuan, Y. Liu, S. Luo, and R. Burridge. Babich's expansion and high-order Eulerian asymptotics for point-source Helmholtz equations. *Journal of Scientific Computing*, 65:1–26, 2015.

[64] J. Qian, L. Yuan, Y. Liu, S. Luo, and R. Burridge. Babich's expansion and high-order Eulerian asymptotics for point-source Helmholtz equations. *Journal of Scientific Computing*, 67:883–908, 2016.

[65] J. Qian, Y. T. Zhang, and H. K. Zhao. Fast sweeping methods for eikonal equations on triangulated meshes. *SIAM J. Numer. Analy.*, 45:83–107, 2007.

[66] J. Qian, Y. T. Zhang, and H. K. Zhao. Fast sweeping methods for static convex Hamilton-Jacobi equations. *J. Sci. Comp.*, 31:237–271, 2007.

[67] F. Qin, Y. Luo, K. B. Olsen, W. Cai, and G. T. Schuster. Finite difference solution of the eikonal equation along expanding wavefronts. *Geophysics*, 57:478–487, 1992.

[68] J. O. A. Robertsson, J. O. Blanch, and W. W. Symes. Viscoelastic finite-difference modeling. *Geophysics*, 59:1444–1456, 1994.

[69] S. Serna and J. Qian. A stopping criterion for higher-order sweeping schemes for static Hamilton-Jacobi equations. *J. Comput. Math.*, 28:552–568, 2010.

[70] J. A. Sethian and A. M. Popovici. 3-D traveltime computation using the fast marching method. *Geophysics*, 64:516–523, 1999.

[71] W. W. Symes and J. Qian. A slowness matching Eulerian method for multivalued solutions of eikonal equations. *J. Sci. Comp.*, 19:501–526, 2003.

[72] A. Toflove and S. C. Huganess. *Computational Electrodynamics: The Finite Difference Time Domain Method, Second Editions*. Artech House, Norwood, MA, 2000.

[73] J. van Trier and W. W. Symes. Upwind finite-difference calculation of traveltimes. *Geophysics*, 56:812–821, 1991.

[74] V. Vavrycuk. Real ray tracings in anisotropic viscoelastic media. *Geophysical Journal International*, 175:617 –626, 2008.

[75] V. Vavrycuk. Velocity, attenuation and quality factor in anisotropic viscoelastic media: A perturbation approach. *Geophysics*, 73(5):D63 –D73, 2008.

[76] V. Vavrycuk. On numerically solving the complex eikonal equation using real ray-tracing methods: A comparison with the exact analytical solution. *Geophysics*, 77(4):T109 – T116, 2012.

[77] J. Vidale. Finite-difference calculation of travel times. *Bull. Seis. Soc. Am.*, 78:2062–2076, 1988.

[78] U. Waheed, C. E. Yarman, and G. Flagg. An iterative, fast-sweeping-based eikonal solver for 3D tilted anisotropic media. *Geophysics*, 80(3):C49 –C58, 2015.

[79] B. S. White. The stochastic caustic. *SIAM J. Appl. Math.*, 44:127–149, 1984.

[80] Y. Xie, J. Sun, Y. Zhang, and J. Zhou. Compensating for visco-acoustic effects in TTI reverse time migration. pages 3996–4001, 2015.

[81] Y. Xie, K. Xin, J. Sun, and C. Notfors. 3D prestack depth migration with compensation for frequency dependent absorption and dispersion. pages 2919–2913, 2009.

[82] K. F. Xin, Y. He, Y. Xie, W. Q. Xu, and M. Wang. Robust Q tomographic inversion through adaptive extraction of spectral features. pages 3726–3730, 2014.

[83] T. Xiong, M. Zhang, Y. T. Zhang, and C.-W. Shu. Fast sweeping fifth order weno scheme for static hamilton-jacobi equations with accurate boundary treatment. *J. Sci. Comput.*, 45:514–536, 2010.

[84] L. Ying. Sparse Fourier transform via butterfly algorithm. *SIAM J. Sci. Comput.*, 31:1678–1694, 2009.

[85] L. Zhang, J. W. Rector, and G. M. Hoversten. Eikonal solver in the celerity domain. *Geophys. J. Internat.*, 162:1–8, 2005.

[86] Y. Zhang, P. Zhang, and H. Zhang. Compensating for visco-acoustic effects in reverse time migration. pages 3160–3164, 2010.

[87] Y. T. Zhang, H. K. Zhao, and J. Qian. High order fast sweeping methods for static Hamilton-Jacobi equations. *J. Sci. Comp.*, 29:25–56, 2006.

[88] H. K. Zhao. Fast sweeping method for eikonal equations. *Math. Comp.*, 74:603–627, 2005.